RESEARCH AND DEVELOPMENT OF SUPER PERMEABILITY NiFe/Cu COMPOSITE WIRES FOR MICRO MAGNETIC SENSORS

SEET HANG LI

(B.Eng. (Hons.), NUS)

A THESIS SUBMITTED

FOR THE DEGREE OF DOCTOR OF PHILOSOPHY

DEPARTMENT OF MECHANICAL ENGINEERING

NATIONAL UNIVERSITY OF SINGAPORE

2008

Acknowledgements

The author will like to express his utmost sincere gratitude to Prof. Li Xiaoping (*National University of Singapore*) for providing undivided attention and inspiring guidance throughout the entire project, without which this project could not be completed successfully.

The author will also like to offer special thanks to Dr. Zhao Zhenjie (*East China Normal University, Shanghai*) for his valued guidance and important advices, A/Prof. Lee Kim Seng (*National University of Singapore*) for his invaluable advices and important technical contributions to the project, Dr. N.S. Perov (*Moscow State University, Moscow*), Dr. A.B. Granosky (*Moscow State University, Moscow*), Dr. A.S. Antonov (*Institute of Theoretical and Applied Electrodynamics (ITAE), Moscow*) for their precious guidance during the student exchange period as well as their invaluable discussions on matters of magnetism, Dr. E.E. Shalyguina (*Moscow State University, Moscow*) for discussing, performing and analysing magneto-optical measurements on developed composite wires, Ms. See Shu Hui, Dr. Yi Jiabao, Mr. Fan Jie, Mr. Ning Ning, Mr. Ng Wu Chun for their precious discussions and assistance in executing the project, former undergraduate students for their important and wonderful contributions to the project, staff from Advanced Manufacturing Laboratory (AML) and Workshop 2 for their valuable assistance in developing some of the experimental setups and all others who have contributed to this project.

Finally, the author will also like to express his gratitude to his family who has constantly offered tremendous support throughout the execution of this project.

Table of Contents

Summary

Extremely high permeability magnetic materials are essential as sensing elements for ultra-weak magnetic field detection sensors. Enhancement in the magnetic permeability of sensing elements will result in improvements in sensing performance of magnetic sensors. Thus, to obtain super permeability magnetic materials and therefore ideal sensing elements, the project focuses on investigations and optimization of fabrication processes.

The investigations were carried out on $Ni_{80}Fe_{20}$/Cu micro composite wires due to near-zero magnetostriction and high initial permeability of $Ni_{80}Fe_{20}$, and high sensing performance arising from wire structures. An extensive literature review was conducted. The research approach was considered and implemented. Parametric investigations on plating current density, pH value, coating thickness and alloying effect of molybdenum were conducted on DC electrodeposited NiFe/Cu composite wires. Localized magnetic properties and magnetic domains of DC electrodeposited NiFe/Cu composite wires were investigated. Nanocrystalline grain size of deposited NiFe layers was controlled through saccharin addition and plating current manipulation. Effect of imposed longitudinal magnetic field during DC electrodeposition was conducted. Properties of annealed wires were characterized to obtain optimum annealing conditions. Cold-drawn and magnetron sputtered NiFe/Cu composite wires were developed and magnetic properties compared within different methods.

It was revealed that in composite NiFe/Cu wires, there are circular domains with alternating left- and right-handled magnetization in adjacent domains, with size of circular domains and saturation field dependent on Fe%. A critical value of plating current density was found, below which soft magnetic properties decreased and above

which soft magnetic properties increased, with increasing current density. Electrolyte pH value was found to affect plated layer composition. Coercivity can be in a dynamic constant state as the coating thickness varies. Under such circumstance, coating thickness has mainly geometrical effect on MI effect of composite wires. The magnetic properties of $Ni_{78}Fe_{18}Mo_4$ have been found to be much better than $Ni_{79}Fe_{21}$. The coercivity of nanocrystalline permalloy decreases and MI effect increases as grain size decreases from 52 nm to 11 nm. For pulse-reverse electrodeposition, reducing anodic current amplitude resulted in lower coercivity and larger MI effect. Introducing an off-time period to plating current reduces average crystallite sizes of deposited material. An imposed longitudinal magnetic field during electroplating makes composition more uniform, enhances uniformity and therefore increases magnetic softness. This field shifts the magnetic anisotropy from circumferential to longitudinal, with level of anisotropy change proportional to field intensity. For furnace annealing, as annealing temperature was increased, reduction in MI% ratio and sensitivity as well as increase in coercivity was observed, due to permeability decrease that was attributed to grain growth and inter-diffusion, despite stress relief effects. For DC joule annealing, the highest MI ratio of 1110% was obtained. For cold-drawing of composite wires, ratio of NiFe:Cu has been found to remain unchanged. During final anealing, an optimum annealing temperature was found. The coercivities of composite wires, fabricated by different methods, decrease as the grain size decreases. However, since different deposition methods produce specimens of varying level of residual stress and uniformity, the range of the coercivity trends is according to the deposition methods used.

List of Tables

List of Figures

List of Symbols

a	inter-atomic distance
a_l	Lattice constant
a_s	Plated Surface Area
A	Exchange stiffness
A_{const}	Exchange constant
A_{wt}	Atomic weight of metal
b	Number of coil layers
B	Magnetic flux density
CE	Current Efficiency
C_{Fe}	Content of Fe
d	Density of deposit
DC	Critical diameter for single domain
D	Grain size
D_{diff}	Diffusion coefficient
e	Charge of a single electron
E_a	Anisotropy energy
E_e	Exchange energy per unit volume
E_{ex}	Exchange energy
F	Faraday Constant
F_D	Drawing Stress
h	Thickness
h_p	Planck constant
H_c	Coercivity
H_k	Anisotropy field
H_s	Saturation field
H_0	Static magnetic field
H_{max}	Maximum magnetic field
H_{ex}	External magnetic field
I	Current
I_{ac}	Harmonic current
I_A	Plating anodic current

J	Plating current density
J_m	Average current density
J_p	Pulsed current density
k	Strength constant
K	Anisotropy constant
K_B	Boltzmann constant
K_1	Magnetocrystalline anisotropy
K_u	Uniaxial anisotropy constant
L_{ex}	Ferromagnetic exchange length
L_i	Internal inductance
m	Length of the magnetic moments
m_e	Mass of electron
M_s	Saturation magnetization
M_r	Remanence magnetization
n	Strain hardening exponent
n_e	Number of electrons
n_i	An integer representing the order of the diffraction peak
N	Number of cycles
P_{Ar}	Argon pressure
Q	Electrical Charge (coulomb)
R	Resistance
R_{DC}	DC resistance
S	Surface of conductor
t	Time (in seconds)
t_{FM}	Coating thickness of ferromagnetic material
t_{pp}	Single period cycle
T_c	Curie temperature
T_{on}	Pulse duration (on-time)
T_{off}	Interval between two pulses (off-time)
T_s	Substrate temperature
T_m	Coating material melting point
T_A	Annealing Temperature
U_{ac}	Harmonic voltage
U_R	Resistive voltage

U_L	Inductive voltage
V	Volume of the deposit
w	Weight
w_{wall}	Domain wall width
X	Reactance
Z	Impedance
Z_e	Electrochemical equivalent
α	Approach angle
β	Positive constant for ferromagnetism
χ	Susceptibility
μ	Permeability
μ_i	Initial permeability
μ_0	Permeability of free space
μ_ϕ	Circumferential permeability
μ_t	Transverse permeability
μ_f	Friction coefficient
δ_0	Critical radius
δ_p	Thickness of pulsating diffusion layer
δ_s	Thickness of the stationary diffusion layer
σ_{tm}	Mean true flow stress
ε	Energy per unit volume
γ	Total energy per unit area
ν	Pulse frequency
ν_{cr}	Volume fraction
ω	Circular frequency
ρ	Resistivity
δ	Skin depth
$\hat{\zeta}$	2x2 surface impedance tensor
λ	Wavelength (in angstroms)
Δp	Uncertainty momentum
σ	Electrical conductivity

Chapter 1 Introduction

1.1. Motivation

In the development of extremely high sensitivity, very weak magnetic field bio-sensors, extremely magnetically soft materials are essential as sensing elements. At sufficiently high sensitivity, these magnetic sensors can be used, with immense effect, in magnetoencephalography (MEG) for brain wave monitoring in bio-applications or in magnetic signature detection in defense related applications. Composite wires $Ni_{80}Fe_{20}$/Cu have so far displayed promising potential to achieve the extremely high sensitivity as required by the sensing element in biosensors. This high permeability and high sensitivity properties can be affected by key factors, such as the material composition, nanocrystalline grain size, coating thickness, level of residual stress and anisotropy. $Ni_{80}Fe_{20}$ has high initial permeability and near-zero magnetostriction. According to the random anisotropy model (RAM), below a critical grain size as the nanocrystalline grain size decrease, the coercivity of the ferromagnetic material will decrease.

The careful selection of the fabrication process as well as optimization of the process parameters can lead to optimized performance of the sensing elements in magnetic sensors. Currently, composite wires can be fabricated by three main approaches: namely, electrodeposition, cold-drawing and magnetron sputtering. The electrodeposition method is reported to be capable of producing specimens of superior material and magnetic properties, although the method faces problems of consistency. The sputtering method is capable of depositing uniform layers, but it faces the limitation of weak adhesion and high stress of deposited material, leading to the

deposition of only very thin (less than 1μm) layers. The cold-drawing method can achieve consistent specimens. However, the process requires a long period of execution.

Researches on influence of the synthesis method and parameters on the resulting magnetic properties have been virtually non-existent, despite its potential scientific and physical impact. This challenge thus leads to the motivation behind this project of developing a technology that optimizes the fabrication process technology to achieve super permeability NiFe for NiFe/Cu composite wires.

1.2. Objectives of present study

For the sensing elements in GMI sensor or orthogonal fluxgate sensor, the main objective of this project is to develop the fabrication technology of super peameabillity NiFe/Cu composite wires, focusing on a nanocrystalline electrodeposition approach to deposit super permeability permalloy on micro copper wires, as well as other approaches including magnentic field assisted electrodeposition of permalloy on copper wires, cold-drawing of NiFe/Cu composite wires, and magnetron-sputtering of peramlloy on copper wires, as detailed below:

1. To investigate localized magnetic properties and magnetic domain of DC electrodeposited NiFe/Cu composite wires
2. To investigate various process parameters in relation to materials and magnetic properties of the deposited layer for electrodeposited NiFe/Cu composite wires.
3. To develop a nanocrystalline deposition technology for electrodeposited NiFe/Cu composite wires through manipulation of the plating current waveform: namely, direct current electrodeposition, pulsed electrodeposition, pulse-reverse (PR) electrodeposition; and the addition of additives such as saccharin.

4. To study effects of imposition of a longitudinal magnetic field during electrodeposition on resulting material, magnetic properties and magnetic sensing performance of electrodeposited NiFe/Cu composite wires.
5. To investigate effects of post heat treatment (i.e. furnace annealing and DC joule annealing) on material and magnetic properties, and magnetic sensing performance of electrodeposited NiFe/Cu composite wires.
6. To explore and develop a cold-drawing technology of NiFe/Cu composite wires.
7. To fabricate sputtered NiFe/Cu composite wires and compare all the developed composite wires in relation to the material and magnetic properties.

1.3. Organisation of Thesis

In this thesis, the project motivation, the project objectives and the organization structure of the thesis are given in *Chapter 1.* The implications and importance of the magnetic sensors, an overview of the current magnetic sensing technology as well as an overview of the available sensing elements are given in *Chapter 2*. *Chapter 2* also reviews the current technology for various deposition methods, such as electrodeposition, cold-drawing and magnetron sputtering. Relevant and important magnetic theories are also discussed in this chapter. *Chapter 3* describes the proposed research approach as well as various fabrication and characterization setups used in the study conducted. *Chapter 4* describes the conducted investigations on localized magnetic properties and magnetic domains of DC electrodeposited NiFe/Cu composite wires while *Chapter 5* describes the investigations conducted on the electrodeposition parameters in relation to material and magnetic properties of the deposited NiFe/Cu composite wires. A technology to manipulate the grain sizes of the electrodeposited NiFe/Cu through the control of the plating current waveform and the

addition of additive saccharin was proposed and investigated. Details of these investigations are given in *Chapter 6*. The influence of an imposed longitudinal magnetic field during electrodeposition of the NiFe/Cu ccomposite wires was discussed in *Chapter 7. Chapter 8* describes the implications of furnace and DC joule annealing on material and magnetic properties of electrodeposited NiFe/Cu composite wires. *Chapter 9* provides a detailed description of the development of cold-drawing as an alternative to fabricating NiFe/Cu composite wires as welll as the magnetic properties of such composite wires. *Chapter 10* describes results on the development of magnetron sputtered NiFe/Cu wires and compares such wires with electrodeposited wires. Finally, conclusions were given in *Chapter 11*.

Chapter 2 Literature Review

2.1. Implications of magnetic sensors in defense, bio-medical and other industries

There are a multitude of magnetic sensor applications, many of which are encountered in everyday life. Today, no automobile, computer or factory can operate efficiently without the help of magnetic sensors. Nearly all applications can be sorted into four main categories, with the distinction between the first three categories determined by how the sensor is used in relation to the ever-present magnetic field of the Earth as well as the sensitivity of the sensor and the fourth category being identified as the medical/biological applications [1, 2, 3, 4, 5].

1) Low-sensitivity application: current sensing: Basically the low sensitivity, industrial applications are for magnetic fields greater than the Earth's magnetic field (considered a background nuisance), which varies from 10^4 to 10^5 nT. Some major applications for such sensors are non-contact switching, alternating current measurement, magnetic memory readout and electronic article surveillance [6]. The most common sensor is the search-coil magnetometer, hall-effect sensor and the magnetometer.

2) Medium-sensitivity application: magnetic compassing: Sensors under this category measure perturbations in the magnitudes and/or direction of Earth's field due to induced or permanent dipoles. Magnetic compassing involves determining the orientation of the sensor with respect to the Earth's magnetic field lines. The magnetic field measurements must be projected onto the horizontal plane and this is often accomplished by either using gimbal method that allows gravity to orient the sensors

with a mechanical system or using tilt sensors and performing the orientation electronically. For land navigation, pointing accuracies are also affected by magnetic anomalies such as mineral deposits and bridges. Magnetic heading has been a reliable measurement for navigation for many centuries. It forms the basis for aviation with airport runways named by their magnetic heading. However, using a magnetic compass to determine the magnetic heading has some challenges to achieve high accuracy. The first main challenge involves developing magnetic field sensors that can measure field with absolute accuracy while the second main challenge involves developing calibration algorithms that can compensate the magnetic field measurements for local variations in Earth's magnetic field due to nearby noise sources such as ferrous metals and electrical currents. Most common sensors used in these applications are the search-coil magnetometer, fluxgate magnetometer and the magnetoresistive magnetometer.

3) High-sensitivity application: magnetic anomaly detection: A heavily researched magnetic sensor application is magnetic anomaly detection (MAD), involving detecting at some distance away a ferromagnetic object (e.g. mine, ship, tank or aircraft) [7]. The magnetic dipole moment of ferromagnetic objects has two contributions. One is a permanent dipole moment. The second contribution is the induced magnetic dipole moment of the ferromagnetic material that is the response to the Earth's magnetic field. The induced magnetic dipole is due to the magnetic permeability. The total magnetic signature from a vessel or any other object is the superposition of these two contributions. Depending on the object and its past history, either the permanent moment or the induced moment may dominate or the two moments may be comparable to each other. The effect of the two moments superimposes to form what is called a magnetic depression in the ambient field. The

main distinct advantages of magnetic sensing of objects are that the sensing technique is nearly independent of weather conditions, covert, does not need a visual of the sensed objects and it is nearly impossible to eliminate the signatures of ferromagnetic objects. A major factor in MAD is the detection range. As a ferrous object moves past a stationary magnetic sensor, a signature can be recorded. An important consideration in MAD is the stability and uniformity of the Earth's magnetic field. In time tracking a magnetic anomaly, it may not be possible to distinguish the anomaly from a time variation in the Earth's magnetic field. In general, there must be relative motion between the target and sensor for practical tracking of targets using only frequencies of 1 Hz or below. Relative motion is not required if one can detect AC or internal motion of ferromagnetic components in targets. High sensitivity magnetometers are one of the important research tools used extensively in space exploration [8]. The main problems faced in this application are the need for a very large dynamic range as well as the need to remove the effect of magnetic fields due to the spacecraft since the spacecraft may not be magnetically clean. Some common sensors used are the SQUID gradiometer and the optically pumped magnetometer.

4) Medical/Biological Applications: Magnetic tags can be attached to detect the presence of specific molecules. Magnetic microbeads were used as labels in a multianalyte biosensor to detect DNA hybridization on a micro-fabricated chip. The presence of the beads was detected by giant magnetoresistance (GMR) magnetoelectronic sensors embedded in the chip [9]. The motion of body parts such as the slight mechanical vibrations of eyelids or the movements of the fingers [10] can also be measured using magnetic sensors. Extremely weak magnetic fields generated by the brain can also be measured using SQUID [11]. In particular, a protype of a

mobile, multichannel magnetoencephalography (MEG) system, named babySQUID, for assessing brain functions in newborns and infants [12] has been reported.

2.2. Overview of existing types of magnetic sensors

Existing magnetic sensing techniques exploit a broad range of ideas and phenomena from the field of physics and material science. The working principles of the various types of magnetic sensors will be briefly introduced and discussed under this section. Currently, magnetic sensors have been broadly classified under two categories: vector magnetometers and total field magnetometers.

There are several problems affecting most vector magnetometers. One key issue is the noise problem, particularly the $1/f$ noise. Another major problem is that they are affected by rotational vibrations.

1) Search-coil Magnetometer: the operation of this type of magnetometer is based on Faraday's law of induction. If the magnetic flux through a coiled conductor changes, a voltage proportional to the rate of change of the flux will be generated between its leads. The flux through the coil will change if the coil is in a magnetic field that varies with time, if the coil is rotated in a uniform field or if the coil is moved through a non-uniform field. Typically, a rod of a ferromagnetic material with a high magnetic permeability is inserted inside the coil to "attract" the surrounding magnetic field and increase the flux density. The signal detected by a search-coil magnetometer depends on the permeability of the core material, the area of the coil, the number of turns and the rate of change of the magnetic flux through the coil. The frequency response of the sensor may be limited by the ratio of the coil's inductance to its resistance, which determines the time it takes the induced current to dissipate when the external magnetic field is removed, and in some cases, by the inter-winding capacitance. In

practice, the voltage readout electronics can limit both the sensitivity and the frequency response of the sensor. This type of sensors can detect fields as weak as 20fT (2 x 10^{-5} nT), their useful frequency range is typically from 1 Hz to 1MHz, require between 1 – 10 mW of power (consumed in the readout electronics) and are very small in size (sensor's coil length can be from 2 – 50 inch). This type of sensor is primarily used in harsh environments where high reliability sensing can be afforded such as on aircraft door checks or for indicating the position of slats and landing gear.

2) Fluxgate magnetometer: This type of sensor consists of a ferromagnetic material wound with two coils, a drive and a sense coil. It exploits magnetic induction together with the fact that all ferromagnetic materials become saturated at high fields. When a sufficiently large sinusoidal current is applied to the drive coil, the core reaches its saturation magnetization once each half cycle. As the core is driven into saturation, the reluctance of the core to the external magnetic field being measured increases, thus making it less attractive for any additional magnetic field to pass through the core. This change is detected by the sense coil. When the core comes out of saturation by reducing the current in the drive coil, the external magnetic field is again attracted to the core, which is again detected by the second sense coil. Thus, alternate attraction and lack of attraction causes the magnetic lines of flux to cut the sense coil. The voltage output from the sense coil consists of even-numbered harmonics of the excitation frequency. For read-out, the second harmonic is extracted and rectified, since the voltage associated with this harmonic is proportional to the external magnetic field. The sensitivity of this sensor depends on the shape of the hysteresis curve. For maximum sensitivity, the magnetic field B-H curve should be square since this produces the highest induced electromotive force (e.m.f.) for a given value of the magnetic field. For minimum power consumption, the core material should have low

coercivity and saturation values. The sensitivity range is from 10^{-2} to 10^{7} nT. The frequency response of the sensor is limited by the excitation field and the response time of the ferromagnetic material and the upper limit on the frequency is about 10 kHz. The major advantage of fluxgate magnetometers over search coils is their ability to precisely measure direct current fields [13, 14]. An example of the application of such sensors is an aircraft compass system.

3) Superconductor Magnetometers: a) Superconducting quantum interference device (SQUID) sensors: these sensors are the most sensitive instruments for measuring a magnetic field at low frequencies (less then 1 Hz) and the operating principle is based on the interactions of electric currents and magnetic fields observed when certain materials are cooled below a superconducting transition temperature. At this temperature, the materials become superconductors and they lose all resistance to the flow of electricity [15].

4) Hall Effect Sensor: as the name suggests, the sensor exploits a physical phenomenon (Hall effect) whereby a voltage difference appears across a thin film, placed in a strong magnetic field perpendicular to the plane of thin film when an electric current is sent along the its length. An electron moving through a magnetic field experiences a force (Lorentz force), that is perpendicular both to its direction of motion and to the direction of the field. It is the response to this force that creates hall voltage. The Hall effect is very minute in metallic conductors but is larger in semiconductors. Since there are fewer conduction electrons in a semiconductor, if the total current through the semiconductor is similar to that of the metal, the electrons in the semiconductor must have a much higher drift velocity than those in the metal. The faster the electrons are moving, the stronger the force the electrons will experience and the greater the Hall voltage produced at equilibrium. Inexpensive Hall effect

sensors are generally made of silicon while more sensitive sensors can be made of III-V semiconductors (e.g. indium antimonide), which have higher electron mobilities than silicon. The silicon sensors have a sensitivity range of 10^6 – 10^8 nT and the indium antimonide sensors extend the lower limit to 10^2 nT. Hall effect sensors can either measure a constant or a varying field and the upper frequency limit is about 1 MHz. They are light, occupy a mere 0.1 in^2, their power requirement is between 0.1-0.2 W, and they can be operated over an extremely wide temperature range limited only by packaging and lead attachment to the semiconductor. Due to their numerous advantages and low costs, Hall effect devices have found hundreds of uses in low costs position sensor applications [16].

5) Magnetoresistive Magnetometer: Magnetoresistance (MR) magnetometers use a change in resistance caused by an external magnetic field *H*. These magnetometers are very attractive for low cost applications due to the fact that they are simply energized by applying a constant current and the output voltage is a measure of the magnetic field [17].

6) Spin–valve Transistors: Spin-valve transistors are spin-valves sandwiched between a pair of semiconductors, one of which is the emitter and the other the collector. The current through the device changes as a function of magnetic field. Current changes with increasing magnetic field (as large as 200%) have been observed, but at present, the output currents are of order microamps and are too small for most sensor applications [18].

7) Giant Magneto-impedance (GMI) Magnetic Sensors: The operation of these sensors are based on the phenomenon that impedance of amorphous wires, ribbons and nanocrystalline materials decreased sharply in fields less than 50 Oe, due to skin depth effect [19,20]. The impedance has been found to be a strong function of both

the magnetic field and the magnitude and frequency of the drive current. This effect has been termed as giant magneto-impedance effect (GMI) effect.

8. Magnetodiode: a magnetodiode is essentially a semiconductor diode; or *pn* junction. In a magnetodiode, however, the *p* region is separated from the n region by an area of undoped silicon. The device is fabricated by depositing silicon and then silicon dioxide on a sapphire substrate. If a metal contact on the p-doped region is given a negative potential, holes in the p-type material and electrons in the n-type material will be injected into the undoped silicon. The current is the sum of the holes' current and the electron current. Some of the carriers, particularly those near the interface between the silicon and the sapphire, will recombine. The loss of charge carriers increases the resistance of the material. In the absence of a field, recombination at both interfaces contributes to the resistance. A magnetic field perpendicular to the direction of travel of the charge deflects them either down or up, depending on the direction of the field. Both holes and electrons are deflected in the same direction because they are traveling in opposite directions. Charge carriers near the interface between the silicon and the sapphire have a greater tendency to recombine than those near the interface between the silicon and the silicon dioxide. Thus, if the magnetic field deflects the charge carriers down, the resistance of the material is increased; if it deflects them up, the resistance is decreased. The response of a magneodiode to a magnetic field is about ten times larger than the response of a silicon Hall-effect device.

9. Magnetotransistors: This sensor is actually an integrated silicon device. If the magnetodiode is a version of a pn junction, the magntotansisitor is a version of a npn transistor. Like the transistor, it consists of an n-doped emiiter separated from a n-doped collector by a p-doped base. The difference is that there are two collectors

instead of one. In the absence of a magnetic field, equal numbers of charge carriers arrive at both collectors. If there is a magnetic field perpendicular to the direction of travel of the charge carriers, they are deflected towards one collector or the other, depending on the direction of the field. The two-collector voltages are fed to a difference amplifier, whose output is proportional to the applied magnetic field. Two different effects are used in magnetotransistors to detect magnetic fields: Hall and Suhl effects. The Hall effect has been described earlier while the Suhl effect takes place when the Lorentz force is not compensated. An external magnetic field causes a change in trajectory of the moving carriers, resulting in a variation in the current distributions that is detected between the collector outputs. Although both effects occur simultaneously, it is possible to design devices in which one effect is dominant. The magnetotransistor is expected to be 100 times more sensitive than the silicon Hall-effect device and is based on a standard fabrication technology (i.e. silicon substrates).

Table 1 Table showing sensitivity of different types of sensors with the grey colored bars representing current achievable sensitivity range of the sensors and the shaded bars depicting potential enhancements.

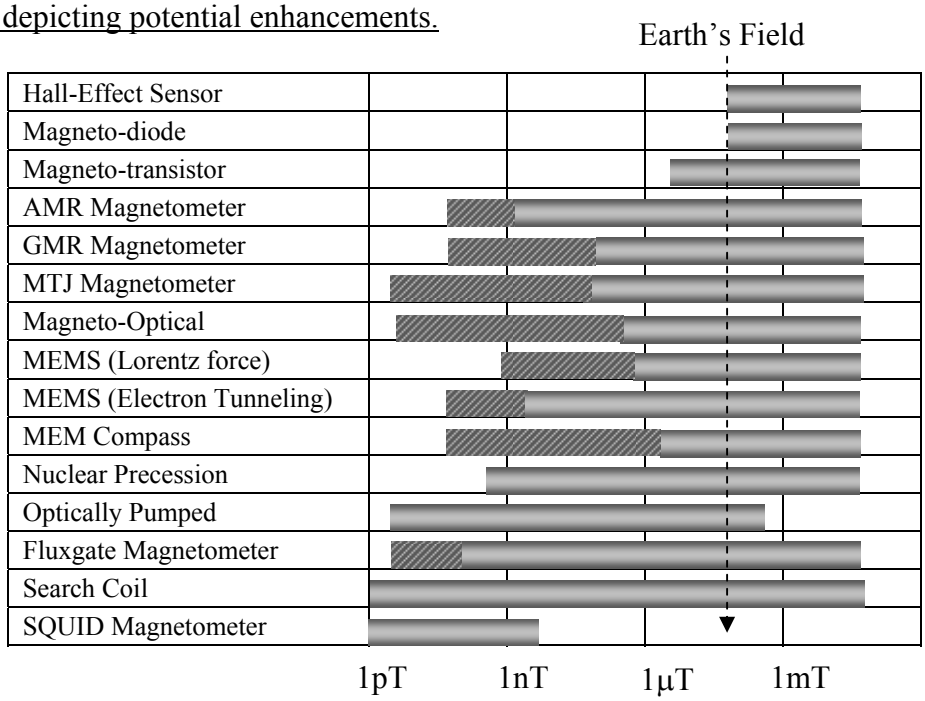

10. *Magnetooptical Sensor:* This sensor exploits Faraday's effect, which involves the rotation of the plane of polarized light when traveling through a magnetic material [21]. This effect is largest in a few crystals when the propagation directions of the light, the crystal axis, and the applied magnetic field are all aligned.

2.3. Overview of different types of magnetic sensing elements

Weak magnetic field sensors, such as giant magnetoimpedance effect sensors or orthogonal fluxgate sensors, essentially utilize soft magnetic sensing elements in their systems to pick up signatures from magnetic sources. Beside the electrical output circuitry (readout) design and the pick-up coils parameters, the quality of the soft magnetic sensing elements greatly affects the performance of the sensors in terms of sensitivity, resolution and also the range of sensing. As such, immense scientific interests have been focused on the development of such sensing elements [22, 23, 24, 25, 26].

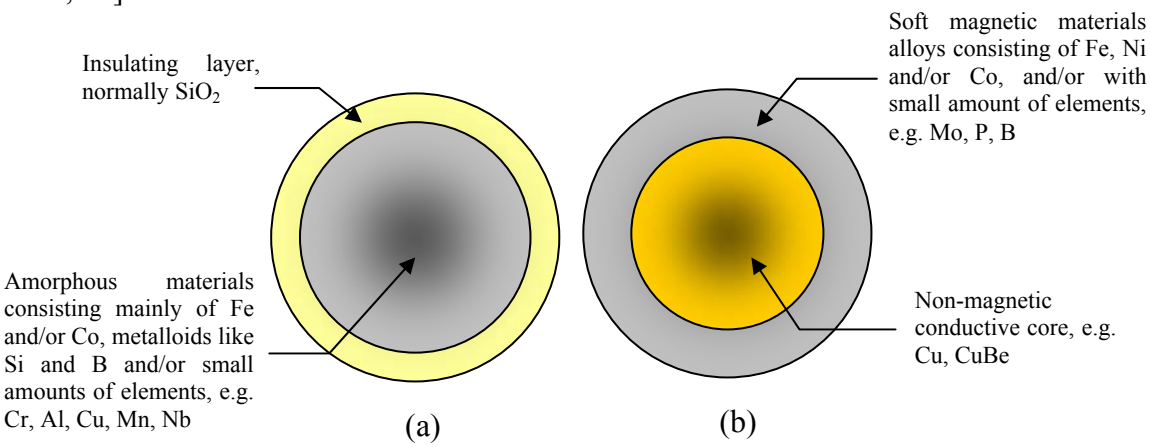

Fig. 1 Schematic diagram showing structures of (a) an amorphous wire; (b) a nanocrystalline composite wire.

To date, research interests and efforts have mainly been focused on two main types of sensing elements: 1) amorphous wires and ribbons; and 2) composite wires and films. The main differences between the structures of the two types of sensing

elements are the presence of an insulating layer in the amorphous wires and a non-magnetic conductive core in the composite wires (Fig. 1).

For the past two decades, increasing efforts have been placed on developing and understanding the mechanisms responsible for the properties of amorphous wires [27, 28, 29, 30, 31, 32, 33, 34]. Glass-coated amorphous microwires are fabricated either by the quenching [28] or drawing [33] technique or a combination of the two techniques [34]. These wires typically consist of an amorphous metallic nucleus covered by Pyrex-like insulating coating [23]. The general composition of the families of rapidly quenched microwires consists of mainly Fe and/or Co (70-80%), metalloids like Si and B and sometimes small amounts of other elements such as Cr, Al, Cu, Mn and/or Nb in order to improve the mechanical, corrosion resistant or magnetic properties. Although prepared already three decades ago, interest has risen, since the last decade, with the advancement of the preparation techniques as well as the measurement techniques, due to the arising number of technological applications derived from their outstanding magnetic properties and small dimensions [35, 36, 37].

Amorphous magnetic materials are usually produced by rapid quenching techniques that lead to rather large frozen-in stresses within the samples. In particular, amorphous wires are subjected to radial gradients of temperature, giving rise to a complex distribution of internal stresses that leads to a peculiar domain structure, known as core-shell structure [28]. This structure consists of a core magnetized along the axial direction and an outer shell, whose magnetic moments points either radially (for wires with positive magnetostriction) or circumferentially (for wires with negative magnetostriction). These stresses determine their magnetic properties [38]. It is well known that low-temperature annealing can alter the magnetic properties of the as-cast amorphous samples, simply by relaxing the internal stresses. As such, Joule

heating, furnace annealing or stress annealing has been extensively employed in amorphous materials to improve their soft magnetic characteristics [39, 40, 41, 42]. N. Bayri et al. [42] observed a maximum stress-impedance ratio of 255% in the wire annealed for 10 mins under an applied tensile stress of 250 MPa. Investigations have also been carried out on the magnetoresistance (MR) [43] and magnetoimpedance (MI) effect [44, 45, 46, 47, 48, 49]. A maximum MI ratio of 330% at 1MHz ac testing current was achieved for $Co_{68.1}Fe_{4.4}Si_{12.5}B_{15}$ amorphous wires. In particular, asymmetric giant magnetic impedance (AGMI) behaviour studies (arising due to a crystallized layer created by annealing the wires in open air) have been conducted on $Co_{68.18}Fe_{4.32}Si_{12.5}B_{15}$ amorphous wires [50].

As compared to amorphous wires, fewer scientific studies have been conducted on composite wires. One of the earlier works on GMI was demonstrated in NiFe-plated conductive wires [51]. This approach led to the fabrication of permalloy-copper wire composites, prepared by cold-drawing a permalloy-clad Cu rod [52, 53]. Anatoly S. Antonov et al. [52] demonstrated the importance of the role of a Cu core and the circumference magnetic anisotropy to achieve GMI effect comparable to that found in more conventional soft magnetic wires, despite the fact that the properties of the measured permalloy were not optimized. It must be noted that the composite wire fabrication techniques, namely electroplating and cold-drawing, are versatile, providing means of adjusting process parameters that will directly control the obtained materials and magnetic properties. However, works by other authors on these areas have been few [54, 55].

Magnetic properties and MI effect of the composite wires have been conducted on different types of composite wires [56, 57, 58]. In particular, a MI% ratio of 1200% has been achieved for $Fe_{20}Ni_{64}Co_{16}/Cu_{97}Be_3$ microwires at ac testing current

frequency of 4 MHz [57] while a MI% ratio of 800%-900% has been achieved for $Ni_{69.4}Fe_{22.4}Mo_{8.2}$/Cu microwires at ac testing current frequency of 2 MHz [58]. Theoretical studies on the current distribution in the composite structures have also been conducted [59, 60].

2.4. Magnetic Materials

2.4.1 Basic Classification of Magnetic Materials

The origin of magnetism lies in the orbital and spin motions of electrons and how the electrons interact with one another. The best way to introduce the different types of magnetism is to describe how materials respond to magnetic fields. The magnetic behavior of materials can be classified into the following five major groups:

i. Diamagnetism – a fundamental property of all matter, although it is usually weak. It is due to the non-cooperative behavior of orbiting electrons when exposed to an applied magnetic field. Diamagnetic materials consist of atoms which have no net magnetic moments (all the orbital shells are filled and there are no unpaired electrons). However, when exposed to a field, a negative magnetization is produced and thus the susceptibility is negative. Some examples of such materials are quartz, calcite, water, etc.

ii. Paramagnetism - Some of the atoms or ions in these materials have a net magnetic moment due to unpaired electrons in partially filled orbitals. However, the individual magnetic moments do not interact magnetically, and like diamagnetism, the magnetization is zero when the field is removed. In the presence of a field, there is now a partial alignment of the atomic magnetic moments in the direction of the field, resulting in a net positive magnetization and positive susceptibility. In addition, the efficiency of the field in aligning the moments is opposed by the randomizing effects of temperature. This results in a temperature dependent susceptibility, known as the

Curie's Law. At normal temperatures and in moderate fields, the paramagnetic susceptibility is small. Unless the temperature is very low or the field is very high, paramagnetic susceptibility is independent of the applied field. Some examples of such materials are clay, Fe-rich clay, silicate and carbonate.

iii. Ferrimagnetism – In ionic compounds, such as oxides, more complex forms of magnetic ordering can occur as a result of the crystal structure. One type of magnetic ordering is called ferrimagnetism. The magnetic structure is composed of two magnetic sublattices separated by oxygen. The exchange interactions are mediated by the oxygen anions. When this happens, the interactions are called indirect or superexchange interactions. The strongest superexchange interactions result in an antiparallel alignment of spins between the two sub-lattice. In ferrimagnets, the magnetic moments of the two sublattices are equal and this results in a net magnetic moment and is therefore related to ferromagnetism.

iv. Antiferromagnetism – If the two sublattice moments are exactly equally opposite, the net moment is zero. This type of ordering is called antiferromagnetism. The clue to antiferromagnetism is the behavior of susceptibility above a critical temperature, called the Neel temperature. Above this temperature, the susceptibility obeys the Curie-Weiss law for paramagnets but with a negative intercept indicating negative exchange interactions.

v. Ferromagnetism – The atomic moments in these materials exhibit very strong interactions. These interactions are produced by electronic exchange forces and result in a parallel or antiparallel alignment of atomic moments. Exchange forces are very large, equivalent to a field on the order of 1000 Tesla or approximately 100 million times the strength of the earth's field. The exchange force is a quantum mechanical phenomenon due to the relative orientation of the spins of two electrons.

Ferromagnetic materials exhibit parallel alignment of moments resulting in large net magnetization even in the absence of a magnetic field. Two distinct characteristics of ferromagnetic materials are their spontaneous magnetization (magnetization inside the materials without external application of a magnetic field) and the existence of magnetic ordering temperature. Examples of such materials are Fe, Ni, Co and their various alloys. These magnetic dipoles are coupled in parallel by the exchange interaction (as proposed by Heisenberg) between spins:

$$E_{ex} = -2J_{ij}\vec{s}_i.\vec{s}_j \tag{1}$$

where s_i and s_j being the resultant spin on adjacent atoms i and j, and J denoting the inter-atomic exchange and when $J_{ij}>0$: ferromagnetism, $J_{ij}<0$: antiferromagnetism, $J_{ij}<0$, $s_i>s_j$: Ferrimagnetism. The difference in the alignment of magnetic moments for the different categories of magnetic materials is given in Fig. 2.

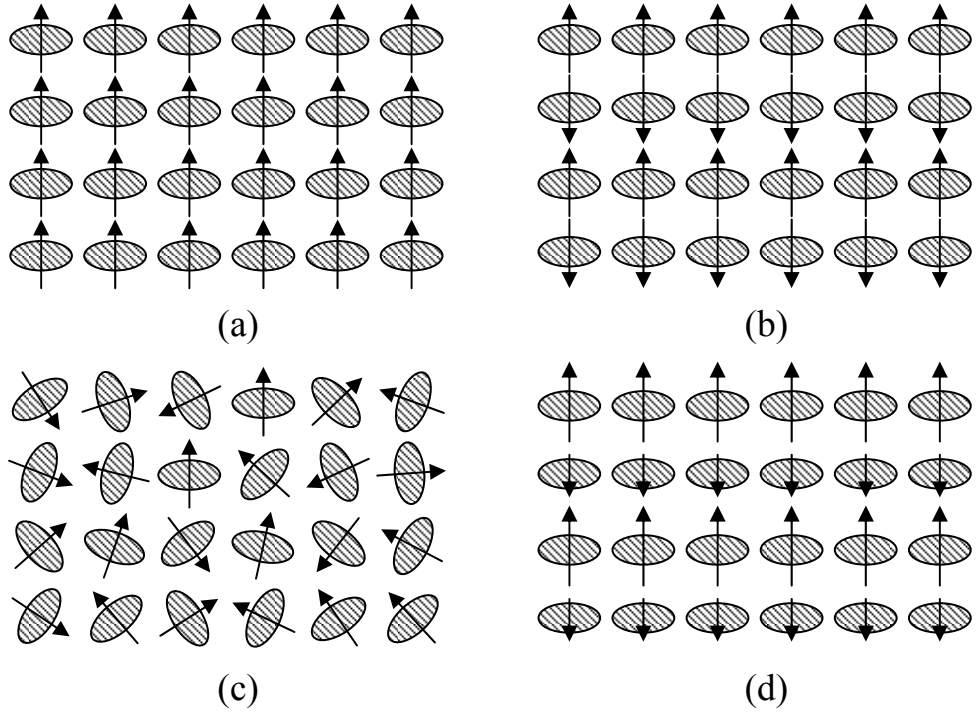

Fig. 2 Schematics showing alignment of magnetic moments for materials that are (a) ferromagnetic; (b) anti-ferromagnetic; (c) paramagnetic; (d) ferrimagnetic.

2.4.2 Ferromagnetic Materials and Their Properties

Perhaps the most important class of magnetic materials is the ferromagnets: iron, nickel, cobalt and manganese, or their various alloys. These materials exhibit a unique magnetic behavior which is called ferromagnetism. Ferromagnetic materials exhibit a long-range ordering phenomenon at the atomic level which causes the unpaired electron spins to line up parallel with each other in a region called a domain. These materials can be permanently magnetized upon the application of an external magnetic field.

The long range order which creates magnetic domains in ferromagnetic materials arises from a quantum mechanical interaction at the atomic level. This interaction is incredible in that it locks the magnetic moments of neighboring atoms in spite of the thermal agitation which tends to randomize any atomic-level order. Sizes of domains range from a 0.1millimeter to a few millimeters. When an external magnetic field is applied, the domains already aligned in the direction of this field grow at the expense of their neighbors. For a given ferromagnetic material the long range order abruptly disappears at a certain temperature which is called the Curie temperature for the material.

2.4.3 Curie Temperature T_c

Even though electronic exchange forces in ferromagnets are very large, thermal energy eventually overcomes the exchange forces and produces a randomizing effect. This occurs at the Curie temperature. When the ferromagnetic materials are heated above the Curie temperature, the materials become disordered and thus paramagnetic and magnetization of the material will become zero.

As the temperature continues to increase, the susceptibility (ratio of magnetization to magnetic field) decreases continually according to the Curie-Weiss law for strongly paramagnetic substances, except where there is a change in the phase structure of the material. The ferromagnetic curie temperatures for Fe, Co and Ni are 1043 K, 1388 K and 627 K respectively.

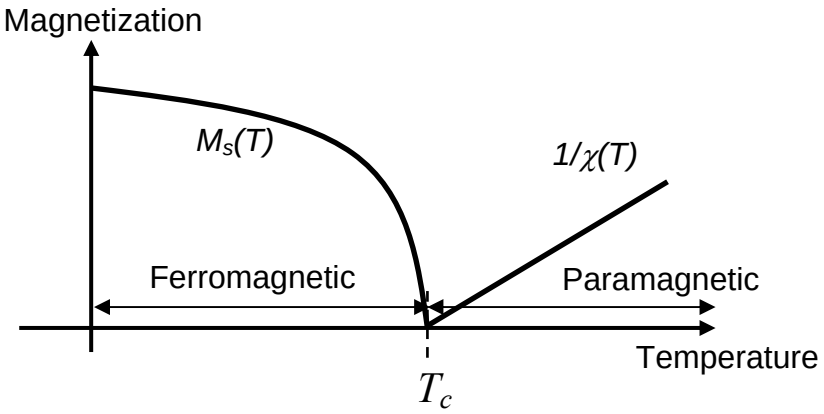

Fig. 3 Effect of temperature on magnetization.

2.4.4 Magnetic Domains

The microscopic ordering of electron spins characteristic of ferromagnetic materials leads to the formation of regions of magnetic alignment called domains. There is already a high degree of magnetization in ferromagnetic materials within individual domains, but that in the absence of external magnetic field, those domains are randomly oriented. A modest applied magnetic field can cause a larger degree of alignment of the magnetic moments with the external field, giving a large multiplication of the applied field. An illustration of the domain structure in ferromagnetic materials, such as iron, is given in Fig. 4. The microscopic evidence about magnetization of ferromagnetic materials in response to an external magnetic field may occur more by the growth of the domains parallel to the applied field at the

expense of other domains rather than the reorientation of the domains themselves (as shown in Fig. 5.

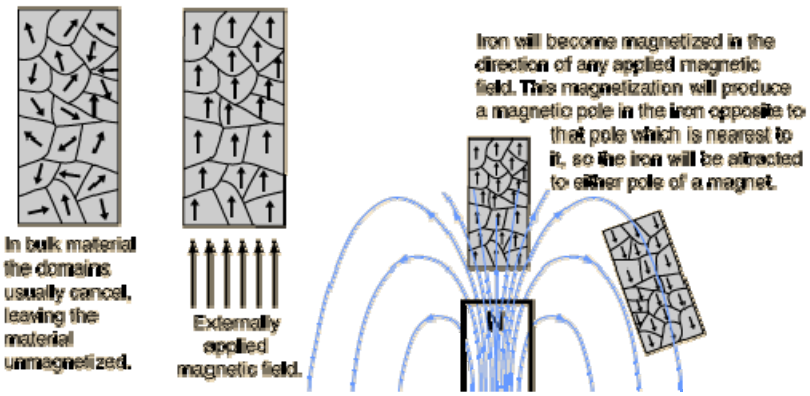

Fig. 4 Domain structures in ferromagnetic materials.

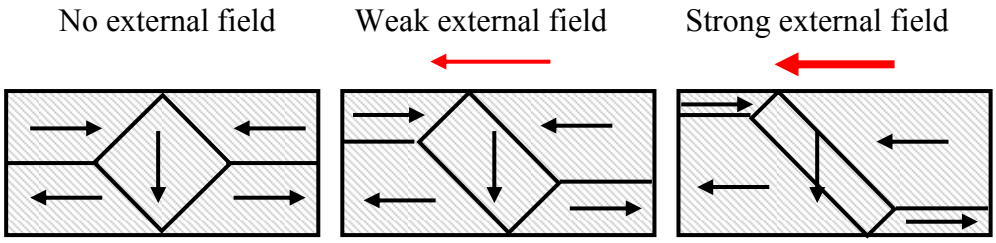

Fig. 5 Effect of magnetic field on magnetic domains

2.4.4. Hysteresis

When a ferromagnetic material is magnetized in one direction, it will not relax back to zero magnetization when the imposed magnetizing field is removed. It must be demagnetized by a field in the opposite direction. If an alternating magnetic field is applied to the material, its magnetization will trace out a loop, most commonly named as the hysteresis loop (Fig. 6). The lack of retraceability of the magnetization curve is the property called hysteresis and it is related to the existence of magnetic domains in the materials. Once the magnetic domains are reoriented, it takes some energy to turn them back again. This property is useful as a magnetic memory.

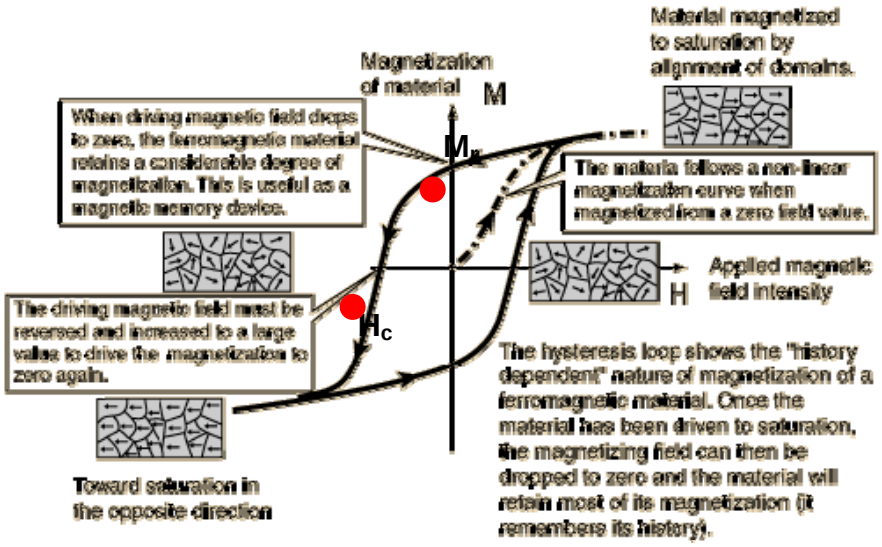

Fig. 6 Hysteresis Loop

From the hysteresis loops, the following data can be obtained about the ferromagnetic materials.

a) Remanence value (M_r) – a measurement of the remaining magnetization when the driving field is dropped to zero – can be obtained.

b) Coercive force (H_c) – amount of reverse magnetic field which must be applied to a magnetic material to make the magnetization return to zero.

c) Permeability (μ) – a property of a material that describes the ease with which magnetization is established in the material. The value is obtained by the value of the slope of the curve at any point on the hysteresis loop (usually from B-H loops).

d) Maximum amount of useful work – measure of the maximum amount of useful work that can be performed by the magnet and the value is represented by $(BH)_{max}$.

e) Anistropy – The shape of the hysteresis loop can indicate the anisotropy of the measured specimens. If the hysteresis loop obtained is box-shaped, the anisotropy should be near longitudinal while if it is rather curvy and round, the anisotropy will be circumferential for the case of wires.

2.4.5. Factors Affecting Magnetic Quality

The properties of the magnetic materials depend on chemical composition, fabrication techniques, and heat treatment. Some properties, such as saturation magnetization, change slowly with chemical composition and are usually unaffected by fabrication or heat treatment. However, permeability, coercive force and hysteresis loss are highly sensitive and show changes which are extreme among all the physical properties, when changes are made in impurities or heat treatment. Saturation magnetization, curie point, magnetostriction at saturation and crystal anisotropy constant, change only slowly with chemical composition and are usually unaffected by fabrication and heat treatment.

2.4.6. Chemical Composition

Although many elements besides iron are purposely present in magnetic materials, nevertheless iron is present as the major constituent in by far the greatest number of useful ferromagnetic materials. These may be divided into two classifications: Magnetically “soft” materials used in transformers, motors, relays, and other electromagnetic apparatus; and magnetically “hard” materials – Permanent Magnets – used in loud speaker, relays, telephone receivers, and a variety of other instruments. In the magnetically soft materials a substantial portion of the iron is used unalloyed as “magnetic iron.” Larger quantities are consumed in the iron-silcon alloys containing up to 6% silicon, and smaller amounts in the iron-nickel alloys (Permalloys) and some iron-cobalt and iron-cobalt-nickel alloys. The permanent magnet materials include the steels containing some essential carbon and the alloying elements cobalt, chromium, tungsten, and manganese in various proportion; also the Alnicos containing iron, cobalt, nickel and aluminum in various proportions and some times also copper and

titanium; and finally iron-cobalt alloys with additions of molybdenum, chromium, vanadium, tungsten, and others. The last two classifications, although often referred to as steels, do not contain essential carbon and, indeed, carbon is usually harmful; the designation “steel” is to be avoided here.

2.4.7. Effects of Impurities

Impurities, such as oxygen, carbon and sulphur, may seriously affect the aging of certain magnetic properties- the coercive force and hysteresis loss of some specimens at room temperature. This aging is caused by the precipitation of an impurity such as carbon or nitrogen which is present in an amount exceeding its solid solubility The effectiveness of hydrogen treatment lies in the fact that magnetic properties are affected by small amount of the common impurities only if they are non-metallic in character, and that such impurities can be removed by the treatment. These elements are probably injurious because they have only limited solid solubility in iron and cause dispersion hardening; and they can be removed in a reasonable time because they diffuse through the metal and combine with hydrogen at high temperatures. Oxygen, carbon and nitrogen are removed in this way more readily than sulphur, and carbon is removed probably more readily in moist than in dry hydrogen. Phosphorus is not appreciably affected by hydrogen nor does it affect the magnetic properties of otherwise pure iron if it is present in small amounts; in iron it may be regarded as metallic character as it is indicated by the fact that it forms a solid solution of the substitution type when present in amounts less that 1%. Before a given impurity can cease to be harmful it must diffuse through the iron to the surface of the specimen, then it must leave the surface either by evaporation or combination in a reasonable time when a practically attainable flow of hydrogen or other suitable gas is passed

over the surface. The residual impurity must be less than its solid solubility at or somewhat above room temperature.

2.4.8. Temperature

Temperature is one of the important factors beside magnetic field and stress, in causing change in magnetization. The greatest influence of temperature is rarely near room temperature but rather just below the curie point or near the temperature of a phase transformation. At higher temperatures the curves rise more quickly- at lower values of H – and then flatten out and saturated at lower inductions. The saturation continues to decrease and approaches zero at some temperature called the curie point. When a magnetic material is subjected to a high constant field, an increase in temperature normally brings about a continuously accelerating decrease in induction; the induction comes down abruptly, almost to zero, at the curie point. The curve is retraced when the temperature is lowered again. Conversely, when the iron is subjected to a weak field, the induction will first increase with increase in temperature and, after passing through a maximum, will drop as before to a low value at the curie point. In any material which may be called “normal” the curves are likely to have this same general character; e.g. the initial and maximum permeabilities first increase and then decrease with increasing temperature, and the coercive force and hysteresis loss continually decrease. The characteristic maximum in the initial and maximum permeabilites, just below the curie point, is associated with the low magnetic anisotropy at this temperature. The change from the ferromagnetic to the paramagnetic state is not perfectly sharp, and it is difficult to define and determine the curie point exactly. All materials that exhibit ferromagnetism are paramagnetic when they are heated above the curie temperature. As the temperature continues to increase,

the susceptibility decreases continually according to the Curie-Weiss Law for strongly paramagnetic substance, except where there is a change in the phase structure of the material. When the saturation magnetization decreases rapidly and finally disappears at the curie point, changes becomes evident in other physical properties, e.g. resistivity, specific heat, thermal expansivity and elastic constants.

2.4.9. Fabrication Methods (resulting in stressed materials)

Magnetic materials require a wide variety of modes of fabrication. The methods include hot and cold rolling, forging, swaging, drawing, pulverization, electrodeposition, and numerous operations such as punching, pressing and spinning. Sputtering and pulsed laser deposition, are some of the current methods used to produce high quality magnetic materials. Different fabrication or deposition methods produce materials of different magnetic properties due to the difference in the induced residual stress in the materials and also maybe due to the level of impurities in the materials associated to the methods. Materials with near zero magnetostriction possess the best magnetic properties.

2.4.10. Heat Treatment

Some of the most drastic changes in properties occur when the fabrication or heat treatment has about a change in structure of the material. High permeability materials are annealed primarily to relieve the internal strains introduced during fabrication. However, permanent magnet materials are heat-treated to introduce strains by precipitating a second phase. Heat treatments are decidedly characteristic of the materials and their intended uses. Some common heat treatments for magnetic materials are purification, double treatment (may be cooled rapidly to room

temperature and reheated to 600°C), bake, air quench, and furnace cool. The purposes of these various heating and cooling cycles, and typical materials subjected to them, may be listed as follows.

i. Relief of internal strains due to fabrication or phase changes, e.g. magnetic iron.

ii. Increase of internal strains by precipitation hardening, e.g. Alnico type of permanent magnets.

iii. Purification by contact with hydrogen or other gases, e.g. Silicon-iron (cold-rolled), hydrogen-treated iron.

There are also special treatments, such as those used for "double-treated" Permalloy, "magnetic annealed" Permalloy, and Perminvar. Occasionally it is necessary to homogenize a material by maintaining the temperature just below the freezing point for many hours. Heat treatments also may affect grain size, crystal orientation, or atomic ordering [61,62,63].

2.5. Well-known Magnetic Alloys

Permalloy is the term for a nanocrystalline magnetic alloy with a composition of 20% iron and 80% nickel. This material has good magnetic properties like high initial permeability, extremely low coercivity and near-zero negative magnetostriction [64]. It is used as a high-quality magnetic recording material [65] and is commonly used as memory elements in computers [66].

Supermalloy is composed of 79% nickel, 4-5% molybdenum, and the rest being iron [67]. Molybdenum is added to increase the resistivity of the material and thus, reduce eddy current loss. It is a magnetically soft material with high magnetic permeability and low coercivity. Resistivity of supermalloy is 0.6 μΩ·m and it is

commonly used in manufacturing of components of radio engineering, telephony, and telemechanics instruments.

Mu-metal is a made of 75% nickel, 15% iron, copper and molybdenum. Mu-metal is a soft magnetic alloy, having very high magnetic permeability, relatively stable crystalline structure with respect to thermal or mechanical treatments, and good thermal conductivity [68]. The high permeability makes mu-metals very effective at screening static or low-frequency magnetic fields, which cannot be attenuated by other methods. Mu-metal is used to shield equipment from magnetic fields, for example vacuum chambers for experiments with low-energy electrons and magnetic resonance imaging equipment.

Alcomax is a permanent magnetic material consisting of an alloy of iron, nickel, aluminum, cobalt and copper. This material offers the best temperature coefficient (0.02% per °C) of all permanent magnets, thus making it an ideal choice when a constant field over a wide (-270°C to +500°C) temperature range is required [69]. The high nickel content results in good stability against corrosion and oxidation, and this metallic composition is also a good electrical conductor. The principal applications of alcomax are for triggering of proximity switches such as reeds and Hall effects. Other applications include instrumentation and holding magnets.

Alnico alloys are composed primarily of alloys of aluminum, nickel, and cobalt, with the addition of iron, copper, and sometimes titanium. Alnico alloys can be magnetized to produce strong magnets with magnetic field strength as high as 0.15 Tesla at their poles. This material has excellent temperature stability even at temperatures up to 550°C and has a Currie temperature of around 800°C. Besides that, alnico has high residual induction and relatively high energies [70]. They are

manufactured through either a casting or sintering process. This material is used extensively in applications like rotating machinery and sensing devices.

CuNiFe is an alloy of copper, nickel, iron, and in some cases cobalt. This material can be used for making magnets and gives good shape-forming freedom since they are wrought metallic material. The alloy has the same linear coefficient of expansion of certain types of glass, thus making them an ideal material for the lead out wires in light bulbs and thermionic valves.

2.6. Considerations for High Permeablility Materials

The fundamental requirements for a high permeability material are:

1. High saturation magnetization M_s
2. Very low magnetocrystalline anisotropy energy K_1 (or K_u near zero for amorphous alloys)
3. Very low coercivity H_c – so that domain walls are easily nucleated and displaced, and this ensures that hysteresis energy losses are small. As such, the materials should be as homogenous as possible and free from second phases, inclusions, impurities, stress and crystallographic defects.
4. High curie temperature T_c
5. High electrical resistivity to minimized energy losses due to eddy currents
6. Good temperature stability

2.7. Magnetic Materials Deposition Methods

2.7.1 Electrodeposition

2.7.1.1 Background information

The birth of electroplating may be considered to have taken place with Volta's discovery of the production of electricity by chemical means in 1799 [71]. Electrolysis was mainly a scientific curiosity until about 1839 when the value of electrodeposition for the production of surfaces and objects was announced by several workers at about the same time. Just to whom the credit should go to for the discovery is a matter of controversy.

Since then, electrodeposition has, over recent decades, evolved from an art to an exact science. This development is seen as responsible for the ever-increasing number and widening types of applications of this branch of practical science and engineering. Some of the technological areas in which means and methods of electrodeposition constitute an essential component include macro and micro electronics development, optics, opto-electronics and sensors fabrications. In addition, key industries such as automobile industry utilizes this method over other available options (such as evaporation, sputtering, chemical vapor deposition (CVD) based on reasons of economy and convenience.

2.7.1.2 Atomistic aspects of electrodeposition

Basically, electrodeposition is the process of producing a coating, usually metallic, on a surface by the action of electric current, by placing a negative charge on the object to be coated and immersing it into an electrolyte solution that contains the salt of the metal to be deposited (with the object to be plated made the cathode of an electrolytic cell). In the electrodeposition of metals, generally a metal ion M^{z+} is transferred from the solution into the ionic metal lattice [71, 72, 73, 74]. A simplified atomistic representation of this process is

$$M^{z+}\ (\text{solution}) \rightarrow M^{z+}\ (\text{lattice}) \qquad (2)$$

This reaction is accompanied by the transfer of z electron from an external electron source (e.g. power supply) to the electron gas in the metal M. A metal may be considered to be a fixed lattice of positive ions permeated by a gas of free electrons. Positive ions are the atomic cores, while the negative charges are the valence electrons. The free electrons form what is known as the electron gas in the metal, and they move freely through the volume of the metal. Each metal atom thus contributes its single valence electron to the electron gas in the metal. Interactions between the free electrons and the metal ions are largely responsible for the metallic bond. Surfaces may be characterized into ideal and real. Ideal surface exhibit no surface lattice defects (vacancies, impurities, grain boundaries, dislocation, etc). Real surfaces have a variety of defects. The structure of real surfaces differs from those of ideal surfaces by surface roughness. While an ideal surface is atomically smooth, a real surface may have defects, steps, kinks, vacancies and clusters of adatoms.

The atomic processes that make up the electrodeposition process, Eqn. 2, can be viewed considering the structure of the initial M^{z+} (solution), and the final state, M^{z+} (lattice). Since metal ions in an aqueous solution are hydrated the surface of the initial state in Eqn. 2 should be represented by $[M(H_20)_x]^{z+}$. The structure of the final state is an M adion (adatom; absorbed ion, atom) at a kink site since it is generally assumed that a atoms (ions) are attached to a crystal via a kink site. Thus the final step of the overall reaction, Eqn. 2, is the incorporation of the adion in to the kink site. Due to the surface inhomogeneity the transition from the initial state M^{z-} (solution), and the final state, M^{z+} (kink), may proceed via either of the two mechanisms: (1) step-edge site ion-transfer or (2) terrace site ion-transfer; or a combination of the two mechanisms.

$$[M(H_20)_x]^{z+} \text{ (solution)} \rightarrow M^{z+} \text{ (kink)} \qquad (3)$$

2.7.1.3 Faraday's Law of Electrolysis

Faraday's law states that the amount of electrochemical reaction that occurs at an electrode is proportional to the quantity of electric charge Q passed through an electrochemical cell.

If the weight of a product of electrolysis is w, then Faraday's law states that

$$w = Z_e.Q \tag{4}$$

where Z_e is the electrochemical equivalent, the constant of proportionality. Since Q is the product of the current I, in amperes, and the elapsed time t, in seconds,

$$Q = I.t \tag{5}$$

$$W = I.t.Q \tag{6}$$

The production of one gram equivalent of a product at the electrode, W_{eq}, in a cell requires 96,487 coulombs, according to Faraday's law. Since the coulomb is the quantity of electricity transported by the flow of one ampere for one second, therefore Faraday constant F is given by:

$$F = N_A e = 96,487 C mol^{-1} \tag{7}$$

where N_A is Avogadro's number (6.0225 x 10^{23} molecules mol^{-1}) and e is the charge of a single electron (1.6021 x 10^{-19} coulombs, C).

Fraction of a molar (atomic) unit of reaction that corresponds to the transfer of one electron, w_{eq},

$$W_{eq} = A_{wt} / n_e \tag{8}$$

where A_{wt} is the atomic weight of metal deposited on the cathode, and n_e is the number of electrons involved in the deposition reaction.

Thus, $$Z_e = W_{eq} / F = A_{wt} / n_e F \tag{9}$$

Finally, $$w = Z_e.Q = (A_{wt} / n_e F).Q \tag{10}$$

Note: The electrochemical equivalent of a metal M, Z_e (M), is the weight in grams produced, or consumed, by one coulombs (one ampere second)

2.7.1.4 Current Efficiency

When two or more reactions occur simultaneously at an electrode, the number of coulombs of electricity passed corresponds to the sum of the number of equivalents of each reaction. The current efficiency CE of the jth process, namely of any one of the simultaneous reactions, is defined as the number of coulombs required for that reaction, Q_j, divided by the total number of coulombs passed, Q_{total}:

$$CE = \frac{Q_j}{Q_{total}} \tag{11}$$

An alternative equation defining current efficiency is

$$CE = \frac{w_j}{w_{total}} \tag{12}$$

where w_j is the weight of metal j actually deposited and w_{total} is that which would have been deposited if all the current had been used for depositing the metal j. Thus, in general, at a current efficiency under 100%, the remainder of the current is used in side processes, such as the reduction of hydrogen and nitrate ions in the example above.

2.7.1.5 Deposit thickness predictions

The deposit thickness may be evaluated by considering the volume of the deposit. Since the volume of the deposit V is the product of the plated surface area a_s, and the thickness h, it follows that $h = V / a_s$. The volume of the deposit is related to the weight of the deposit w and the density of the deposit d, by the relationship defining the density $d = w / V$. Thus

$$h = \frac{V}{a_s} = \frac{w}{a_s d} \tag{13}$$

In the case where it is necessary to calculate the time t (seconds) required to obtain the desired deposit thickness h (cm), at a given current density, Faraday's law was introduced in Eqn. 10 and Eqn. 13, giving

$$h = \frac{w}{a_s d} = \frac{Z_e Q}{a_s d} = \frac{Z_e I t}{a_s d} \tag{14}$$

$$t = \frac{h a_s d}{Z_e I} \tag{15}$$

2.7.1.6 Effect of additives on electrodeposition

Affect deposition and crystal building processes as adsorbates (absorbed substances) at the surface of the cathode. There are two basic types of absorption: 1) chemical adsorption; 2) physical adsorption. In chemical adsorption, the chemical attractive forces of adsorption act between the surface and the adsorbate (usually these are covalent bonds). Thus there is a chemical combination between the substrate and the adsorbate where electrons are shared and/or transferred. New electronic configuration may be formed through this sharing of electrons. In physical adsorption, the physical forces of adsorption, Van der Waals or electrostatic forces, act between the surface and the adsorbate; there is no electron transfer and no electron sharing.

Absorbed additives affect the kinetics of electrodeposition and the growth mechanism by changing the concentration of growth sites on a surface, the concentration of adions on the surface, the diffusion coefficient $D_{diff,}$ and the activation energy of surface diffusion of adions. In the presence of adsorbed additives, the mean free path for lateral diffusion of adions is diminished, which is equivalent to a decrease in the diffusion coefficient D_{diff} of adions. This decrease in D_{diff} may result in an increase in adion concentration at steady state and thus an increase in the

frequency of the two-dimensional nucleation between diffusing adions. Additives can also influence the propagation of microsteps and cause bunching and the formation of macrosteps. The type of deposit obtained at constant current density may depend on the surface coverage of additives.

2.7.1.7 Electrodeposition of alloys

Alloy deposition is an old art and science as the electrodeposition of individual metals (e.g. brass, which is an alloy of copper and zinc). As expected, alloy deposition is subjected to the same principles as single metal plating. Progress in both types of plating has depended on similar advances in electrodeposition science and technology. The subject of alloy electroplating is being dealt with by an increasing number of scientific and technical publications. The reason for this is the vastness of the number of possible alloy combination and the concomitant possible practical applications.

Properties of alloys deposits superior to those of single metal electroplates are common place and are widely described in the literature. It is recognized that alloy deposition often provides deposits with properties not obtained by employing electrodeposition of single metals. Alloy deposits can have different properties in certain composition ranges relative to the single component metals. They can be denser, harder, more corrosion resistant, more protective of the underlying basis metal, tougher and stronger, more wear resistant, different (better) in magnetic properties, more suitable for subsequent electroplate overlays and conversion chemical treatments, and superior in antifriction applications.

The electrodeposition of an alloy requires, by definition, the co-deposition of two or more metals. In other words, their ions must be present in an electrolyte that provides a “cathode” film where the individual deposition potentials can be made to

be close or even the same. The three main stages in the cathodic deposition of alloys (or single metals) are to be recognized:

1. *Ionic migration*: the hydrated ion(s) in the electrolyte migrate(s) toward the cathode under the influence of the applied potential as well as through diffusion and/ or convention
2. *Electron transfer*: At the cathode surface area, the hydrated metal ion(s) enter the diffusion double layer where, because of the higher field present, the hydrated shell is lost. Then on the cathode surface, the individual ion may be neutralized and is absorbed.
3. *Incorporation*: The absorbed atom wanders to a growth point on the cathode and is incorporated in the growing lattice.

2.7.1.8 Anomalous Deposition

The electroplating of Ni-Fe is an example of "anomalous" co-deposition [66, 75, 76, 77, 78,79], whereby the less noble metal gets deposited preferentially and its relative composition in the deposit is higher than that in the electrolyte solution. In Ni-Fe alloys the Ni reduction is inhibited in the presence of ferrous ions, while the Fe deposition rate is enhanced, comparing to their respective deposition rates in single metal electroplating systems. Some researchers have proposed explanations behind the co-deposition phenomenon observed in alloys composing of the ferromagnetic elements nickel, iron or cobalt.

One earlier theoretical explanation is that the formation of $Fe(OH)_2$ on the cathode surface function as a selective membrane that permits Fe to be deposited while inhibiting Ni reduction. However, this explanation is not very possible, as it does not explain how the Fe reduction rate is enhanced. Moreover, the phenomenon was

observed by some researchers even at minor hydrogen evolution conditions in which $Fe(OH)_2$ is not likely to form. Thus, the implied high pH condition for the phenomenon occurrence is not a convincing explanation. [79]

Another theoretical explanation, based on compiling experimental investigations of the phenomenon by various researchers, is that as a result of hydrogen evolution, which is the side reaction of metal reduction of these iron-group alloys at the cathode surface, the concentration of protons, H^+, is depleted. This leads to the increase in local concentration of the hydroxyl ions, OH^-. With the increase concentration of OH^- ions, the formation and adsorption of metal hydroxide ions on the cathode surface occurs, suggesting the important role of metal hydrolysis reactions and that $Fe(OH)^+$ and $Ni(OH)^+$ are the main reactants in the alloy plating. Since the sequence of the competing adsorption ability of metal hydroxide ions is as such: $Fe(OH)^+ > Co(OH)^+ > Ni(OH)^+$, the formation of an $Fe(OH)^+$-enriched adsorption layer on the cathode surface aids the subsequent discharge of Fe ion, while inhibiting Ni deposition, as the sequence of metals with respect to increasing the equilibrium concentration of $M(OH)^+$ in a constant pH plating bath was expected to be: Zn > Fe > Co > Ni. The reaction equations involved are as follows [66,75,76,77,78,79]:

$$2H_2O + 2e^- \rightarrow H_2 + 2OH^- \quad (16)$$

$$M^{2+} + OH^- \rightarrow M(OH)^+ \quad (17)$$

$$M(OH)^+ \rightarrow M(OH)_{ads}^+ \quad (18)$$

$$M(OH)_{ads}^+ + 2e^- \rightarrow M + OH^- \quad (19)$$

where M represent Ni, Fe, Co atoms.

The electrodeposition mechanism of Ni-Fe alloys involves the controlling of Ni deposition rate by the ion discharge while controlling of Fe deposition rate by the transport of ferrous (Fe^{2+}) ions to the electrolyte diffusion layer near the cathode

surface. Deposition and dissolution rates of the respective ions depend on the composition of the plating bath. In general, changes in composition imply changes in the magnetic properties, surface morphology, crystalline arrangement, and deposited thickness [66, 76].

2.7.1.9. Current status in DC electrodeposition technology

As compared to different deposition methods for the composite wire development, electrodeposition has always been a well accepted method, due to its relatively higher efficiency, easier control and lower cost. The influence of electrodeposition parameters on the magnetic properties of coating layer have been previously studied [71, 72, 80, 81]. The Ni^{2+}/Fe^{2+} ratio of the solution, plating temperature, pH value and plating current density have been found to exert significant effects on the coating composition. There have been studies on the effect of plating current density on the composition and grain sizes of the plated layer [71, 72, 82]. However, so far there has been no detailed research on the effect of plating current density on the magnetic properties of plated material. The circumferential magnetic field, induced by the plating current in electrodeposition, affects the magnetic domain structure as well as the surface morphology of the plated NiFe layer. This will result in changes in the magnetic properties of the plated material. Thus, it is interesting to study the effect of current density on the magnetic properties of $Ni_{80}Fe_{20}$/Cu composite wire.

While parameters of electroplating, such as current density, plating time and formulas of plating solutions have been studied, little has been known about the effect of varying pH on the magnetic properties of the plated layer in NiFe electroplating. It is known that the pH is vital for electroless plating. However, it is not clear how the pH value in the plating solution would play a part in the electroplating of Ni-Fe. For

pure nickel deposition, it was reported [73] that excess NH_3 (high pH) would lower cathode efficiency and embrittle the deposit. Also, if the pH is too high and/or the chloride ion concentration is too low, the hydroxide ions might be discharged in preference to the dissolution of nickel, and oxygen would be evolved. In addition, due to the fact that the anode and cathode efficiencies are not equal, the NiFe concentration and pH would slowly increase as the plating proceeds. It is therefore interesting to note if such phenomenon would occur in varying the pH of the plating solution. It is also worth noting the trend involved for the change in the composition as this might enable us to know the interdependence relationship between Ni and Fe. Several explanations [77, 81] were used to explain why the composition of NiFe was highly dependent on the pH values of the plating solutions. Kieling *et al* [81] pointed out that anomalous co-deposition occurs when the surface pH is high enough to cause ferrous hydroxide to be formed. This hydroxide would be absorbed preferentially on the electrode and blocks the deposition of Ni. Yin *et al* [77] pointed out that the hydroxide precipitate might act as additional barrier to nickel deposition.

A critical factor affecting the performance of composite wires is the thickness of the magnetic coating layer. Interestingly, Atalay [83] showed that within the studied thickness range of 1 – 10 μm of the electrodeposited magnetic layer on 50 μm in diameter Cu wires, larger thicknesses resulted in higher MI% ratios.

It was also discovered that the addition of a trace amount of molybdenum to about the permalloy composition [84] would greatly enhance the magnetic properties. There have been several reports on the physical and magnetic properties of such NiFeMo alloy [85, 86, 87], but there has been no study on the relationship of the synthesis parameters with the magnetic properties of the alloy material.

Several studies have been conducted on the effect of magnetic field on the grown structures [88, 89, 90, 91, 92, 93, 94, 95, 96, 97]. Through growing fractal electrodeposits in different orientations with and without an applied magnetic field, J.M.D. Coey et al [88, 89, 95] demonstrated that the magnetic field increases the effective diffusion coefficient, thereby promoting mass transport during electrodeposition. This effect is well-known as the magnetohydrodynamic (MHD) effect. K. Msellak et al [93] showed that the Ni-Fe morphology and chemical composition change, due to the enhancement of surface concentration of the inhibiting iron species by the MHD convection. Ibro Tabakovic et al [97] observed that external magnetic field applied parallel to the cathode affects electrochemical behavior, compositrion of NiFe films, stress, magnetic properties, crystalline structure, and surface roughness.

2.7.2 Pulse Deposition

2.7.2.1 Background Information

In electrolysis, in contrast to chemical synthesis, one can easily control the reaction rate of a system by working at a given current density, or easily select the magnitude of the driving force for the reaction by adjustment of the electrode potential. Modern electronics has greatly enhanced this inherent advantage of electrolysis by allowing current or voltage to be applied as almost any function of time. Pulse plating takes full advantage of this possibility. Typical waveforms include cathodic pulse followed by a period without current and/or by an anodic pulse; DC with superimposed modulations; a train of cathodic pulses; square-wave or modified sine-wave pulses. It should be noted, however, that owing to the fundamental nature of the phenomena involved in the deposition process, one cannot make full use of the

range of conditions that would be allowed by modern electronics. There are two main limiting factors: 1) the charging of the electrical double layer at the metal-electrolyte interface; and 2) the mass transport considerations [98].

2.7.2.2 Limiting factor 1: capacitance effects

The electrical double layer at the electrode solution interface can be approximated to a plate capacitor with an interpolate distance of a few angstroms and therefore with a high capacitance. Charge must be provided to this double layer in order to raise its potential to the value required for metal deposition at the rate corresponding to the applied current which is supplied by the generator. The electrode behaves like a capacitor with a resistance in parallel (Fig. 7), the resistance being a function of the current density. The charging of the double layer requires a certain time which depends on the current density and on other physico-chemical parameters of the system. For practical purposes the charging time should be much shorter than the pulse duration, otherwise the current pulse is strongly distorted. Moreover, the time required for discharge of the double layer should be much shorter than the off-time between two pulses. In an extreme case, where the charging and discharging times of the double layer are much longer than the on-time and off-time of the pulse respectively, the pulse current is virtually a direct current and the term “pulse plating” is hardly applicable. The current required at the beginning of the pulse for charging the electrical double layer is not lost for the metal deposition, which the charge is recovered at the end of the pulse which the capacitor is discharging. Pulses in a frequency range where capacitive effects are relevant do not significantly influence the current efficiency, but affect the amplitude of the pulse and hence the energy of the electrodeposition reaction.

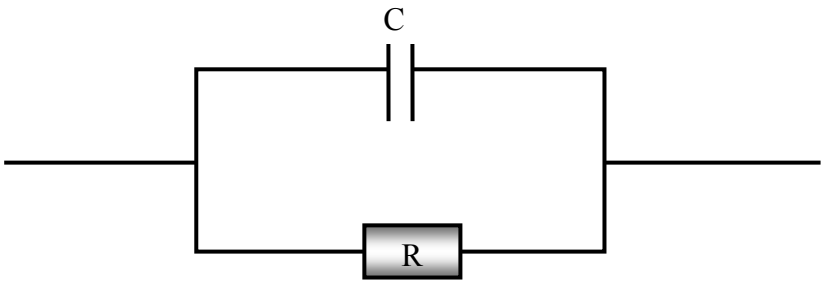

Fig. 7 Equivalent circuit of an electrode

2.7.2.3 Limiting factor 2: mass transport effects

The limitations of the useful range of pulse conditions due to mass transport effects arise from the depletion of cations in the diffusion layer (Fig. 8). In pulse plating with short pulse duration, two distinct cathodic diffusion layers can be defined instead of one as in DC. In the immediate vicinity of the cathode the concentration pulsates with the frequency of the pulsating current, decreasing during the pulses and relaxing in the interval between them. Thus a pulsating layer exists close to the cathode. If the duration of the pulse is short, the diffusion layer does not have time to extend very far into the solution and in particular does not extend to the region where convention takes over mass transport. Therefore the metal deposited during the pulse must be transported from the bulk of the solution towards the pulsating diffusion layer by diffusion, which means that a concentration gradient also builds up into the bulk of the electrolyte. The thickness of this diffusion layer corresponds essentially to that which would be established under the same hydrodynamic conditions in DC electrolysis. Through this outer diffusion layer cations are also supplied towards the cathode during the off-time and it is this supply that allows the relaxation of the pulsating diffusion layer during the off-time. The outer diffusion layer is essentially stationary.

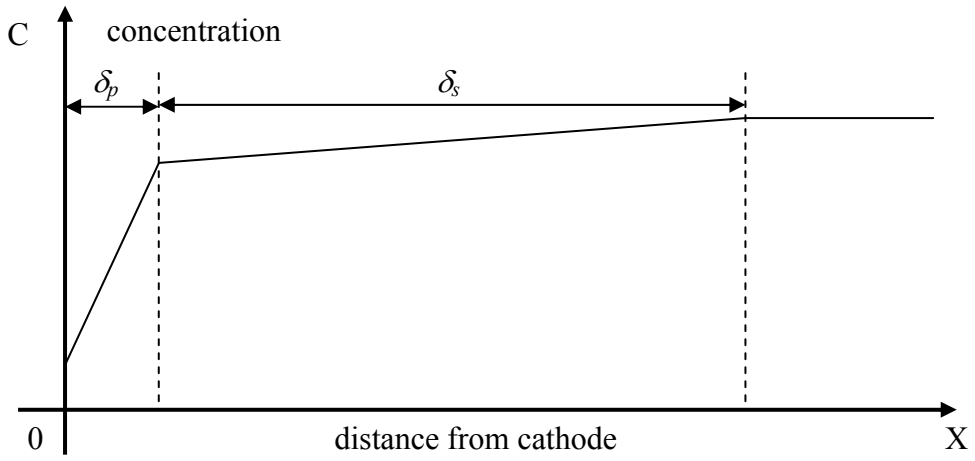

Fig. 8 Concentration profiles of the two diffusion layers in pulse electrolysis at the end of a pulse, showing thickness of the pulsating diffusion layer δ_p and thickness of the stationary diffusion layer δ_s.

The two distinct diffusion layers are related to two kinds of limitation; the depletion of the cationic concentration in the pulsating diffusion layer limits the pulse current density, and the depletion of the cationic concentration in the outer diffusion layer limits the average current density. Since the concentration gradient in the pulsating diffusion layer can be very high, increasing with shorter pulse length, the pulse current density can reach extremely high values, e.g. up to 10,000 times the usual DC values, without decrease of current efficiency because of hydrogen evolution. The first limitation due to the mass transport effect in pulse plating is that the pulse duration should not exceed the transition time, while the second is that the maximum average current density cannot exceed the DC limiting current density.

2.7.2.4 Crystallization

The crystallization of the electrodeposited metal is a very important step of the electrogrowth since it influences directly the structure of the deposit and therefore its properties which represent the main interest for the user. The crystallization is the process by which the adatoms or adions incorporate in the crystal lattice. Crystallization occurs either by the build up of old crystals or the formation and

growth of new ones. These two processes are in low population of adatoms and low over potentials are factors enhancing the build-up of old crystals, while conversely low surface diffusion rates, high population of adatoms and high overpotentials on the surface enhance the creation of new nuclei. In pulse plating, since the pulse current density is usually considerably higher than the corresponding DC density, the population of adatoms on the surface during pulse deposition is higher than during DC deposition, resulting in an increased nucleation rate and therefore in a finer grained structure. Grain refinement in pulse plating is also favored by the enhancement of nucleation rates due to high overpotentials which results from high pulse current densities.

Another phenomenon that might occur in pulse plating during the off-period is recrystallization. Small grains are thermodynamically less stable than large ones because of high surface energy, and as in bubble coalescence, small grains tend to recrystallize. For this to occur, the surface should remain active during the off-time. Again depending on different absorbed species, the surface may be inhibited, in which case no crystallization will occur, and the fine grains obtained during the on-time of electrolysis are stabilized.

2.7.2.5. Pulsed current vs pulsed voltage

Electrolysis can be controlled by regulation of either current or voltage. In current regulation mode, the reaction rate is kept constant and the potential varies as a function of time. In voltage regulation, the driving force for the reaction is kept constant and the reaction rate varies as a function of time. The advantages and disadvantages of these two modes of electrolysis are briefly discussed here for pulse

plating. In current regulation, the average deposition rate can be very simply derived from the following equation:

$$j_m = j_p \frac{T_{on}}{(T_{on} + T_{off})} \tag{20}$$

while in voltage regulation the average deposition rate can be predicted only from computations of a speculative nature. The main advantage of voltage regulation is a better control of the current efficiency and of alloy composition. High over potentials resulting from excessive concentration depletions are avoided. However, from a practical point of view, regulation of pulsed voltage is very difficult to achieve. A third reference electrode should be added to the system to regulate the pulsed voltage. Moreover, to get instantaneously a given potential at the electrode, the current should start theoretically from an infinite value, which is obviously not feasible because of apparatus limitations. On the other hand, at the end of a pulse, for instantaneous reestablishment of the starting potential (which might be the rest potential of the system), some metals should be re-dissolved; hence a constant voltage pulse requires a short inversion of current at the end of the pulse, which might not be desirable. Furthermore, passivation may occur during the inversion. For most applications, current regulation is more preferred.

2.7.2.6 Pulse reverse

As the name implies, the main purpose of inverting the current from cathodic to anodic during a short fraction of the total period is to remove metal preferentially from areas that tend to overplate during the cathodic part of the cycle. It is thus possible to considerably retard the development of dendrite formation or to improve the plating thickness distribution over complicated shapes. Changes in deposit structure, mainly grain size, can also be achieved because of forced nucleation at each

new cathodic pulse. It is clear that from adsorption-desorption as well as recrystallization phenomenon will be quite different from those in pulse plating. It should be pointed out that pulse reverse is usually applied when the deposit is easily soluble in the electrolyte, otherwise passivation can occur. Sometimes, as in palladium deposition, the purpose of inverting the current is to remove co-deposited hydrogen. In most cases, the objective of the application of pulse reverse is to improve the plating thickness distribution. Areas exposed to concentrations of current density are preferentially plated in the cathodic cycle, but for the same reason, metal is preferentially removed in the anodic cycle.

To take full advantage of pulse reverse, the anodic current density should be adjustable independently of the cathodic current density. The reason for this is to increase the dissolution rate of peaks by applying very high anodic current densities, but for short time durations. It is obvious that the balance of electrical charges over a total period should remain cathodic. The manufacture of power supplies offering this capability involves complications, but this remains, nevertheless, an important requirement.

2.7.2.7 Current status in pulsed and PR electrodeposition technology

Extensive researches have been carried out since the last decade on the synthesis processes and applications of nanocrystalline materials due to their excellent enhanced mechanical and chemical properties. Much attention has been devoted on the synthesis techniques [23, 24, 81, 99] as the optimization of these techniques can greatly enhance the properties of the synthesized materials.

The electrodeposition mechanism of Ni-Fe alloys involves the controlling of Ni deposition rate by the ion discharge while controlling of Fe deposition rate by the

transport of ferrous (Fe^{2+}) ions to the electrolyte diffusion layer near the cathode surface. Deposition and dissolution rates of the respective ions depend on the composition of the plating bath. In general, changes in composition imply changes in the magnetic properties, surface morphology, crystalline arrangement, and deposited thickness. [66, 75]

Reducing the grain size has been reported to greatly increase the mechanical strength of the materials [100]. The decrease in grain size has also been reported to result in an enhancement in the magnetic permeability of the magnetic materials. According to the random anisotropy model [101] (RAM), magnetic properties can be drastically improved when the grain size is decreased below the critical magnetic interaction exchange length, which was calculated to be 270 nm for $Ni_{80}Fe_{20}$.

Pulse-reverse electrodeposition has been reported to produce specimens of excellent magnetic properties [98]. The introduction of an off-time period in the electrodeposition current waveform in pulse electrodeposition was reported to result in specimens of smaller grain sizes [98]. The absorption of inhibiting species during the off-time blocks growth centers of the cathode and thus forces the system to create new nuclei at each new pulse. There have been several previous studies on the method of pulse-reverse electrodeposition [75, 76] but there have not been a detailed study on the effect of pulse-reverse electrodeposition with off-time on the resulting grain sizes of the deposited material.

2.7.3 Cold-drawing

Cold-drawing is a metal forming technique which involves pulling wires through successive dies at temperatures below the material's recrystallization temperatures.

The diameter of the wire is reduced every time the wire goes through a die (See Fig. 9).

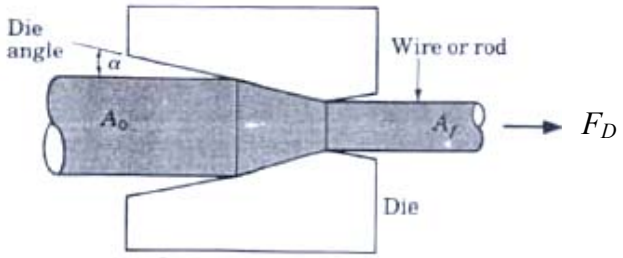

Fig. 9 Diagram of cold-drawing of wire.

In commercial practice, drawing stress is restricted to approximately 60% of the flow stress of the product, which restricts diameter reduction to 35% in most cases. Drawing stress F_D can be determined by Eqn. 21 [102]:

$$F_D = \sigma_{tm}\left(\frac{3.2}{\Delta + 0.9}\right)(2\alpha + \mu_f) \tag{21}$$

where α = approach angle,

μ_f = friction coefficient,

$\Delta = \frac{2\alpha}{r}\left[1 + (1-r)^{1/2}\right]^2$,

Reduction ratio, $r = 1 - \frac{A_f}{A_o}$, and

Mean true flow stress $\sigma_{tm} = \frac{k\varepsilon^n}{n+1}$

where k = strength constant,

ε = energy per unit volume, and

n = strain hardening exponent.

2.7.3.1 Current status in cold-drawing technology

Cold-drawing is one of the most common metal forming processes. It is considered to be one of the most effective and flexible methods to improve surface finish and obtain precise dimension and specified mechanical properties. Furthermore, it was postulated that cold-drawn wires have good mechanical and electrical properties as there is a uniform distribution of fine filaments [103].

However, during the cold-drawing process, residual stresses are induced in the wire, which can affect the functional properties of the finished product, such as a change in dimension during cutting and heat treatment. Axial tensile stresses induced in the surface can also decrease the fatigue strength of the final product. Finite element simulations were performed on cold-drawn wires [104], in order to study the influence of bearing geometry on the residual stress-state. Besides that, utility programs for the cold-drawing process are also being developed [105]. This shows the importance of such method, hence the need to optimize the various parameters.

The possibility of using cold-drawn wires as soft magnetic materials has been studied. MI effect has been measured in commercial HyMu80® permalloy wires of composition $Ni_{80}Mo_{4.2}Fe_{bal}$, subjected to annealing and cold-drawing [106]. The outer diameter of 44μm was reached and the largest MI ratio of 150% is found, at a frequency of 3 MHz, and its respective coercivity is 30 A/m (0.38 Oe).

Pure wire drawing has long been looked into and cold-drawn copper wires as thin as 18μm can be easily bought from the market. Cold-drawing, an inexpensive technique, can also be used to produce composite wires consistent in material composition and mechanical properties [107].

Antonov et al. [52] fabricated NiFe/Cu composite wires by a modified cold-drawn technique. The minimal outer diameter reached of the wire is 49μm. It was found that

the amplitude of the MI effect is significantly larger than that of NiFe wires without Cu inner core. The composite wires exhibit soft magnetic behavior. The MI effect of the wire is about 100%, and the coercivity does not exceed 0.8 Oe.

2.7.3.2 Annealing Process

As a result of cold-working, the hardness, tensile strength and electrical resistance increases, but the ductility of the material decreases. There is also an increase in the number of dislocations and distortions in the crystal structure, resulting in the strain hardening effect. Energy used to cold-work the material is most often dissipated as heat, but a certain amount of energy is stored as internal energy associated with the lattice defects caused by the deformation. It is thus, crucial to restore the ductility and relief the high internal stress of the material by annealing, to facilitate further draws before the material fails.

The annealing process can be categorized into three stages namely recovery, recrystallization and grain growth [108], as shown in Fig. 10.

Recovery occurs at low temperatures, where the temperature is insufficient to cause changes in microstructures and mechanical properties. The primary purpose of this stage is to stress relief the cold-worked material, to prevent stress corrosion cracking and to minimize distortions produced by residual stresses. This low temperature treatment in the recovery range is also known as stress relief annealing or process annealing.

In the recrystallization temperature range, new undeformed crystals appear in the microstructure. The cold-worked structure gradually gets replaced with strain-free grains. During the recrystallization stage, tensile strength and hardness significantly decreases while ductility is greatly increased.

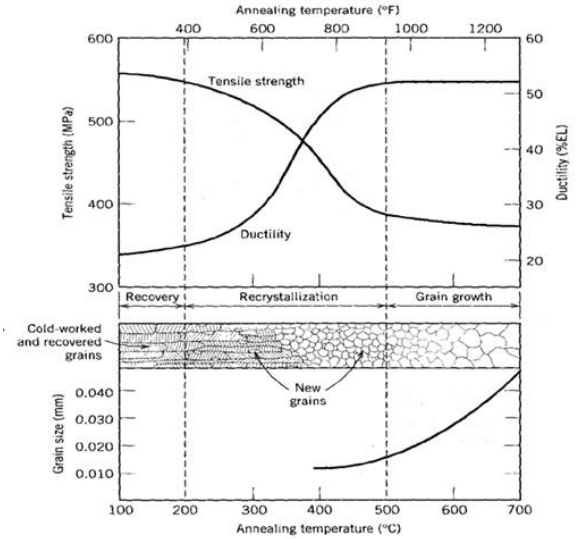

Fig. 10 Annealing processes and its effects on brass.

The grain growth stage of annealing is characterized by a slower rate of decrease of tensile strength and hardness compared to the recrystallization stage. However, there is a significant growth of the grain boundaries and restoration of the original grain size when further heat is supplied to the material.

2.7.3.3 Intermediate Annealing

Intermediate annealing is often conducted on materials that would be subjected to further cold-work as it improves the ductility of the semi-finished material to enable subsequent cold-working without breakages. Annealing is done at a relatively low temperature, just above recrystallization temperature, to reduce the incidence of scale oxidation. Recrystallization temperature of a metal is the temperature at which the metal reaches complete recrystallization in 1 hour. It is estimated to be around half to one-third of the absolute melting point of metals. The melting points and recrystallization temperatures of elements involved in the specimen concerned are indicated in below Table 2 [109].

Table 2 Melting points and recrystallization temperatures of elements in composite wire.

Material	Melting point (°C)	Recrystallization temperature (°C)
Nickel	1455	370
Iron	1538	450
Copper	1085	120

It was determined that the annealing temperature is 550° C, which is about half of the lowest melting point of the three elements involved.

2.7.3.4 Post Treatment

To improve the sensitivity of the sensors, one of the methods is to improve the permeability of the ferromagnetic deposited material of the composite wire. Material composition, grain size and amount of residual stress are some crucial factors affecting the permeability of magnetic materials. As such, the GMI effect of composite wires may be enhanced, by improving its soft magnetic properties through suitable heat treatment, which releases residual stresses in the ferromagnetic coating layer [110,111].

Over the last decade, considerable research has been done regarding Permalloy/Cu wires. As compared to hard magnets, a soft magnet that has higher permeability will have a lower coercivity and hence, higher sensitivity. Such aspects can be improved by modifying the hysteresis, which is related to anisotropy of the wires, through field annealing [112]. It is also observed that the magnetic homogeneity of layers improved near annealing temperature of 200ºC and inter-diffusion observed at above 250ºC,

with the Ni content observed to diffuse preferentially to copper layer above the critical temperature [113, 114].

Post heat treatment is an essential post synthesis process that is vital in improving the properties of the as-cast specimens. As such, the understanding and optimization of the annealing process is critical. Thus, this work is directed to investigate the effect of furnace annealing parameters as well as joule heat annealing in relations with the resulting magnetic properties of $Ni_{80}Fe_{20}$/Cu wires. In this study, furnace annealing will be conducted on electrodeposited $Ni_{80}Fe_{20}$/Cu specimens. The materials (composition and, surface roughness and grain size) and magnetic properties (sensitivity, coercivity and magneto-impedance effect) will then be characterized accordingly.

2.7.4 Magnetron Sputtering

Magnetron sputtering has developed rapidly over the last decade to the point where it has become established as the process of choice for the deposition of a wide range of industrially important coatings. The driving force behind this development has been the increasing demand for high-quality functional films in many diverse market sectors.

Sputtering is accomplished by applying a voltage between the target (or cathode) material and the substrate to be sputtered in a vacuum chamber containing a sputtering gas. The function of the gas is to provide a medium in which a glow discharge can be initiated and maintained to continuously supply bombarding particles. Usually, argon (Ar) is used as working gas due to its low cost and large atomic mass, leading to good sputtering yields. When the voltage between the substrate and target exceeds a threshold value, stable glow discharge appears. In the

presence of negative potential, free electrons are accelerated and ionize the gas atoms (plasma is obtained). The target, which has a negative potential would attract the argon ions. Argon ions would be accelerated towards the target material and as a result, the target materials are displaced and transferred to the substrate. Secondary electrons are also emitted from the target surface as a result of the ion bombardment, and these electrons play an important role in maintaining the plasma [115].

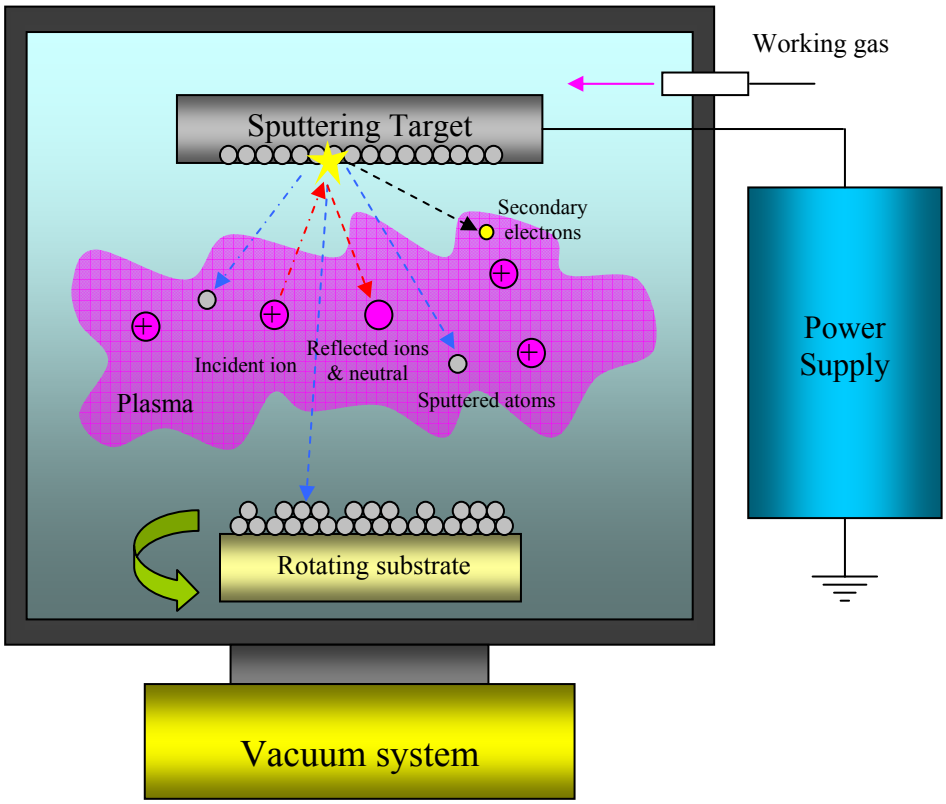

Fig. 11 Schematic diagram showing mechanism of sputtering.

The basic sputtering process has been known for many years and many materials have been successfully deposited using this technique. However, the process is limited by low deposition rates, low ionization efficiencies in the plasma, and high substrate heating effects. These limitations have been overcome by the development of magnetron sputtering, and more recently, unbalanced magnetron sputtering.

Magnetrons make use of the fact that a magnetic field configured parallel to the target surface can constrain secondary electron motion to the vicinity of the target. The magnets are arranged in such a way that one pole is positioned at the central axis of the target and the second pole is formed by a ring of magnets around the outer edge of the target [116]. Trapping the electrons in this way substantially increased the probability of an ionizing electron-atom collision occurring. The increase ionization efficiency of a magnetron results in a dense plasma in the target region. This, in turn, leads to increase ion bombardment of the target, giving higher sputtering rates and, therefore, higher deposition rates at the substrate. In addition, the increased ionization efficiency achieved in the magnetron mode allows discharge to be maintained at lower operating pressures (typically, 10^{-3} mbar, compared to 10^{-2} mbar) and lower operating voltages (typically, -500 V, compared to -2 to -3 kV) than is possible in the basic sputtering mode.

The differences in design between a conventional magnetron and an unbalanced magnetron are only slight. However, the difference in performance between the two types of magnetron is very significant. In a conventional magnetron, the plasma is strongly confined to the target region. A region of dense plasma typically extends some 60 mm from the target surface. Films grown on substrates positioned within this region will be subjected to concurrent ion bombardment, which, as mentioned earlier, can strongly influence the structure and properties of the growing film. Substrates placed outside this region, however, will lie in an area of low plasma density. Consequently, the ion current drawn at the substrate (typically, < 1 mA/cm^2) is generally insufficient to modify the structure of the film. The energy of the bombarding ions can be increased by increasing the negative bias applied to the substrate. However, this can lead to defects in the film and increased film stress, and

therefore, be detrimental to the overall film properties. Thus, it is difficult to deposit fully dense films on large or complex components using conventional magnetrons.

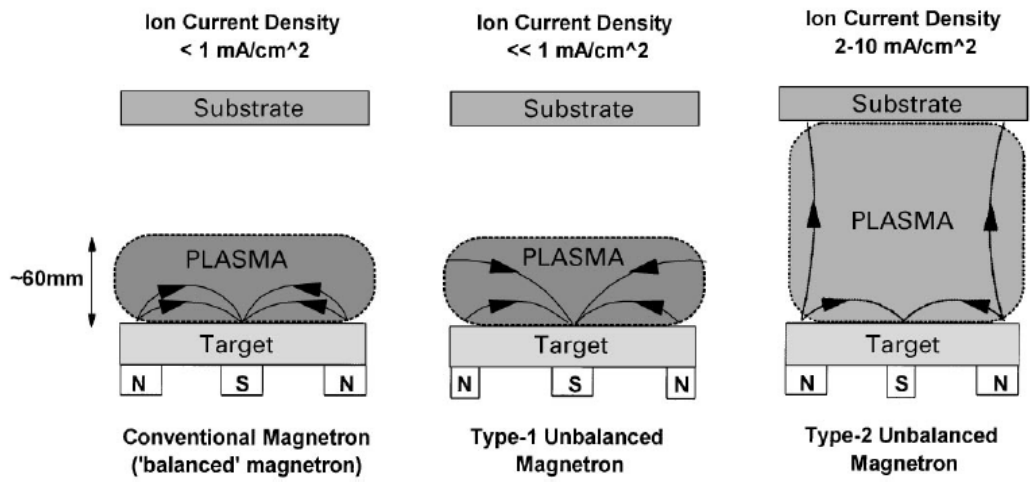

Fig. 12 Schematic representation of the plasma confinement observed in conventional and unbalanced magnetrons [116].

In an unbalanced magnetron, the outer ring of the magnets is strengthened relative to the central pole. In this case, not all the field lines are closed between the central and outer poles in the magnetron, but some are directed towards the substrate, and some secondary electrons are able to follow these field lines. Consequently, the plasma is no longer strongly confined to the target region, but is also allowed to flow out towards the substrate. Thus, high ion currents can be extracted from the plasma without the need to externally bias the substrate. It was Windows and Savvides who first systematically varied the magnetic configuration of an otherwise conventional magnetron [117, 118]. They, and other researchers, have subsequently shown that substrate ion current densities of 5mA/cm^2 and greater, i.e., approximately an order of magnitude higher than for a conventional magnetron, can be routinely generated when using an unbalanced magnetron [116, 118]. A comparison between the plasma confinement obtained in different magnetron modes is shown schematically in Fig. 12.

Thus, in addition to providing a high flux of coating atoms (as compared to a basic sputtering source), an unbalanced magnetron also acts as a very effective ion source. Furthermore, the ion current drawn at the substrate is directly proportional to target current. Deposition rate is also directly proportional to target current. As a result, the ion-to-atom arrival ratio at the substrate remains constant with increasing deposition rate [119]. The design of unbalanced magnetron discussed above was termed ‘type-2’ by Windows and Savvides. However, they also considered the opposite case ‘type-1’, where the central pole was strengthened relative to the outer pole. In this case, the field lines, which do not close in on themselves, are directed towards the chamber walls and the plasma density in the substrate region is low.

Despite the benefits offered by unbalanced magnetrons, it is still difficult to uniformly coat complex components at acceptable rates from a single source. Therefore, in order to commercially exploit this technology, multiple magnetron systems have been introduced. In a multiple magnetron system, the magnetic arrays in adjacent magnetrons can be configured with either identical, or opposite magnetic polarities. In the former case the configuration is described as ‘mirrored' and in the latter case ‘closed field', and both configurations are shown in Fig. 13. In the mirrored case, the field lines are directed towards the chamber walls. Secondary electrons following these lines are lost, resulting in a low plasma density in the substrate region. Conversely, in the closed field configuration, the field lines are linked between the magnetrons. Losses to the chamber walls are low and the substrate lies in a high density plasma region. Operating in the closed field mode results in an ion-to-atom ratio incident at the substrate some 2-3 times greater than that obtained under the same conditions in the mirrored, or single unbalanced magnetron configurations [120].

Also, the influence of the closed magnetic field on the ion-to-atom ratio becomes more marked as the distance from the target increases.

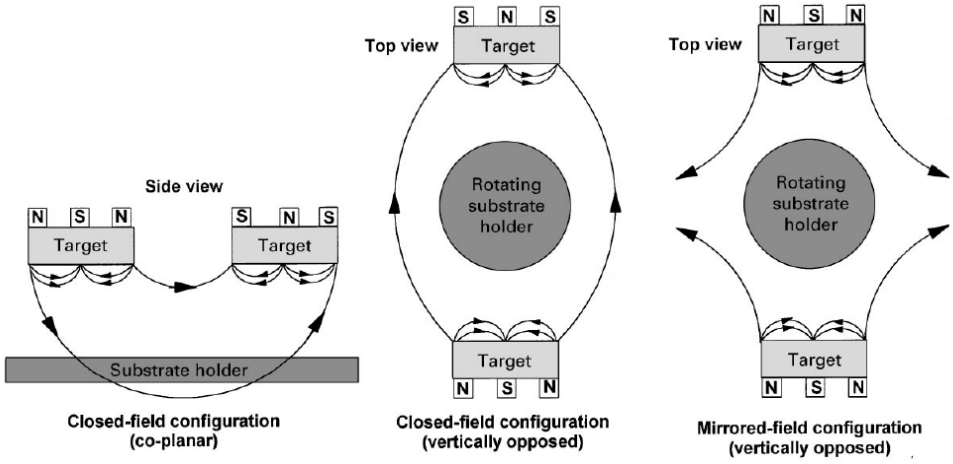

Fig. 13 Dual unbalanced magnetron configurations [119].

The sputtering process has been extensively used to deposit ultra thin films with the sputtering parameters intensively investigated in relation to the materials [121,122] and magnetic properties of the deposited materials [123,124, 125, 126, 127]. A microstructure zone diagram was obtained by John A. Thornton [121, 122] showing the relationship between the substrate temperature and coating temperature, argon pressure and the type of sputtered microstructures obtained (Fig. 14). Granular structure is affected by the adatom mobility on the substrate. When sputtering at low substrate temperatures T_s and high Ar pressure P_{Ar}, the adatoms have low atomic mobility and the films consist of columns separated by voids as shown in Zone 1. As the adatom mobility increases with increasing T_s and decreasing P_{Ar}, the films become denser as shown in Zone T. With further increase of T_s, grain growth occurs and the dense films have rough surfaces as shown in Zone 2 where the surface diffusion dominates. In Zone 3, volume diffusion dominates and the grains become larger.

Coercivity H_c of Mo-permalloy was found to increase with rising preheating temperature [128]. High effective permeability can be acquired at low argon pressure,

adequate preheating temperature, and bias voltage. The coercivity of Co films was also found to increase directly with sputtering pressure up to about 10mTorr [126]. The quality of the sputtered seed layer has been found to influence the property of the layer above [129].

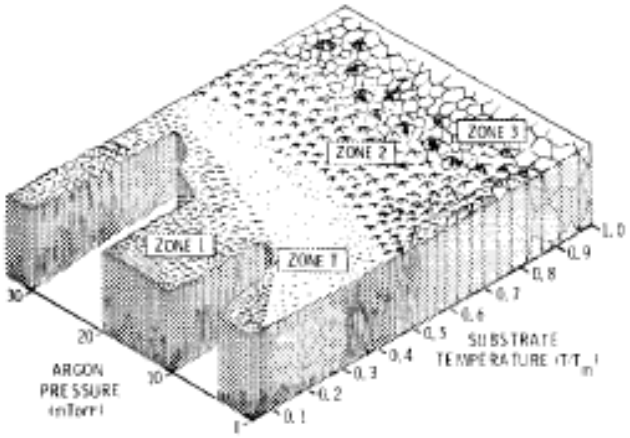

Fig. 14 Microstructure zone diagram for metal films deposited by magnetron sputtering, where T_s denotes the substrate temperature and T_m denotes the coating material melting point [122].

2.8 Magnetic Theories

2.8.1 Domain Wall Theories

A remarkable property of ferromagnetic materials is not so much that they have a spontaneous magnetization, but rather that their magnetization can be influenced by the application of very low magnetic fields. Even the earth's field (50μT) can cause magnetization changes even though the inter-atomic exchanges force that is responsible for the spontaneous magnetization are equivalent to a field of about 1000T, almost 100 million times greater than the earth's field.

What allows this to occur is the fact that the sample is actually composed of small regions called magnetic domains, within each of which the local magnetization is saturated but not necessarily parallel. Domain are small (1-100 microns), but much larger than atomic distances. Consider a large single crystal and assuming the crystal is uniformly magnetized, and hence a single domain. Surface charges will from on the

ends due to the magnetization and are themselves a second source of a magnetic field (the demagnetizing field). The energy associated with the surface charge distribution is called the magnetostatic energy. This is just the volume integral of the field over all space. The magnetostatic energy can be approximately halved if the magnetization splits into two domains magnetized in opposite directions. This brings the positive and negative charges closer together, thus decreasing the spatial extent of the demagnetizing field. This subdivision into more and more domains cannot continue indefinitely since the transition region between domains (domain wall) requires energy to be produced and maintained. Eventually an equilibrium number of domains will be reached for a given particle size, i.e. total energy = magnetostatic energy + wall energy.

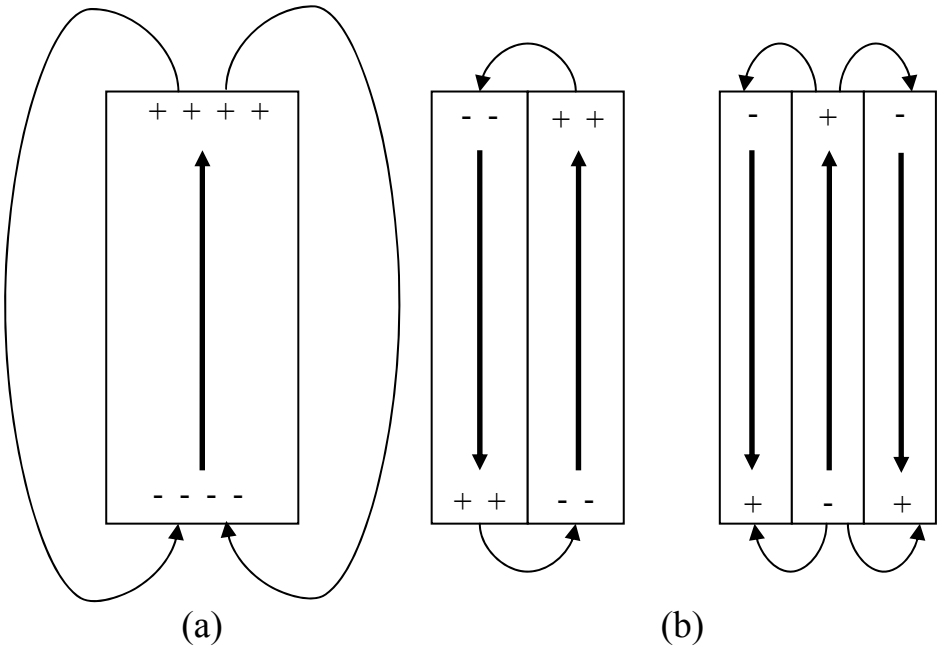

Fig. 15 Domain formation for (a) single domain; (b) multidomain.

Domain walls are interfaces between regions in which the magnetization has different directions. Within the wall, the magnetization must change direction from that in one domain to that in the other domain. Domain walls have a finite width that is determined principally by the exchange and magnetocrystalline energy [130].

Considering a domain wall in which the magnetization changes by 180°. The change in magnetization within the wall can be gradual as in Fig. 16(a) or abrupt in Fig. 16(b). In the case of a wide wall in Fig. 16(a), there have been suggestions of two possible types of domain wall, namely: the Neel wall (where magnetization of wall is in the place of a material) and the Bloch wall (where magnetization of wall is perpendicular to the plane of the material). The exchange energy acts to keep spins parallel and can be kept small if the 180° rotation takes place gradually, over many atomic units. Thus, the exchange energy is small in Fig. 16(a) but large in Fig. 16(b). However, the spins within the wall are no longer aligned along an easy axis of magnetization. This produces an anisotropy energy, which is high in (a) but low in (b).

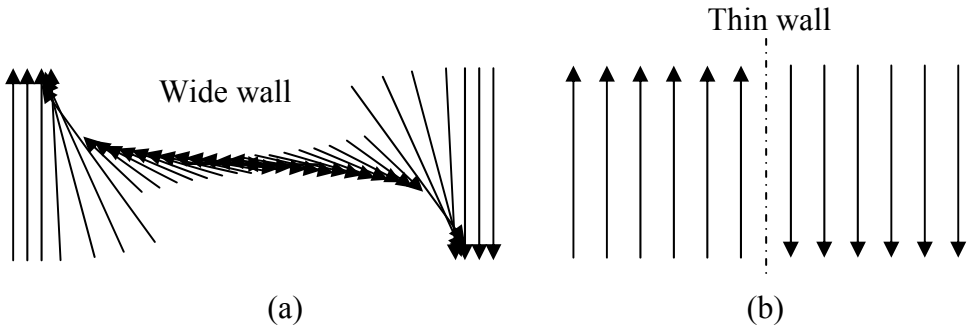

Fig. 16 Schematics showing two different types of domain wall: (a) wide domain wall; (b) thin domain wall.

The exchange energy tends to make the wall as wide as possible whereas the anisotropy tends to make the wall as thin as possible. As a result of this competition between the exchange energy and anisotropy energies, the domain wall has a finite width (in the order of 100 nm) and surface energy. The interplay between long range and short range effects results in the domain states being grain-size dependent. In addition, the number of domains for a given grain size depends on the magnitudes of the exchange, magnetocrystalline, and saturation magnetization. These factors are in turn dependent on temperature as well as composition. Hence, domain states in

different magnetic materials will have different grain size dependence. The domain states will also vary with temperature for a single grain size. As a rule of thumb, the larger the grain size, the more domains it contains.

The energy of this domain wall can be estimated. Assuming that the magnetization rotates by an angle $\delta\theta$ in a distance a (Fig. 17), until θ reaches of $\pm\frac{1}{2}\pi$ on either side of the plane $x = 0$, and beyond that, it remains constant. The region in which θ varies is the domain wall. As in this case, the wall separates two domains magnetized in opposite directions (i.e. a 180° wall). Denoting the width of the wall by w_{wall}, if the wall extends over N inter-atomic distances, then

$$w_{wall} = Na \tag{22}$$

and

$$\delta\theta = \frac{\pi}{N} \tag{23}$$

In a unit volume of material, the number of pairs of neighboring magnetic moments at an angle $\delta\theta$ to each other is $1/a^3$. Hence,

$$E_e = \frac{\beta m^2}{a^3}(\delta\theta)^2 \tag{24}$$

where β is a positive constant for ferromagnetism and m is the length of the magnetic moments. Hence, using Eqn. 22 and Eqn. 24 and writing exchange constant $A_{const} = \beta m^2/a$ (only for simple cubic crystals), the exchange energy per unit volume inside the domain wall is

$$E_e = \frac{A_{const}\pi^2}{a^2 N^2} \tag{25}$$

Assuming that the two domains are magnetized in easy directions such that there is no anisotropy energy associated with the domains, there is however some anisotropy energy associated with the wall, since the magnetization in the wall is in

general not parallel to an easy direction. As a rough approximate, the anisotropy energy per unit area of wall can be assumed to be:

$$\gamma_a = KNa \tag{26}$$

where K is the anisotropy constant. The width of the wall, i.e. the value of N, will adjust itself to make the total energy per unit area a minimum.

$$\gamma = \gamma_e + \gamma_a = \frac{A_{const}\pi^2}{Na} + KNa \tag{27}$$

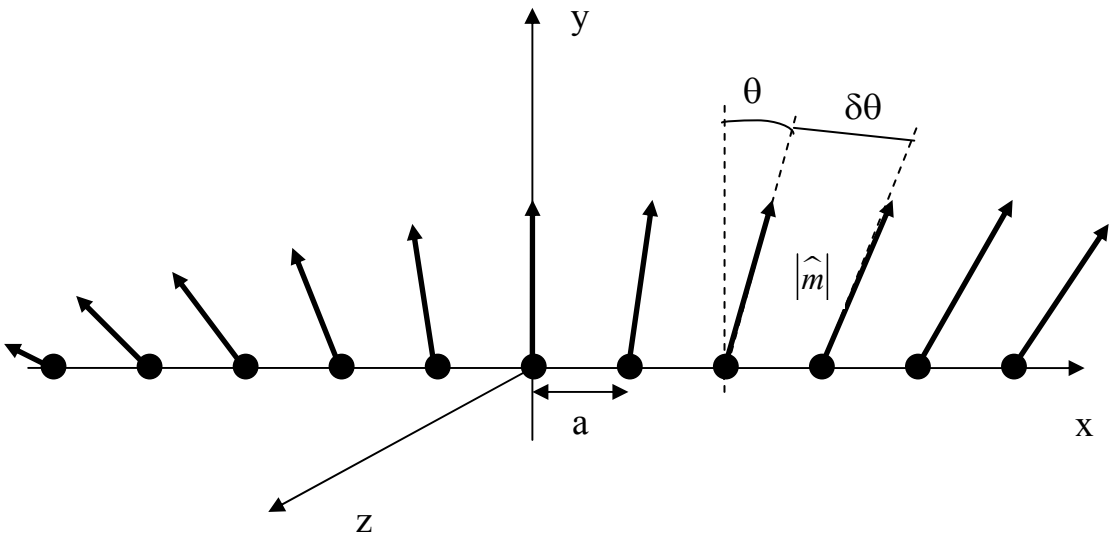

Fig. 17 Schematics showing the rotation of the magnetic moments of atoms along the x axis.

Hence $d\gamma/dN = 0$, which gives

$$-\frac{A_{const}\pi^2}{N^2 a} + Ka = 0 \tag{28}$$

Rearranging Eqn. 28:

$$N = \frac{\pi}{a}\left(\frac{A_{const}}{K}\right)^{\frac{1}{2}} \tag{29}$$

Substituting Eqn. 29 into Eqn. 27, the wall energy unit area can be calculated to be:

$$\gamma = 2\pi (A_{const} K)^{\frac{1}{2}} \tag{30}$$

In a typical material, $A_{const} \approx 10^{-11}$ Jm^{-1} and K is of the order of 10^3-10^5 Jm^{-3}. This shows that w_{wall} is of the order of 100 nm, which is a few hundred inter-atomic distances. Now, the observed size of domains is usually much larger than this, which explains why magnetic materials are subdivided into domains within which the magnetization is uniform, rather than the magnetization rotating slowly throughout the specimen. With the earlier mentioned for A_{const} and K, γ can be estimated to be of the order of 10^{-3} Jm^{-2} and it must be emphasized that this domain wall energy is not a separate type of energy. This clearly showed that the exchange and anisotropy energies are normally concentrated in the domain walls.

In many materials, domain walls move reversibly in very small applied fields. In other words, the walls are displaced by a small amount when the field is applied, but return to their original positions when the field is removed. In larger magnitude of the fields, this motion becomes irreversible – the walls do not return to their original positions even when the field is removed. This is because the energy of the domain walls is not constant, but instead varies in an irregular manner because of non-homogeneities in the specimen, such as inclusions of a second phase, dislocations, grain boundaries, internal stresses, groups of point defects or impurity atoms, voids, etc. In reality, when a wall moves, it encounters obstacles distributed randomly throughout the specimen, and therefore parts of the wall are retarded while other parts bulge forward. Hence, it is therefore not usually possible to represent the wall energy as a simple function of one variable or even three variables.

2.8.2 Magnetization Rotation

For the case in which the magnetization rotates coherently (i.e. it remains uniform even while it is rotating), the theory is well understood [131,132,133]. The simplest case is that of a uniformly magnetized (ellipsoid shape) particle with a positive uniaxial anisotropy K_u (Stoner-Wohlfarth rotation model). The anisotropy energy E_a of such a non-interacting particle can be written as:

$$E_a = K_u V \sin^2 \varphi \tag{31}$$

where V is the volume of the particle, and φ is the angle between the magnetization M and some fixed direction in the particle [131].

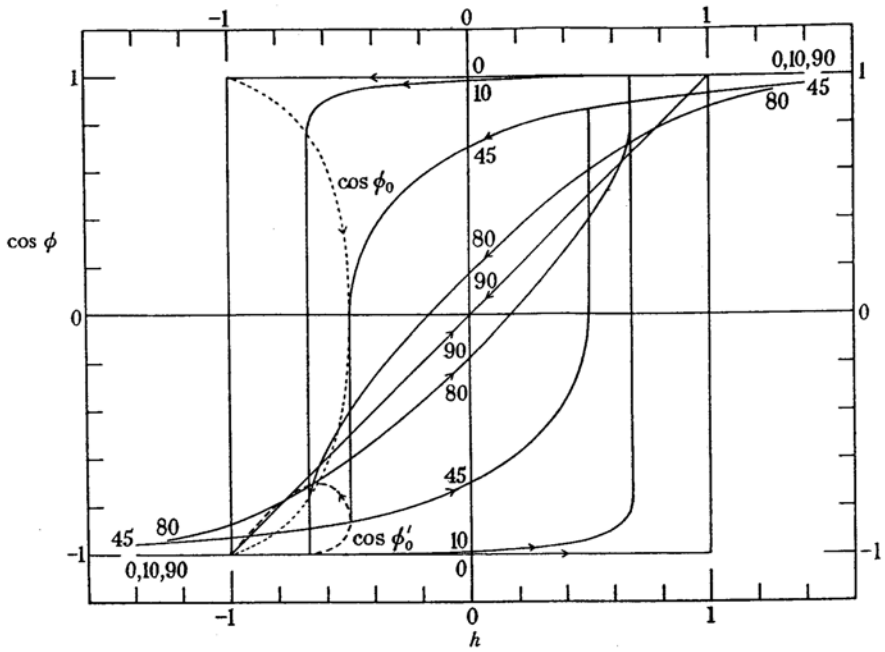

Fig. 18 Magnetization curves for prolate spheroids, calculated from the model by Stoner and Wohlfarth [132]

The magnetic hysteresis properties of ellipsoidal single-domain particles with uniaxial shape anisotropy have been investigated in detail by Stoner and Wohlfarth [132], who showed that for a prolate ellipsoid of revolution there are only two stable positions of the magnetization vector, i.e. parallel to the long easy axis of

magnetization. According to the model, as θ increases, the coercivity decreases, and for $\theta = 90°$, it is zero (Fig. 18). The largest coercivity, at $\theta = 0°$, can be shown to be $2K_u/\mu_0 M_s$. In the case when the anisotropy is due to the crystal structure, this maximum coercivity is referred to as the anisotropy field H_k, because it is the field needed to rotate the magnetization from an easy to a hard direction.

2.8.3 Random Anisotropy Model (RAM)

Classical rule of soft magnetic engineering states that, soft magnetic properties of polycrystalline magnets deteriorate with decreasing grain size [134]. However, this rule seems to be at odds with the phenomenon displayed by the novel nanocrystalline materials. As a matter of fact, this rule only applies as long as the grain diameter is larger than the ferromagnetic exchange length L_{ex}. Otherwise, the magneto-crystalline anisotropy K_1 of the grains is suppressed due to the smoothing part of ferromagnetic exchange interaction. This mechanism seems to provide the basis for the soft magnetic properties of the nanocrystalline structure [135]. This mechanism resembles much the case of amorphous alloys where atomic-scale local anisotropies are randomly averaged out so that there would be no anisotropy net-effect on the magnetization process. The degree to which this mechanism is effective has been successfully addressed by Alben et al. [136] in terms of the so-called random anisotropy model.

The magnetic properties of an assembly of small grains depend strongly on the counterplay of local magnetic anisotropy energy and ferromagnetic exchange energy [101]. For large grains, the magnetization can follow the easy magnetic directions in the single grains. Thus, the magnetization process is determined by the magneto-crystalline anisotropy K_1 of the crystallites. However, for very small grains,

ferromagnetic exchange interaction further forces the magnetic moments to align parallel and thus impeding the magnetization to follow the easy direction of each individual grain. As a consequence, the effective anisotropy for the magnetic behavior is an average overall several grains and thus reduced in magnitude. The dividing line between these two cases is given by the ferromagnetic exchange length L_{ex}:

$$L_{ex} = \sqrt{A / K_1} \tag{32}$$

where A denotes the exchange stiffness that is a basic parameter in domain wall theory, representing a characteristic minimum scale over which the magnetization can vary appreciably.

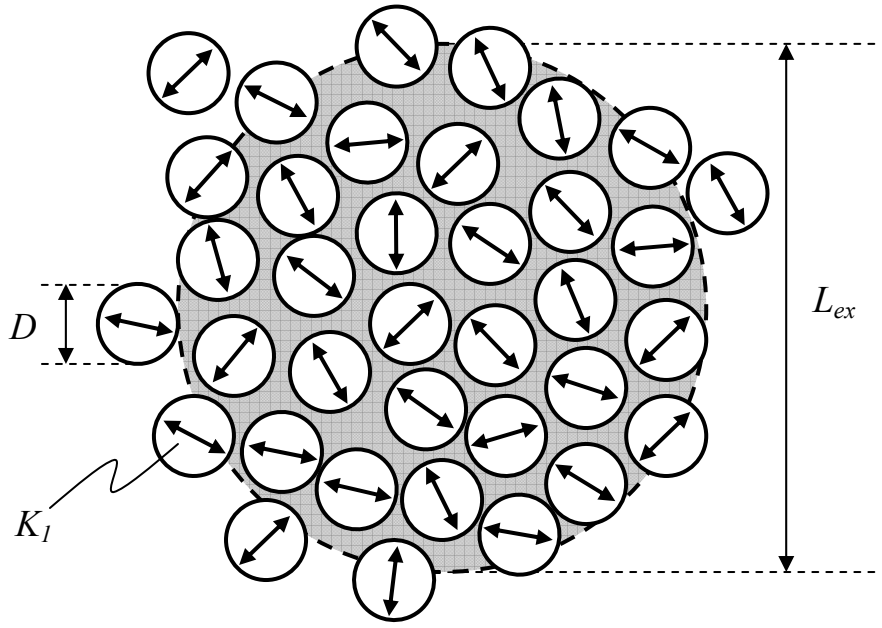

Fig. 19 Schematic representing the random anisotropy model, for grains embedded in an ideally soft ferromagnetic matrix. The double arrows indicate the randomly fluctuating anisotropy axis, the hatched area represents the ferromagnetic correlation volume determined by the exchange length $L_{ex} = (A / \langle K \rangle)^{1/2}$.

In order to interpret the behavior of the magnetic properties for very small grain sizes, the random anisotropy model, originally proposed by Alben et al. [136] for amorphous ferromagnets, was used. The proposed idea [101,137] starts from an assembly of ferromagnetically coupled grains of size D and volume fraction v_{cr} with

magneto-crystalline anisotropies K_1 oriented at random, as depicted in Fig. 19.

The effective anisotropy affecting the magnetization process results from averaging over the total number of grains $N_G = \nu_{cr}(L_{ex}/D)^3$ within the volume $V = L_{ex}^3$ of the exchange length. For a finite number of grains N, there will always be some easiest direction determined by statistical fluctuations. As a consequence, the resulting anisotropy density $\langle K \rangle$ is determined by the mean fluctuation amplitude of the anisotropy energy of the N grains, i.e.

$$\langle K \rangle \approx \frac{\upsilon_{cr} K_1}{\sqrt{N_G}} = \sqrt{\upsilon_{cr}} K_1 (\frac{D}{L_{ex}})^{3/2} \tag{33}$$

In turn, the exchange length L_{ex} is related self-consistently to the average anisotropy by substituting $\langle K \rangle$ for K_1 in Eqn. 33, i.e.

$$L_{ex} = \sqrt{\frac{A}{\langle K \rangle}} \tag{34}$$

This renormalization of L_{ex} results from the counterplay of anisotropy and exchange energy as magneto-crystalline anisotropy is suppressed by exchange interaction in the scale on which exchange interactions dominate expands at the same time. Thus, the local anisotropies are averaged out even more effectively. Combining, Eqn. 33 and Eqn. 34 yields:

$$\langle K \rangle \approx \upsilon_{cr}^{\,2} K_1 (\frac{D}{L_{ex}})^6 = \upsilon_{cr}^{\,2} \frac{K_1^4}{A^3} . D^6 \tag{35}$$

which holds as long as the grain size D is smaller than the exchange length L_{ex}. It should also be noted that this result is essentially based on statistical and scaling arguments and therefore not limited to the case of uniaxial anisotropies, but also holds for cubic or other symmetries. The most significant feature of the above analysis is the strong variation of $\langle K \rangle$ with the sixth power D^6 of the grain size. If coercivity H_c

and initial permeability μ_i, are related to $\langle K \rangle$ using the results for coherent spin rotation [61]:

$$H_c = p_c \frac{\langle K \rangle}{M_s} \approx p_c \frac{K_1^4 . D^6 \nu_{cr}^2}{M_s . A^3} \tag{36}$$

$$\mu_i = p_\mu \frac{M_s^2}{\mu_0 \langle K \rangle} \approx p_\mu \frac{M_s^2 . A^3}{\mu_0 K_1^4 . D^6 \nu_{cr}^2} \tag{37}$$

where M_s denotes the saturation magnetization, p_c and p_μ denotes dimensionless pre-factors that are close to unity. Accordingly, the sensitive grain size dependence of $\langle K \rangle$ should be also reflected in the soft magnetic properties. It should also be noted that the above results for H_c and μ_i are not bound to the case of coherent magnetization rotation, in the regime $D << L_{ex}$, but can also be derived, assuming domain wall pinning as the prevailing magnetization mechanism.

In the case of large grains, if the grain size exceeds the exchange length, the effective anisotropy $\langle K \rangle$ for the magnetization process is given by the magnetocrystalline anisotropy K_1 itself. For $D = L_{ex}$, coercivity and permeability approach their maximum or minimum value, respectively given by:

$$H_c = p_c \frac{K_1}{M_s} \tag{38}$$

$$\mu_i = p_\mu \frac{M_s^2}{\mu_0 K_1} \tag{39}$$

Finally, if the grain size exceeds the domain wall width, $w_{wall} = \pi L_{ex} = \pi (A / K_1)^{1/2}$, the magnetization process is determined by domain wall pinning at the grain boundaries. For that case, theory predicts [101]:

$$H_c = p_c \frac{\sqrt{AK_1}}{M_s.D} \tag{40}$$

$$\mu_i = p_\mu \frac{M_s{}^2.D}{\mu_0 \sqrt{AK_1}} \tag{41}$$

The theoretical predictions for very small grains and large grains can be verified and reflected accurately in the experimental results obtained in [101], as shown in Fig. 20.

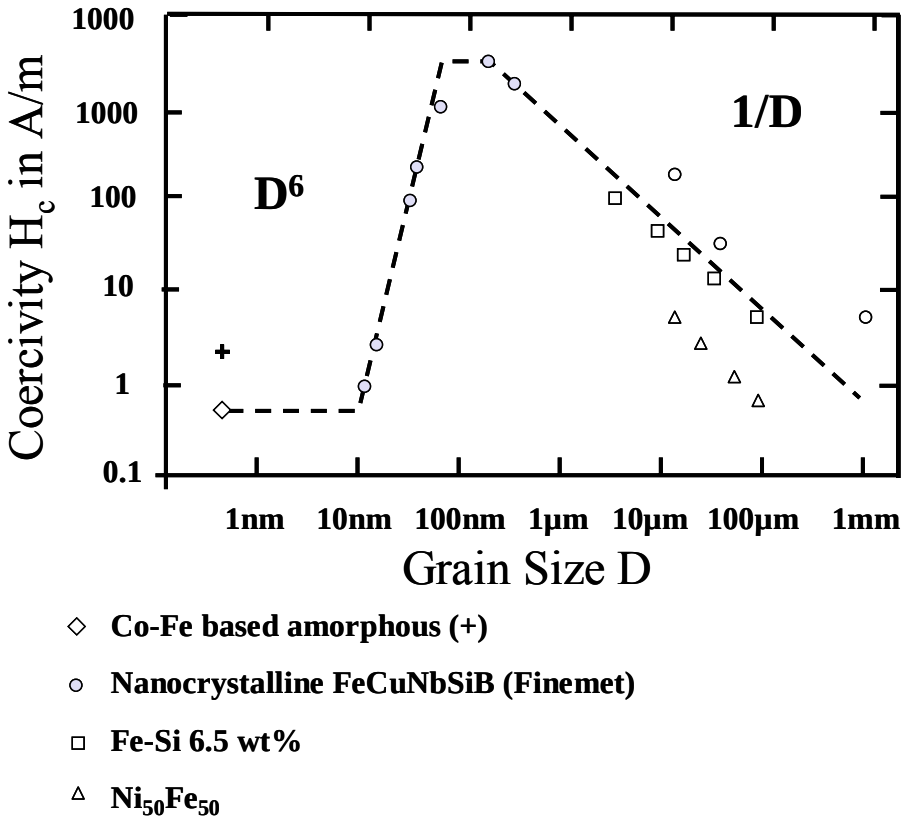

Fig. 20. Grain size and coercivity H_c for various soft magnetic metallic alloys [101].

2.8.4 Single Domain

As the grain size decreases, a critical size will be reached where the grain can no longer accommodate a wall. Below this critical size, the grain contains a single-domain, which is uniformly magnetized to its saturation magnetization. It is an energetically easy process to change the magnetization of a multi-domain grain since the transition of the domain wall can be accomplished in relatively low fields. Thus,

the multi-grains are magnetically soft with low values of coercivities and remanence. However, the only way to change the magnetization of a single-domain grain is to rotate the magnetization, an energetically difficult process. Thus, single-domain grains are magnetically hard and have high coercivities and remanence. The critical size for single-domain behavior depends on several factors, including the saturation magnetization and the shape of the grain. The single-domain and multi-domain transition size can be determined either through theoretical calculations [61] or through experimental determinations [138, 139,140]. The critical diameter *DC* for which the multi-domain structure becomes single-domain can be estimated from the balance between the energy to form a single wall and the alternative magnetostatic energy as

$$d_c = 9\left(AK\right)^{1/2}/(2\pi M_s{}^2) \tag{42}$$

where A_{const} and K are the exchange and the anisotropy constants respectively [**Error! Bookmark not defined.**].

2.8.5 Superparamagnetism

As grain size continues to decrease within the single domain range, another critical threshold is reached, at which remanence and coercivity go to zero. When this happens, the grain becomes superparamagnetic, a phenomenon by which magnetic materials may exhibit a behavior similar to paramagnetism at temperatures below the curie or the Neel temperature. Normally, coupling forces in magnetic materials cause the magnetic moments of neighboring atoms to align, resulting in very large internal magnetic fields. At temperatures above the curie temperature (or the Neel temperature for antiferromagnetic materials), the thermal energy is sufficient to overcome the coupling forces, causing the atomic magnetic moments to fluctuate randomly. Since

there is no longer any magnetic order, the internal magnetic field no longer exists and the material exhibits paramagnetic behavior.

Superparamagnetism occurs when the material is composed of very small crystallites (usually in the region of 1-10 nm). In this case even though the temperature is below the curie or Neel temperature and the thermal energy is not sufficient to overcome the coupling forces between neighboring atoms, the thermal energy is sufficient to change the direction of magnetization of the entire crystallite. The resulting fluctuations in the direction of magnetization cause the magnetic field to average to zero. The material behaves in a manner similar to paramagnetism, except that instead of each individual atom being independently influenced by an external magnetic field, the magnetic moment of the entire crystallite tends to align with the magnetic field.

The energy required to change the direction of magnetization of a crystallite is called the crystalline anisotropy energy and depends both on the material properties and the crystallite size. As the crystallite size decreases, so does the crystalline anisotropy energy, resulting in a decrease in the temperature at which the material becomes superparamagnetic.

2.8.6 Magneto-impedance (MI) Effect

The magneto-impedance (MI) effect can be observed in soft magnetic metals, and generally consists of the change of the AC impedance, $Z = R + iX$, where R is the resistance (real part) and X is the reactance (imaginary part) when subjected to a static magnetic field, H_0 [141]. The MI ratio $\Delta Z/Z$ is usually defined as

$$\Delta Z/Z = \frac{Z(H_0) - Z(H_{\max})}{Z(H_{\max})}(\%) \tag{43}$$

where Z is the impedance modulus and H_{max} is the maximum measuring field at which the specimen is considered to be magnetically saturated. In general, when the MI ratio is above 100%, the term giant magneto-impedance (GMI) effect is used instead. It has been reported that maximum GMI ratios of up to 600% have been achieved by amorphous microwires, at frequencies around 1 MHz for maximum applied fields H_{max} in the order of hundreds of Oe [142], and maximum GMI ratios of up to 1200% have been achieved by nanocrystalline composite wires at similar testing conditions [142].

In general, the complex impedance of a linear electronic element at the circular frequency ω is given by:

$$Z(\omega) = U_{ac} / I_{ac} = R + iX \tag{44}$$

where I_{ac} is the harmonic current with frequency ω flowing through the element and U_{ac} is the harmonic voltage of the same frequency, measured between its terminals. However, it must be noted that Eqn. 44 is not fully applicable to ferromagnetic conductors because such materials are usually not linear as U_{ac} is generally not proportional to I_{ac} and it is not a harmonic function of time (it contains higher order harmonics) [143 , 144]. Only under certain circumstances the ferromagnetic conductor can be considered as a linear element and can be approximated using the procedure for the calculation of complex impedance. Although the definition of GMI ratio $\Delta Z/Z$ (the ratio $\Delta Z/Z$ linearly depends on $|Z|$) is widely used and useful for quantifying the huge attained variations of impedance, the definition by means of the ratio of Z/R_{DC} (where R_{DC} is the DC resistance of the sample) should be a better choice due to the shortcomings of the earlier simpler definition. The shortcomings include: (i) the information about the phase shift is lost; (ii) it depends on the ambiguously chosen H_{max} since the specimen might be apparently magnetically

saturated does not necessarily mean that GMI is also saturated; (iii) the ratio $\Delta Z/Z$ is rather sensitive to how much of the measuring circuit is included in $Z(H_{max})$.

Beside the magnitude and direction of the applied DC field, the main parameter determining GMI is the frequency of the driving current that generates the circular AC driving magnetic field. Depending on this frequency, approximately three main regions can be roughly defined.

A. Very low frequency regime (frequency range of 1-10 kHz)

In this frequency regime, the driving current simply generates a circumferential time dependent magnetic field. Such a field causes a circular magnetic flux change and generates a longitudinal electric field that in turn gives rise to an inductive voltage across the specimen. In other words, the inductive voltage is determined by the internal inductance L_i that in turn depends on the spatial distribution of the transverse permeability within the specimen. Thus, when a time varying current is flowing through a ferromagnetic wire, an AC voltage U_{ac} appears between the ends of the wire. This total voltage is the complex sum of a resistive voltage U_R and an inductive voltage U_L:

$$U_{ac} = U_R + iU_L = R_{dc}I_{ac} + i\omega L_i I_{ac} \tag{45}$$

where R_{DC} is the DC resistance of the sample. When an external DC magnetic field H_0 is applied, both the circular component of magnetization and the circular permeability changes, giving rise to a large change in U_{ac}. The complex impedance of the specimen is defined as the ratio between U_{ac} and the driving current I_{ac}, i.e.

$$Z = \frac{U_{ac}}{I_{ac}} = R_{dc} + i\omega L_i \tag{46}$$

It can thus be concluded that at very low frequencies, the field dependence of impedance is attributed to its inductive part, that is simply proportional to the circumferential permeability $\mu_\phi(I, H_{ext}, f)$. Therefore, at very low frequencies, the change of the material's impedance is exclusively attributed to the magneto-inductive effect arising from the circular magnetization process [145]. Due to large Barkhausen jumps in the domain wall motion, the inductive voltage U_L can be very far from the harmonic waveform, especially for high amplitudes of driving current. This allows for easy distinguish of the resistive and inductive components of the total voltage U_{ac} [44].

In the range of frequencies typical of the magneto-inductive effect, simple experimental setup can be used. It is even possible to use the regular four probe method with an AC current source for the probe current and a measurement performed with a conventional lock-in amplifier. If phase information is not necessary, a simple AC voltmeter or oscilloscope can be used to measure the voltage drop across the magneto-inductive element.

B. Low and intermediate frequency regimes (frequency range of 10kHz to a few hundreds MHz)

The changes of complex impedance in the moderate frequency range, induced by magnetic field, were first identified as the GMI effect. This phenomenon was soon explained in terms of classical skin effect in magnetic conductors with a large effective permeability and its strong dependence on the magnitude of external DC magnetic field [146]. Therefore, the explanation of GMI response of a particular sample is equivalent to the understanding of the dependence of its permeability on the external magnetic field and frequency. In the classical description of skin depth, the permeability is considered as a scalar quantity. In real ferromagnetic materials, the

situation is much more intricate. Magnetic induction *B* and magnetic field *H* are usually not parallel and the relationship between them is not linear. Thus, the AC permeability is generally a complex tensor that depends on a number of parameters such as frequency *f*, magnetic field *H*, amplitude of the AC magnetic field associated to the driving current, anisotropies, stress distribution and the domain structure in the specimen.

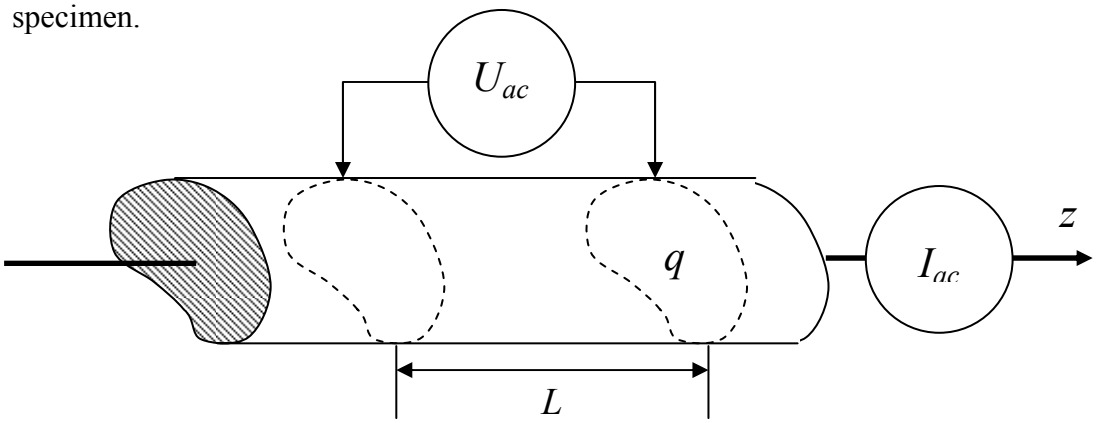

Fig. 21 Schematic to the definition of impedance.

The skin effect, which is responsible for GMI at medium and high frequencies, is a phenomenon well described by the classical electrodynamics [147] many years ago. As a consequence of induced eddy currents, the high frequency AC current is not uniformly distributed in the conductor volume but is confined to a shell close to the surface, with depth $\delta = \sqrt{2\rho/\omega\mu}$ (where ω is the circular frequency, ρ the resistivity and μ the magnetic permeability).

Let us assume an infinite straight conductor (satisfying the Ohm's Law $e = \rho j$, where e is the AC electric field vector, ρ is the resistivity and j is the AC current density vector) with a uniform cross section of the area q (see Fig. 21). The impedance Z measured between two points at the distance L is given by the formula.

$$Z = \frac{U_{ac}}{I_{ac}} = \frac{\int_L e_z(S)dz}{\iint_q j_z dq} = \rho \frac{\int_L j_z(S)dz}{\iint_q j_z dq} \tag{47}$$

where j_z and $e_z = \rho j_z$ are the amplitudes of longitudinal components of AC current density and electric field respectively. The symbol S refers to the surface of conductor. If the current density j_z is independent of coordinate z one gets from Eqn. 47.

$$\frac{Z}{R_{dc}} = \frac{j_z(S)}{\langle j_z \rangle_q} \tag{48}$$

where $R_{DC} = pL/q$ is the DC resistance and $\langle q \rangle$ denotes the average value over the cross section q. As can be seen, the ratio Z/R_{DC} is given by ratio of the current density at the surface to its average value.

Using the Ampere's law $I = \oint_C hdl$, where C is the contour of the area q, the total current is given by $I_{ac} = Ih_\phi(S)$, where $h_\phi(S)$ is the circumferential component (tangential to the surface and perpendicular to z) of AC magnetic field on the surface and I is the length of the contour C. In metals, the relationship between the tangential components of e and h at the surface can be described by the 2x2 surface impedance tensor $\hat{\zeta}$ [147]:

$$e_t(S) = \hat{\zeta} n \times h_t(S) \tag{49}$$

where n is the normal vector of the surface (directed outside the conductor). Using Eqn. 47 and Eqn. 49 one gets the relation between Z and the surface impedance.

$$Z = \frac{L}{l}(\zeta zz - \zeta_{z\phi} \frac{h_z}{h_\phi}) \tag{50}$$

In the case of special symmetry, when the surface impedance tensor is diagonal or the axial component h is zero, the 2nd term on the right side vanishes and the

impedance is proportional to the surface impedance ξ_{zz}. The off-diagonal component $\xi_{z\phi}$ is responsible for "cross-magnetization" and asymmetric GMI. The impedance shown above was derived under the assumption of an infinitely long conductor. In a closed measuring circuits, the "external" self-inductance L_e of the conductor, which is related to the magnetic energy stored in the circuit (outside the conductor volume) [147] should be added to the impedance Z. The self-inductance L_e, however, is not an intrinsic property of the conductor and depends on the particular geometry of the measuring circuit. If it is properly determined, it can be included into the impedance of the measuring circuit itself.

The very essence of GMI lies in the fact that in extremely soft magnets, the skin effect appears at frequencies several orders of magnitude lower than those expected for a non-magnetic conductor with equivalent conductivity. Besides that, GMI requires a high efficiency of the static fields to modify the AC permeability, the skin depth and consequently the impedance. Moreover, in ferromagnetic metals, the AC permeability is not isotropic. It depends on the orientation of both the AC and DC magnetic fields as well as on the magnetic and shape anisotropies of the sample. Therefore the AC permeability, which takes part in GMI, is the effective transverse permeability μ_t. In summary, to observe GMI, the transverse permeability μ_t (H, f) (or circumferential permeability μ_ϕ in the case of cylindrical geometry) has to be large enough and must be significantly modified by the static field.

Generally, both the domain wall motion and magnetization rotation contribute to the effective transverse permeability [148]:

$$\mu_t = \mu_{t(rot)} + \mu_{t(dw)} \tag{51}$$

where $\mu_{t(rot)}$ and $\mu_{t(dw)}$ are the corresponding contributions to the effective transverse permeability. At relatively low frequencies (<1 MHz), both contributions are effective

in the transverse magnetization process. At relatively higher frequencies, the domain wall motion is strongly damped by eddy currents and the magnetization rotation dominates the process. Both contributions for the magnetization process can be accurately separated by means of complex permeability formalism, as employed by Valenzuela et al in soft magnetic amorphous wires [149, 150, 151].

Special care must be taken to ensure the correct measurement of the driving current amplitude while measuring MI effect in the moderate frequency range. There is a need for impedance match over all connections. As the frequency is increased, this impedance match becomes critical to ensure the power delivery to the MI element. Samples leads can produce the unbalancing of the whole impedance and thus special care should be taken for them. Another possibility (which works for a limited range of frequencies) is to use a relay to measure a voltage drop across a series resistor and adjust the current flowing through the sample for each frequency and field value. In this case, a perfect impedance match is less important once the actual current value is measured, although cables with higher characteristic impedance, e.g. oscilloscope probes, are needed. The careful choice of the relay is also crucial.

C. High frequency regime (frequency range in the order of GHz)

Although ferromagnetic resonance (FMR) is usually studied in saturated specimens placed in a cavity subjected to a microwave excitation at about 9 GHz (X-band) or higher, it is now widely accepted that the GMI effect is a fingerprint of FMR, even in the low frequency ranges [152, 153, 154]. Therefore, the description of MI should take into account the dynamical effects on the magnetization, related to FMR. The basic conditions to obtain the resonance are: (i) presence of an effective static field $H_{eff(0)}$ that fixes the spin orientation and (ii) presence of a component of AC

magnetic field *h* perpendicular to the static field. This field may exhibit either planar symmetry, for film conductors, or circumferential symmetry, for wires. Close to the resonance, *h* supplies energy to compensate the losses associated to the interaction of the rotating magnetic moments with the surrounding medium, thus maintaining the magnetization precession. The FMR regime results in drastic changes of magnetic permeability with frequency and/or field, with this behaviour being reflected in the impedance as well. At resonance, a small change in the static magnetic field results in a large change of the impedance.

At frequencies above 10 MHz, where the electromagnetic radiation becomes important, the use of microwave lines and cavities is recommended. In most cases, in order to facilitate the experimental methods, the coaxial line technique (for wires) [155, 156] and the stripline cavity technique (for films and ribbons) [157, 158] are used. The theoretical description of GMI in the high frequency regime is based on the simultaneous solution of the Landau-Lifshitz and Maxwell equations, which shows that the maximum theoretical GMI ratio is determined by minimum skin depth that is achieved for the FMR resonance condition [152]. However, this will not be further discussed in this review as the bulk of the studies were based on measurements of impedance at low and intermediate frequency regimes.

2.9. Summary

To explain for the signifance of the project objectives, an overview of magnetic sensors applications was described, with the classification of such applications carried out according to the sensitivity of the sensors. As implicated from the earlier sub-chapters, successful development of high sensitivity magnetic sensors can potentially enhance the performance of existing applications as well as open up new applications.

An extensive review on the existing sensor technology as well as the available sensing elements revealed that composite wires development are a relatively new technology and is potentially beneficial to the high sensitivity of the magnetic sensors. Furthermore, no reported work was carried out in research areas related to the project objectives.

Reviews on relevant magnetism and magnetic material theories, such as domain theory, random anisotropy model (RAM), giant magneto-impedance (GMI) effect, superparamagnetism, provide the author with a strong foundation on which the research approach was designed and implemented to achieve the established project objectives. In particular, based on the basis that: 1) the permeability increases greatly with decreasing grain size as the grain size are below the exchange length; 2) that there must be a lower bound below which the permeability drops rapidly due to superparamagnetism, it will be extremely beneficial for the magnetic properties of the composite wires if the nanaocrystalline grain sizes of the deposited magnetic material are to be reduced.

Chapter 3 Research Approach and Experimental Setups

3.1. Research Approach

In order to fulfill the objectives, which is to develop super permeability $Ni_{80}Fe_{20}$/Cu composite wires, the effect of the synthesis process parameters on the resulting properties of the wire specimens has to be investigated. Thus, this investigation essentially involves several synthesis and characterizing methods and setup. This chapter discusses the fabrication methods as well as the setup used to develop composite wires, namely electrodeposition, cold-drawing and magnetron sputtering. The characterization methods and equipment were also described in this chapter.

Fig. 22 shows the flowchart of the fabrication and characterization steps for the composite wires. The $Ni_{80}Fe_{20}$/Cu composite wires specimens were developed using three different synthesis methods, in order to compare the properties of the wires from different methods. These wire specimens were then characterized according to the following material properties: 1) surface smoothness using scanning electron microscopy (SEM); 2) coating thickness using SEM, since the total thickness of the wire can be obtained from the SEM pictures and the Cu core diameter is known; 3) average nanocrystalline grain size using X-ray diffraction (XRD) and transmission electron microscopy (TEM). In the case of average grain size measurement, XRD has been widely used in this study. However, this method only provides calculated values of the average crystallite size and this calculated value has to be calibrated using TEM, since TEM provides pictures of the actual grains, despite showing unclear grain

boundaries. The main disadvantage associated to the use of TEM is the extremely long hours used for the preparation of the specimens.

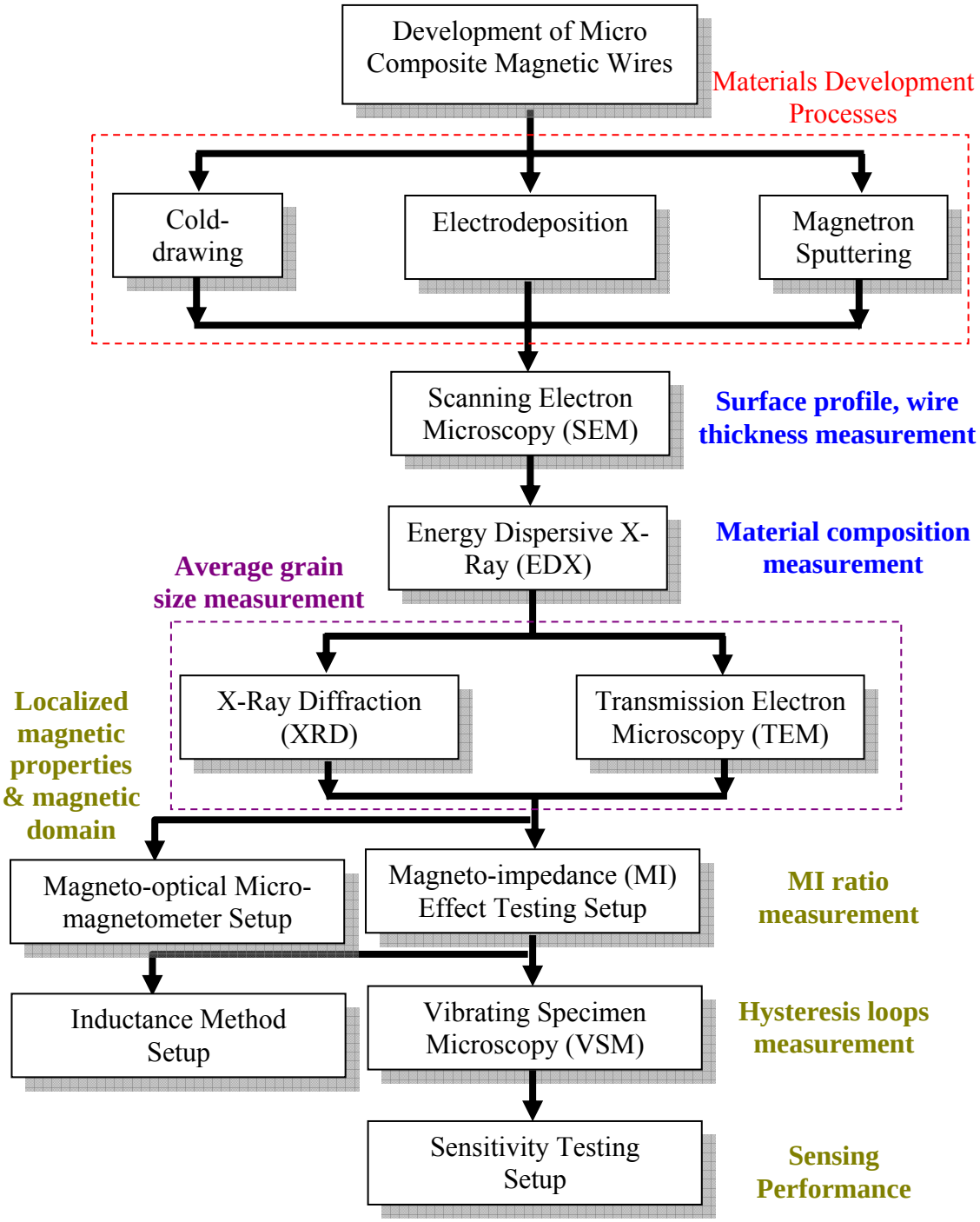

Fig. 22 Flowchart showing the fabrication and characterization methods for the composite wires specimens.

The magnetic properties of the specimen wires were also measured and characterized. These magnetic characterizations include: 1) hysteresis loop using vibrating specimen magnetometer (VSM) and the inductance method, displaying the

values of saturation magnetization and coercivity; 2) magneto-impedance (MI) effect using MI effect setup.

3.2. Materials development and fabrication processes

3.2.1. Electrodeposition

Electrodeposition process essentially involves the flow of current in the electrolyte solution from the anode to the cathode, leading to the anomalous co-deposition of Ni-Fe on the cathode. Some characteristic reaction equations occurring during the deposition process include:

$$Ni^{2+} + 2e^{-} \rightarrow Ni \quad (52)$$

$$Fe^{2+} + 2e^{-} \rightarrow Fe \quad (53)$$

$$Ni^{2+} + 2OH^{-} \rightarrow Ni(OH)_2 \quad (54)$$

$$H_2O \rightarrow H^{+} + OH^{-} \quad (55)$$

$$H^{+} + H^{+} \rightarrow H_2 \quad (56)$$

where Eqn. 52 and Eqn. 53 are the reactions occurring at the cathode and are responsible for the deposition of the ferromagnetic alloy, Eqn, 54 is the reaction causing the deposition of ferromagnetic alloy Ni-Fe to be of a anomalous nature and Eqn. 55 and Eqn. 56 showing the reactions occurring in the chemical electrolyte solution resulting in hydrogen gas evolution during electrodeposition.

In this process, a copper wire of 20μm in diameter was fixed to the centre of a stainless steel plating cell (counter electrode) and cleansed in diluted 20% hydrochloric acid (HCl) and distilled water. The wire, together with the cell, is then submerged in an electrolyte solution (Watts-type) with the concentration listed in Table 3.

Potassium hydroxide pellets, dissolved in distilled water, was used to maintain the pH value of the electrolyte solution throughout the plating process. For NiFe electrodeposition, pH value was maintained at around 3.4. Plating was carried out at a constant temperature of 55°C by means of a water bath. The plating current was fixed at 1 mA, which means the current density J was 2 A/dm^2. A schematic diagram of the electrodeposition process is presented in Fig. 23.

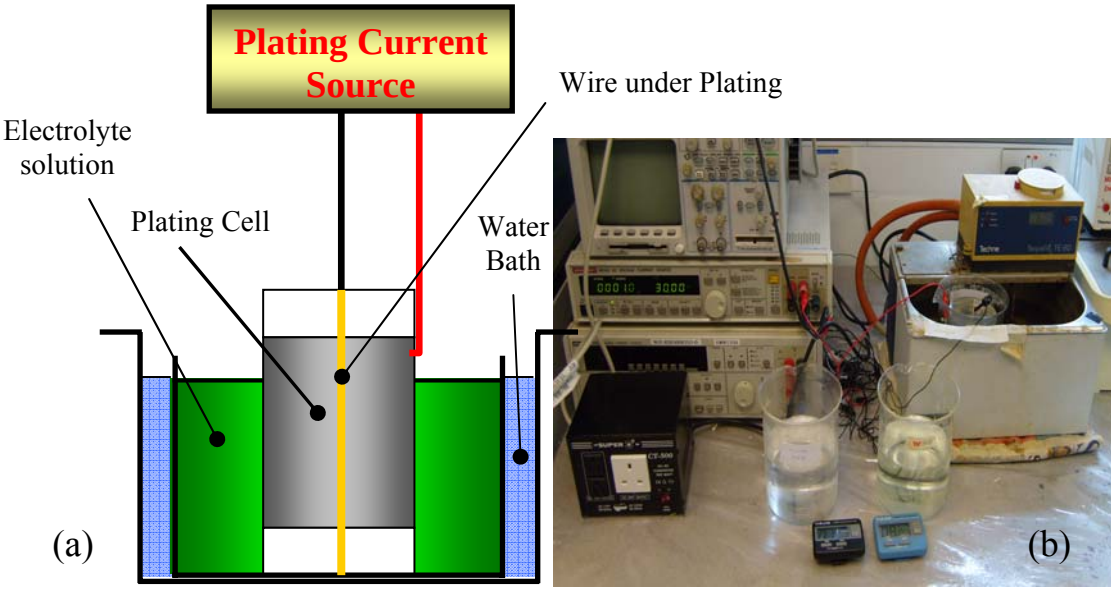

Fig. 23 (a) Schematic diagram for electrodeposition for wires; (b) Photograph showing the equipment involved in the electrodeposition for wires.

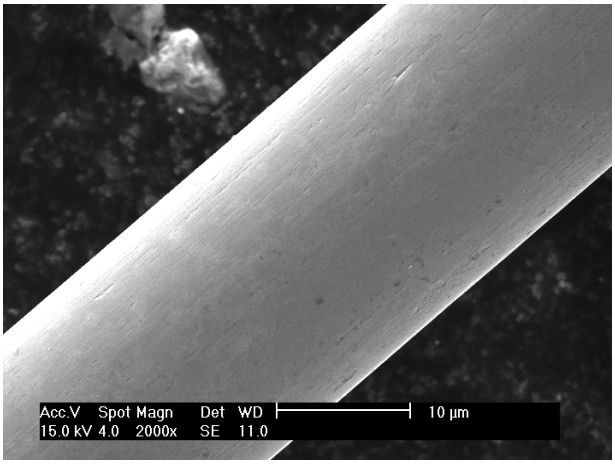

Fig. 24 SEM Picture of the copper wire, displaying the surface smoothness of the wire.

For NiFeMo electrodeposition, plating was carried out at the deposition time of 5 minutes and the current of 6 mA, with ultrasonic agitation. The electrolyte solution

was maintained at a pH of 3.0 at room temperature. The cold-drawn copper wires used in the electrodeposition of wires were obtained from Tanaka Electronics. The surface smoothness of the wire is shown in Fig. 24.

Table 3 Chemical concentration for NiFe and NiFeMo electrolyte plating bath.

Chemical Name / Formula	Concentration For NiFe Plating	Concentration for NiFeMo Plating
$FeSO_4.7H_2O$	Varied	Varied
$NiSO_4.6H_2O$	125 g/L	108.53 g/L
$NiCl_2.6H_2O$	20 g/L	-
H_3BO_3	40 g/L	-
Saccharin	6 g/L	3 g/L
$Na_2MoO_4.2H_2O$	-	15.5 g/L
Sodium Chloride	-	10 g/L
Citric Acid	-	66 g/L

For NiFe electrolyte solution, the chemicals $FeSO_4.7H_2O$ and $NiSO_4.6H_2O$ are the main sources of Fe^{2+} and Ni^{2+} ions in the electrolyte solution. $NiCl_2.6H_2O$ provides Ni^{2+} ions and Cl^- ions to the solution. The presence of Cl^- ions in the solution improves the throwing power of the solution. Boric acid (H_3BO_3) was added to the solution as a pH buffer element, i.e. to maintain consistant pH value of the solution throughout the plating process. Saccharin was included in the solution as a class one brightener in order to obtain deposited layers of smaller average grain sizes. When a current is passed through the plating cell, a potential difference is induced between the plating cell and the cathode (the wire to be electrodeposited) and causes a flow of ions towards the cathode. The rate of deposition is dependent on the deposition parameters:

current densities, deposition time, deposition temperature, pH value and the presence of additives.

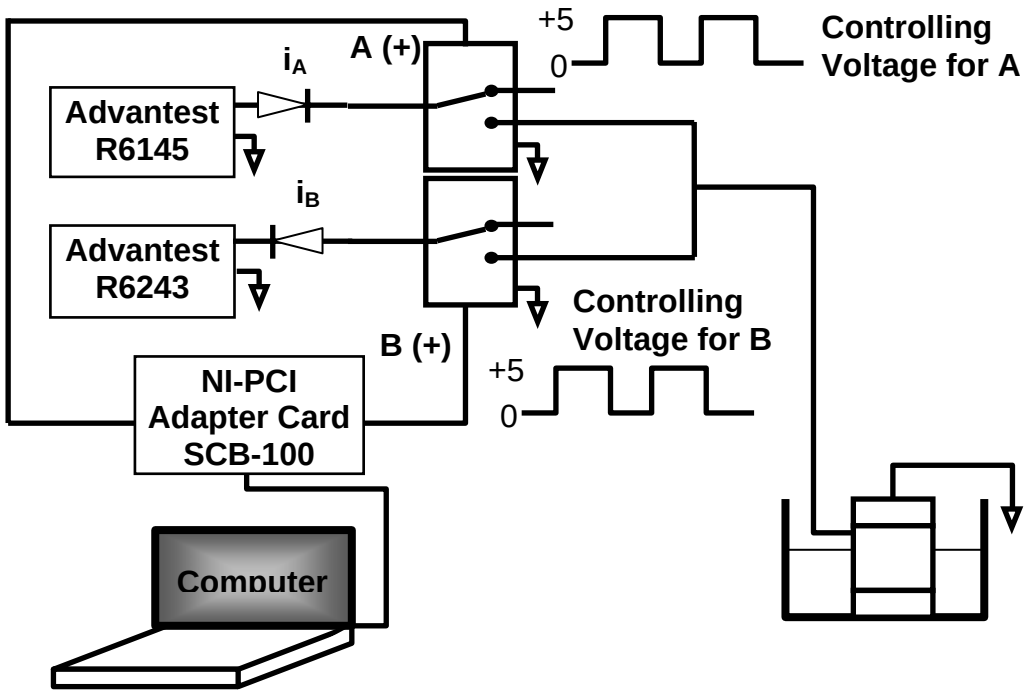

Fig. 25 Schematic Diagram of the Electrical Circuit Setup

For DC and pulsed electrodeposition, the current waveform was supplied by commercially available current source (Advantest R6145 DC Voltage Current Source and Advantest R6243 DC Voltage Current Source). For pulse-reverse electrodeposition, the pulse-reverse current was supplied by customized electrical circuit. The electrical circuit setup basically consisted of relays, diodes and the adaptor card linked to the Labview Software in the computer. Each current source was link to a relay that was connected to the adaptor card which sent out voltage pulse (0V or +5V) to control the switching of the relays, allowing the current sources to be activated at the required time. The voltage pulse signals sent out by the adaptor card was in turn controlled by the data input into the Labview Software. Diodes were used

to ensure current flowing only in one direction. The current waveforms were monitored through the Agilent 54622D Mixed Signal Oscilloscope.

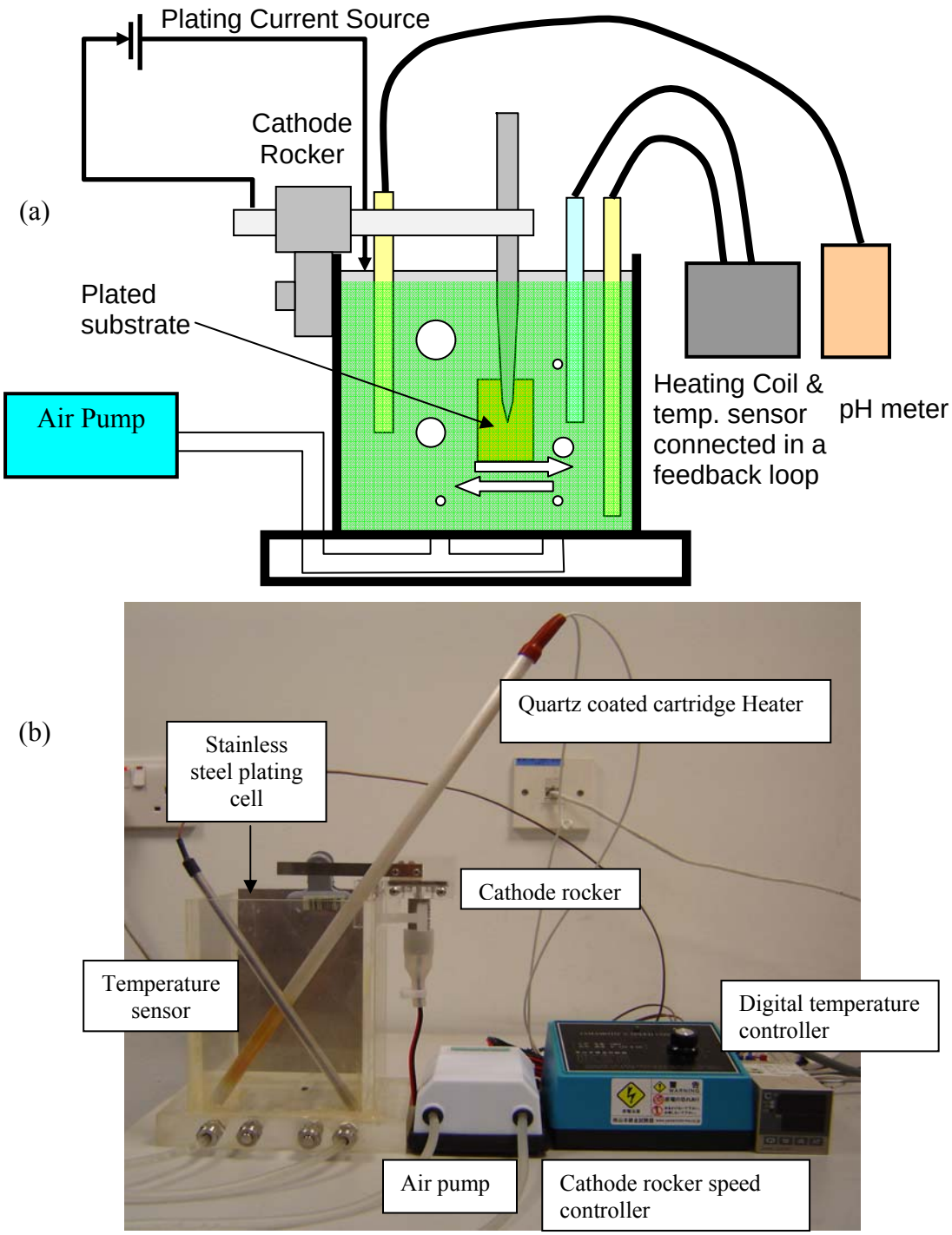

Fig. 26 (a) Schematic Diagram of the Setup for Electrodeposition of Thin Films; (b) Photograph showing setup for thin film electrodeposition

In order to carry out XRD measurements of the electrodeposited layer, thin films have to be deposited, using a customized electrodeposition setup for thin films as

shown in Fig. 26. With the help of the temperature controller with the attached cartridge heater and sensor, the temperature of the plating solution was maintained at 55°C, as with the setup for wire plating. The inclusion of the air pump into the electro-deposition setup allows for a more uniform distribution of the ions concentration in the solution and also aids in preventing heat localization. The back and fro motion of the cathode rocker helps to remove the hydrogen bubbles on the deposited surface, hence creating the "wetting" effect of the substrate This ensures that nickel deposition can be carried out smoothly. In the thin film setup, in order to maintain a current density of 2 A/dm^2, current was determined to be 80.9 mA. Plating time was fixed at 64 minutes and pH of the solution at 3.4.

3.2.2. Cold-drawing

3.2.2.1. Cold-drawing Die

One of the most important design considerations in cold-drawing process is that of the design dies. Fig. 27 shows the cross section of dies used. It has an approach half angle and back relief half angle of 7.5^o. The approach length is maintained at 20% of the original diameter of the wire such that wire will not be deformed too rapidly. Hard, strong, wear resistant materials such as tungsten carbide, cemented carbide, and hardened alloy steel are commonly used as dies for wire drawing.

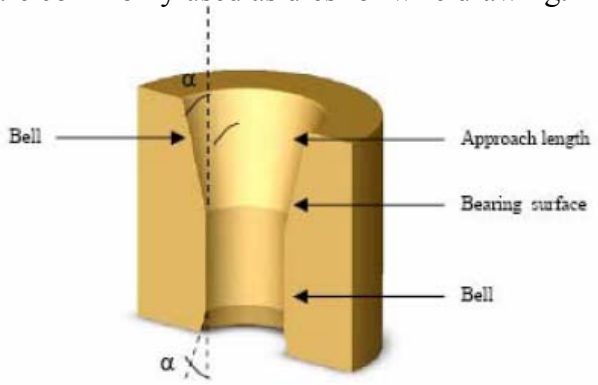

Fig. 27 Cross section of die used in drawing process.

In this project, synthetic diamond dies are used. However, the high cost, brittleness, lack of tensile strength and toughness of this material implies it can only be used as inserts, with a tougher material supporting it. Fig. 28 shows the dies used in this project, comprising synthetic diamond insert supported by tungsten carbide.

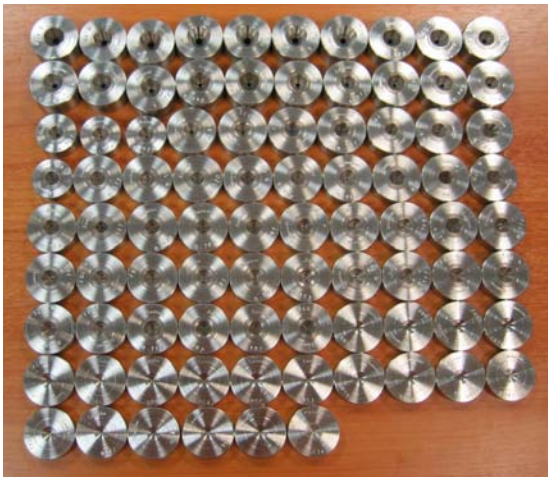

Fig. 28 Photograph showing the 86 drawing dies used in the process.

3.2.2.2. Drawing Equipment - Modified Tensometer Setup

The modified tensometer (shown in Fig. 29) was used in the cold-drawing process. It consist of a die holder to house the dies, wire clamp to attach the specimen for the drawing process, as well as spindle for rough and fine turning to translate the rotational motion into linear translation of the clamp, thus provided the drawing force for the wires.

In order to reduce the amount of human intervention and effort required to draw the wires, the spindle was replaced by an automated system as shown in Fig. 30. A connector was fabricated out of aluminum to connect the tensometer to the motor. In order to mount the motor at a specific height, a labjack was purchased to fix the motor's position. However, due to the speed of the rotational motion, it was critical to fix the platform firmly to the workbench so as to reduce vibrations which could have

negative effects on the drawing of the wires. Hence, 2 G-clamps were used to fix the platform to the workbench.

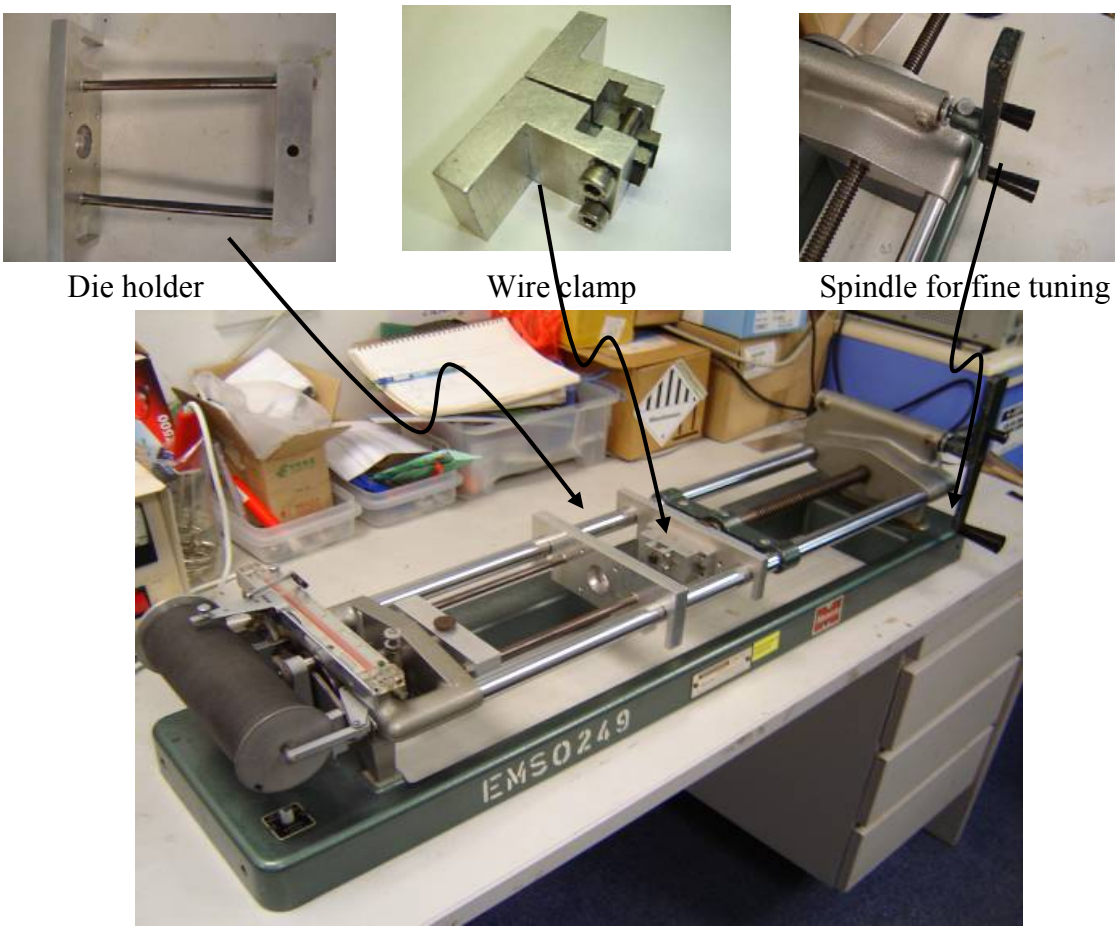

Fig. 29 The modified tensometer.

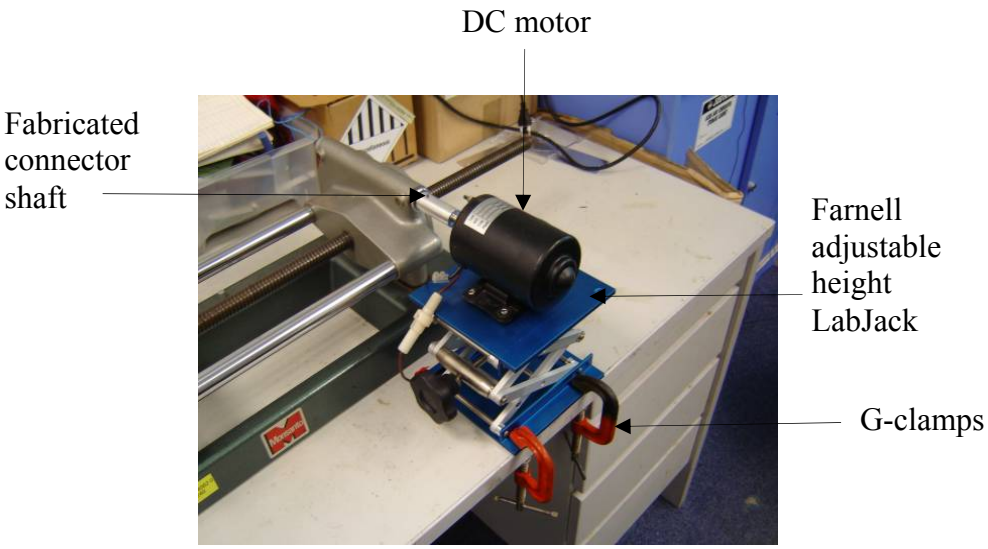

Fig. 30 Implementation of motor to automate drawing process.

3.2.2.3. Fabrication of Initial 3 mm in Overall Diameter $Ni_{80}Fe_{20}$/Cu Composite Rod

$Ni_{80}Fe_{20}$ rods of 3 mm in outer diameter and 40mm in length were cut out from commercially available $Ni_{80}Fe_{20}$ sputtering targets (of purity 99.95%) by wire-cut electrical discharge machining (EDM). Wire-cut EDM is an intricate way of machining metal parts which are impossible to produce with conventional machining techniques. A hole of diameter 2.5mm (and 2mm) and 10 mm in depth was then drilled on one end of the rod. Cu rods of diameter 2.5mm (and 2 mm) were then press fitted into the hole in the $Ni_{80}Fe_{20}$ rods. In order to achieve a good fit of the 2 materials, slight hammering was done. The final step of the fabrication involved filing the end of the composite rod with Cu to remove excess material. The final dimensions of the fabricated composite rods are shown in Fig. 31.

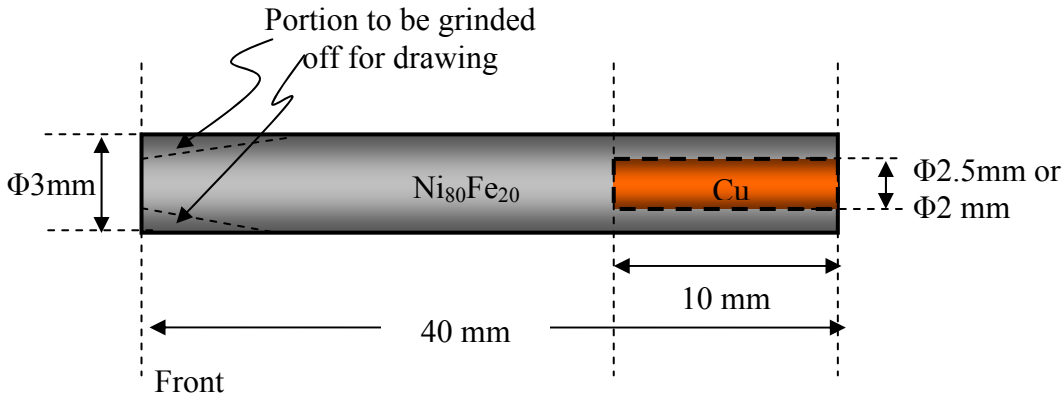

Fig. 31 Schematic diagram of fabricated composite rod.

As shown in Fig. 31, the front portion was to be thinned down by grinding (either with a grinding wheel or sandpaper) to enable passage of that particular portion of the rod to pass through the die and be held by the wire clamp. The structure of the rods was designed such that the front potion consisted of only pure $Ni_{80}Fe_{20}$ due to this reason. In the absence of the pure $Ni_{80}Fe_{20}$ region, Cu will eventually be exposed after consecutive grinding. The tensile strength of pure copper is less than that of $Ni_{80}Fe_{20}$

and hence more susceptible to fracture if the clamping is carried out at the exposed Cu portion. It is thus necessary to have a region of pure $Ni_{80}Fe_{20}$ to facilitate the drawing process.

3.2.2.4. Cold-drawing Procedures

Using the manufactured $Ni_{80}Fe_{20}$/Cu rods (3 mm in diameter), the following described procedures were adopted to reduce the rods to an eventual diameter of 34 μm. A flow chart depicting the various steps was shown in Fig. 32.

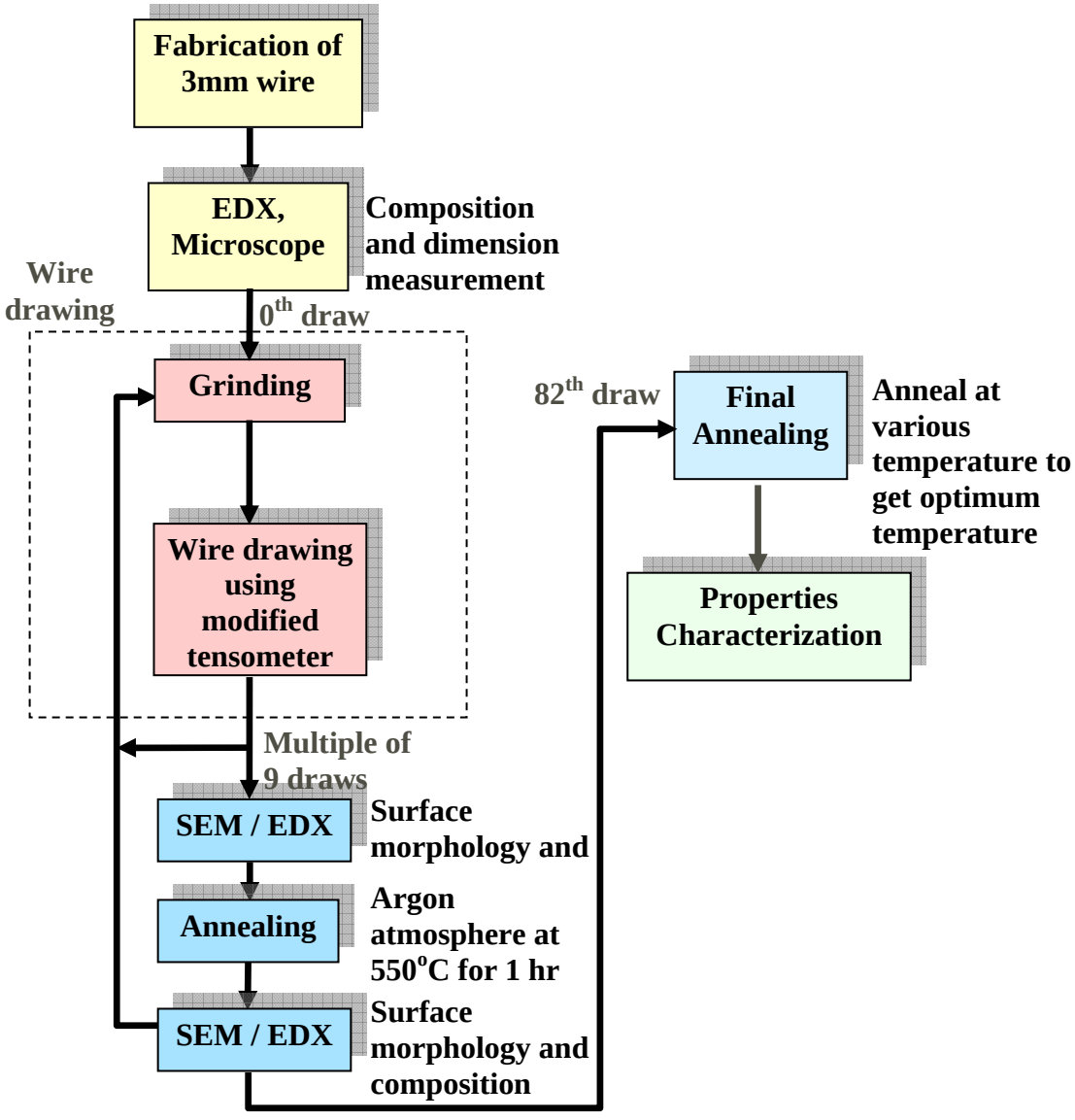

Fig. 32 Flowchart of experimental procedures.

At each individual draws, the initial portion of pure $Ni_{80}Fe_{20}$ region was thinned down. The bench grinder can be used for grinding for the first 27 draws as the diameter was still significant and thus can withstand fracture. Furthermore, there were great amounts of materials to be removed and would be time consuming to do so manually. However, after the 27th draw, the diameters of the rods were reduced to 0.751 mm and thus too delicate to be thinned down by the bench grinder. Hence the process was replaced by the manual grinding with sandpaper. The grinded wire can then be placed through the die, clamped and cold-drawn. This step can be repeated 9 times before an intermediate annealing has to be carried out, after which, cold-drawing of the wires can resume. As the end of the 82 draws, a final annealing was carried out. The details of the intermediate and final annealing setup were provided in the later section of this chapter.

Intermediate annealing was done on the wires after every 9 draws to restore the material's ductility and release the residual stress induced by strain hardening. This intermediate annealing process facilitates subsequent cold-drawing. The total percentage cold-work, as defined as (Eqn. 57) after 9 draws is around 58-62%, where A_i and A_o are the cross sectional areas of the composite wires before and after each cold draw, respectively.

$$\% CW = \left(\frac{A_i - A_o}{A_i} \right) \times 100\% \tag{57}$$

It had been suggested that the percent cold-work should be below 85-95%. Hence annealing after every 9 draws should be adequate as percent cold-work is less than the suggested value, even after giving a safety factor of around 1.5.

The wires were annealed at 550^{o}C in argon atmosphere for 1 hour each time in the furnace shown in Fig. 33(a). The heating curve of this annealing process is shown in

Fig. 33. The rate of oxidation of materials increases rapidly with increase in temperature. Hence, in order to prevent oxidation, the specimens were left in the furnace overnight in argon atmosphere to ensure that they are totally cooled down to room temperature before they were removed from the furnace.

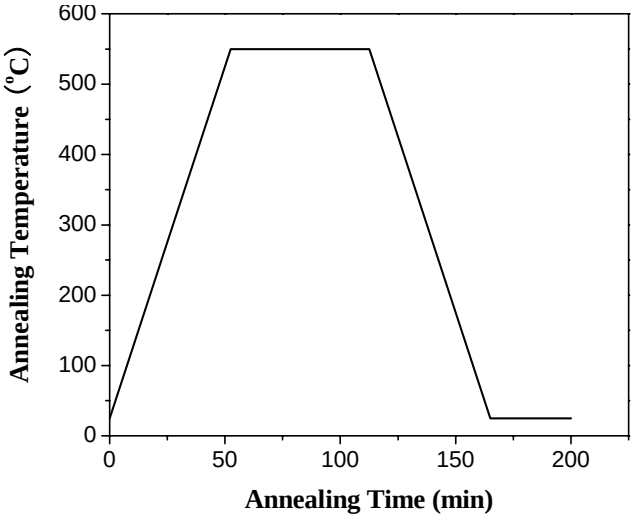

Fig. 33 Graph of annealing temperature against annealing time.

3.2.3. Magnetron Sputtering Setup

In this project, some $Ni_{80}Fe_{20}$/Cu composite wires (described in Chapter 10) were fabricated using the magnetron sputtering system (Denton Discovery 80 System). This system (Fig. 34a) is equipped with three circular magnetron cathode guns, enabling it to sputter three different material layers on a single substrate. The sputtering mode that was used for this project is the DC sputtering mode.

For all the samples obtained in this project, samples generally go through a pre-process treatment before being sputtered with permalloy. This treatment consists of pickling the wires with diluted hydrochloric acid, ethanol rinsing and ending with a final rinse using distilled water. Acid pickling was used to remove all traces of oxides on the surface of the wire while ethanol's function was to remove all traces of oil and grease on the wire. The usage of distilled water was to remove all the chemicals used in the pre-process treatment. After the pre-process treatment, the samples are

immediately mounted onto the wire holders before placing it in the deposition chamber. After the chamber is closed, the vacuum pump is turned on till the vacuum conditions are reached. During this time, deposition parameters are entered into the system. When the targeted vacuum conditions are obtained, the deposition process begins. When the deposition is completed, the sample is removed for characterization. It should be noted at this point of time that along with the wire samples, a glass substrate is also placed inside the chamber so that XRD can be carried out on the deposited layer to determine its grain size.

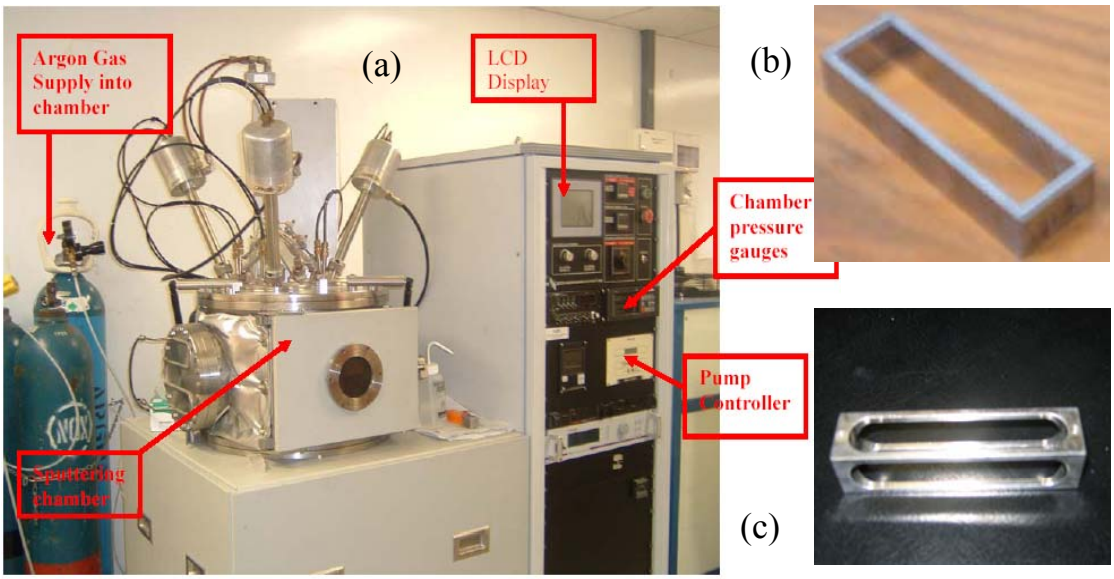

Fig. 34 Photographs showing (a) The Denton Discovery 80 system; (b) wire fixture for 180° rotation; (c) wire fixture for 90° rotation.

3.2.4. Post Annealing Setup

3.2.4.1. Furnace Annealing Setup

The setup for furnace annealing consists of a tube furnace, an argon tank and a bottle of water. The furnace is capable of heating up to a temperature of 1200ºC and will be used in this study to vary the annealing temperature and duration. Unless otherwise stated, the annealing duration will be 1 hour, with heating and cooling rate at 10ºC/min. The argon gas will be turned on 1 hour prior to annealing to purge any

impurities and ensure constant flow of noble gas during annealing. Specimens to be annealed will be placed on a ceramic tray and be positioned at the center of the tube furnace to ensure even heat distribution throughout the entire wire. Fig. 35(a) shows a picture of the furnace used in this project. It consists of an inlet and outlet for the argon gas which flows continuously throughout annealing so as to prevent possible oxidation of the wire. The furnace has an in-built programming device used to control the rate change of temperature, holding temperature and holding time of the heating and cooling process. Initial temperature calibration of the furnace showed that the actual heating temperature was 20°C higher than the displayed value on the display screen, at temperatures below 700°C.

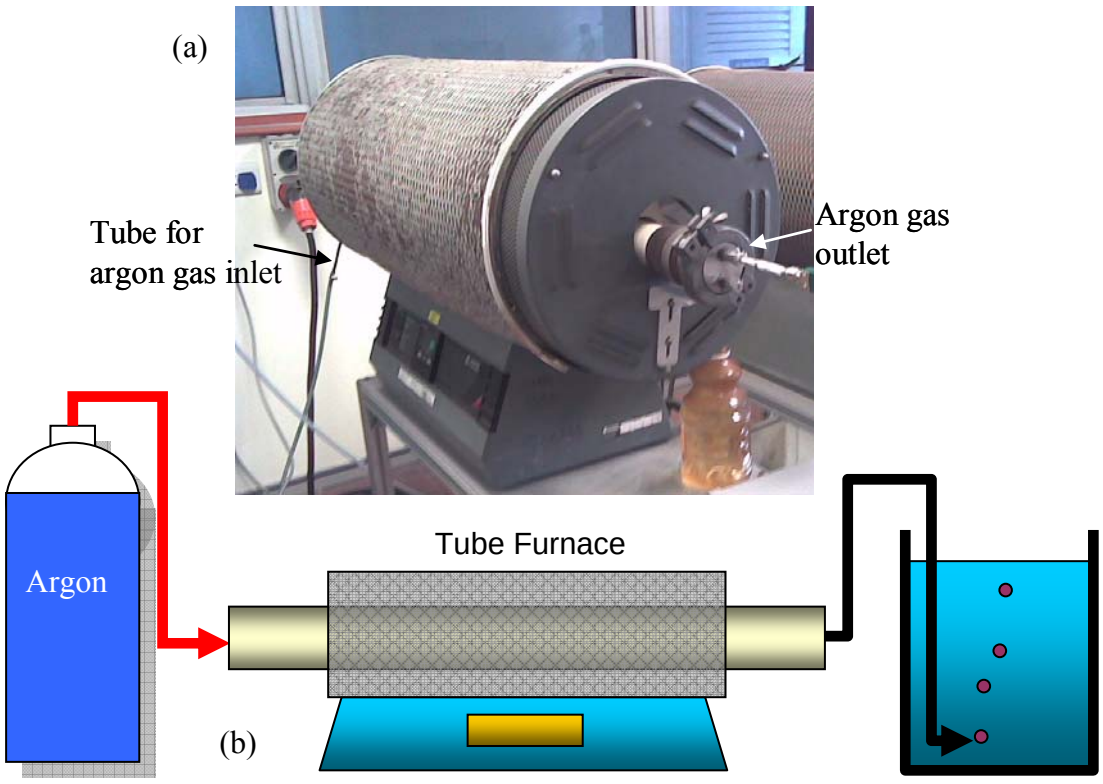

Fig. 35 (a) Photograph showing furnace used in the project; and (b) schematic diagram showing furnace annealing setup.

3.4.2.2. DC Joule Annealing Setup

The argon gas cylinder is connected to a flow meter, which regulates the argon

gas flow into the annealing chamber via gas inlet and the gas outlet is in turn connected to a beaker of water by a plastic tube. The function of the beaker of water is to prevent back flow of pressure and acts as an indicator that signifies purging is taking place when air bubbles are seen upon gas flow. The arrangement is illustrated in Fig. 36. The annealing chamber is electrically connected in series with a DC power source and an ammeter. The annealing chamber is the working platform whereby DC annealing takes place. The composite wire is soldered onto a PCB board, which has two wires at each +/- terminal, before it is placed into the annealing chamber. At the electrical contacts, only one wire from each terminal is being used and DC current flows into one red wire, through the composite wire before flowing out from one black wire back to the power source.

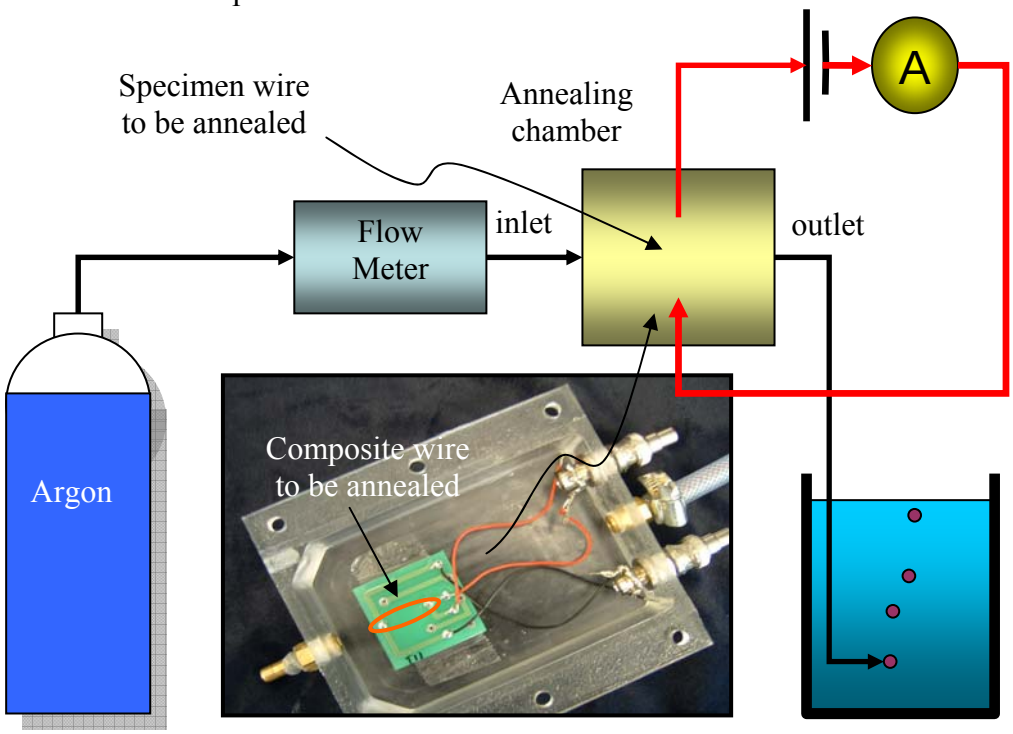

Fig. 36 Schematic representation of the DC joule annealing setup.

Once the set-up for argon gas purging and DC annealing are in place, the first step is the purge the annealing chamber with argon gas, thus:

i. Turn on flowmeter and purge the annealing chamber with argon gas for 10 minutes.

ii. Turn off flowmeter and switch on power supply. Adjust the current from 0 to 100mA. DC anneal the composite wire at this designated current for 1 minute.

iii. After switching off the power supply, turn on the flowmeter to air-cool the composite wire for another 1 minute.

iv. Repeat step 1-3 for 200mA, 300mA and 400mA for each sample.

3.3. Materials Properties Characterization Setup

3.3.1. Scanning Electron Microscopy (SEM)

The surface of the plated wires was examined by using JEOL Scanning Electron Microscopy (SEM) at varing magnifications. The thickness of the deposited layer of the Ni-Fe/Cu composite wire samples was obtained by measuring the external diameter of the plated wires using SEM, subtracting from it the copper core diameter; and halving the calculated value. Fig. 37 is a typical SEM picture of the composite wire specimen.

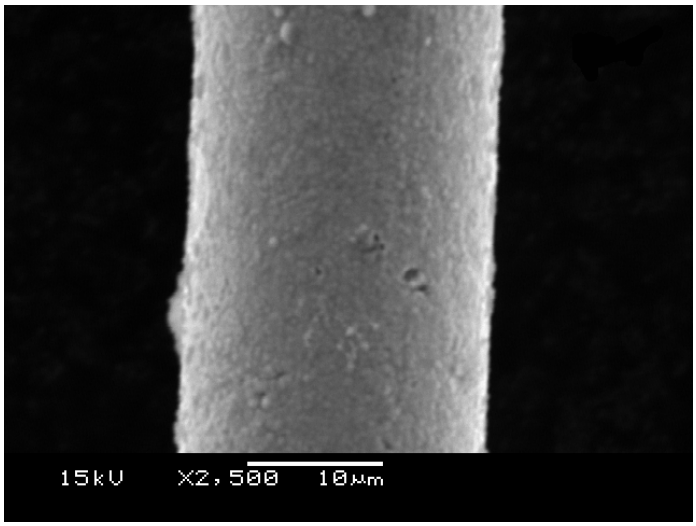

Fig. 37 Typical SEM picture of composite wire specimen.

A schematic representation of the scanning electron microscope with which surfaces are studied is shown in Fig. 38. The electrons are accelerated in a potential difference, typically of the order of 10-20 keV, and the magnetic lenses form an electron spot of a size of the order of a few nm. When the energetic electrons hit the surface under investigation, secondary electrons are emitted (SE), some incident electrons are being backscattered (BSE), x-rays are emitted (X) and a current is measured to the sample (SC and EBIC). A deflection coil system scans the focused electron beam in a raster across the surface. In synchronism with this is an electron beam of a separate cathode-ray tube (CRT) scanned over the screen, while the intensity of the CRT is modulated by one of the signals SE, BSE, X, or SC and EBIC to form an image of the surface.

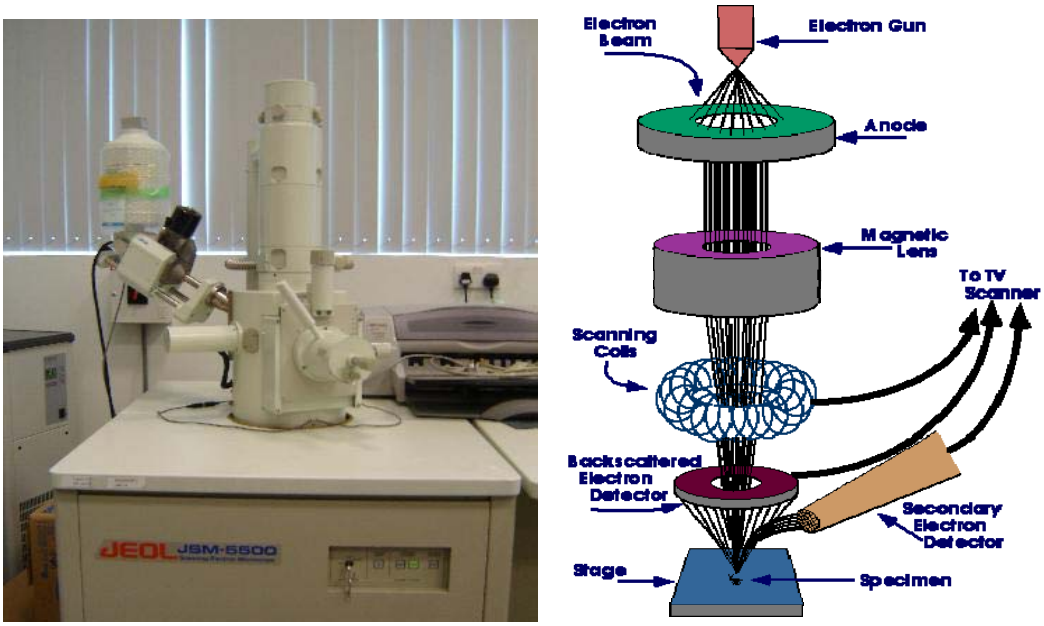

(a) (b)

Fig. 38 (a) Photograph showing SEM/EDX system; (b) Schematic presentation of a scanning electron microscope.

In a typical SEM, electrons are thermionically emitted from a tungsten or lanthanum hexaboride (LaB_6) cathode and are accelerated towards an anode; alternatively electrons can be emitted via field emission (FE). The electron beam,

which typically has an energy ranging from a few hundred eV to 50 keV, is focused by one or two condenser lenses into a beam with a very fine focal spot sized 1 nm to 5 nm. The beam passes through pairs of scanning coils in the objective lens, which deflect the beam in a raster fashion over a rectangular area of the sample surface. As the primary electrons strike the surface, they are inelastically scattered by atoms in the sample. Through these scattering events, the primary electron beam effectively spreads and fills a teardrop-shaped volume, known as the interaction volume, extending from less than 100 nm to around 5 μm into the surface. Interactions in this region lead to subsequent emission of electrons, which are then detected to produce an image. X-rays, which are also produced by the interaction of electrons with the sample, may also be detected in an SEM equipped for energy dispersive X-ray spectroscopy or wavelength dispersive X-ray spectroscopy.

The most common imaging mode monitors low energy (<50 eV) secondary electrons. Due to their low energy, these electrons originate within a few nanometers from the surface. The electrons are detected by a scintillator-photomultiplier device and the resulting signal is rendered into a two-dimensional intensity distribution that can be viewed and saved as a digital image. This process relies on a raster-scanned primary beam. The brightness of the signal depends on the number of secondary electrons reaching the detector. If the beam enters the sample perpendicular to the surface, then the activated region is uniform about the axis of the beam and a certain number of electrons "escape" from within the sample. As the angle of incidence increases, the "escape" distance of one side of the beam will decrease, and more secondary electrons will be emitted. Thus steep surfaces and edges tend to be brighter than flat surfaces, which results in images with a well-defined, three-dimensional appearance. Using this technique, resolutions less than 1 nm are possible.

In addition to the secondary electrons, backscattered electrons can also be detected. Backscattered electrons may be used to detect contrast between areas with different chemical compositions. These can be observed especially when the average atomic number of the various regions is different.

3.3.2 Energy Dispersive X-ray (EDX)

The composition data of the samples are measured using EDX. The JEOL SEM machine used for surface topography and thickness analysis can also operate as an EDX machine. The EDX attachment comprises of Lithium drifted Silicon (SiLi) detector protected with a Beryllium (Be) window, and is to function in a liquid nitrogen atmosphere. In this case, X-rays are also emitted, on top of BE and SE, when incident electrons of the electron beam are scanned across the sample surface. In case when the SE gets knocked out of the orbit, a vacancy is created and an electron from other shells with higher energy can come to occupy the vacancy at this lower energy shell. As such, there would be emission of energy in the X-ray range.

This low intensity emitted X-rays, which are generated in a region about 2 microns in depth, are unique to the element of the sample. A photoelectron is produced when the X-ray photon hits the detector and causes electron-hole pair to form as it moves through the semiconductor that is polarized by high voltage, causing these electrons and holes to be attracted to the opposite ends of the detector, resulting in a current pulse. The amount of the current pulse generated is controlled by the quantity of electron-hole pair, which in turn is determined by the energy of the X-ray. Thus, the X-ray energy spectrum of the scanned area can be obtained, indicating the elemental composition of the sample. The limitations of the EDX are that it has a

maximum error of approximately ±1% and that elements with atomic number smaller than Boron are difficult to identify using this method.

3.3.3. X-Ray Diffraction (XRD)

Diffraction occurs as waves interact with a regular structure whose repeat distance is about the same as the wavelength. When certain geometric requirements are met, X-rays scattered from a crystalline solid can constructively interfere, producing a diffracted beam. In 1912, W. L. Bragg recognized a predictable relationship among several factors [159].

1. The distance between similar atomic planes in a mineral (the inter-atomic spacing), which is known as the d-spacing and measured in angstroms.
2. The angle of diffraction, theta and measured in degrees. For practical reasons the diffractometer measures an angle twice that of the theta angle. The measured angle is named '2-theta'.
3. The wavelength of the incident X-radiation, symbolized by the Greek letter lambda.

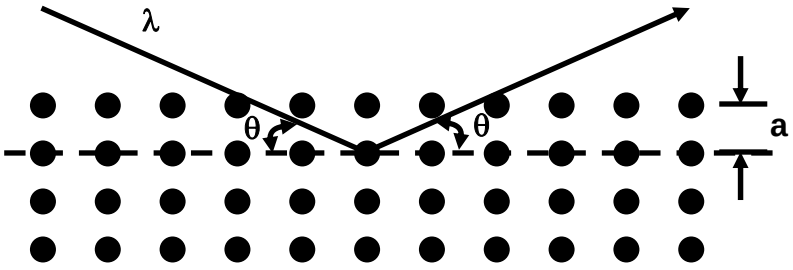

Fig. 39 Bragg's Law

X-ray diffraction technique had its beginnings in von Laue's discovery in 1912 that crystals diffract x-rays, the manner of the diffraction revealing the structure of the crystal. Since then, XRD technique has been used for several purposes. The technique is commonly used for phase identification (search/match), investigation of high/low

temperature phases, solid solutions and determinations of unit cell parameters of new materials. In this project, XRD diffraction patterns were recorded using a Philips 7000 diffractometer (Fig. 40) with Cu Kα radiation. θ-2θ scans were performed at $2°min^{-1}$. For example, Fig. 41 shows measured XRD spectra of NiFe/Cu composite thin films obtained by electrodeposition. The XRD spectra show a FCC Cu layer (with lattice constant a = 0.355 nm) and also a FCC NiFe layer (with lattice constant a = 0.362 nm) on top. The determination of the material crystallinity can also be achieved by the XRD. The crystallinity parts give sharp narrow diffraction peaks and the amorphous component gives a very broad peak. The ratio between these intensities can be used to calculate the amount of crystallinity in the material. Stress analysis of the materials can also be achieved by XRD. The basic principles of stress analysis by the x-ray diffraction are based on measuring angular lattice strain distributions, that is, a reflection at high 2-Theta is chosen and the change in the d-spacing with different orientations of the sample is then measured. Using Hooke's law the stress can be calculated from the strain distribution.

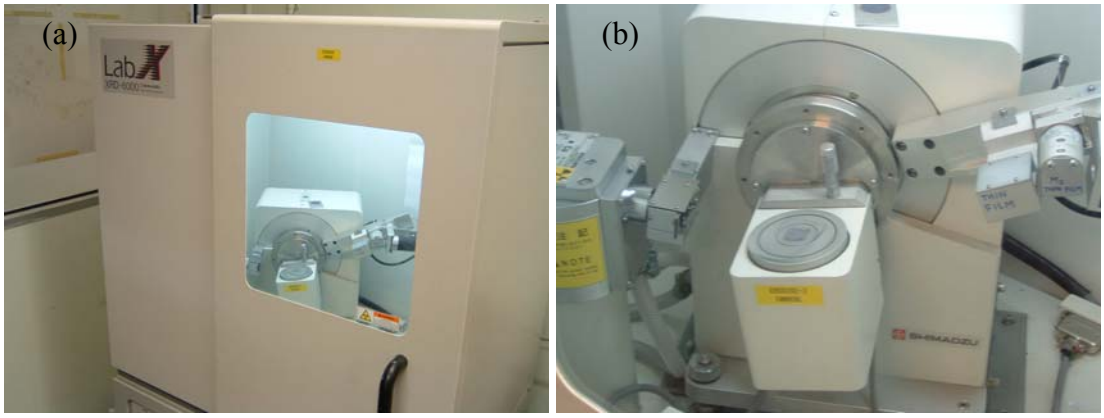

Fig. 40 Photographs showing (a) Philips 7000 diffractometer; (b) measurement stages in the diffractometer.

Another use of XRD is the estimation of the nanocrystalline grain sizes of the measured materials using the equation (Scherrer Formula):

$$B_b = \frac{0.9\lambda}{t\cos\theta}, \tag{59}$$

where B_b = broadening of diffraction line measured at half its maximum intensity (radians) and t = diameter of crystal particle. Note that B_d is essentially zero when particle size exceeds about 1000 angstroms. Using Warren's method to determine B_d from the measured breadth B_M of the diffraction line, the value of B can be obtained by the equation:

$$B_d^{\,2} = B_M^{\,2} - B_S^{\,2} \tag{60}$$

where B_M is the broadening of diffraction line for the measured specimen and B_S is the broadening of diffraction line for the standard.

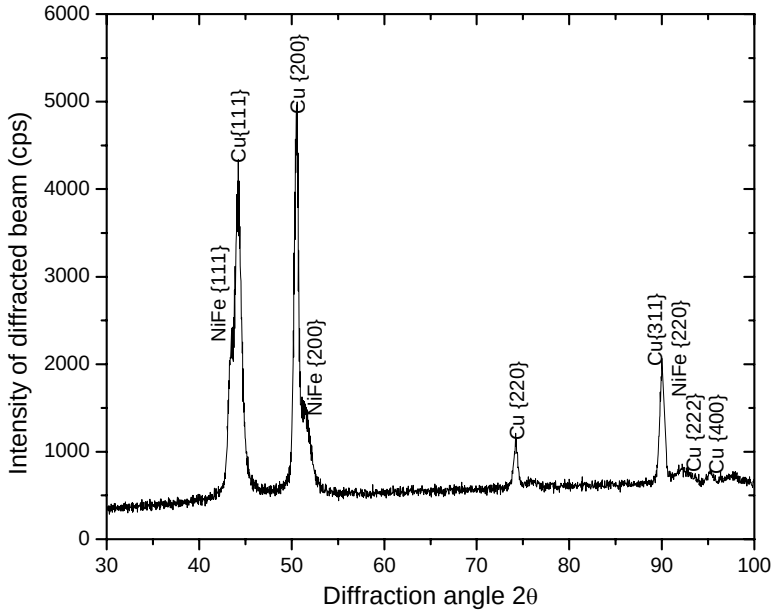

Fig. 41 XRD data of NiFe/Cu composite thin film.

3.3.4. Transmission Emission Microscopy (TEM)

The transmission electron microscope is an optical analogue to the conventional light microscope. It is based on the fact that electrons can be ascribed a wavelength (of the order of 2.5 pm) but at the same time interact with magnetic fields as a point charge. A beam of electrons is applied instead of light, and the glass lenses are

replaced by magnetic lenses. The lateral resolution of the best microscopes is down to atomic resolution. A picture and schematic presentation of the microscope is shown in Fig. 42. With an electron gun, an electron beam is formed, which is accelerated by an electric field formed by a voltage difference of, typically, 200 kV. By condenser lenses, the electron beam is focused to a spot of the order of 1 mm on the thin film to be investigated. The first image, which is formed by the objective lens, is magnified typically x25, and the following lenses give a final magnification of the image of more than $x10^6$. In addition to thin-sample images, electron diffraction patterns can also be formed on the final image screen. The electron rays corresponding to bright field imaging and (selected area) diffraction are shown in the left and right drawings of Fig. 42b, respectively. In bright field imaging, the image of a thin sample is formed by the electrons that pass the film without diffraction, the diffracted electrons being stopped by a diaphragm. In the corresponding dark field imaging mode, a diffracted beam is used for imaging.

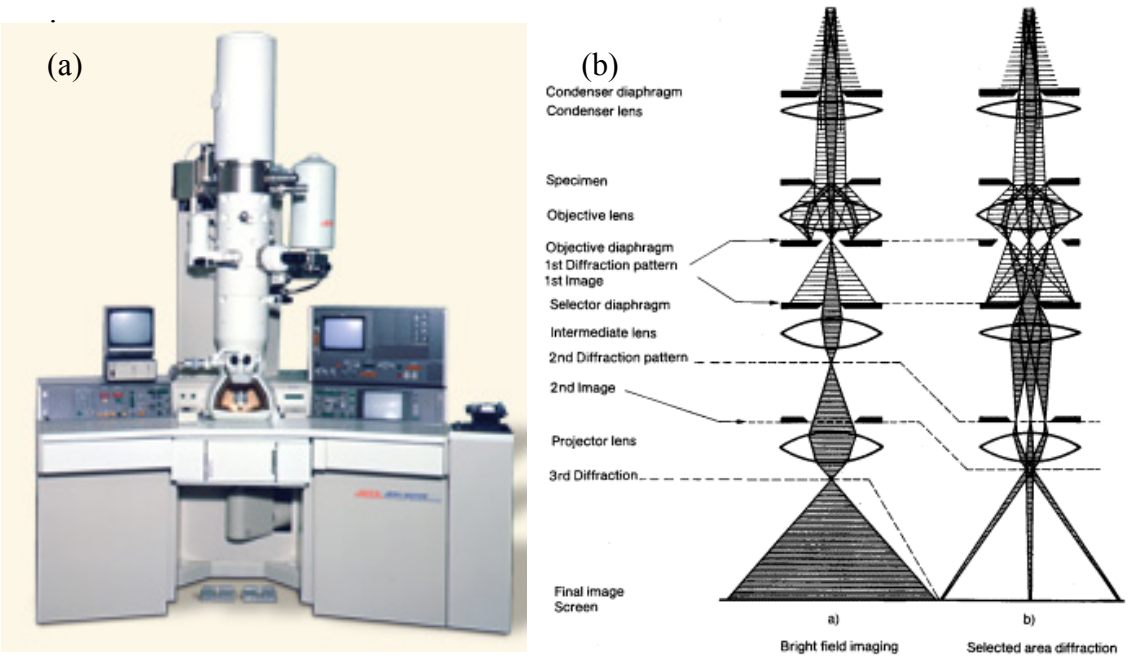

Fig. 42 (a) Picture showing a TEM; (b) Schematic presentation of a TEM.

The microstructure, e.g. the grain size, and lattice defects are studied by use of the image mode, while the crystalline structure is studied by the diffraction mode. In addition, the chemical composition of small volumes, for example grain boundaries, can be obtained by detection of x-rays emitted from the film. Samples for electron microscopy in form of films mounted on fine-meshed grids are required to be very thin. In case near-atomic resolution is required film thicknesses have to be limited to a few tens of Å. Therefore, the quality of the electron microscopy work is sometimes limited by the thinning-down procedure as structural changes may occur during the thinning

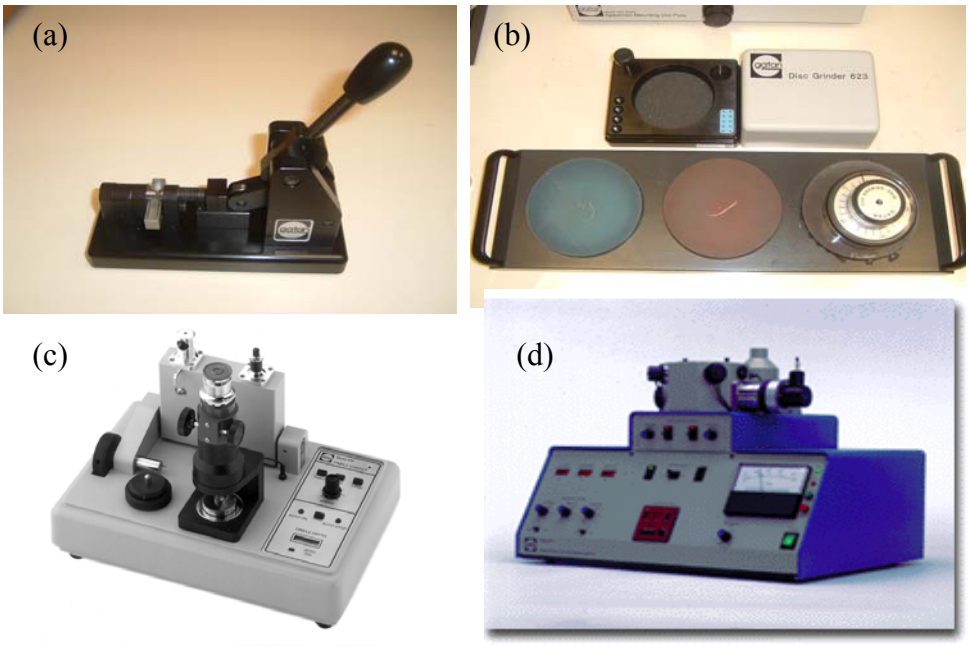

Fig. 43 Pictures showing (a) 3 mm hole puncher; (b) hand grinding set; (c) dimple grinder; (d) ion milling.

It must be noted that immense efforts have to be been placed in the preparation of the specimens for Transmission Emission Microscope (TEM), so that pictorial data of the structure and grain size can be obtained. The preparation steps involve: 1) producing 3mm in diameter specimens (composite thin films) using a 3 mm hole puncher; 2) hand grinding the specimen to 100μm in thickness by the TEM

preparation disc grinder; 3) creating a dimple on the surface of the grinded specimens by means of a dimple grinder; and 4) creating a tiny hole at the center of the created dimple in order to obtain thickness of <100 nm at near hole region. The pictures of the TEM preparation equipment used were given in Fig. 43.

Fig. 44(a) shows the plot obtained by tabulating the number of grains for different grain size diameter for the observed electrodeposited NiFe layer. The average value of the grain size was then presented in the grain size studies in Chapter 6. Fig. 44b shows the TEM pictures obtained.

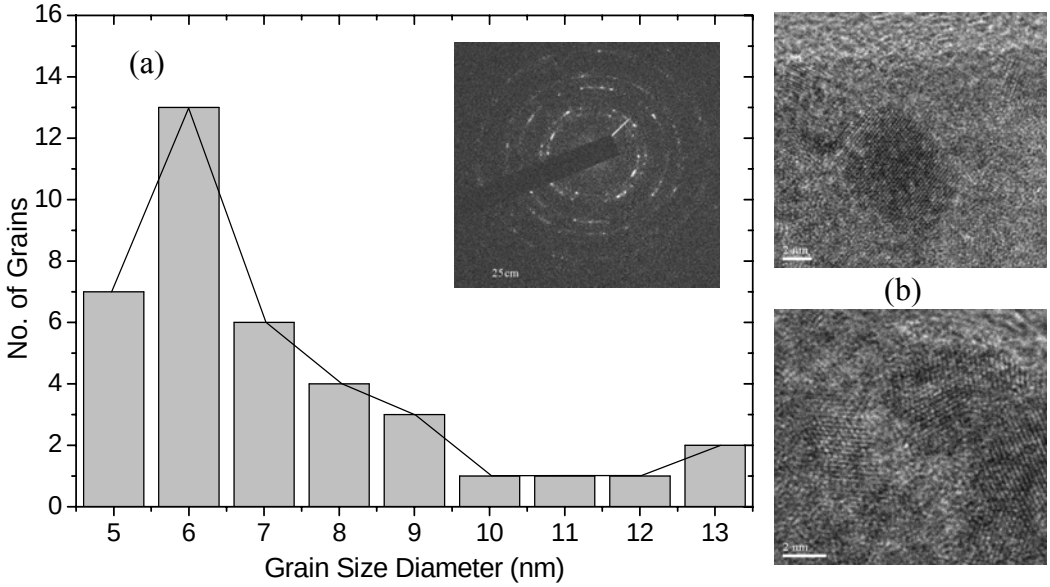

Fig. 44 (a) Plot showing tabulated no. of grains for different grain size diameter for the observed NiFe layer, with in set picture showing diffracted pattern of NiFe; (b) TEM pictures of measured grains.

3.4. Magnetic Properties Characterization Setup

3.4.1 Vibrating Specimen Magnetometer (VSM) Setup

Hysteresis loops (in the longitudinal and perpendicular directions) were derived from the Vibrating Specimen Magnetometer (VSM). In this instrument, an external magnetic field is provided by an electromagnet. This magnetic field magnetizes the sample which is mounted to a glass rod attached to a mechanical resonator vibrating up and down at a fixed frequency of ω, as shown in Fig. 45. As the sample moves, its

magnetic field, which is proportional to its magnetic moment, *M*, alters the magnetic flux through the coils, *dM/dt*. This induces a current directly proportional to *dM/dt*, which can be amplified and detected using lock-in amplifiers.

Once the hysteresis loop of magnetic moment against applied field was plotted, the coercivity of the specimen would be the value of the applied field to demagnetize the specimen to zero magnetic moment.

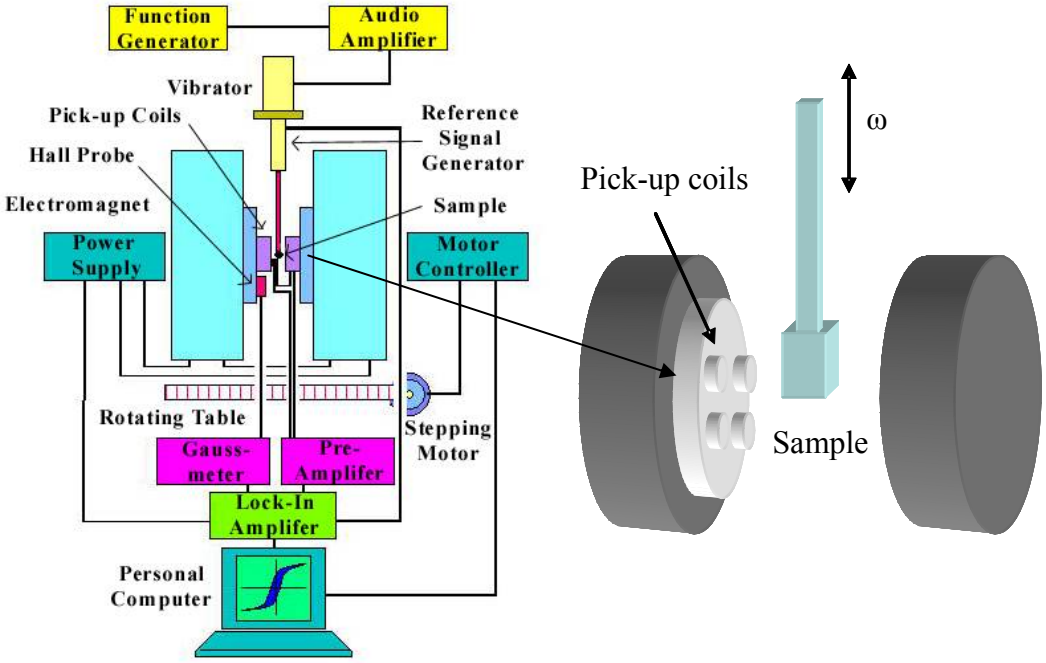

Fig. 45 Vibrating Specimen Magnetometer setup.

3.4.2. Inductance Method Testing Setup

Fig. 46 shows the schematic diagram of the setup that was used to carry out measurements that enable the tabulation of the circumferential coercivity.

The (NiFeMo) wire sample of resistance R_w was mounted on a PCB strip and connected in the circuit with a resistor of known value R_o. By setting an appropriate frequency using the function generator, an alternating current was passed through the wire. A varying magnetic field and thus, induced voltage V_{ind} was generated. By

saving the readings of V_1 and V_2 on the oscilloscope, and processing the data as shown by the following formula, a graph of magnetic flux density B against applied field H (hysteresis loop in the circumferential axis) can be plotted and the circumferential coercivity value can thus be found. Fig. 47 illustrates some of the symbolic dimensions of the NiFeMo wire used in the tabulation process.

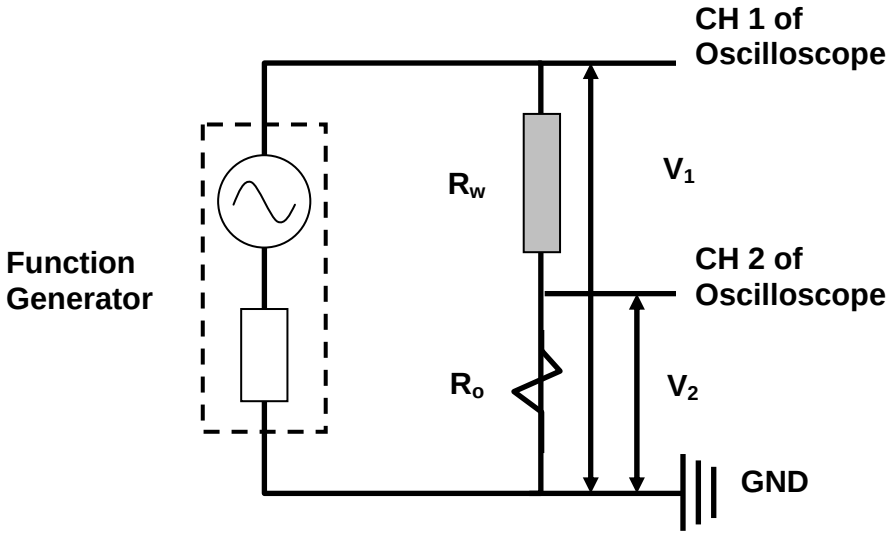

Fig. 46 Schematic diagram for circumferential coercivity testing

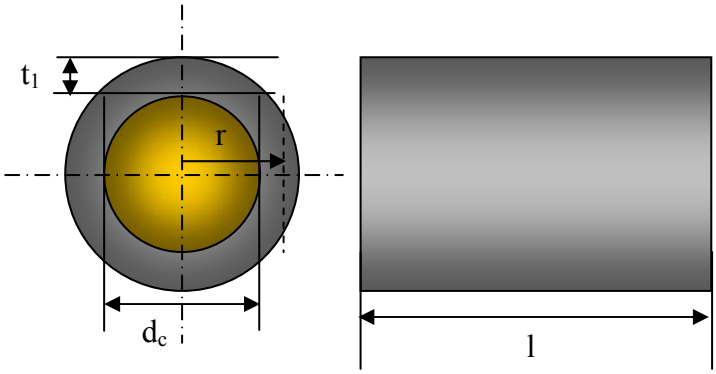

Fig. 47 Schematic representation defining dimensional parameters used in tabulation of circumferential coercivity.

With reference to Fig. 47, the voltage across the measured composite wire and the resistor V_1 is given by:

$$V_1 = I(R_0 + R_w) + V_{ind} \tag{61}$$

The voltage across the resistor V_2 can be approximated by:

$$V_2 = IR_0 \tag{62}$$

Equating both equations:

$$V_{ind} = V_1 - V_2 - (\frac{V_2}{R_0})R_w \tag{63}$$

Since $B = \phi / A$ and $V_{ind} = -\frac{d\phi}{dt}$ (where ϕ is the magnetic flux and A is the area of magnetic field), therefore

$$B = (\frac{1}{A})\int V_{ind} dt = (\frac{1}{t_1 l})\sum V \Delta t \tag{64}$$

The hysteresis loops (circumferential direction) can then be plotted using the tabulated value of B and H (i.e. $H = \frac{I}{2\pi r}$).

3.4.3. Magneto-impedance (MI) Effect Testing Setup

Magnetic properties, such as the magnetic anisotropy of the plated wires from electroplating with and without the longitudinal magnetic controlling field, were determined by the magneto-impedance (MI) effect of the sample wires. An ac current was passed through the Ni-Fe/Cu composite wire and a circumference magnetic field around the wire was induced. By varying the external magnetic field (by changing the DC current through the Helmholtz coils), the magneto-impedance measurements were carried out using a precision impedance analyzer (HP4294A).

The RMS value of the AC driving current was kept constant at 10 mA, and its frequency ranged from 100 kHz to 50 MHz. The relative change of impedance ratio is defined in Eqn. 43. A typical MI curve of a tested specimen composite wire is given in Fig. 49.

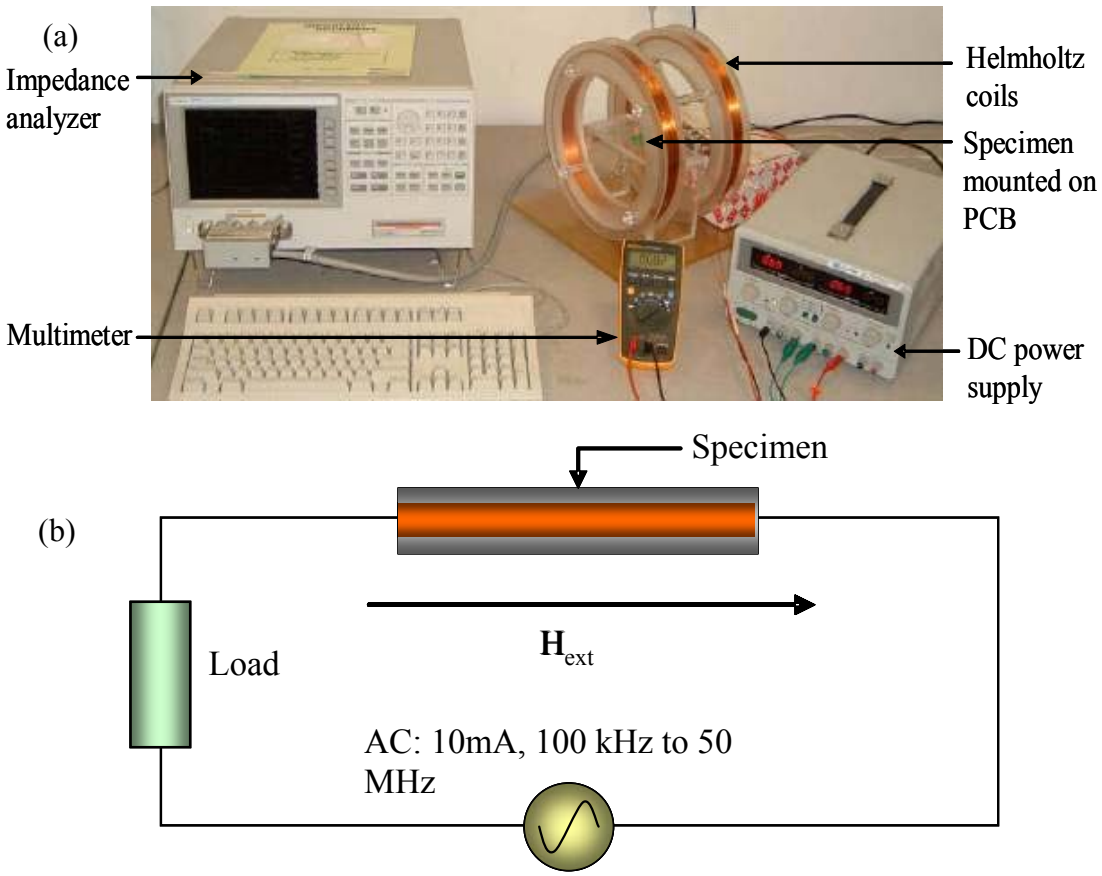

Fig. 48 (a) Photograph showing magneto-impedance (MI) measurement setup; (b) schematic diagram of MI measurement.

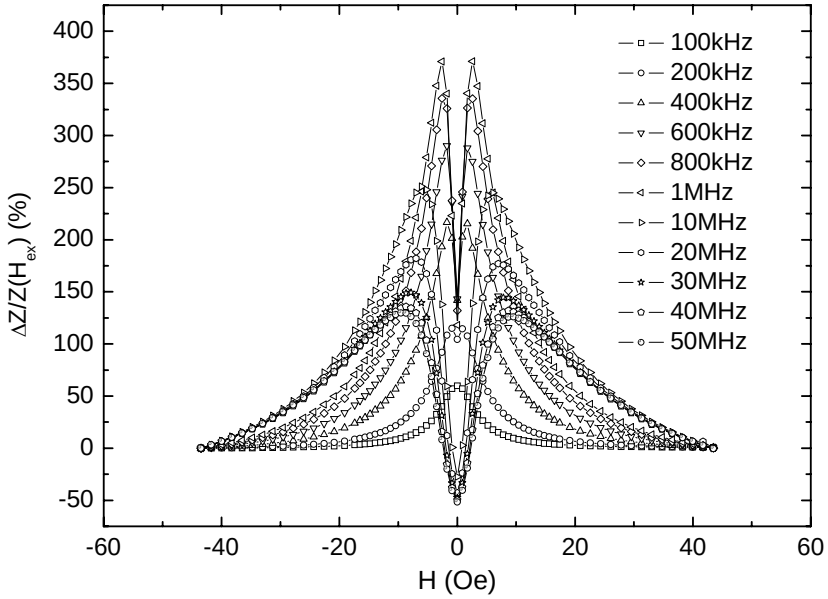

Fig. 49 A typical MI curve of composite wire.

3.4.4. Sensitivity Setup

In order to effectively evaluate the performance of the composite wires as sensing elements in magnetic sensors, the composite wires has to be placed inside the orthogonal fluxgate sensor circuit (Fig. 50) to measure the overall sensitivity of the sensor.

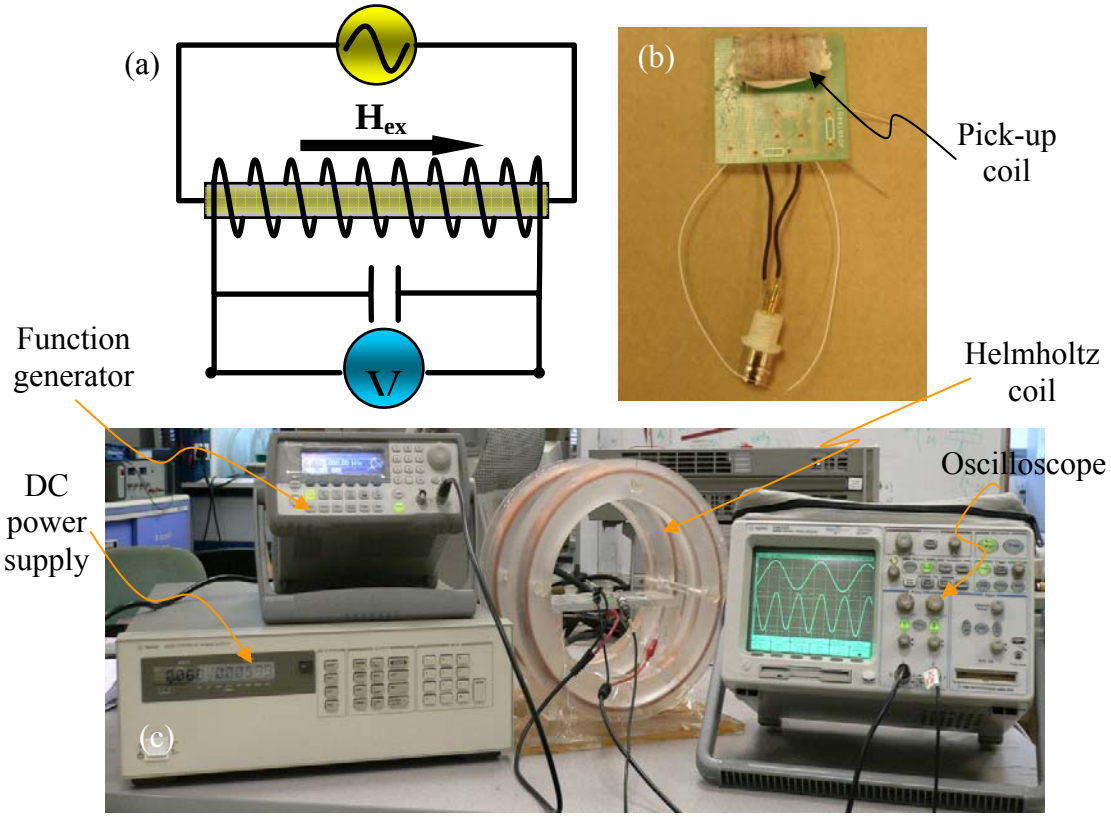

Fig. 50 (a) Schematic diagram showing orthogonal fluxgate sensor setup; (b) photograph showing the testing circuit, including PCB and pick-up coil; (c) photograph showing orthogonal fluxgate sensor setup.

The composite wire will be mounted onto a PCB board and inserted into a 3.25 mm in diameter solenoid of known number of turns. An alternating current will be passed through the wire using a function generator and the induced voltage, which arises from the change of flux ($V = -\frac{d\phi}{dt}$), will be monitored using an oscilloscope that is connected to the solenoid. The magnitude of the alternating current (input) is fixed at 50mV. The frequency of the function generator is adjusted to produce a sine

wave with peak amplitude in the first and second harmonics. The graph of output voltage against the external field is plotted. From the graph, the gradient of the curve gives us the sensitivity (*dV/dH*), and the sensitivity values obtained are subsequently plotted against the external field.

3.4.5. Magneto-optical Micro-magnetometer Setup

The study of the micromagnetic structure (equilibrium distribution of the magnetization) of the composite NiFe/Cu wire samples of 15 mm length was carried out using a magneto-optical micro-magnetometer having a surface sensitivity of about 15 nm of thickness depth and a spatial resolution of up to 0.3 μm. The alternating magnetic field H of the frequency f = 80 Hz was applied parallel to the wire length L. By scanning the light spot of 1 μm diameter along the wire length L, the distributions of magnetization components (both parallel $M_{\parallel}$ and perpendicular $M_{\perp}$ to the applied magnetic field) and also local magnetization curves were measured by the means of the Transverse Kerr effect (TKE) δ. Actually, dependencies of $\delta(L, H)/\delta_S \propto M(L, H)/M_S$ were found. Here δ_S is TKE at $M = M_S$, where M_S is the saturation magnetization. The measurements of the magnetization distributions were performed in the central portion of the studied samples to minimize the influences of edge effects (in particular, variations of local demagnetising factors) by using a half-wave sinusoidal magnetic field.

Chapter 4 Localized Magnetic Properties and Magnetic Domains of DC Electroplated NiFe/Cu Composite Wires

4.1. Localized magnetic properties and magnetic domains of electrodeposited NiFe/Cu composite wires

The typical magnetization curves, $\delta(H)/\delta_S \propto M_{\|}(H)/M_S$, observed for the central and edge microparts of the samples with C_{Fe} = 20.5 and 23.3 %, were shown in Fig. 51. Analogous curves were obtained for the sample with other values of C_{Fe}. Experimental data analysis showed that the magnetization curves of the central and edge microparts differ strongly. This greatly demonstrates the influence of variations of local demagnetising factors on local magnitudes of the saturation field H_S. Moreover, it was found that the values of H_S depend on Fe% in the NiFe layer. For illustration, Fig. 52 displays the dependence of H_S of the central wire microparts on Fe%. In Fig. 52, the increase of H_S is observed at C_{Fe} = 26.8 %. This experimental fact cannot be explained by M_S variations with varying value of C_{Fe}. It is known [61] that with increasing C_{Fe} (from 19% to 27%) in NiFe alloys, the value of M_S changes by about 10 % (see insert in Fig. 52) while the magnitude of $H_S \propto K/M_S$ (K is a constant of magnetic anisotropy) increases approximately by three times. As previously reported, the studied wires possess nanocrystalline structures. In agreement with the random anisotropy model [101], the effective constant of magnetic anisotropy of nanocrystalline materials decreases with decreasing grain size, D. It was found that the grain size D of NiFe layer increases with enlarging value of C_{Fe}. So, the revealed dependence of H_S on C_{Fe} can be attributed to structural changes of the wires.

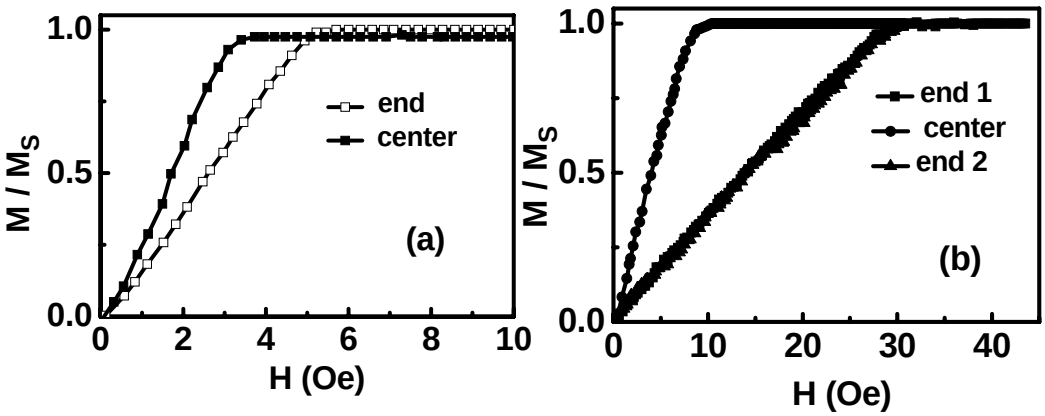

Fig. 51 The near-surface local magnetization curves observed along the central and edge microparts of composite NiFe/Cu wires with (a) C_{Fe} = 20.5%; and (b) 23.3%, respectively.

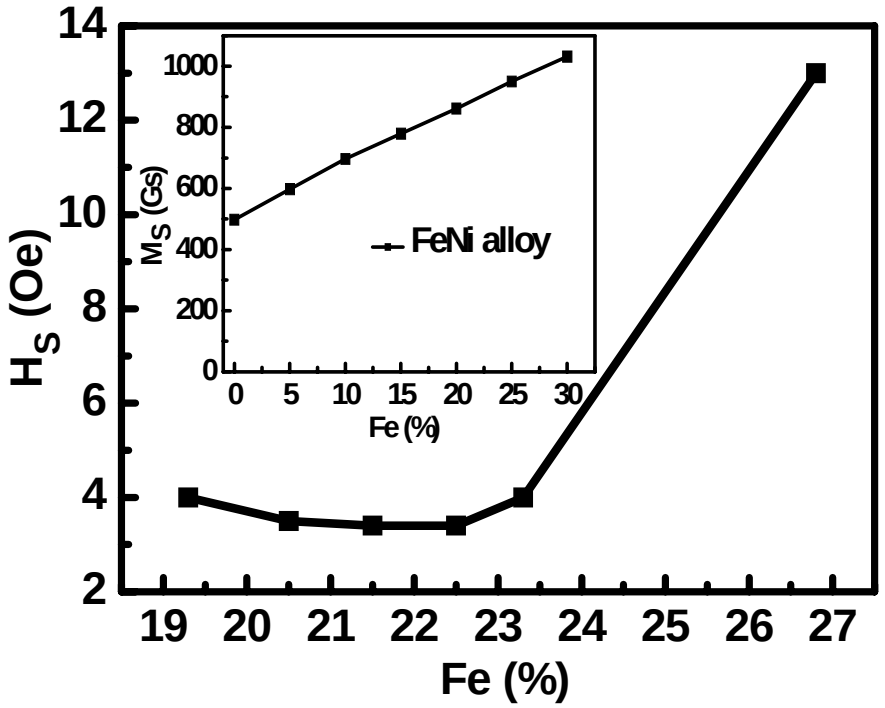

Fig. 52 Dependence of local values of the saturation field on Fe% in the NiFe layer observed for the central microparts of composite NiFe/Cu wires.

The measurements of the magnetization distributions in the examined microwires showed that at $H < H_S$, there are magnetization components both parallel ($M_{\parallel}$) and perpendicular ($M_{\perp}$) to the magnetic field applied along the wire length L. It must be noted that TKE is proportional to the magnetization component perpendicular to the plane of the light incidence. Thus, the measurements of the distributions of $M_{\parallel}(L)$ and

$M_{\perp}(L)$ were respectively performed in the transverse and longitudinal wire orientations with respect to the plane of the light incidence. Fig. 53 shows the distributions of $M_{\parallel}(L)$ and $M_{\perp}(L)$ observed in the wires with C_{Fe} = 19.3 and 26.8 %. In Fig. 53, the near-surface local magnetization components, that were parallel to H, were observed to possess the same sign, and those, that were perpendicular to H, have oscillatory, alternating-sign behaviour. The measurements of Polar Kerr effect also showed that the magnetization component, that is perpendicular to the wire surface, M_n, is absent. Analogous data were obtained for all studied samples. The alternating-sign distributions of the magnetization are possible when the magnetization of different microparts has $\pm\theta_i$ angle orientation with respect to L, and the magnetization reversal of these microparts realizes by means of a rotation of local magnetization vectors. Thus, the obtained experimental data indicate that there are near-surface circular domains in the studied wires, and the magnetization in the adjacent domains points in opposite ($\pm\theta_i$ with respect to L) directions. It was found that the value of θ is about 75 – 80°. The detections of both the component $M_{\parallel}$ and $M_{\perp}$ show that there is the curling mode of the magnetization reversal in the examined samples.

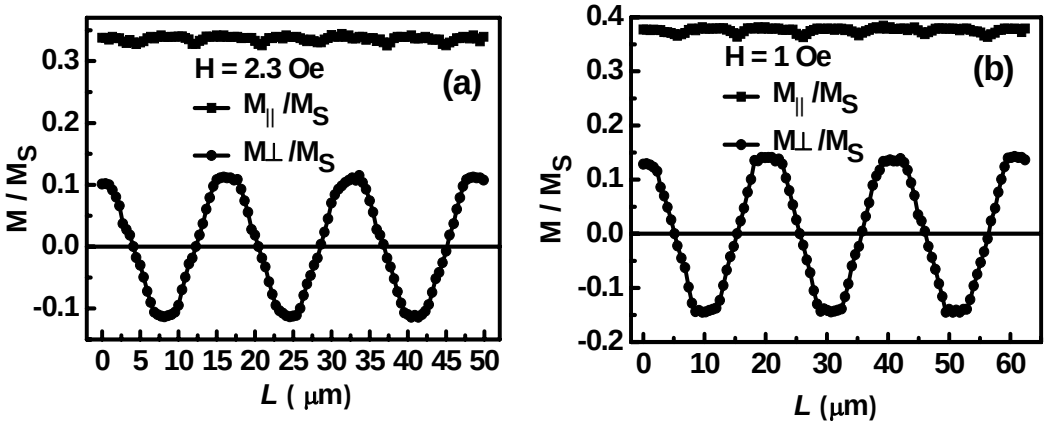

Fig. 53 The typical distributions of $M_{\parallel}(L)$ and $M_{\perp}(L)$ observed in the wires with C_{Fe} = 26.8 and 19.3 %: (a) and (b), respectively.

It is evident that the distance between zero magnitudes on the alternating-sign curves $M_{\perp}(L)$ corresponds to the width W of the circular domains. It was revealed that the value of W decreases with increasing C_{Fe}. In particular, for the wires with C_{Fe} = 19.3 and 26.8 %, W is about 10 and 8 microns respectively. The discovered variations of W can also be ascribed to variations of the effective constant of magnetic anisotropy of the wires.

4.2. Summary

The results revealed, by using a magneto-optical micro-magnetometer, that in the near-surface range of the composite NiFe/Cu wires, there are circular domains with alternating left- and right-handled magnetization in adjacent domains. The size of the circular domains and also the saturation field were found to depend on Fe% in the NiFe layers. This was attributed to variations of the effective constant of magnetic anisotropy, which was caused by structural changes of the wires. The magnetic-field behaviour of the magnetization components parallel and perpendicular to the magnetic field applied along the wire length shows that there is the curling mode of the magnetization reversal in the examined wires.

Chapter 5 Investigation of Electroplating Parameters in relation to Magnetic Properties and Sensing Performance of NiFe/Cu Composite Wires

5.1. Investigating the Current Density *J* Effect

In order to investigate the effect of plating current density *J* on the magnetic properties of plated NiFe in electroplating of NiFe/Cu composite wires, specimens of the same composition and thickness have to be obtained.

Since plating current density greatly affects the composition of the deposited layer as well as the deposition rate, there was a need to alter the electrolyte solution concentration and the plating time to compensate for changes in the composition and thickness due to varying current densities in order to conduct an unbiased study. This was achieved by increasing the Fe^{2+} concentration and reducing the plating time for higher plating current densities.

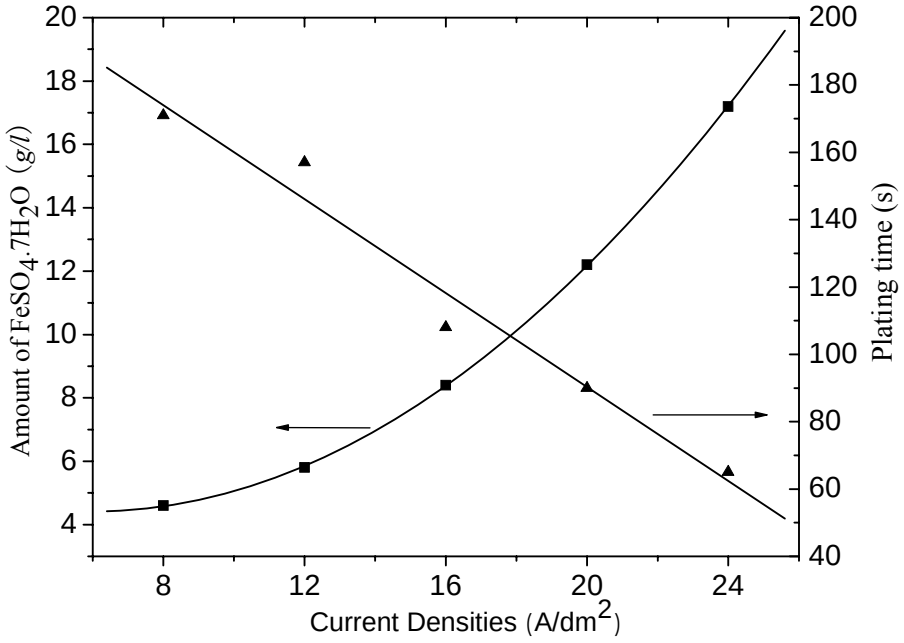

Fig. 54. Amount of $FeSO_4.7H_2O$ and the deposition time required to achieve permalloy composition and of 2μm thickness under different current densities.

Fig. 54 shows in order to maintain the required NiFe composition ratio of 80:20, the required amount of $FeSO_4.7H_2O$ in the plating solution has to be increased exponentially with increasing plating current density. Fig. 54 also shows that in order to achieve a plated $Ni_{80}Fe_{20}$ layer of 2 μm thickness, the plating time has to be decreased linearly with increasing plating current density.

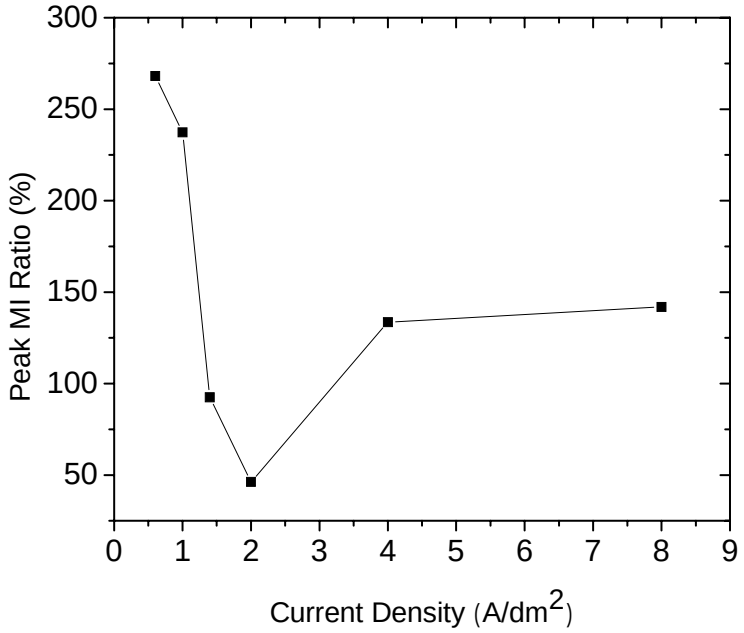

Fig. 55 Effect of current density on the MI ratio of the plated wire, showing a decreasing trend with current density in the lower range till a turning point of J = 2A/dm^2, and then an increasing trend with current density in the higher range.

With reference to the above trends, $Ni_{80}Fe_{20}$/Cu composite wire samples were produced under a range of values of plating current density. The current density J was varied from 0.6 to 8 A/dm^2. It must be noted that the composition and thickness of the deposited layer was fixed to be the same, in order to compare the wires. The magnetic properties, in terms of the magneto-impedance (MI) effect, for each of these samples were tested. Since the MI effect is related to the magnetic permeability variations of the plated NiFe layer, and that the magnetic permeability is a comprehensive measure of the soft magnetic properties of the material, the soft magnetic properties of the plated samples under different plating current density can be compared using the

maximum MI effect ratios of the wire samples. This is shown in Fig. 55, where the maximum MI effect ratios for the $Ni_{80}Fe_{20}$/Cu composite wires plated under a range of current density (from J = 0.6 A/dm^2 to J = 8 A/dm^2) are presented. It can be seen that the maximum MI ratio decreased with increasing plating current density initially till the current density reached 2 A/dm^2, and then increased with further increases in current density.

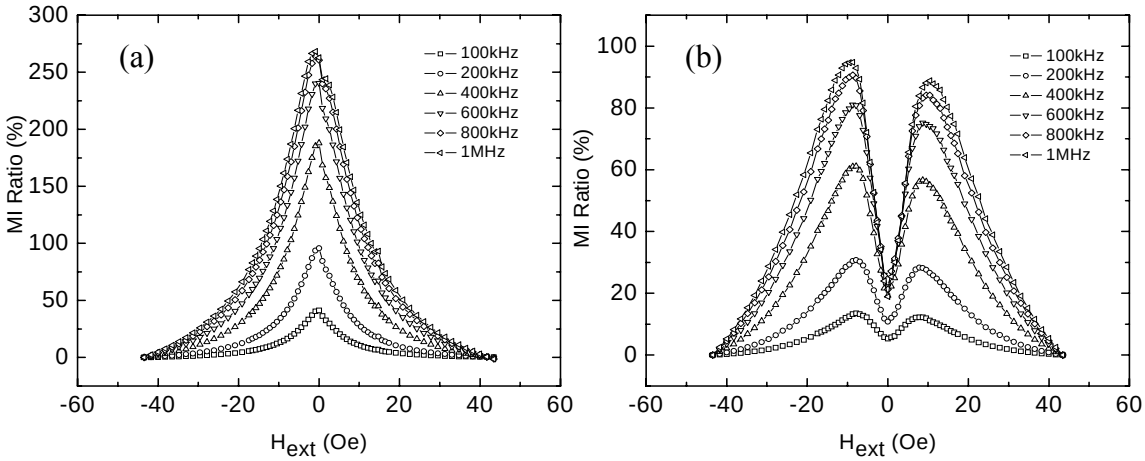

Fig. 56 MI ratio curve at different current densities (a) 0.6A/dm^2 (b) 1.4A/dm^2.

A current passing through the wire under plating would generate a circumferential induced magnetic field of flux density B_c around the wire. Since the length of the wire (8 cm) is much larger than its radius (~10μm), and the plated layer at two ends was not under consideration, the circumferential field generated by the plating current at the plating surface can be calculated using:

$$B_c = \frac{\mu_0 I}{2\pi r} \tag{65}$$

where μ_0 is the permeability in vacuum, r is the distance from the center of the core. Hence, B_c increases linearly with the plating current density. During plating, a higher current density would generate a stronger circumferential magnetic field around the wire. In the presence of a stronger circumferential magnetic field around the wire, the

magnetic domains in the deposited NiFe layer will have a closer alignment to the circumferential direction. A greater circumferential anisotropy will in turn result in improved circumferential permeability since it takes less energy to realign the magnetic domains circumferentially. This enhanced circumferential permeability will result in increased sensitivity of the plated NiFe layer in response to the external magnetic field and thus result in higher MI effect of the composite wire.

Fig. 56 (a) and (b) show the MI ratio curves for wires plated with current densities J = 0.6 A/dm^2 and 1.4 A/dm^2 respectively. The single-peak MI curves shown in Fig. 56a indicates dominantly longitudinal anisotropy while the double-peak MI curves shown in Fig. 56b, indicates dominantly circumferential anisotropy in the plated wires. There results show a transition of anisotropy of the plated wire from longitudinal to circumferential as the plating current density increased from J = 0.6 A/dm^2 to J = 1.4 A/dm^2. As the plating current density was increased, the induced circumferential magnetic field also increased, leading to the anisotropy of the wires becoming dominantly more circumferential.

When saccharin was added to the electrolyte solution for the electrodeposition of the NiFe layer, the crystalline grain size is about 20 nm. With higher plating current densities, more inhibiting species such as hydrogen may be adsorbed on the surface at a given instant. This may reduce the surface diffusion length of the metal adatoms, which in turn may lead to a higher nucleation density and, consequently, smaller crystalline grains and lower surface roughness.

Crystals grow based on the mechanism described here. The Fe^{2+} or Ni^{2+} ions will be absorbed onto the metal lattice surface as adatoms in the reactions as described in Eqn. 52 and 53. These adatoms will move across the surface to an area (surface diffusion) where the surface energy is the lowest and join the metal lattice surface

(Fig. 57a). Note these adatoms can still move into the aqueous solution but this is inhibited by the repulsive charges in the ions in the solution. The crystals will grow outwards and sidewards (nucleation) due to the joining of atoms from the aqueous solution or from the adatoms that diffuse to it on the surface (Fig. 57b). The crystal will continue to propagate in size till it encounters another growing crystal and the boundaries between the two crystals forms the grain boundaries (Fig. 57c).

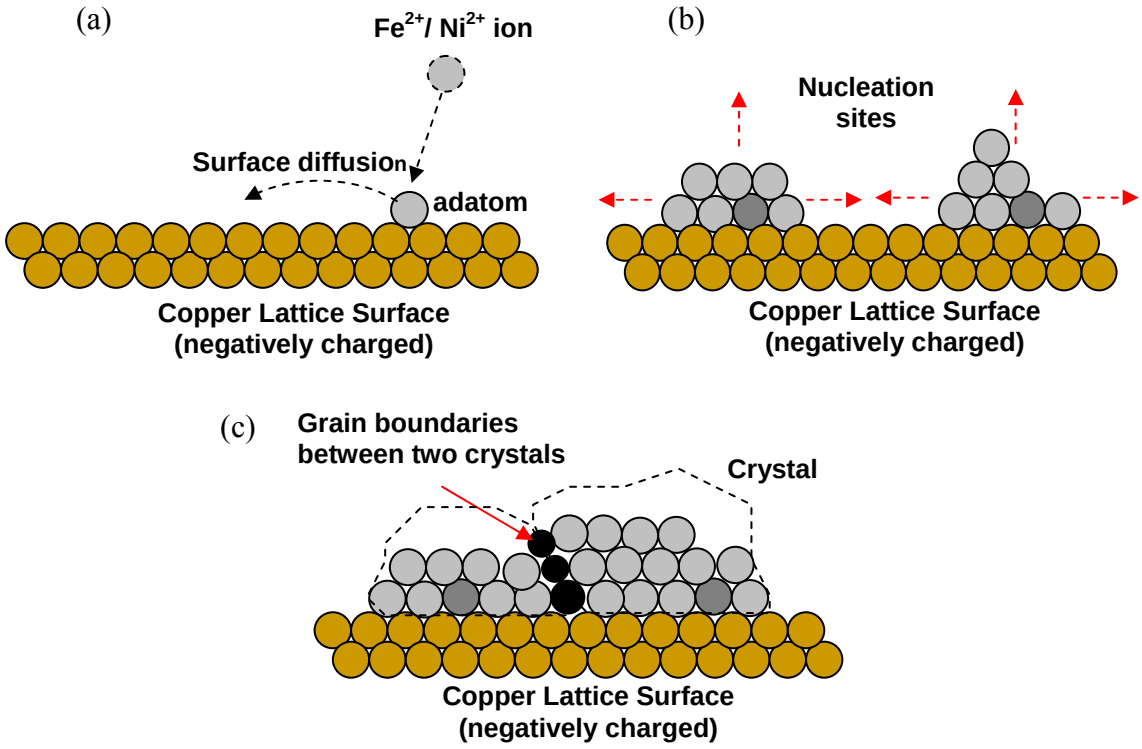

Fig. 57 Crystal nucleation process occurring at deposition times (a) time = x; (b) time = y; (c) t = z; where x<y<z.

During electrodeposition, a direct current is passed through the plating cell, the electrolyte solution and the wire under deposition. A potential difference is thus induced between the plating cell and the copper wire under deposition, causing a flow of Fe^{2+} and Ni^{2+} ions towards the wire under deposition (attractive forces of different charges). Fe and Ni will be deposited as an adatom on the surface of the wire by the reactions as given above. Noting that at this point of time, the adatom has the capability to be changed back into its ionic form. However, the Fe^{2+} and Ni^{2+} ions,

that are still in the Nernst diffusion layer solution and near the cathode (wire), will inhibit this phenomenon because of repulsive forces (of the same charges). Depending on the current densities used, there will be many nucleation sites occurring along the surface of the wire and the grains will propagate till they reach other grains of opposing growth direction and thus lead to the formation of grain boundaries.

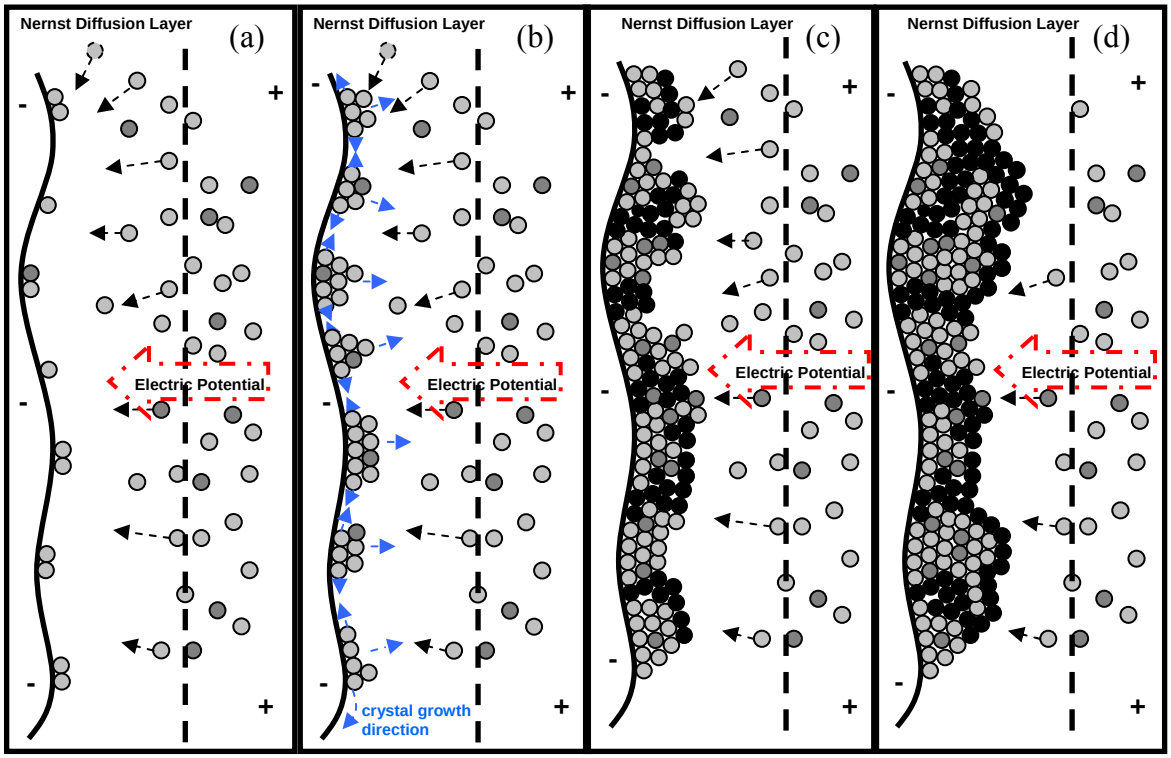

Fig. 58 Electrodepostion process mechanism at different deposition times: (a) time = *w;* (b) time = *x*; (c) time = *y;* (d)time = *;* where $w<x<y<z$.

A crystal consists of several grains and a grain consists of several cells that have atoms that are arranged, which in this case, from XRD results, in a face-centered cubic (FCC) structure. As shown in Fig 58a - Fig. 58d, nucleation sites occur on the surface of the wire under deposition. These nucleation sites will grow outwards and sidewards by "absorbing" adatoms by surface diffusion. This growth will continue until it encounters an opposite growth of another grain and the boundaries of the grains are called the grain boundaries. Thus, it can be clearly seen that in order to vary the sizes of the grains, the number of nucleation sites occurrence must also be varied.

High surface diffusion rates, low population of atatoms and low overpotentials (low current densities) are factors enhancing the build-up of crystals while conversely low surface diffusion rates, high population of adatoms, and high overpotentials (high current densities) on the surface enhance the creation of new nuclei. Surface diffusion rates are influenced not by electrical parameters but possibly by the presence of the absorbed organic additives, e.g saccharin. The prescence of these organic additives lowers the surface diffusion rates and great details will be given on the mechanism of these additives in Chapter 6.

From Fig. 59, it can be seen that the grain size was reduced as the current density was increased from 2 to 20 A/dm^2. As a result, the soft magnetic properties can be improved, because for nanocrystalline NiFe electrodeposition, as far as the crystalline grain sizes are smaller than the ferromagnetic exchange interaction length (and larger than superparamagnetic size), smaller grain size will result in higher permeability or softer magnetic properties [101].

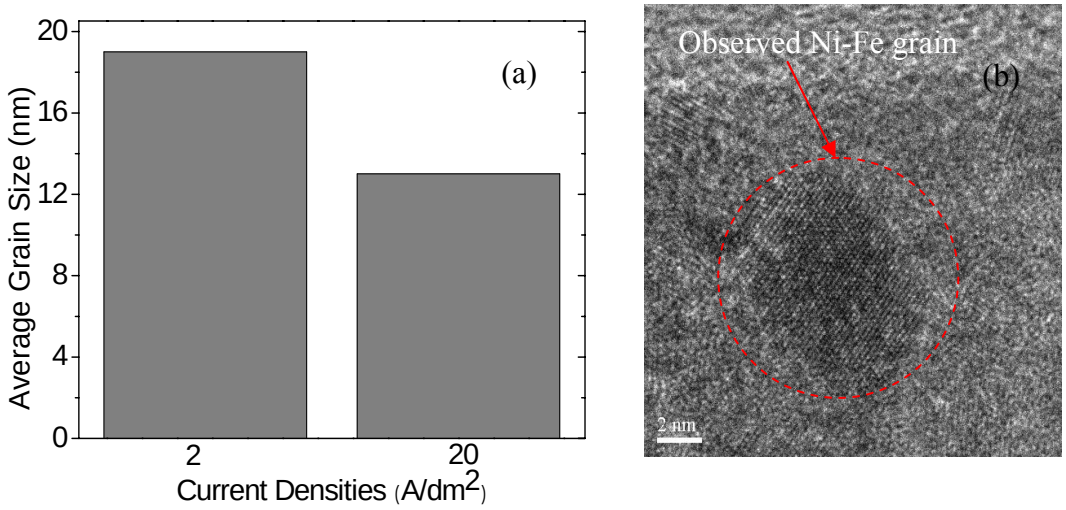

Fig. 59 (a) Variation of grain size against current density *J*; (b) TEM picture of measured specimen.

The increase of the plating current density, however, will induce larger stresses in the plated NiFe layer, which will reduce the permeability of the plated NiFe [160].

According to the results shown in Fig. 55, it seems that when the plating current density is lower than a critical value (2 A/dm^2 in the present tests), the stress induction dominates the overall effect. Therefore, when current density is lower than 2 A/dm^2, lower plating current density will result in larger MI effect ratio of the plated NiFe/Cu wire. As the plating current density is higher than the critical value, the induced circumferential magnetic field and crystalline grain size reduction dominate the overall effect. Hence, higher plated current density resulted in larger MI effect ratios of the plated NiFe/Cu wire.

This phenomenon can also be evidently seen in Fig. 60 which displays the trend of the material's coercivity in relation to the plating current densities. The coercivity is the highest for plating current density of 2 A/dm^2. The trend is similar to that of GMI effect.

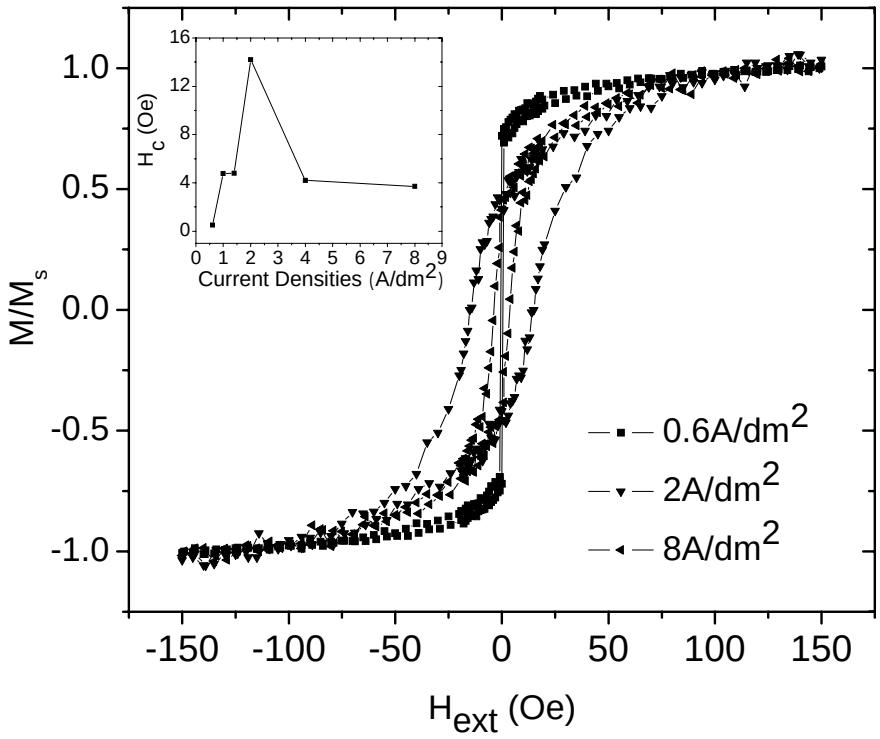

Fig. 60 The hysteresis loops of the wires plated under a range of current densities from J = 0.6 A/dm^2 to 8 A/dm^2, showing an increasing trend of coercivity with increasing the current density in the lower range till a turning point of J = 2A/dm^2, and then an decreasing trend with increasing current density in the higher range (see the inset).

5.2. Investigating the pH Value Effect

In this study, the current density J was maintained constant at 2 A/dm^2. The plating time was 5 minutes for all the samples, resulting in the plated layer thicknesses for all the wires to be about 1 μm.

Fig. 61 shows the average Fe content percentage of the plated layer in variation with the pH value of the plating solution. The Fe percentage showed an overall increasing trend against the variation of the pH value from 2.5 to 4.5, although there was a slight drop of the Fe percentage when the pH was raised from 3.5 to 4. Values of pH greater than 4.5 were not used as the deposition of metals would not be as good as those plated at a more acidic condition. Instability of the plating solution might also arise due to the overwhelming presence of OH^- ions. It should be noted that the composition of the plating solution might be altered during electroplating, thus affecting the concentration of Ni and Fe ions. The increase of Fe percentage with increasing the pH in plating solution could be due to the chemical equilibrium favoring the deposition of Fe at higher pH values, when the concentration of hydroxide ions is in higher concentration. Reduction of Fe (III) to Fe (II) in the plating solution might also be more favorable at higher pH values.

Fig. 61 inset shows the magneto-impedance (MI) in variation with an external magnetic field for NiFe electroplated wires from plating solutions of different pH values, ranging from 2.4 to 4.5. The MI testing current and frequency were 20 mA and 50 MHz, respectively. A positive increase in MI ratio was observed for all the samples. Sample plated using a pH value of 3 exhibited the highest increase in MI ratio, about 85% at 12.5 Oe. However, the two samples plated at pH values of 2.5 and 3.5, respectively, showed the smallest increase in the MI ratio, around 5% at 12.5 Oe.

It should be noted that the sample plated at a pH value of 4.5 exhibited the highest sensitivity against the external magnetic field.

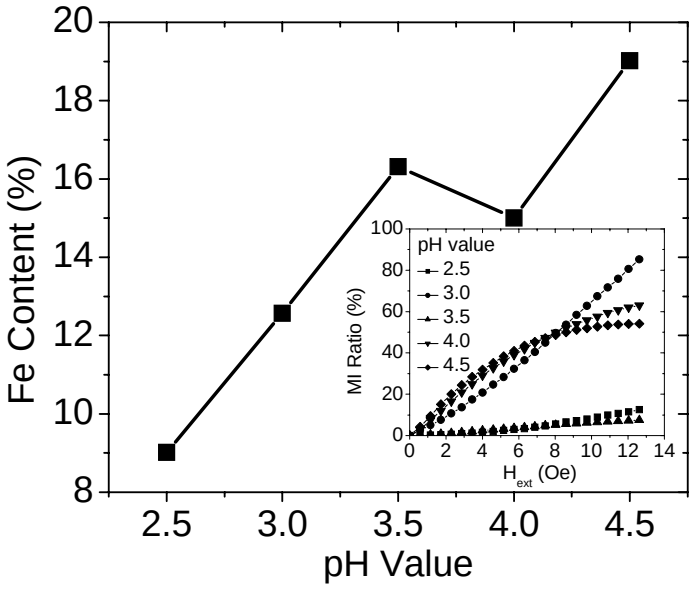

Fig. 61 Fe content varying with pH value of electrolyte. The inset graph displays the MI effect curves for the plated wires under different pH value at 50MHz testing frequency.

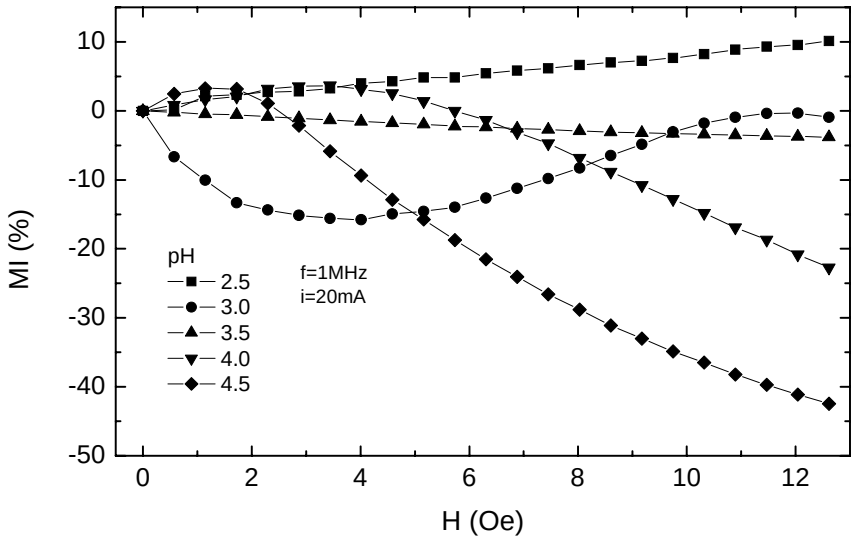

Fig. 62 MI curves measured at 1 MHz.

For the same samples tested as shown in Fig. 61, further tests were conducted to measure the MI ratios under different testing frequencies. Fig. 62 shows the MI curves measured at the frequency 1 MHz. It was found that only the sample plated at a pH value of 2.5 exhibits a positive increase in MI ratio. Samples plated at pH

values of 4 and 4.5 had their MI ratios increased to a peak at the lower field, then decreased at the higher field. On the other hand, sample plated at a pH value of 3 behaves anomalously and had its MI ratio decreased at the lower field, then increases to a peak at the higher field.

Fig. 63 shows the MI curves measured at 100 kHz. The MI ratios for all samples decreased with increasing the magnetic field. The largest decrease in the MI ratio was found on sample plated at a pH value of 3. The sample plated at a pH value of 4.5 exhibited the highest sensitivity. The difference of the magnetic properties in terms of the MI behavior can be explained by permeability and magnetization process changes due to the anisotropy. First of all, the composition is an important factor to affect the shape and size of MI. The soft magnetic property is good for Fe-Ni alloys only if their composition ratio is very near 80%:20%. Since the composition is close to the ideal composition, the sample displays high MI ratio and high sensitivity. Secondly, at low frequency, domain displacement dominants the magnetization process, the permeability decrease with respect to the external field. At high frequency, the domain wall movement was damped, the moment rotation dominants the magnetization process. The permeability increases with the increasing of the external field till to their anisotropy field.

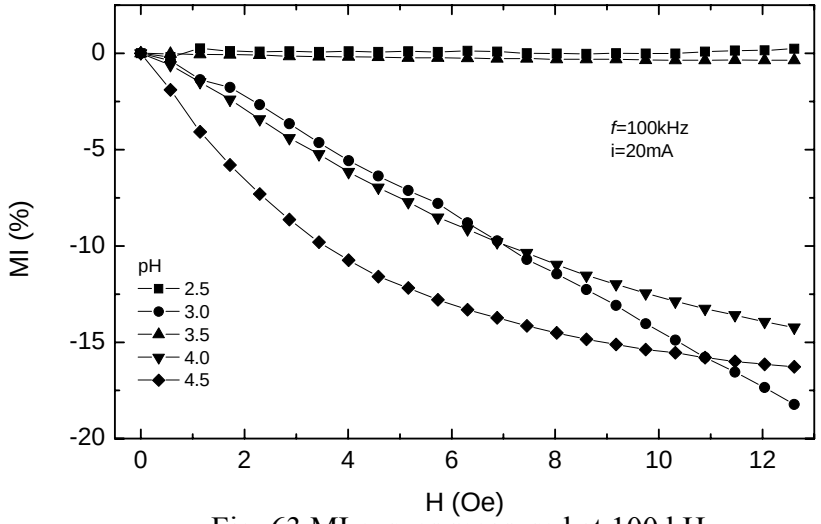

Fig. 63 MI curves measured at 100 kHz.

5.3. Investigating the Coating Thickness t_{FM} Effect

In this study, the plating current density J used was 2 A/dm^2. The electrodeposition time was varied from 3 - 60 mins to obtain deposited layers of a range of thickness. The composition ratio of $Ni_{80}Fe_{20}$ was controlled by adjusting Ni^{2+}/Fe^{2+} ion ratio of the electrolyte solution.

In order to confirm the existence of a composition distribution across cross-section of the wire in the radial direction, composite wires were electrodeposited using a single solution at different deposition times to obtain specimens of different t_{FM}. Using EDX, the surface Fe% was measured. As shown in Fig. 64, as t_{FM} was increased from 1 – 12 μm, the surface Fe concentration decreased from 28% to 18%, suggesting a distribution of composition across the radial direction of the wire. This distribution may arise from the inability of the electrolyte solution to replenish Fe^{2+} ions fast enough at the Nernst layer, thus eclipsing the effect due to decreasing plating current density as t_{FM} increases during the electrodeposition process. This distribution of composition increased as t_{FM} was increased.

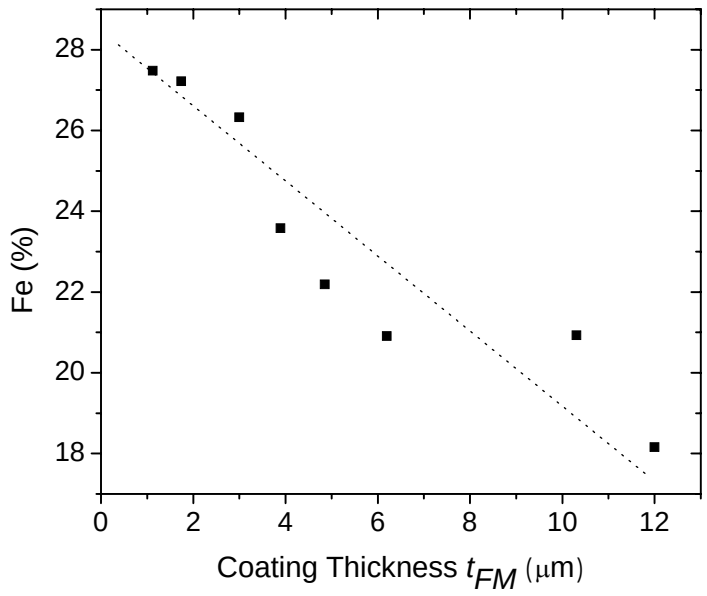

Fig. 64 Surface Fe% variations with coating thickness.

Specimens of $Ni_{80}Fe_{20}$/Cu composite wires with varying t_{FM} of 1 – 12 μm were

synthesized. It must be noted that the composition of the Ni-Fe layer was fixed at 80:20 by the manipulation of the electrodeposition electrolyte. From observations using SEM, the surface smoothness and thickness uniformity improved significantly with increasing thickness (Fig. 65). The improved uniformity will result in an enhancement of the soft magnetic properties of the ferromagnetic layer [161] such as a decrease in coercivity.

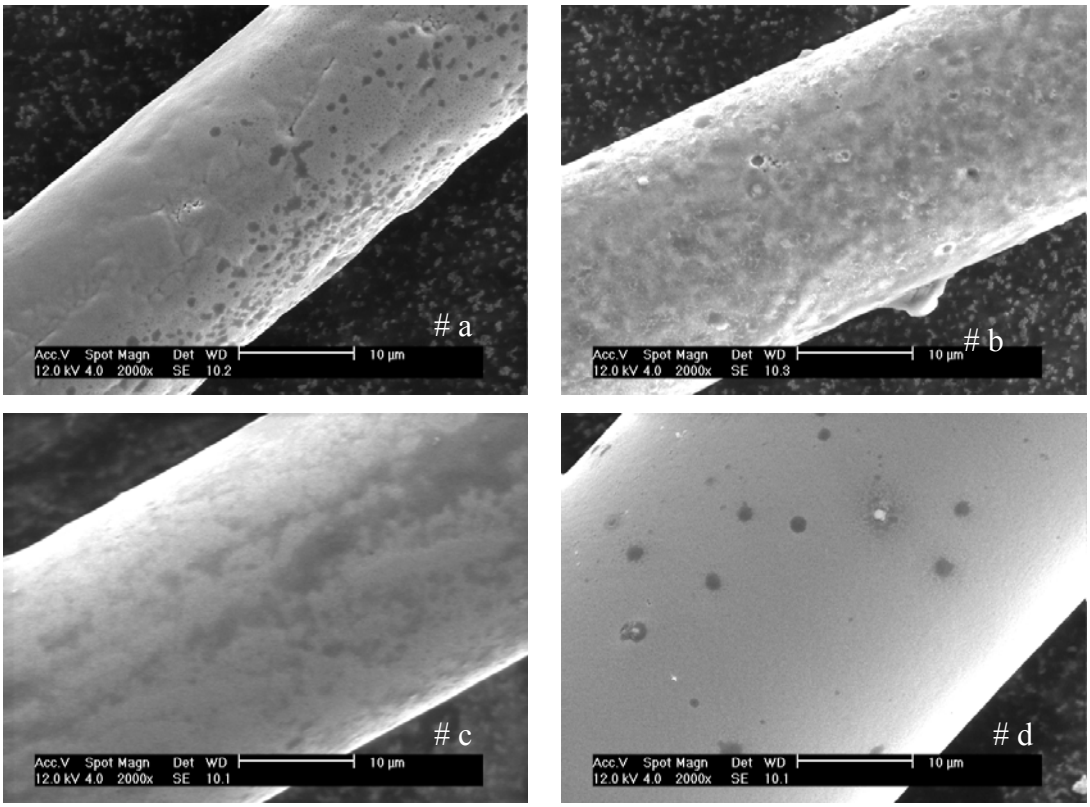

Fig. 65 SEM photos of composite wires of coating thickness (a) 1 µm; (b) 1.5 µm ; (c) 4.45 µm ; (d) 10.2 µm.

During electrodeposition, the plating current was held fixed at 1 mA throughout the entire process. Thus, the plating current density decreases as the volume of Ni-Fe increased during the plating process. The calculated decrease in current density with increasing t_{FM} is shown in Fig. 66. The decrease of plating current density with increasing t_{FM} will lead to an increase of the average grain size of the $Ni_{80}Fe_{20}$ layer with increasing t_{FM} (see inset of Fig. 66).

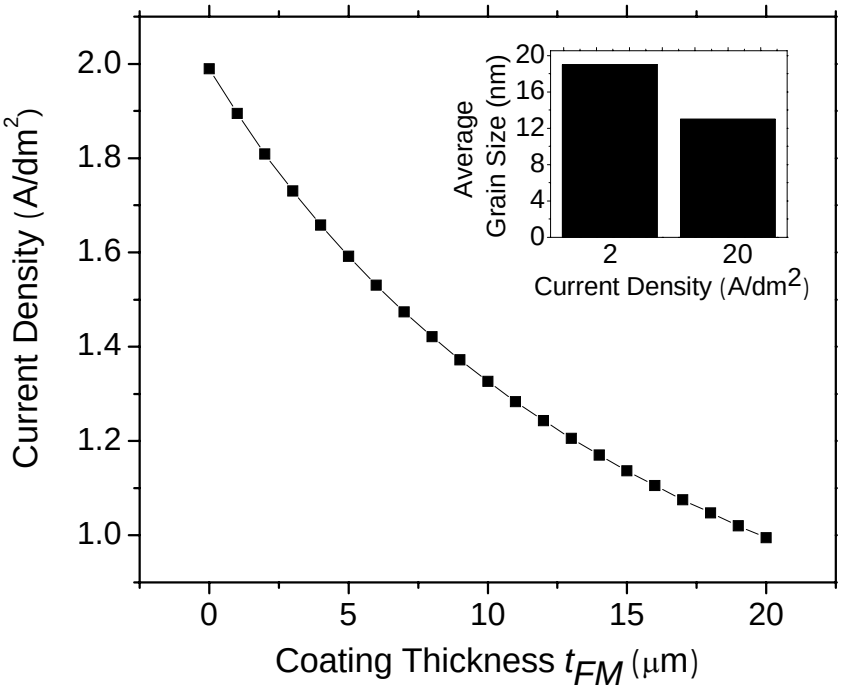

Fig. 66 Calculated plating current density with coating layer thickness. The inset shows the effect of current density on average grain size.

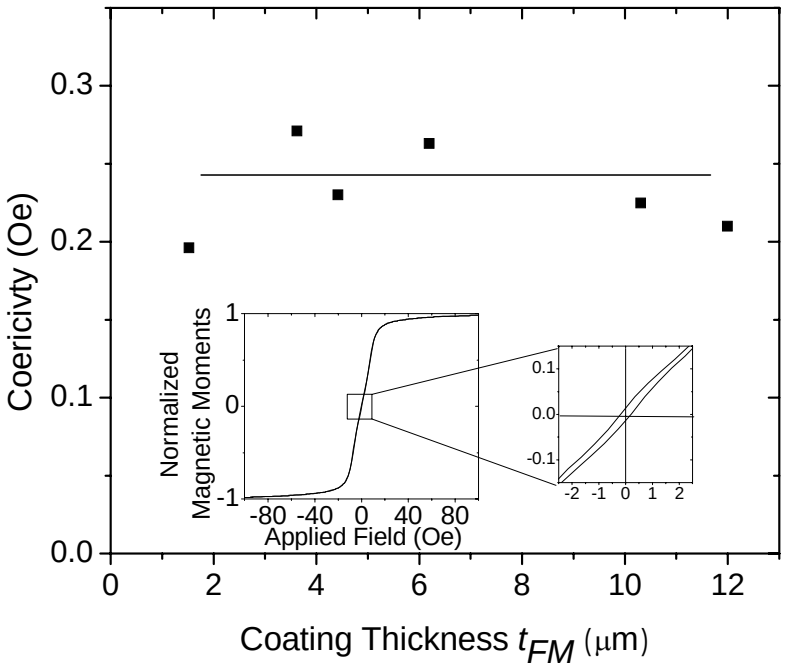

Fig. 67 Variation of coercivity H_c with coating thickness. Inset shows hysteresis loop of specimen with t_{FM} at 1.5 μm.

Increasing t_{FM} will increase the composition distribution across the radial direction, increase the average grain size of the deposited layer and enhance the uniformity of the layer. The increasing distribution of composition will cause the value of magnetostriction to deviate from zero, resulting in an increase in coercivity.

Increasing grain sizes will result in increased coercivity when the size is below the critical interaction length [101]. The enhanced uniformity will cause the coercivity to decrease. These effects balanced each other and thus the coercivity of the deposited layer changes insignificant over a range of t_{FM} (Fig. 67). Note that the surface composition of the specimen wires measured for the coercivity (Fig. 67) and magneto-impedance effect (Fig. 68) were ensured to be $Ni_{80}Fe_{20}$ by EDX. This composition was achieved by the manipulation of the electrolyte concentration in the electrodeposition process. The inset graph in Fig. 67 shows the hysteresis loop of the specimen with t_{FM} at 1.5μm, displaying a low coercivity value of 0.2 Oe.

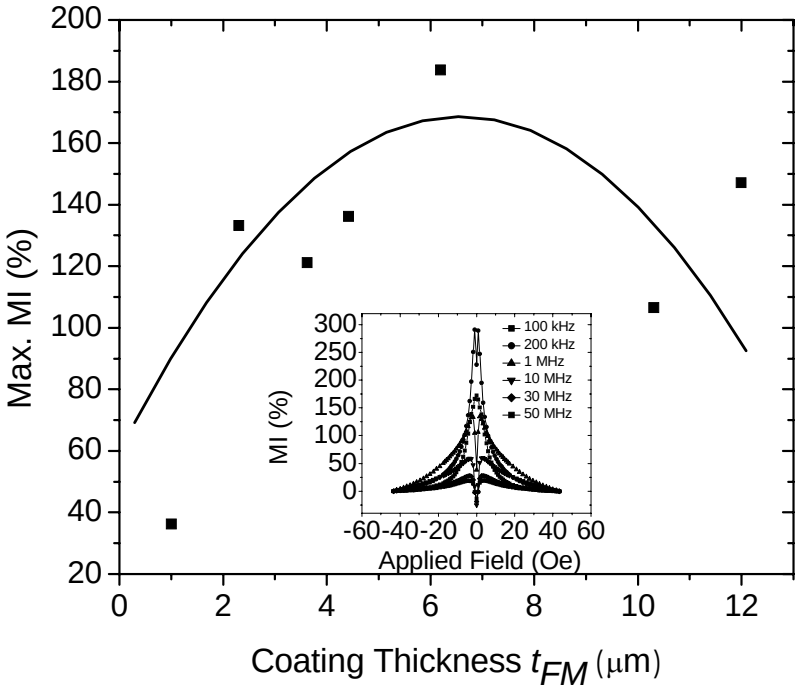

Fig. 68 Variation of maximum MI% with coating thickness at 1 MHz testing frequency. Inset graph shows the MI% variation with external field for specimen with t_{FM} of 2.3 μm for different frequencies.

As shown in Fig. 68 the max. MI% initially increases as t_{FM} is increased till a critical range of 4-9 μm and later decreases with further increase in t_{FM}. The trend of maximum MI ratio over t_{FM} was probably mainly due to the coating thickness variation. Note that coercivity and permeability has an inverse relationship with each other [101]. In the absence of an externally applied field, the skin depth δ in the

ferromagnetic layer is lower than its thickness at sufficiently high frequencies [162]. Thus, almost all the alternating current will be flowing in the outer Ni-Fe layer and the resistance (and thus impedance) is sufficiently high. Due to the influence of the externally applied field, the effective transverse permeability μ_t decreases, resulting in an increase in the skin depth in the outer Ni-Fe layer and impedance decrease. Thus, the alternating current can also flow in the inner Cu core. As a result, the resistance of the wire decreases and the ratio Z/Z_0 increases. Thus, for a given frequency of the alternating current, there is an optimum value of t_{FM} at which the variation of the wire impedance is the maximum. Outside this critical range, the maximum MI% ratio will deteriorate drastically. When δ is thicker than or near t_{FM}, most of the alternating current will flow in the inner core with or without the presence of an applied magnetic field. When δ is smaller than t_{FM}, even when the maximum reference magnetic field is applied, most of the alternating current will flow in the outer Ni-Fe shell in any situation. Both situations will result in low MI% ratios.

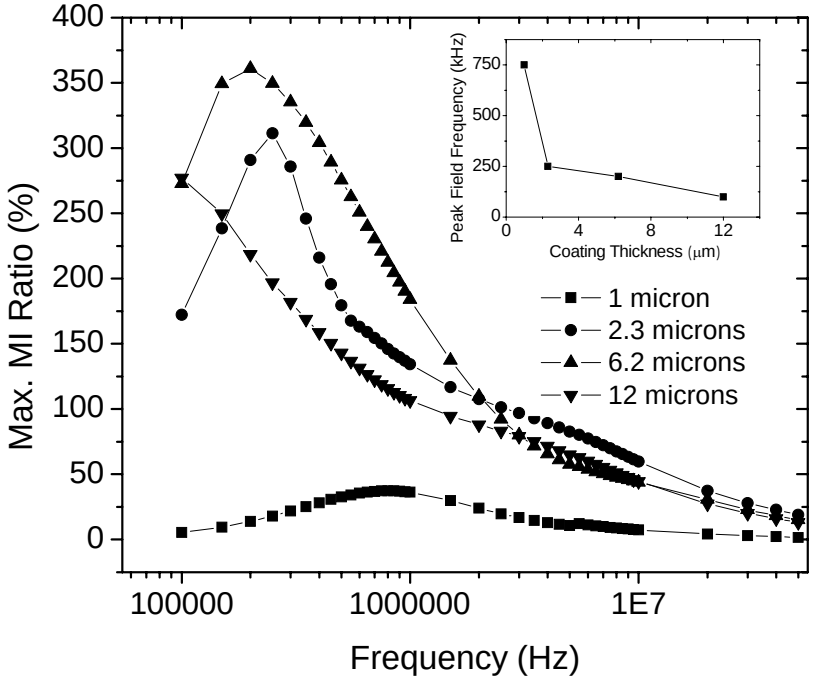

Fig. 69 Maximum MI frequency dependence on coating thickness

Furthermore, as shown in Fig. 69, as the coating thickness was increased from 1μm to 12μm, the frequency at which max MI occurs drastically reduced from 750 kHz to 100 kHz. This trend is most probably due to changes in the skin depth δ as the effective critical frequency of skin effect ω is qualitatively described as

$$\omega = \frac{2}{\mu_\phi \sigma \, \delta^2} \tag{66}$$

where σ is the conductivity, and μ_ϕ is the circumferential permeability of the composite wire.

5.4. Investigating the Alloying Effect of Molybdeum

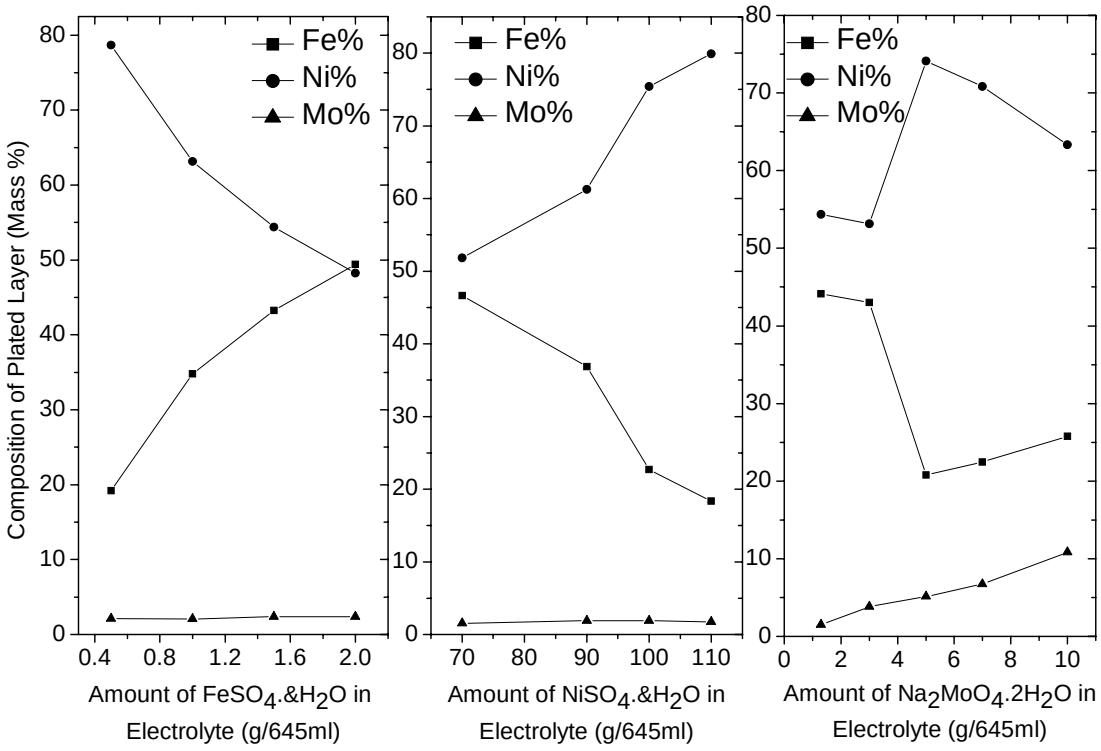

Fig. 70 Effect of variation of $FeSO_4 \cdot 7H_2O$, $NiSO_4 \cdot 6H_2O$, $Na_2MoO_4.2H_2O$ in the electrolyte on the plated layer composition.

In order to obtain NiFeMo/Cu composite wires of various composition ratios, the effect of the variations of the main chemicals concentrations ($NiSO_4.6H_2O$, $FeSO_4.7H_2O$ and $Na_2MoO_4.2H_2O$) in the electrolyte solution on the composition of

the plated layer has to be known. The concentration of $FeSO_4 \cdot 7H_2O$, $NiSO_4 \cdot 6H_2O$ and $Na_2MoO_4.2H_2O$ was varied individually in the electrolyte solution with other synthesis parameters being held fixed, and the dependency of the composition ratios on the concentration is displayed in Fig. 70. It can be observed that as the amount of $FeSO_4.7H_2O$ and $NiSO_4 \cdot 6H_2O$ in the electrolyte increased, Fe % and Ni% in the plated layer increased accordingly, with very negligible effect on the Mo%. The Mo% in the plated layer can only be significantly controlled by the variation of the chemical $Na_2MoO_4.2H_2O$.

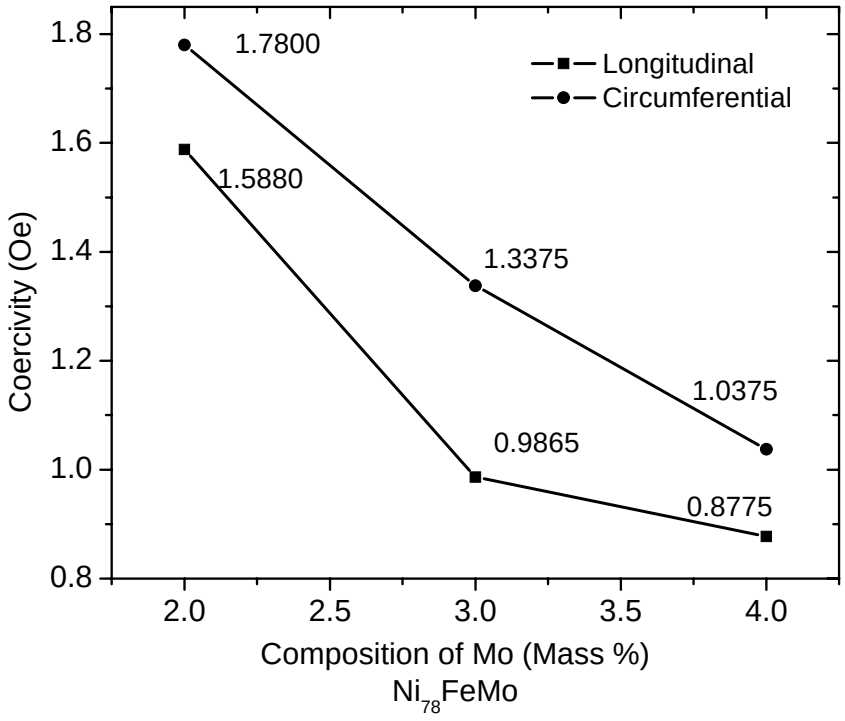

Fig. 71 Effect of the Mo% for $Ni_{78}FeMo$ specimens on the circumferential and longitudinal coercivity.

For soft magnetic materials to be used for sensor applications, the coercivity must be small. Fig. 71 shows the effect of the composition ratios on the circumferential and longitudinal coercivity of wire specimens with composition ratios of $Ni_{78}Fe_{20}Mo_2$, $Ni_{78}Fe_{19}Mo_3$ and $Ni_{78}Fe_{18}Mo_4$. From Fig. 71, it can be observed that when the Mo% increased from 2% to 4% in the $Ni_{78}FeMo$ batch of wires, both the longitudinal and

the circumferential coercivity decreased. On the whole, the longitudinal coercivity values were lower than that in the circumferential direction. This suggests that it is easier to demagnetize and magnetize the wire specimens along the longitudinal axis than along the circumferential direction. The wire specimen with plated layer of composition ratio $Ni_{78}Fe_{18}Mo_4$ was found to possess the lowest longitudinal and circumferential coercivity values of 0.88 Oe and 1.04 Oe, respectively. Fig. 72 shows the hysteresis loop of the wire specimen with the plated layer having composition of $Ni_{78}Fe_{18}Mo_4$. The low coercivity, and thus high permeability, of $Ni_{78}Fe_{18}Mo_4$ can be attributed to two main factors, namely, the near-zero magnetostriction as achieved by the composition ratio of Ni:Fe and the effect of addition of molybdenum.

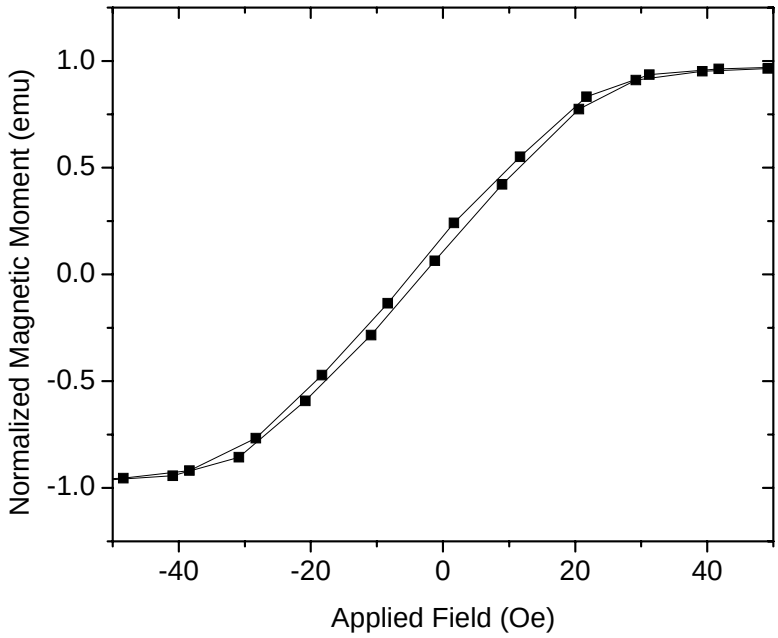

Fig. 72 Hysteresis loop of $Ni_{78}Fe_{18}Mo_4$ plated layer.

From Fig. 73, it can be observed that when Mo% increased from 2% to 4% in the $Fe_{22}NiMo$ batch of wires, circumferential coercivity decreased. This trend is identical to that shown in Fig. 71 and verifies that the addition of molybdenum improves coercivity. However, the magnitudes of the coercivity were higher than that of the

$Ni_{78}FeMo$ batch. This suggests that the coercivity of NiFeMo is also dependent on the composition ratio of Ni:Fe, other than the addition of molybdenum.

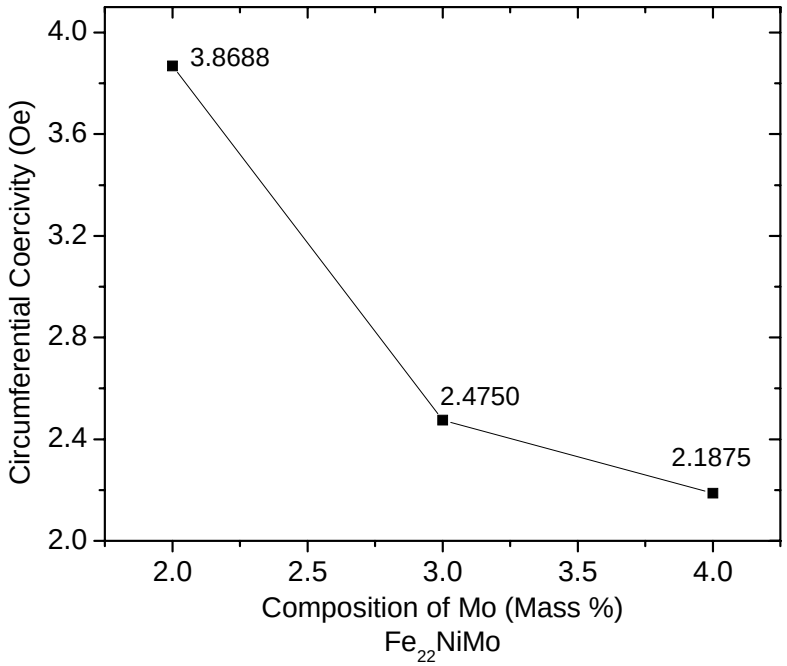

Fig. 73 Effect of Mo% for $Fe_{22}NiMo$ specimens on circumferential coercivity.

The MI effect curves for the different composition ratios are presented in Fig. 74. The peak field intensity (the applied field at which MI effect ratio is the largest) represents the permeability of the material such that a lower value indicates a higher value of magnetic permeability. In general, it is known that permeability and coercivity have in broad terms a reciprocal relationship such that materials with a low coercivity necessarily have a high permeability. From Fig. 71 and Fig. 73, it can be observed that when the Mo% increased from 2% to 4% in both the $Fe_{22}NiMo$ and $Ni_{78}FeMo$ batches of wires, the peak field intensity decreased. This clearly indicates that the addition of molybdenum enhances the magnetic permeability of the alloy. However, the magnitudes of the peak field intensity are higher for the $Fe_{22}NiMo$ batch of wires. This trend is similar to the case of coercivity values as well. Hence, the extent of permeability of NiFeMo as a ferromagnetic material may still depend much on the composition ratio of nickel and iron. The well-known material permalloy,

$Ni_{79}Fe_{21}$ (having the ratio of iron to nickel of 0.25), was found to obtain zero magnetostriction which gives rise to its high permeability. For the batch of $Ni_{78}FeMo$ wires, the ratio of iron to nickel was between 0.23 and 0.26 whereas for the $Fe_{22}NiMo$ batch of wires, the ratio was between 0.29 and 0.30. This shows that by keeping the ratio of Fe:Ni closer to the region of 0.25, despite addition of molybdenum, permeability is generally higher as indicated in Fig. 75 and Fig. 76.

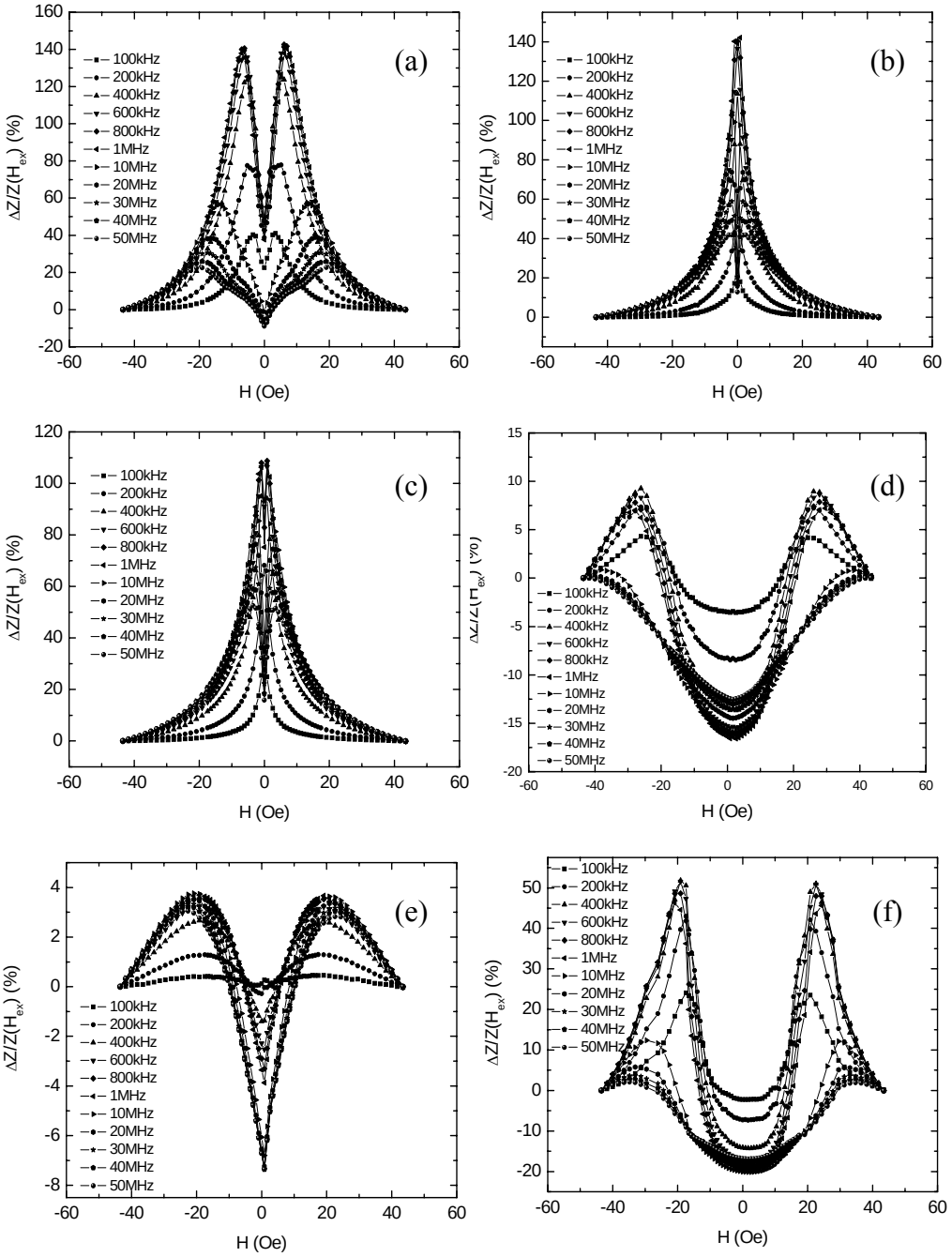

Fig. 74 MI effect curves for (a) $Ni_{78}Fe_{20}Mo_2$, (b) $Ni_{78}Fe_{19}Mo_3$, (c) $Ni_{78}Fe_{18}Mo_4$, (d) $Fe_{22}Ni_{76}Mo_2$, (e) $Fe_{22}Ni_{75}Mo_3$, and (f) $Fe_{22}Ni_{74}Mo_4$.

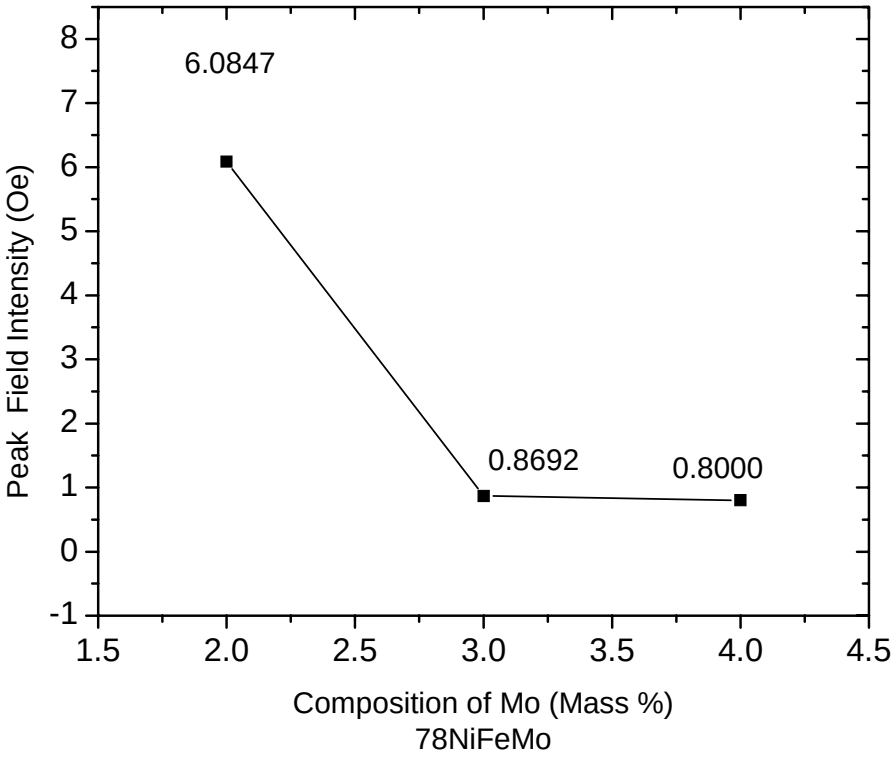

Fig. 75 Variation of peak field intensity against the Mo% for $Ni_{78}FeMo$.

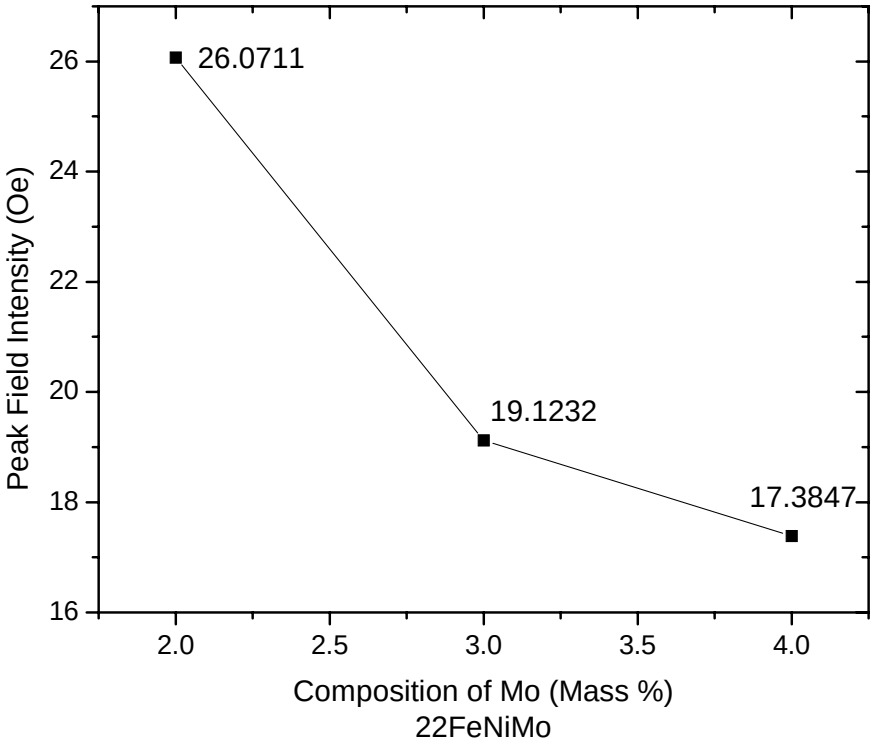

Fig. 76 Variation of peak field intensity against the Mo% for $Fe_{22}NiMo$.

The magnetic properties of supermalloy $Ni_{78}Fe_{18}Mo_4$ were compared to that of permalloy $Ni_{79}Fe_{21}$, synthesized using the same process and conditions. From Fig. 77,

it can be observed that both the circumferential coercivity and the peak field intensity of supermalloy $Ni_{78}Fe_{18}Mo_4$ were significantly lower than that of permalloy $Ni_{79}Fe_{21}$. This drastic enhancement in magnetic permeability can be mainly attributed to the beneficial effect of the addition of molybdenum.

The addition of a few percentage of molybdenum inhibits development of the undesirable short and long–range crystallographic order [84]. As such, the domains can be easily aligned to the direction of the applied external magnetic field, giving rise to high permeability. Furthermore, the molybdenum ions also act as electron-scattering centers and therefore increase the electrical resistivity. When electrical resistivity increases, eddy currents will be reduced. This reduction in eddy currents enhances the permeability of the material as the magnetic field produced by these internal eddy currents in the coating layer normally acts in opposition to the applied magnetic field and have the effect of reducing the internal flux density.

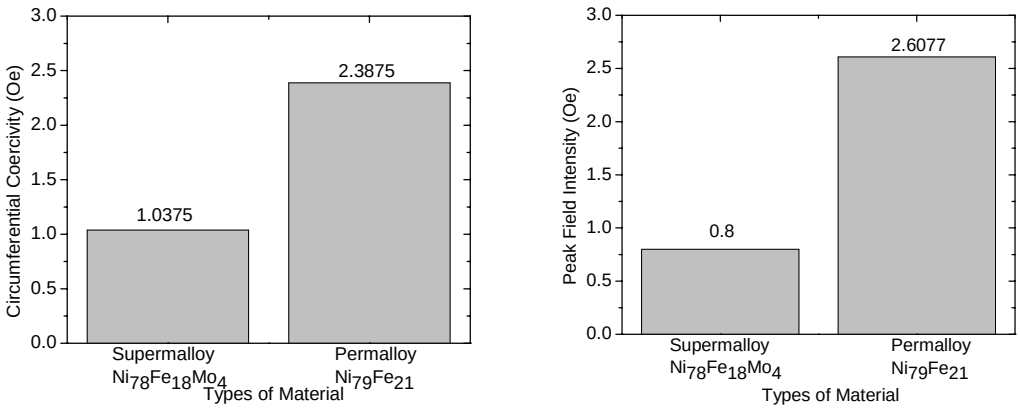

(a) (b)

Fig. 77 Comparison between supermalloy and permalloy in: (a) circumferential coercivity, and (b) peak field intensity.

5.5. Summary

In this chapter, the influence of the electroplating parameters was investigated in relation to the resulting magnetic properties of the electrodeposited NiFe/Cu wires.

1. The effect of plating current density J on the magnetic properties of plated material in the electroplating of NiFe/Cu composite wires has been studied through experiments. The results showed that the soft magnetic properties (as indicated by the maximum MI ratios and coercivity of the plated $Ni_{80}Fe_{20}$/Cu composite wires) of the plated NiFe varies with plating current density significantly. A critical value of plating current density J of 2 A/dm^2 was found, below which the soft magnetic properties decreased with increasing current density and above which the soft magnetic properties increased with increasing current density. The results also showed that plating current density affects the magnetic anisotropy of the plated wire.
2. The pH value of the electroplating solution affects the composition of plated layer in NiFe plating. The Fe percentage generally increases as the pH value increases from 2.5 to 4.5. The magnetic property of the plated layer in terms of MI ratio depends directly on the composition of plated layer rather than the pH value of plating solution.
3. The magnetic properties of the deposited material in variation with thickness t_{FM} of deposited layer have been investigated. The results showed that thickness affects composition of the deposited material, which makes coercivity increase with increasing thickness. It also affects the average grain size of e deposited material, which causes coercivity to increase with increasing thickness. It further affects the uniformity of deposited material, which causes coercivity to decrease with increasing thickness. As a combined effect of thickness on the magnetic properties of the deposited material, the coercivity of the material can be in a dynamic constant state as thickness varies. Under such circumstances, the thickness has mainly geometrical effect on the MI effect of the composite wire.

4. Various composition ratios of NiFeMo/Cu wire samples have been developed by DC electrodeposition through the variation of electrolyte solution concentration. It has been found that at the composition of $Ni_{78}Fe_{18}Mo_{4,}$ the material alloy is magnetically softest, as indicated by the lowest longitudinal and circumferential coercivity of 0.88 Oe and 1.04 Oe, respectively, and also by the lowest peak field intensity of 0.80 Oe in the MI effect curve obtained. The magnetic properties of the supermalloy $Ni_{78}Fe_{18}Mo_4$ has also been compared with permalloy $Ni_{79}Fe_{21}$ and found to be much better than that of permalloy.

Chapter 6 Development of a Nanocrystalline Deposition Technology for Super Permeability Permalloy for NiFe/Cu Composite Wires

In this chapter, different techniques are employed to manipulate the grain size for the electroplated composite wires; including using additivities such as saccharin and changing the electrodeposition current waveform, so as to deposite NiFe layers of varying average grain size. The difference in the average grain sizes by changing the electrodeposition current waveform was due to the mechanisms occurring during the introduction of off-time and anodic current I_A.

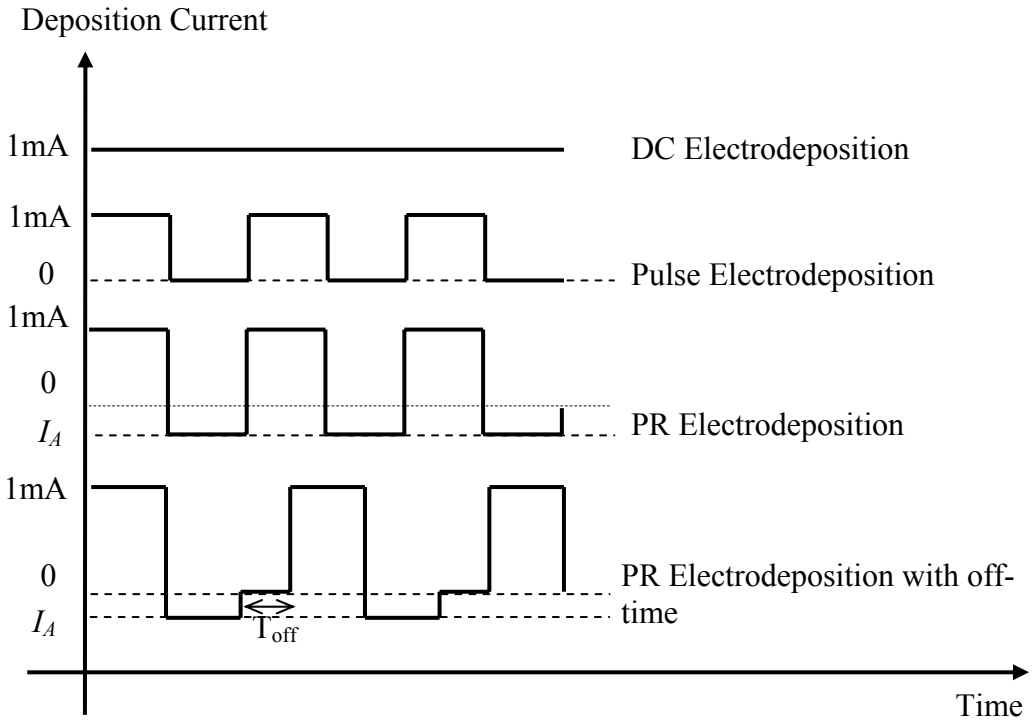

Fig. 78 Different Electrodeposition Current Waveforms.

For DC electrodeposition, the deposition cathodic current was fixed at 1 mA. The positive cathodic current was fixed at 1 mA, while the negative anodic current I_A was maintained at 0 mA for pulse electrodeposition and 0.1 mA for pulse-reverse electrodeposition. The duty cycles of both the electrodeposition pulsed current and pulse-reverse current were fixed at 50% and the frequencies were fixed at 1 Hz, but the total number of electrodeposition cycles used for pulse-reverse electrodeposition was varied according to the anodic current, in order to obtain similar thickness for comparisons. An off-time period was also introduced into the pulse-reverse electrodeposition current waveform and the differences in the electrodeposition current waveforms used are shown in Fig. 78.

6.1. Theoretical predictions of the upper and lower bound of nanocrystalline grain size

According to the random anisotropy model (RAM) (Chapter 2.5.3), within a range of nanocrystalline grain size, when the grain size is decreased, the magnetic properties, in terms of permeability or coercivity, are enhanced significantly. This range of grain size, however, is material specific. However, the values of the upper and lower bound of this range of grain size can be estimated theoretically.

The upper bound of this range for $Ni_{80}Fe_{20}$ (permalloy) can be predicted using RAM. For permalloy, $K_1 = 0.35 \times 10^3$ J/m^3, $A = 26 \times 10^{-12}$ J/m. Thus, the upper bound can be estimated to be about $L_{ex} = \sqrt{\frac{A}{K_1}} \approx 270nm$.

During these measurements, the lower bound of the nanocrystalline grain sizes, at which superparamagnetism occurs will be obtained. Superparamagnetism occurs in very small crystallite size whereby because of the size, the crystalline anisotropy

energy and thus temperature of occurrence of superparamagnetism is significantly reduced. Thermal energy is enough to change the magnetization of entire crystallite, causing magnetic field to average to zero and the occurrence of superparamagnetism. Based on the Heisenberg Uncertainty Principle,

$$\Delta p = \tilde{h} / \delta_0 \tag{67}$$

where $\tilde{h} = h_p / 2\pi$, h_p is the planck constant, δ_0 is the critical grain size and Δp is the uncertainty momentum. The energy fluctuations is given by

$$\Delta\varepsilon_0 = (\Delta p)^2 / 2m_e \approx \tilde{h}^2 / 2m_e\delta_0^2 \tag{68}$$

where m_e is the mass of electron. At Curie temperature (T_c), the maximum exchange energy is given by

$$\Delta\varepsilon_{\max} = E_{ex}V / a_l^3 \tag{69}$$

where E_{ex} is the exchange energy, V is the volume of body and a_l is the lattice constant. At the Curie temperature (T_c), the exchange energy fluctuations are equivalent to the thermal energy fluctuations. Thus,

$$\Delta\varepsilon_{\max} = K_B T_c V / a_l^3 \tag{70}$$

where K_B is the Boltzmann constant and V/a_l^3 is equivalent to a value near 1. Thus,

$$\Delta\varepsilon_{\max} = K_B T_C \tag{71}$$

Equating Eqn. 68 and Eqn. 71 and substituting the values of $\tilde{h}$ = 1.05 x 10^{-34} J.s, m_e = 9.1093897 x 10^{-31} kg, K_B = 1.380658 x 10^{-23} J/K, and T_c for permalloy = 850K, the predicted nanocrystalline superparamagnetic grain size is approximated to be of the value of about 1.4 nm. However, since this model does not consider other factors such as the level of residual stress of the specimens, the accurate range of superparamagnetism grain sizes will be still in the region of 2-10 nm.

6.2. Effect of Addition of Saccharin on the grain size

Saccharin ($C_7H_5NO_3S$) (Fig 79), a first class brightener, is well known to be efficient in Watts and sulphamate nickel plating baths as well as in copper electroplating baths. Those in the first class have two functions: firstly they provide bright plating over a bright substrate (though not able to build lustre) and furthermore they permit the second class of brighteners to be present over a wide range of concentrations. Brighteners of the second class are used to build mirror-like lustre on platings, but suffer most from the fact that, in the absence of a first class brightener, they can often induce excessive brittleness and stress in the deposit.

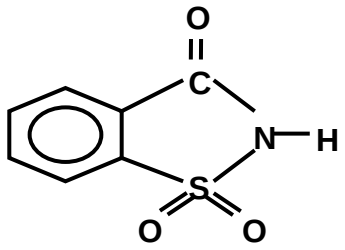

Fig. 79 Chemical structure of saccharin

In this experiment, the amount of saccharin added to the electrolyte solution was varied with the rest of the deposition parameters fixed to investigate its effect on the chemical composition and thickness of the deposited layer. It is well known that brighteners, such as saccharin, have the property of grain refinement of the deposits and it is well accepted that additives inhibit surface diffusion of adatoms towards preferential growth centers and favorize the density of grain precursors, therefore promoting nucleation and reducing the grain size [163,164,165,166,167].

As shown in Fig. 80, a potential difference causes a flow of the positively charged ions towards the wire surface but is inhibited by the large molecules of saccharin. Saccharin molecules will eventually eventually be pushed towards the wire surface by

the ions. At the plated surface, saccharin molecules presence inhibit surface diffusion of adatoms. However, these adatoms will join the metal lattice at the voids beneath the molecules and eventually push the saccharin molecules outwards into the solution.

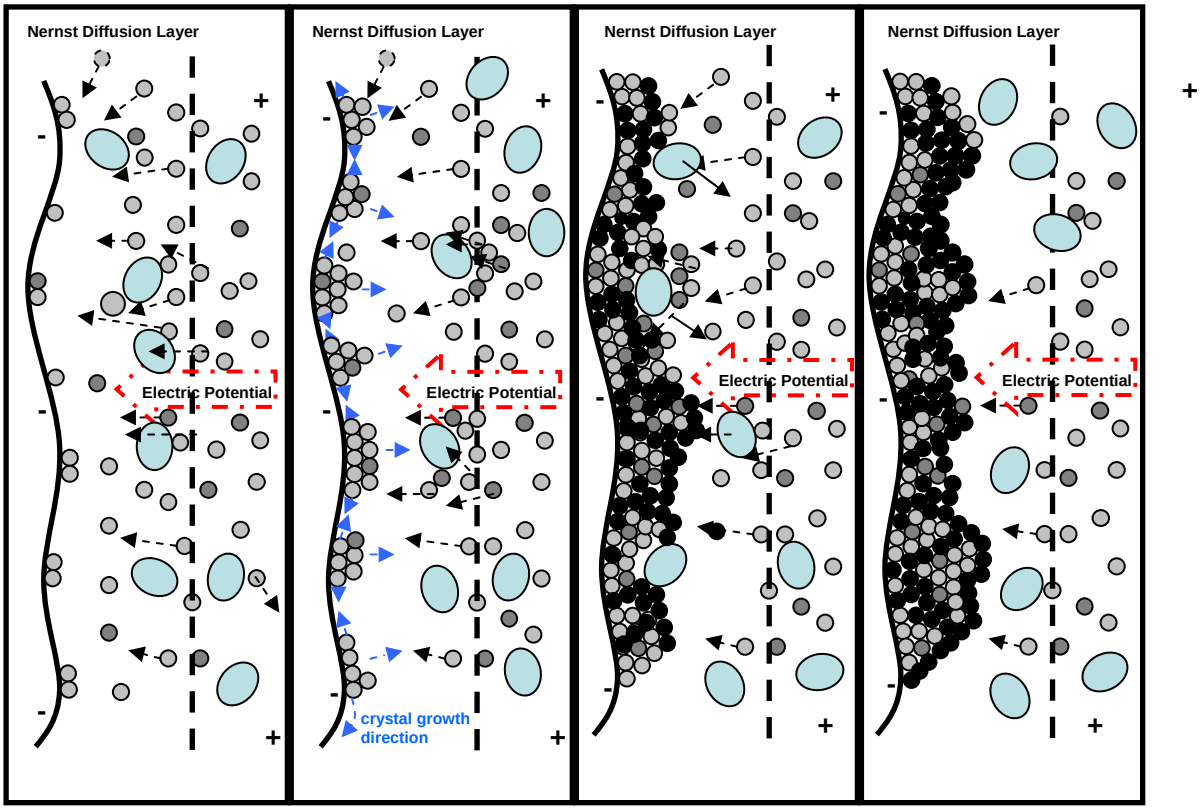

Fig. 80 Saccharin refinement process (whereby Time=W<X<Y<Z)

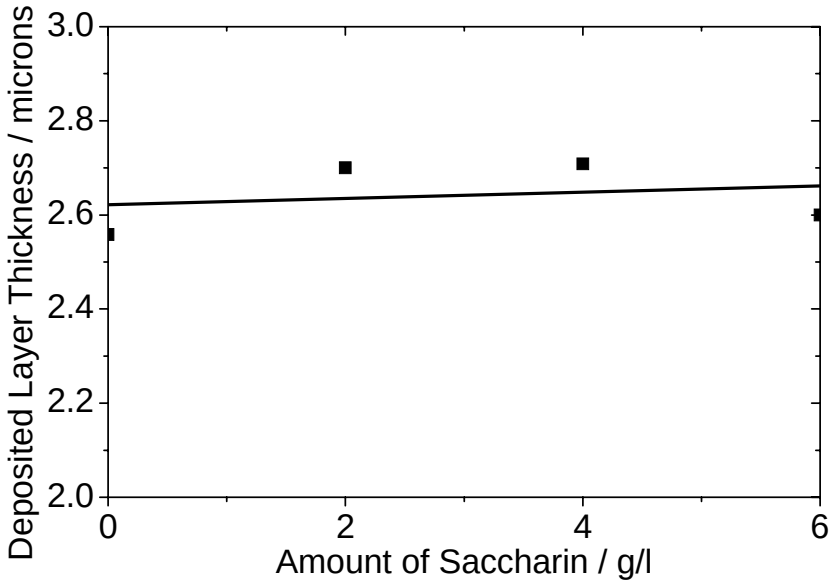

Fig. 81 Effect of saccharin on deposited layer thickness

However, the addition of saccharin results in differences in the composition of the deposited layer (Fig. 81), no significant difference in the thickness of the deposited layer has been observed (Fig. 82) and thus must be compensated by an increase in the electrolyte solution concentration of $FeSO_4.7H_2O$.

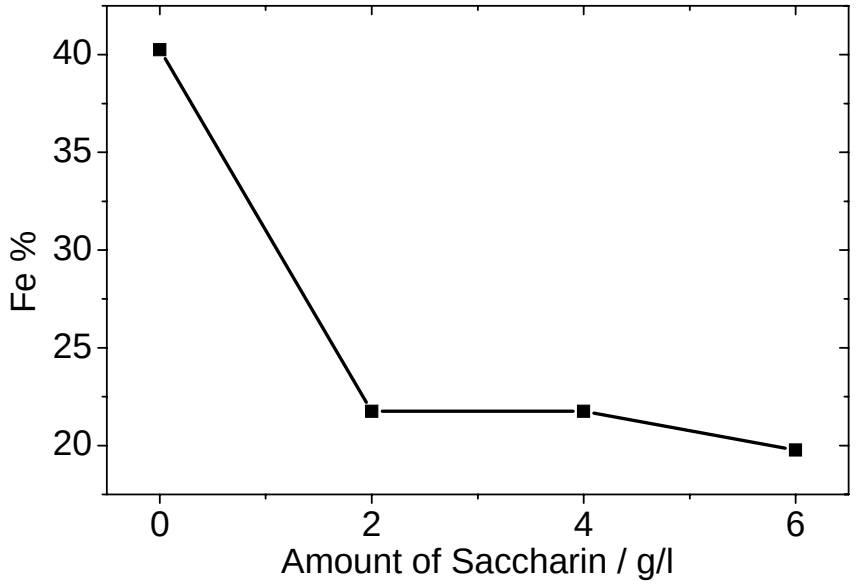

Fig. 82 Effect of saccharin on chemical composition

The grain sizes of specimen composite wires using DC electrodeposition, without saccharin and with saccharin, were found to be 21.5nm and 51.4nm respectively. Results showed that the addition of saccharin to the electrolyte solution improved the deposited layer's magnetic performance from 58.4% to 248.6%.

6.3. Effect of pulse plating duty cycle on grain size and magnetic properties

Pulse deposition parameters consist of the pulse current density i_p, the current that flows during the off-time i_{off}, the duty cycle γ and the pulse frequency ν. For one cycle, duty cycle is defined as the ratio of on-time to the period, i.e.

$$\gamma = \frac{t_{on}}{t_{on} + t_{off}} = \frac{t_{on}}{t_{pp}} \tag{72}$$

where t_{on} is the amount of on-time and t_{off} is the amount of off-time in a single period cycle t_{pp}. The pulse frequency ν is simply the inverse of the pulse period cycle, ν = 1 / t_{pp}.

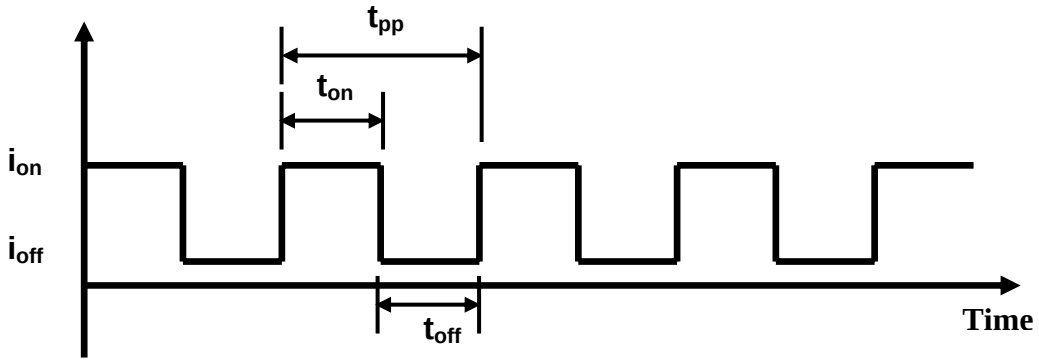

Fig. 83 Pulsed Current Waveform

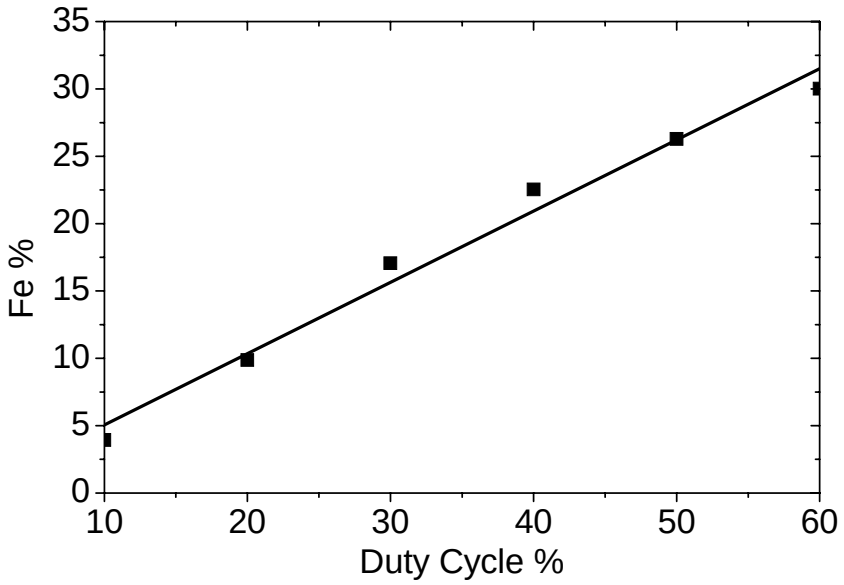

Fig. 84 Effect of duty cycle on Fe% of plated layer.

The difference between the mechanism of electrodeposition and that of pulse deposition is that during the off-time, there is minimal deposition of the metallic ions. Replenishment of ions in the diffusion layer occurs during the off-time. This leads to a higher concentration of ions in the diffusion layer during the next on-period, thus resulting in higher numbers of adatoms on the surface causing the occurrence of more

nucleation sites. When there are more nucleation sites, it would mean that there will be less growing space thus it results in a smaller grain size in the deposited layer.

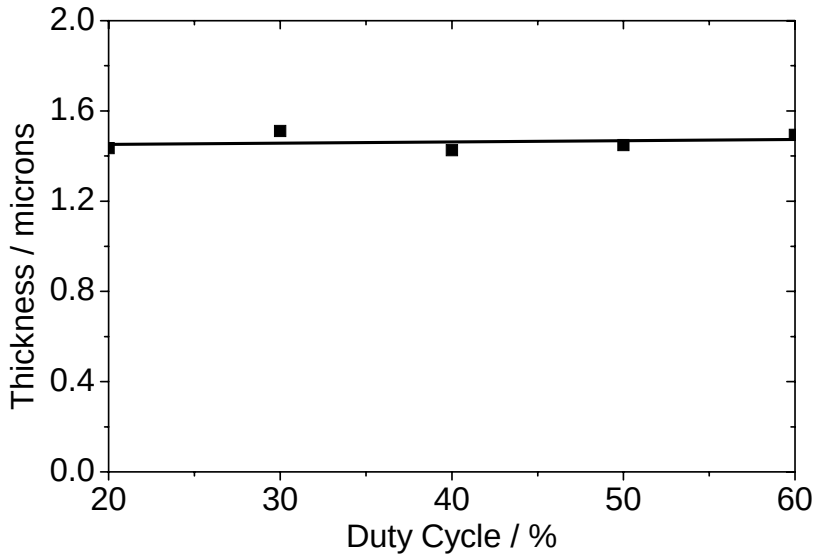

Fig. 85 Effect of duty cycle on thickness of plated layer.

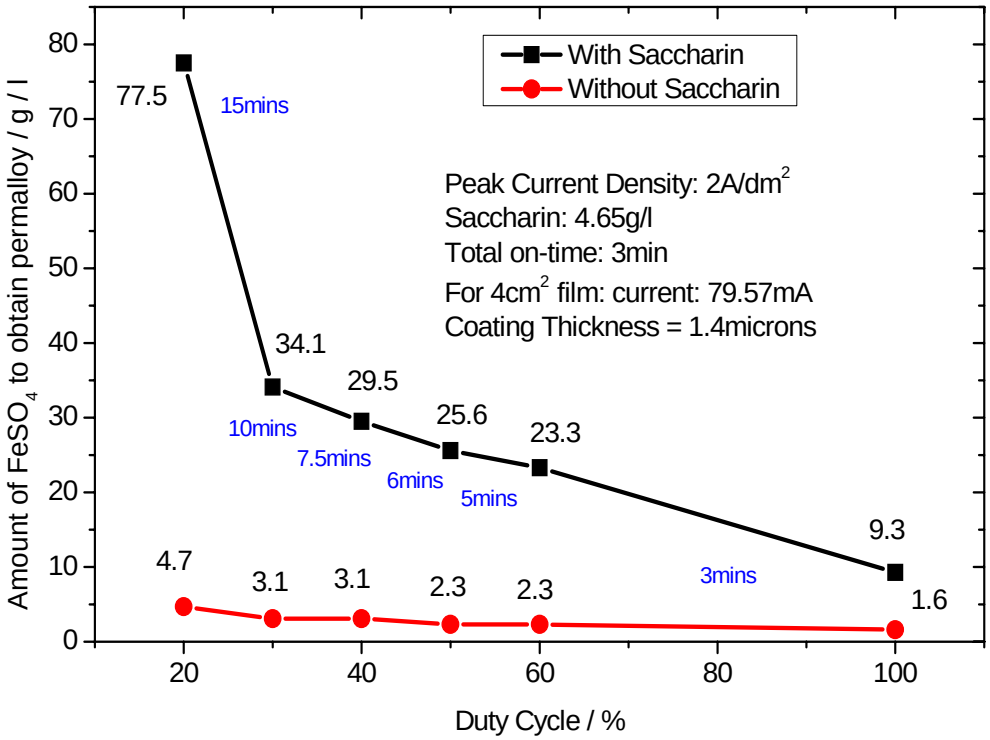

Fig. 86 Plot showing the concentration of required electrolyte concentration and plating time to achieved permalloy composition and 2.5μm thickness

In order to make comparisons between the wire samples for different grain sizes, the relationships of the pulsed current duty cycle and the chemical composition and thickness were investigated and shown in Fig. 84 and Fig. 85 respectively.

The increases in Fe% of the coating layer due to variations in the duty cycle were probably due to the occurring phenomenon: the displacement reactions taking place during the pulse off-time, due to a similarity between the chemical reactivity of both elements:

$$Ni^{2+} + Fe \rightarrow Fe^{2+} + Ni \tag{73}$$

Using the relationships in Fig. 84 and Fig. 85, the electrolyte solution concentration and the plating time was altered to obtain specimens of the same permalloy compositions and (2.5μm) thickness (Fig. 86).

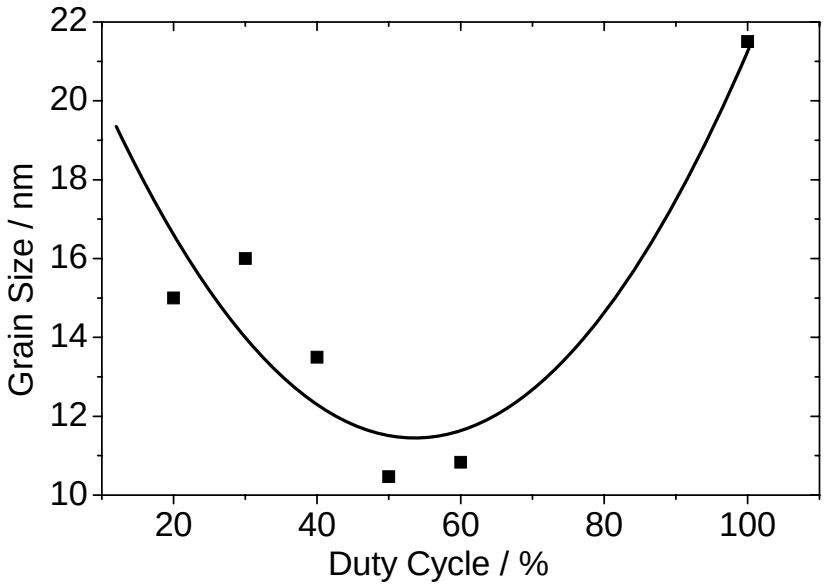

Fig. 87 Variation of grain sizes with pulse plating duty cycle.

Wire specimens were produced using different deposition methods and measured under XRD for their grain size. The results are shown in Fig. 87. It is well known that brighteners, such as saccharin, have the property of grain refinement of the deposits and it is well accepted that additives inhibit surface diffusion of adatoms towards preferential growth centers and increase the density of grain precursors, therefore

promoting nucleation and reducing the grain size. In pulse plating, the grain size of the plated material was found to be dependent on the duty cycle, as shown in Fig. 87. In pulse plating with saccharin, it appears that the optimum value for the duty cycle is at 50% for which the grain size reached the minimum.

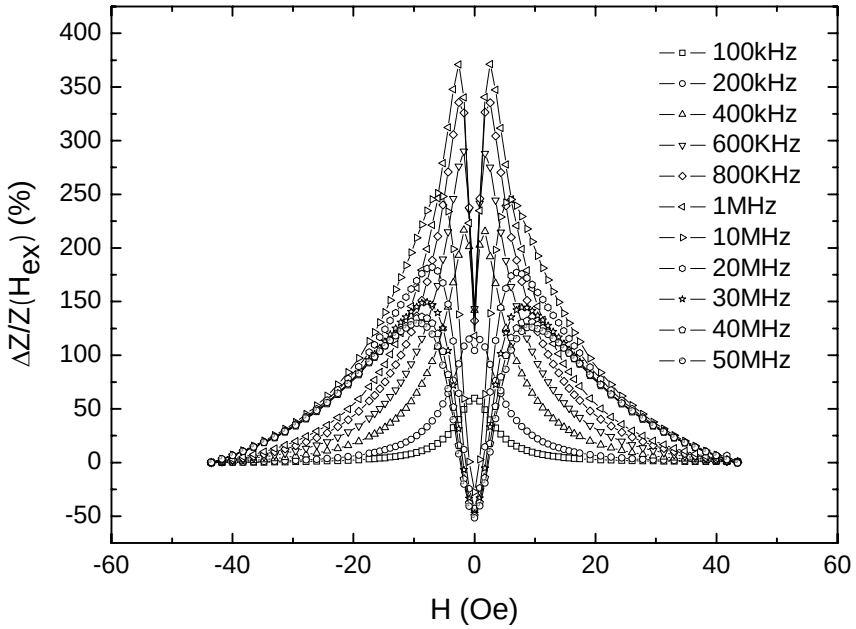

Fig. 88 Typical MI ratio curve of pulse plated composite wires for different testing frequencies.

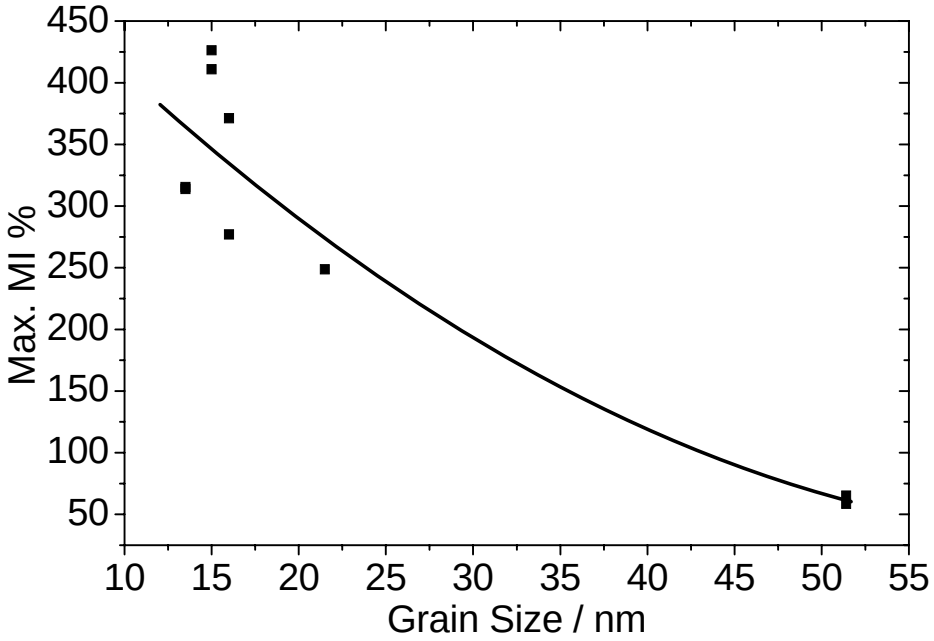

Fig. 89 Variation of the maximum MI ratio with crystalline grain size of the permalloy coating.

The magnetic permeability of the plated materials of different nanocrystalline grain sizes in the composite wires was estimated through the measuring of the MI ratios of the wires. The results are shown in Fig 88 and Fig 89. As shown in Fig 89, the permeability of the permalloy increases as the grains size decreases. This can be explained by the random anisotropy model [101] for small grain size ferromagnetic materials, in which the grain sizes are smaller than the ferromagnetic exchange interaction length L_{ex} = 270 nm for $Ni_{80}Fe_{20}$.

6.4. Comparison of different electrodeposition methods

Fig. 90 a and 90b show the typical SEM pictures of $Ni_{80}Fe_{20}$/Cu composite wire made by DC conventional plating and pulse plating, respectively. It can be observed that the surface from pulse plating is much smoother than that from DC conventional plating, indicating a better uniformity as a result of smaller grain size.

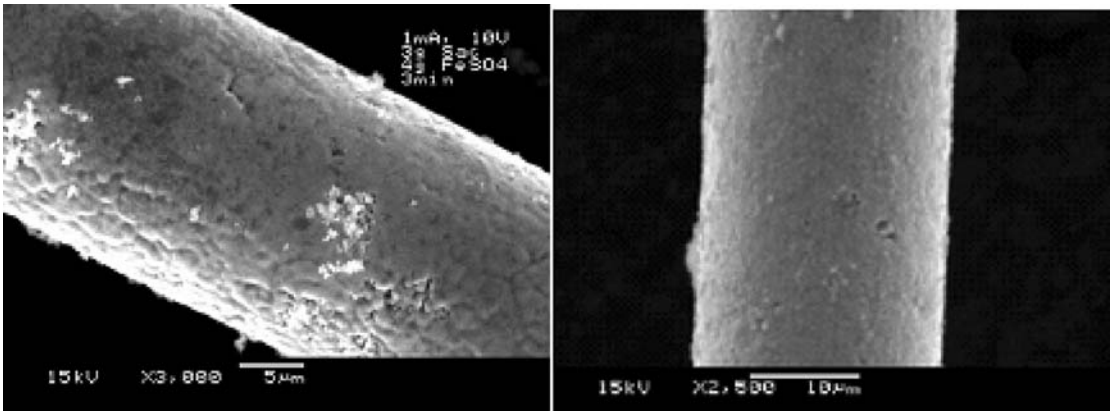

Fig. 90 Typical SEM pictures of the wire samples: (a) from DC plating without saccharin; (b) from pulse plating with saccharin.

Fig. 91 shows the grain size in variation with plating parameters. The grain size was reduced from 52 nm to 15 nm as a result of change from DC plating without saccharin to DC plating with saccharin added. The grain size was further reduced from 15 nm (DC plating with saccharin) to 11 nm by pulse plating with saccharin.

Pulse plating affects the reaction kinetics in two ways. First, the abrupt changes in the applied current density at both the beginning and the end of a pulse cause a change in the state of the electrical double layer. The charge and discharge of the electrical double layer affect the faradic current which governs the rate of plating. Second, the change in the surface concentration of the metal ions influences both the kinetics and the structural aspects of plating system. A decrease in grain size by application of a pulse current has often been reported in the literatures. The pulse current density has an impact on the grain size. The duty cycle of the pulse current affects the material composition.

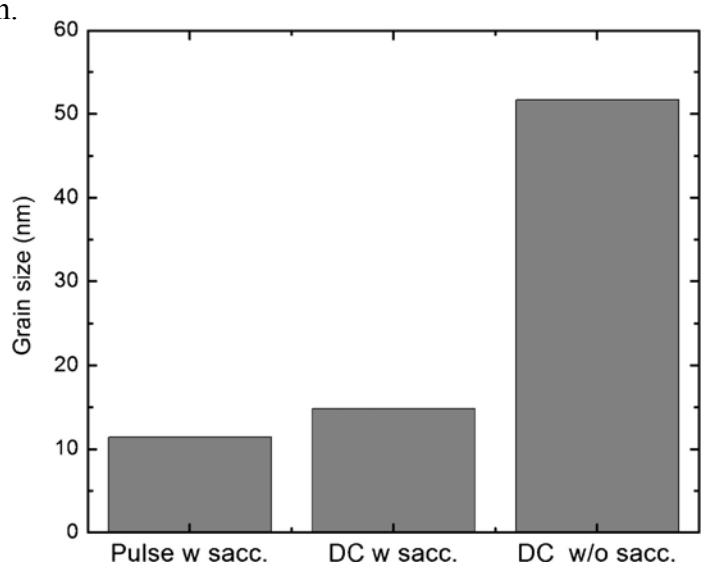

Fig. 91 The grain size in variation with plating method.

Saccharin, being a well-known brightener, is used to refine the grains of the deposits by inhibiting surface diffusion of adatoms towards preferential growth centers and thus promoting nucleation, exists as molecules in the electrolyte solution. When a current passes through the wire, the potential difference setup causes the Fe^{2+} and Ni^{2+} to be moved towards the wire surface. At the same time, the saccharin molecules were also being “pushed” to the wire surface by the moving ions. At the surface, the saccharin molecules inhibit surface diffusion of the adatoms. The subsequent adatoms will join the metal lattice at the voids beneath the saccharin

molecules, pushing the saccharin molecules outwards eventually back into the electrolyte solution. Thus, saccharin acts for refining the grain size in plating.

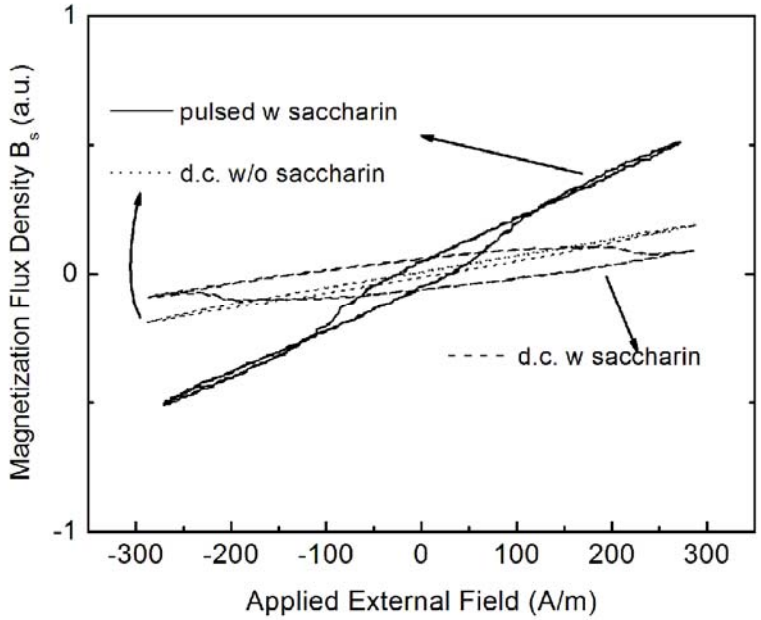

Fig. 92 Hysteresis loops of samples from DC with and without saccharin and pulse plating with saccharin.

The magnetic properties of the plated permalloy were greatly changed as the grain size was reduced. Fig. 92 shows the hysteresis loops of the samples from DC plating with and without saccharin and pulsed plating with saccharin. The coercivity of the plated permalloy decreased rapidly from 250 A/m to 80 A/m as the grain size was reduced from 15 nm to 11 nm, in the same trend as that of Fe-based nanocrystalline materials [23]. The coercivity of samples from DC plating without saccharin could not be measured due to the limitation of the instrument used, which could not reach magnetization saturation within the applied external field of about 400 A/m. The experimental result is in good agreement with the random anisotropy model.

The effect of grain size on the magnetic properties of nanocrystalline permalloy was further investigated by testing the MI effect of the $Ni_{80}Fe_{20}$ /Cu composite wire sample from different plating processes. As shown in Fig. 93, the MI% increased from 65.23% for sample from DC plating without saccharin to 120% for sample from

DC plating with saccharin added. Since for the wires all other conditions were controlled to be the same, it should be the decrease of the grain size that caused the increase in the permeability of the $Ni_{80}Fe_{20}$ and thus the increase in the MI effect ratio.

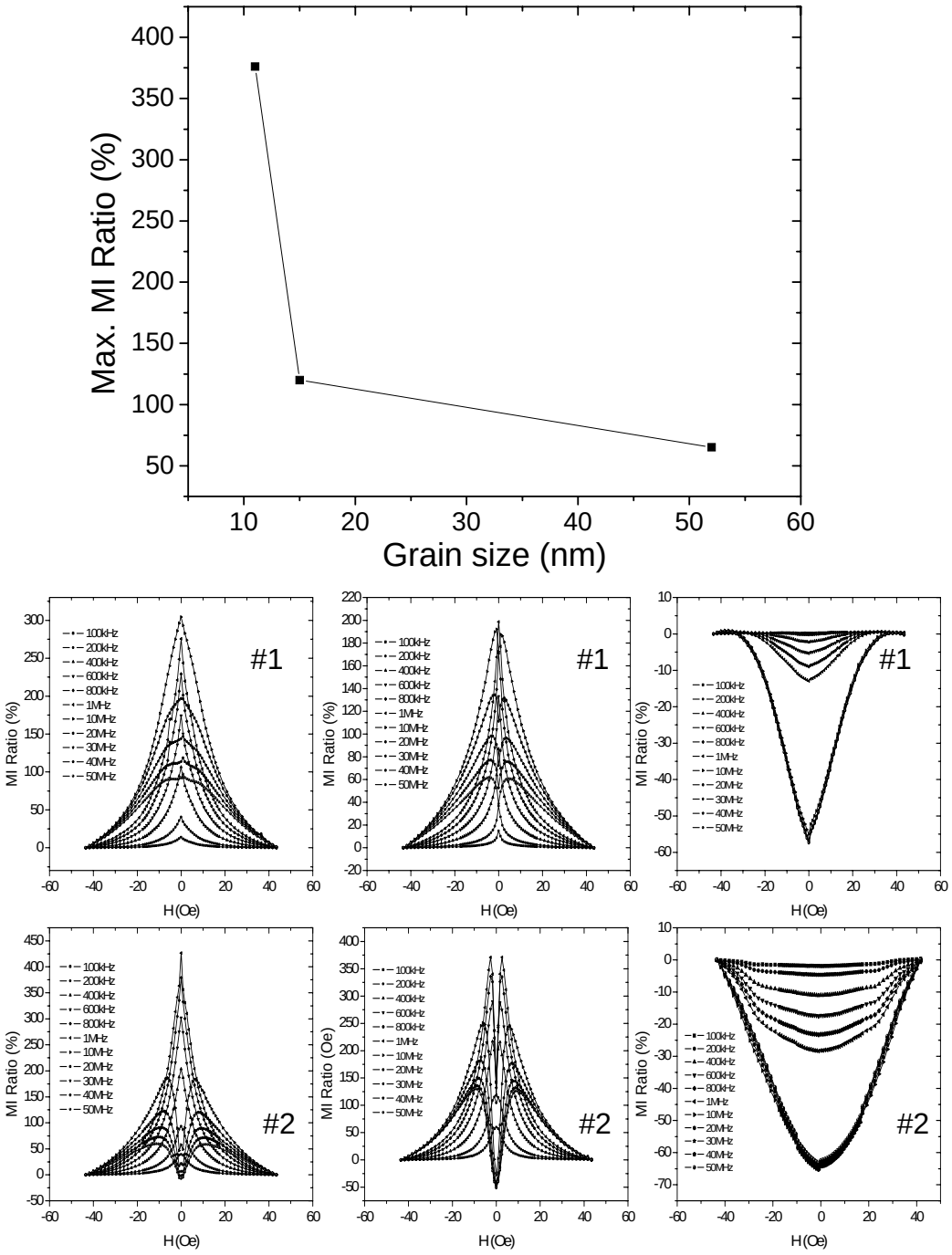

Fig. 93 MI effect ratio varying with the grain size.

As grain size was further decreased from 15 nm (from DC plating with saccharin) to 11 nm (from pulse plating with saccharin), the MI% was further increased significantly to 376%. The MI values were for permalloy as-plated to study the influence of crystal grain size and therefore, could not be the optimum values. For other materials reported in the literature, such as for $Fe_{73.5}Cu_1Nb_3Si_{13.5}B_9$, $Fe_{4.9}Co_{71.8}Nb_{0.8}Si_{7.5}B_{15}$, and $Co_{68.1}Fe_{4.4}Si_{12.5}B_{15}$, the MI ratios were reported to be up to 150% [168], 180% [169], and 300% [169], respectively. However, for these materials there have been no reported results showing the MI ratios in variation with the grain size.

6.5. Effect of PR anodic current on material and magnetic properties

6.5.1. Theoretical analysis on the working current efficiency

According to Faraday's law, the amount of electrochemical reaction that occurs at an electrode is proportional to the quantity of electric charge Q passing through an electrochemical cell. If the weight of a product of electrolysis is w, then Faraday's law states that

$$w = Z \times Q_{tot} \tag{74}$$

where Z is the electrochemical equivalent, the constant of proportionality. Since Q can be written as:

$$Q_{tot} = \int I dt \tag{75}$$

For pulse-reverse electrodeposition (Fig. 94), the electrodeposition current can be given by:

$$\int Idt = N \times \left[\int_{t0}^{t1} I_C dt - \int_{t1}^{t2} I_A dt \right] \tag{76}$$

where N is the number of cycles for the total electrodeposition time, I_c is the magnitude of the positive pulse (cathodic) current and I_A is the magnitude of the negative pulse (anodic) current in the period time of $t_2 - t_0$, where $I_C > I_A$. The total deposited weight of material can then be given by:

$$w = (A_{wt} / n_e F) \times N \times \left[\int_{t0}^{t1} I_C dt - \int_{t1}^{t2} I_A dt \right] \tag{77}$$

where A_{wt} is the atomic weight of metal deposited on the cathode, and n is the number of electrons involved in the deposition reaction and F is the Faraday constant. The volume V of the deposited material can be given as:

$$V = w / d \tag{78}$$

where d is the density of deposited material, $Ni_{80}Fe_{20}$ in this case. The volume V of the deposited material on wires can also be given as:

$$V = (r_a^2 - r_b^2)\pi l \tag{79}$$

where r_b is radius of the inner core, r_a is the total radius of the composite wire, l is the length of the deposited wire. The thickness of the coating layer is given as:

$$t_{FM} = r_a - r_b \tag{80}$$

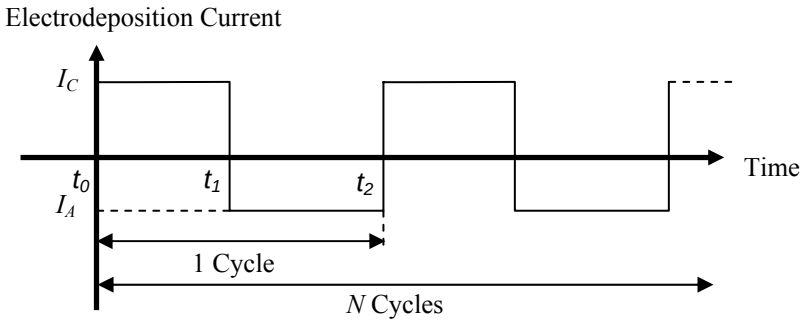

Fig. 94 Schematics representation of pulse-reverse electrodeposition current wavefrom.

Equating Eqn. 79 and Eqn. 80, and Eqn. 81 can be simplified as:

$$t_{FM} = (\sqrt{\frac{w}{d\pi l} + r_b^2}) - r_b \tag{81}$$

Assuming the same current efficiency for both the removal and deposition process, the working current efficiency can be given as:

$$\begin{aligned} \eta_{current} &= \frac{(\int Idt)_{\exp}}{(\int Idt)_{theor}} = \frac{w_{\exp}}{w_{theor}} \\ &= \frac{t_{\exp}(t_{\exp} + 2r_b)}{t_{theor}(t_{theor} + 2r_b)} \end{aligned} \tag{82}$$

where t_{exp} is the experimental thickness of the deposited layer and t_{theor} is the calculated thickness at working current efficiency 100%.

6.5.2. Working current density

In order to obtain an optimum value of the anodic current I_A, the effect of the anodic current on the magnetic properties in terms of magnetoimpedance (MI) effect has to be studied. The compositions of the NiFe layers have to be fixed at the permalloy composition and the thicknesses of the coating layer have to be equal. The effect of I_A on the composition and the thickness of the coating layer were investigated. In an electrolyte solution of fixed concentration, a layer of NiFe was deposited onto copper wires by pulse-reverse electrodeposition with varying anodic current I_A, ranging from 0.1 - 0.9 mA, for the same electrodeposition time of 6 min.

Fig. 95 (a) shows the effect of the anodic current I_A on the Fe% of the coating layer. This decreasing trend of Fe% against I_A could be due to decreasing in the thickness [66] as investigations revealed that the Fe% remains unchanged if the thickness is controlled to be unchanged by the manipulation of the electrodeposition time. Fig. 95 (b) displays the trend of coating thickness with anodic current I_A. The

coating thickness decreased with increasing I_A as the amount of materials removed during each plating cycle was increased. The dotted line in Fig. 95a displays the calculated values of the coating thickness at the working current efficiency of 100%, using Faraday's law of electrolysis. The pulse-reverse electrodeposition system was found to have high working current efficiency and it was calculated to be about 87%.

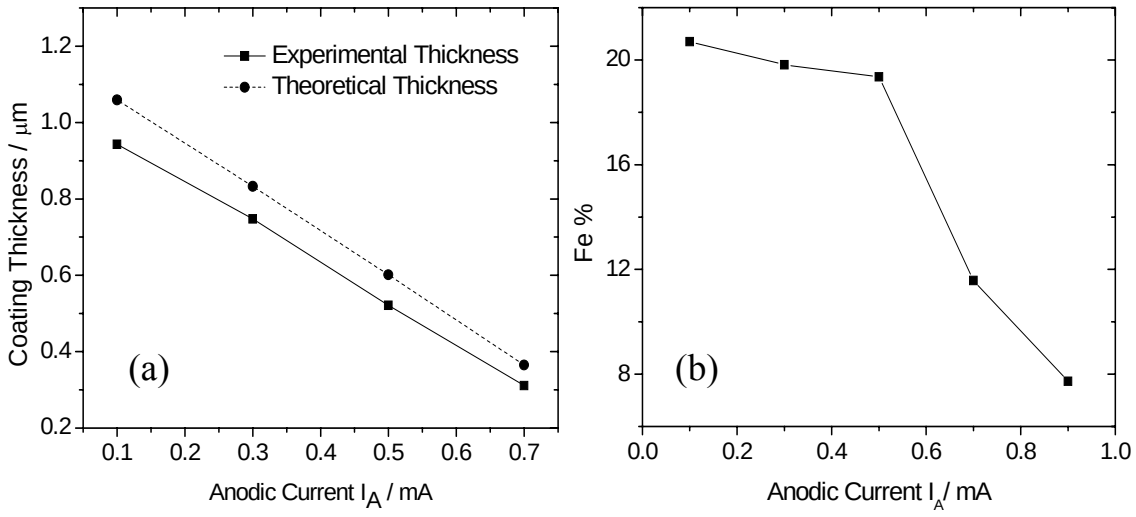

Fig. 95 Effect of anodic current I_A on the (a) Fe% (b) coating thickness.

6.5.3. Grain size enlargement effect

Fig. 96 displays the effect of I_A on the average grain size of the $Ni_{80}Fe_{20}$ deposited layer. The average grain sizes increases from 11 nm to 23.8 nm when I_A was increased from 0.1 mA to 0.9 mA. In the case of a direct current, the saccharin molecules are "pushed" to the wire surface by the moving ions upon the imposition of a current. At the surface, the saccharin molecules inhibit surface diffusion of the adatoms. The subsequent adatoms will join the metal lattice at the voids beneath the saccharin molecules, pushing the saccharin molecules eventually back into the electrolyte solution. Hence, the addition of saccharin in the electrolyte solution reduces the average grain sizes of the deposits. For pulse electrodeposition (I_A = 0), inhibiting

species are absorbed onto the surface to inhibit grain growth during the off-time. However, when $|I_A| > 0$ and as I_A increases, less saccharin molecules will be present at the wire surface during the electrodeposition process due to the alternating plating current to inhibit surface diffusion of adatoms. This results in the average grain sizes increasing with increasing I_A, which may be considered as a side effect of pulse-reverse electrodeposition.

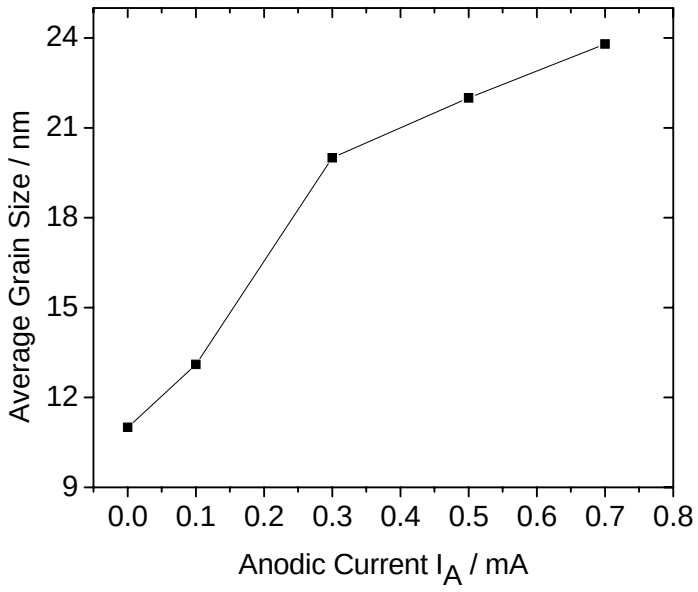

Fig. 96 Effect of anodic current I_A on the average grain size of the $Ni_{80}Fe_{20}$ layer.

6.6. Effect of PR anodic current on magnetic properties

The MI effect graphs of the specimens wires obtained for I_A = 0.1, 0.3, 0.5, 0.7 mA are presented in Fig. 97. All the MI effect curves displayed double-peaks phenomenon at high testing frequencies, strongly suggesting anisotropies of the specimens to be closer to the circumferential direction. It was also observed that the anisotropic field H_k increased as the anodic current I_A was increased, most probably due to the induced magnetic field generated by the anodic current. As shown in Fig. 98(a), the peak MI% ratio was observed to increase as the anodic current I_A decreased. The MI effect is mainly affected by the geometry as well as the magnetic permeability of the specimen.

In this case, since the thickness of the studied specimen wires was fixed constant at 1.35 μm through the manipulation of the electrodeposition time, therefore the observed effect could be inferred to be mainly due to permeability changes.

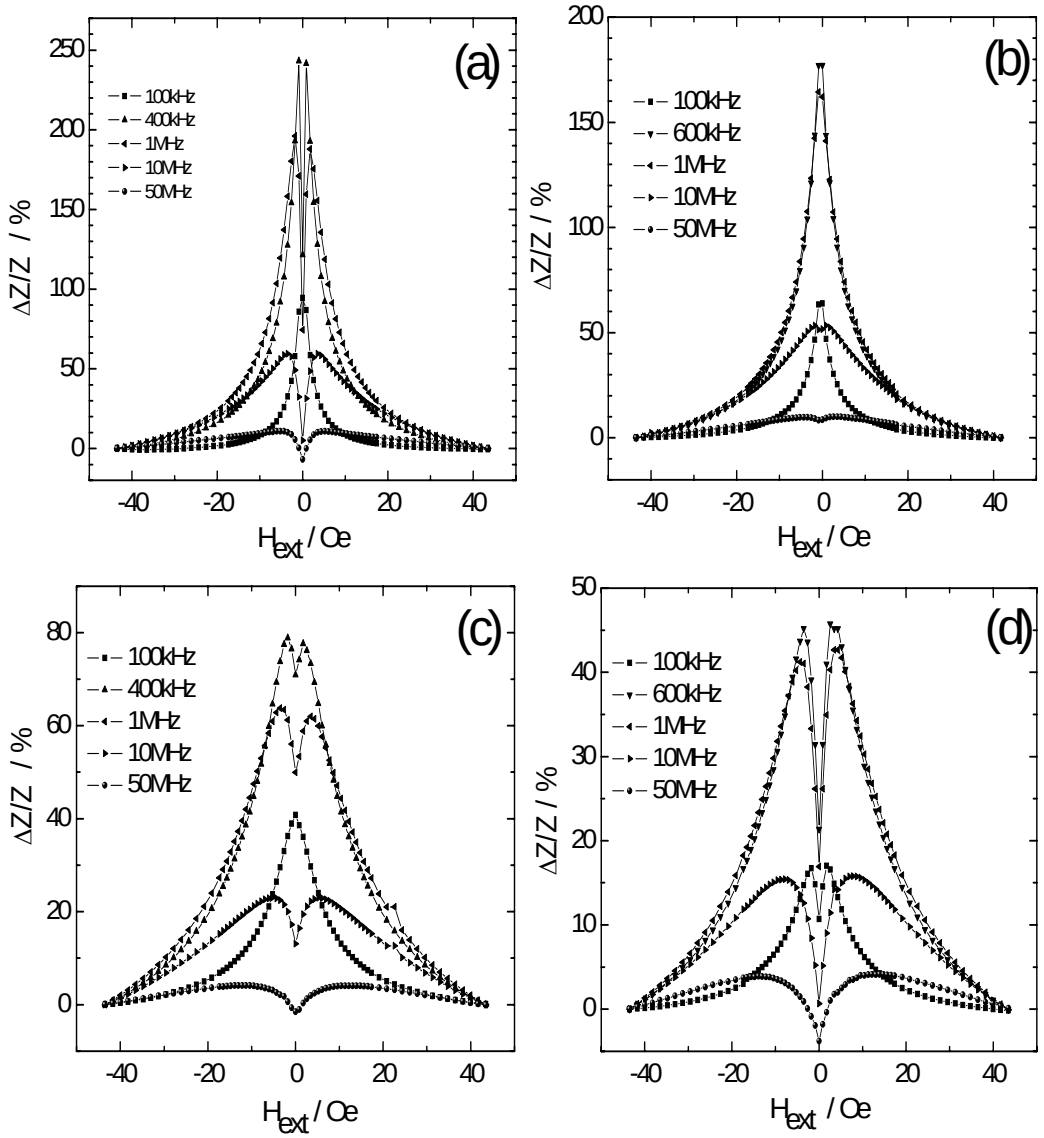

Fig. 97 MI effect curves for pulse-reverse electrodeposited specimens: (a) I_A = 0.1mA; (b) I_A = 0.3mA; (c) I_A = 0.5mA; (d) I_A = 0.7mA; at constant coating thicknesses 1.35 μm.

This change in permeability can be further confirmed, as shown in Fig. 98 (b), which displays the effect of I_A on coercivity. The coercivities of the specimens decreased as the magnitude of I_A decreased, illustrating the relatively reciprocal relation of

coercivity and permeability. This strongly indicates that increasing the anodic current greatly deteriorates the permeability of the magnetic layer.

Fig. 99 compares the hysteresis loops and coercivities of the samples at I_A = 0.1 mA and 0.7 mA. At I_A = 0.1 mA, the coercivity was 0.13 Oe and at I_A = 0.7mA, the coercivity was 1.54 Oe, showing a significant difference.

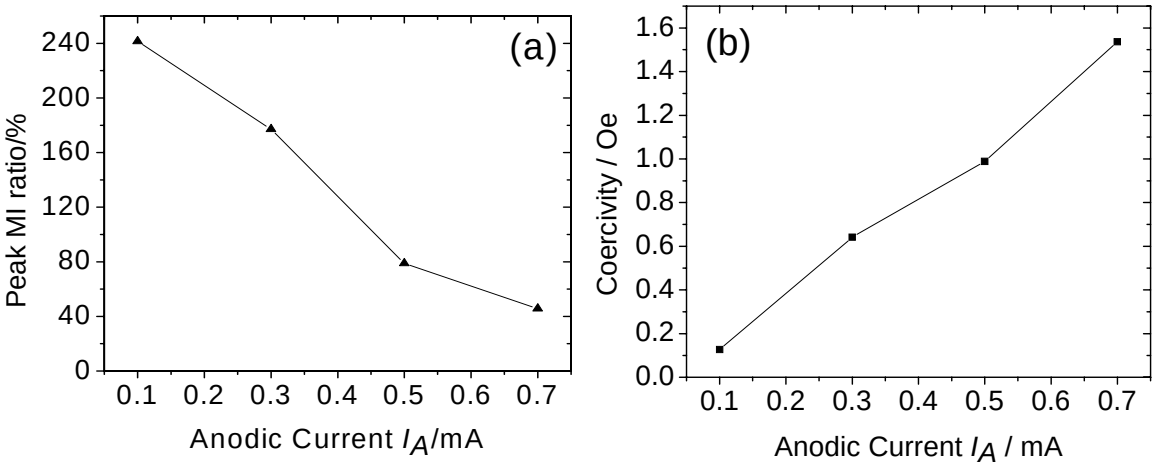

Fig. 98 Effect of anodic current I_A on: (a) peak MI ratio%, (b) coercivity

The observed relationship between the magnetic properties and the magnitude of I_A could be attributed to the effects of I_A on the surface smoothness and average nanocrystalline grain sizes of the deposited material. The SEM photos of the plated specimens of constant thickness are shown in Fig. 100, strongly suggesting that excessive I_A does not bring about smoother plated surface. The surface smoothness increases as I_A decreases. During the application of the anodic current, the specimen surface becomes the anode, repelling the Fe^{2+} and Ni^{2+} cations towards the cathode. Dissolution takes place and results in the deposited NiFe dissolving back into the electrolyte solution in their initial ionic states. Uneven plated protruding peaks, which are formed due to high local deposition rate at these regions, are dissolved first as their reverse dissolution rate is high. Increasing the magnitude of the I_A increases the amount of dissolution and there is an optimum I_A beyond which dissolution is no longer limited to the removal of protruding peaks, but the resulted leveled deposit layer.

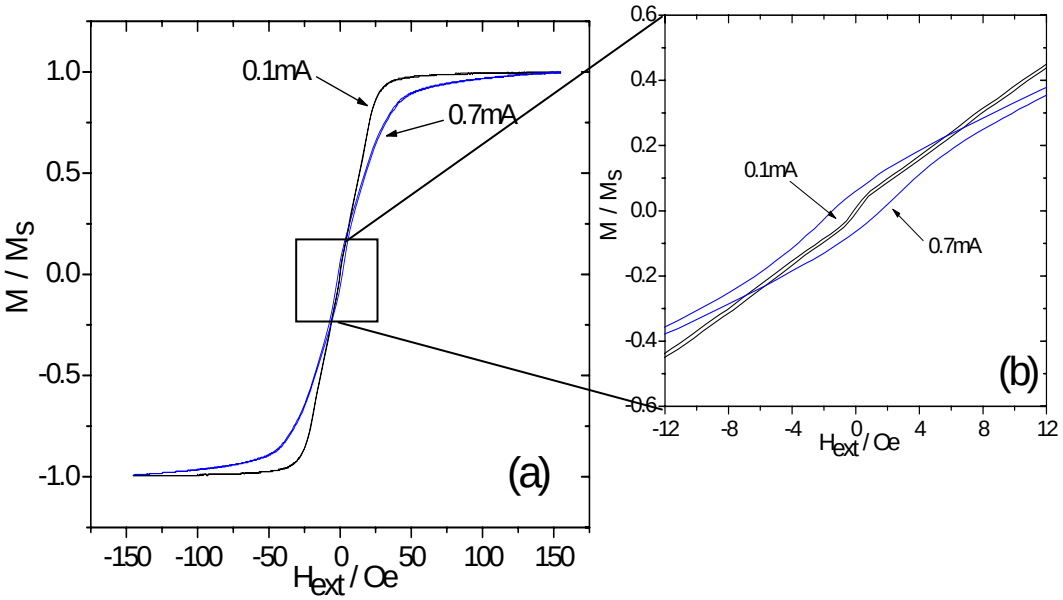

Fig. 99 (a) Hysteresis loops of specimens, comparing I_A = 0.1mA and 0.7mA; (b) Close-up of the hysteresis loops

According to RAM [101], smaller nano-range grain size results in smaller coercivity and higher permeability when the grain size is below the critical exchange length L_{ex}. For $Ni_{80}Fe_{20}$, the exchange interaction length L_{ex} is about 270 nm. Even if the internal stress is considered, the estimated interaction length is still in the region of 100 nm. For the nanocrystalline permalloy tested in the present study, the grain sizes were all below 270 nm, therefore, the coercivity decreased as the grain size decreased. The trend (as shown in Fig. 96) for the increasing average grain size with increasing anodic current, which resulted in degrading magnetic properties, is in agreement with RAM, suggesting that anodic current has an effect on grain size manipulation.

With increasing I_A, grain size increases while peak MI ratio decreases, resulting in a degrading trend in magnetic softness. During application of the cathodic current, Ni^{2+} and Fe^{2+} ions are attracted towards the specimen's surface (cathode) and become deposited. This pushes the larger saccharin molecules to the surface and blocks part of the surface for the metal ions to be deposited. As a result, surface diffusion of adatoms towards preferential growth centers is inhibited and thus promotes

nucleations. Subsequent addition of these adatoms joins deposited crystalline lattice at the voids beneath the saccharin molecules, which eventually push the saccharin molecules back into the electrolyte solution. On the contrary, during the application of I_A, Ni^{2+} and Fe^{2+} ions near the surface (anode) are repelled away, at the same time dragging the larger saccharin molecules along. As I_A increases, Ni^{2+} and Fe^{2+} ions drift further away from the wire surface during application of I_A, bombarding and dragging the saccharin molecules further away from the wire surface as well. Saccharin molecules act as surface inhibitors that prevent surface diffusion of adatoms by lowering surface diffusion rate. Hence, as less saccharin molecules are present at the surface, crystallization in terms of grain growth is promoted instead of grain nucleation.

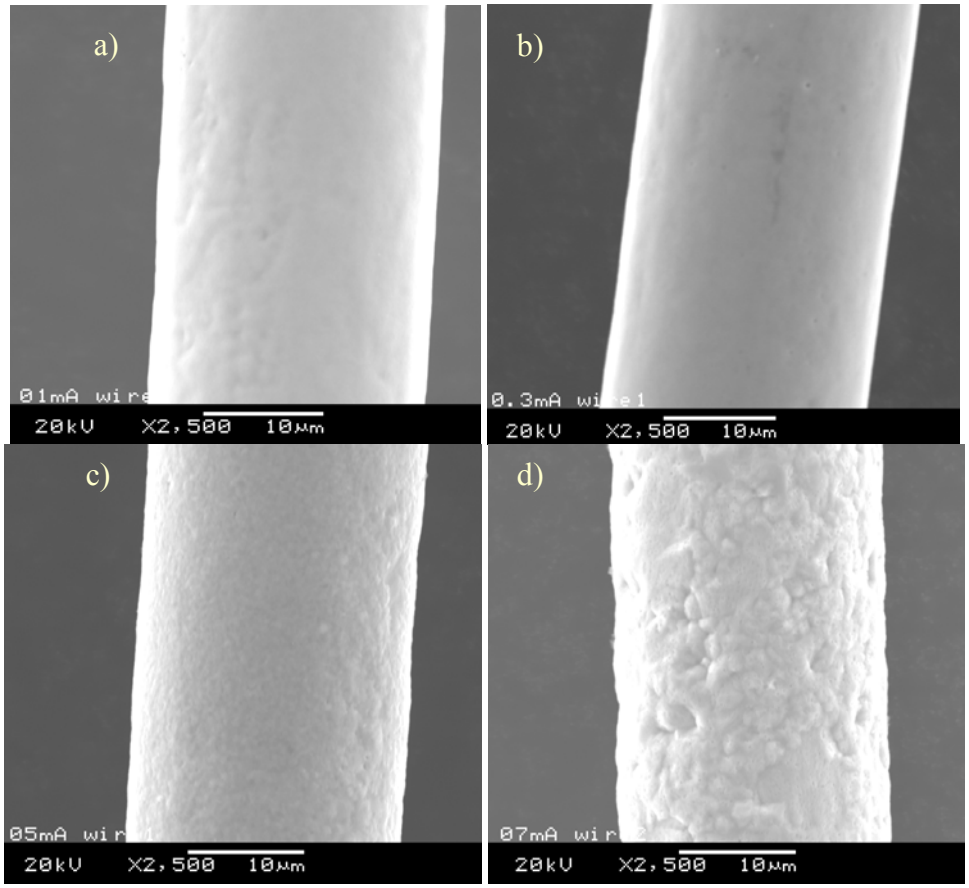

Fig. 100 SEM photos of specimens with: (a) I_A = 0.1 mA, (b) I_A = 0.3 mA, (c) I_A = 0.5 mA, (d) I_A = 0.7 mA.

The pulse-reverse deposited composite wires were then compared with those from direct current electrodeposition and pulse electrodeposition, with similar thickness and composition of the deposited layer. The MI% values were 168%, 39% and 159% for pulse reverse, DC and pulse eletrodeposited samples. Pulse-reverse electrodeposited wires possess the highest peak MI%, followed by those from pulse electrodeposition and direct current electrodeposition. Pulse electrodeposited wires had the smallest average grain size of 11 nm, followed by direct current electrodeposited wires and pulse-reverse electrodeposited wires.

Although the average grain sizes of the pulse-reverse electrodeposited wires are the largest, the uniformity of the specimens across the entire length of the wires, in terms of composition and thickness, has been the best. EDX measurements had been taken across the entire length of the wires and the composition and thickness readings have been found to be more uniform as compared to specimens from the other two methods. The high MI% ratio could be due to high uniformity of the pulse-reverse electrodeposited specimens. The results indicate that the more dominant factor affecting the magnetic properties of the specimens is the uniformity of the deposited layer, rather than the grain size of the deposited material.

6.7. Comparison of PR method on other methods in terms of materials and magnetic properties

Fig. 101 shows the XRD patterns of the samples $Ni_{80}Fe_{20}$/Cu electrodeposited under different current waveforms. It should be noted that the manipulation of the concentration of the Ni^{2+}/Fe^{2+} ions in the electrolyte were carried out in order to obtain 80:20 for the Ni:Fe composition. As shown in Fig. 101, there was no phase change and an *fcc* phase can be observed in both the $Ni_{80}Fe_{20}$ and Cu layers of all the

samples.

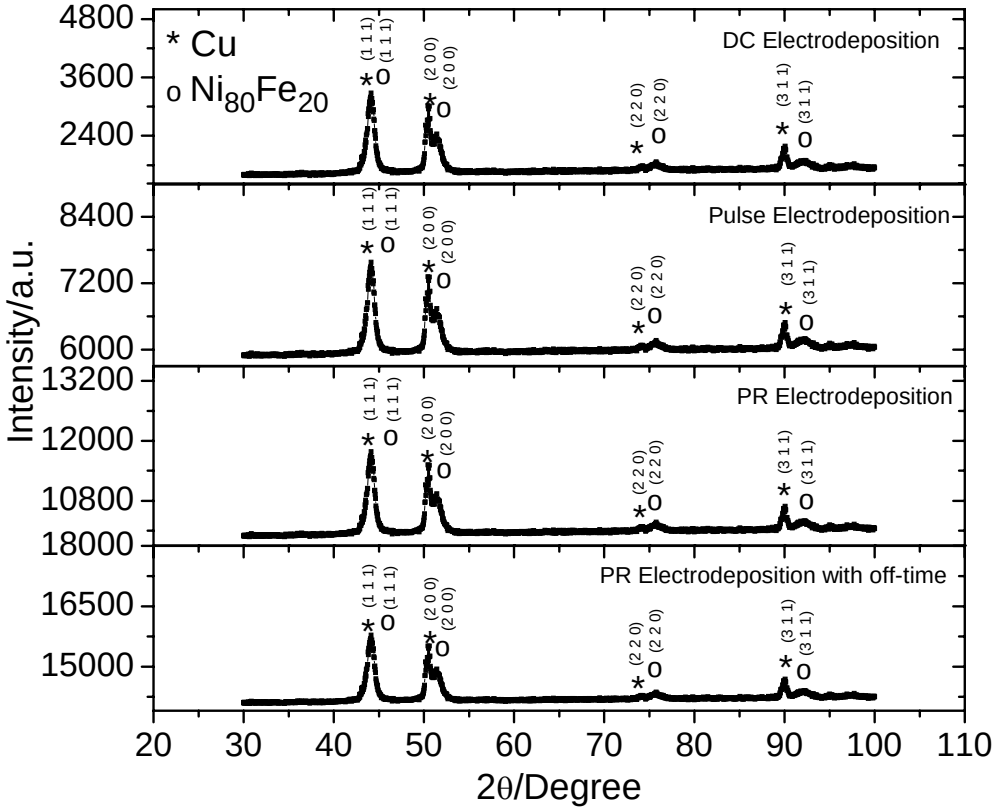

Fig. 101 XRD data obtained for electrodeposited $Ni_{80}Fe_{20}$/Cu specimens from different methods.

Fig. 102 shows the average crystallite sizes of specimens from the 4 different electrodeposition methods. As given Fig. 102, specimens from DC electrodeposition, whereby a static electropotential difference is kept between the electrodes throughout the electrodeposition process, yielded an average crystallite size of 16 nm. Specimens produced using pulse electrodeposition (I_A = 0), whereby the electropotential field generated is more dynamic, yielded a lower average crystallite size of 15 nm. Pulse electrodeposited specimens have lower average crystallite size than that of DC electrodeposition due to the presence of the off-time interval. During the off-time period in each plating cycle, blocking of growth centers of the cathode most probably occurred, as a result of adsorption of inhibiting species. Saccharin, which is a type of inhibiting species, is viewed as dirt that interfere the reaction sites, either by creating

disorder in the incorporation of adatoms into the lattice by being adsorbed on active sites or inhibiting surface diffusion of adatoms towards growing centres. The governing reason is not in terms of chemical reactions, but the mere physical ability of saccharin to be attached on the electrode surface and its relative size to block out the active sites, decreasing the rate of electrode reactions. This promotes nucleation at the start of each new pulse cycle.

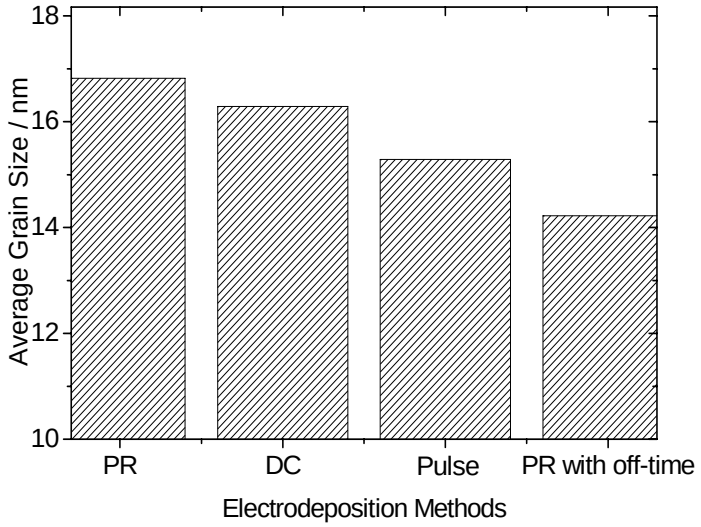

Fig. 102 Average crystallite size of specimens from different electrodeposition methods.

Specimens from PR electrodeposition, which also involves a dynamic electropotential field, were found to possess the largest crystallite sizes of about 17nm. When $I_A > 0$ and as I_A increases, less saccharin molecules will be present at the wire surface during the electrodeposition process to inhibit surface diffusion of adatoms. This is due to the influence of I_A on the ion movements of Fe^{2+} and Ni^{2+}. The application of I_A resulted in the dissolution of deposited NiFe off the specimen's surface and the drifting of the cations away from the specimen's surface. Such ion movements bombard and drag the larger saccharin molecules along their motion path, resulting in a decrease in saccharin population at the surface and hence the promotion

of crystallite growth instead of crystallite nucleation, which are 2 competing crystallite crystallization mechanisms.

Despite the largest crystallite size produced, the leveling of the deposited layer as a result of selective dissolution of surface peaks formed from the uneven distribution of cathodic current due to uneven initial surface profile or surface defects present, contributed to uniformity of the deposited layer. Hence, good quality of magnetic properties can be possibly produced. It was also clearly evident from Fig. 102 that with the introduction of an off-time period in each electroplating cycle in the PR electrodeposition current waveform, the resulting average crystallite sizes of the specimens decreased from 17 nm to 14nm. The off-time interval in PR electrodeposition is believed to have the same function and effect as that present in pulse electrodeposition, by refining the grains of the layer of leveled coated surface after the application of I_A, and before the deposition of the next layer of the magnetic material. It must be noted that the effect of electrodeposition methods on average grain size was not obvious and significant as the coating thickness was at 0.9 μm and not large. Thus, the trend of grain size with electrodeposition methods will be more distinct when the coating thickness is increased.

As an indirect indication of the effect of different deposition methods on the grain size of deposited layer, especially in the PR electrodeposition with and without off-time, the magnetic properties of the deposited layer, in terms of the magneto-impedance (MI) effect of the deposited wire samples, were examined. Fig. 103 shows the magneto-impedance (MI) effect of the specimens from PR electrodeposition with and without off-time. The peak MI% was observed to increase by over 15% for the specimen from PR electrodeposition with off-time than the specimen from the process

without off-time. This could be attributed to the grain size reduction from 17 nm to 14 nm due to the introduction of off-time in the PR electrodeposition.

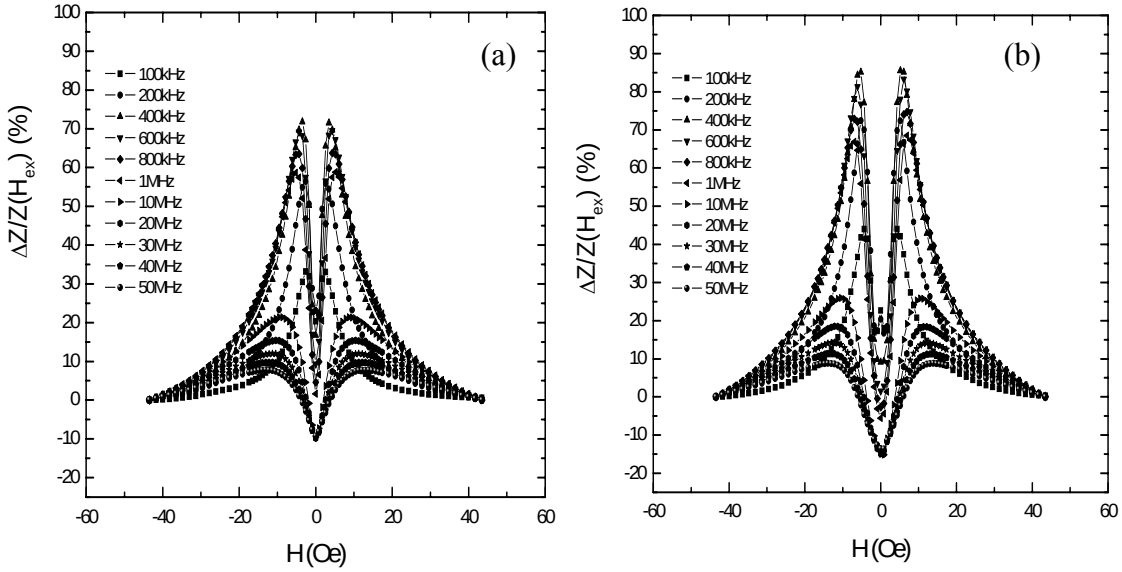

Fig. 103 MI effect curves of the specimens with the deposited thickness at about 0.9μm from pulse-reverse Electrodeposition, (a) without off-time; (b) with off-time.

6.8. Summary

Grain size manipulation was successfully carried out by altering the plating current waveform, i.e. DC plating, pulse plating and pulse reverse plating, and also by varying the various process parameters.

1) The upper and lower limits of the nanocrystalline grain size are theoretically estimated to be between 270 nm and 10 nm separately. Within this range, grain size reduction will benefit greatly magnetic properties.
2) The relationship of the pulse plating parameter duty cycle was investigated in relation to the composition, thickness and the grain size of the coating layer. At duty cycle 50%, the grain size was found to be the smallest.
3) Nanocrystalline permalloy of grain sizes ranging from 52 nm to 11 nm was developed, with the grain size controlled by using different electroplating methods—DC plating without saccharin added, DC plating with saccharin added,

or pulse plating with saccharin added. The coercivity of nanocrystalline permalloy decreases rapidly as grain size decreases in the range of 52 nm to 11 nm, which is consistent with the trend of nanocrystalline Fe-based materials in variation the grain size, and can be explained by the random anisotropy model. The MI effect ratio increases greatly as the grain size of permalloy in the $Ni_{80}Fe_{20}$/Cu composite wire was reduced in the range from 52 nm to 11 nm.

4) Pulse-reverse (PR) electrodeposited $Ni_{80}Fe_{20}$/Cu composite wires have been developed to investigate the key characteristics of pulse-reverse electrodeposited permalloy, namely the current working efficiency, anodic current, grain size variation and the resulting magnetic properties and MI effect. The theoretical calculations and experimental results showed that the working current efficiency of the PR electrodeposition for permalloy is high, up to 87% in the present case studied. With the introduction of an anodic current, the deposited permalloy was found to be better in uniformity, which resulted in higher peak MI% ratio of the deposited $Ni_{80}Fe_{20}$/Cu composite wires, despite the associated side effect in enlarging grain size. It has also been found from this study that the magnetic properties of PR electrodeposited NiFe/Cu composite wires vary significantly with magnitude of anodic current. Within the tested range of the present study, smaller amplitude of anodic current resulted in lower coercivity of deposited material and higher MI effect of the NiFe composite wires. Such a relationship could be due to the nanocrystalline grain size and uniformity of the deposited NiFe in relation to the anodic current magnitude in pulse reverse electrodeposition, in which, smaller anodic current magnitude resulted in smaller average grain size and better uniformity.

5) $Ni_{80}Fe_{20}$/Cu composite wires of a variety of nanocrystalline crystallite sizes have been developed using 4 different electrodeposition methods. The difference in electrodeposition methods lies in plating current waveforms: DC, pulse electrodeposition, PR electrodeposition and PR electrodeposition with off-time. When applied, different electropotential field patterns were created across the electrodes, resulting in different movements of Fe^{2+} and Ni^{2+} ions, and hence the movements and population of crystallite refiner, saccharin molecules, on the specimen surface. Therefore, the manipulation of the competing crystallization mechanisms: crystallite growth and nucleation, to control the nanocrystalline crystallite sizes of coated $Ni_{80}Fe_{20}$. Other than the influence over the crystallite size produced, I_A also has the effect of producing more uniform coated layer through leveling of surface peaks found on the deposited layer as a result of uneven deposition. Introducing an off-time period to the PR electrodeposition current waveform was found to reduce the average crystallite sizes of the resulting deposited material, a similar effect observed in the off-time present in pulse electrodeposition. The comparison of the resultant crystallite size was made and the order was observed to be (in descending crystallite size): PR with off-time electrodeposition, pulse electrodeposition, DC electrodeposition and PR electrodeposition. The magneto-impedance (MI) effect of the specimens produced by pulse-reverse electrodeposition with off-time was higher than those produced by PR electrodeposition without off-time, due to the grain size reduction caused by the off-time.

Chapter 7 Magnetically Controlled Electroplating of NiFe/Cu Composite Wires

The NiFe/Cu composite wire specimens were produced by electroplating $Ni_{80}Fe_{20}$ on a Cu wire of 20 μm in diameter and with and without the imposed longitudinal magnetic field. The current density J was maintained constant at 2 A/dm^2.

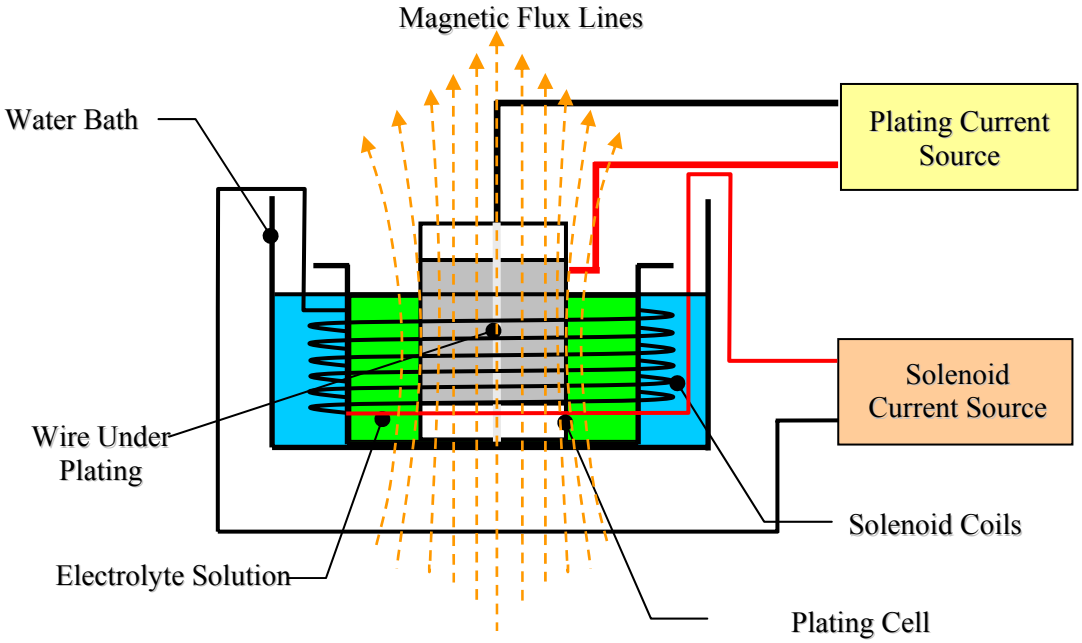

Fig. 104 Schematic diagram of the magnetic controlled electroplating set-up.

The external magnetic field applied in the electroplating process was produced by a current driven solenoid, which was formed by 0.8mm diameter copper wires coiling around the beaker holding filled with the electrolyte solution and the plating cell (Fig. 104). A current was passed though the solenoid to generate a longitudinal magnetic field around the wire under electroplating. The magnitude of the current was varied from 0A, 0.5A, 1.5A, 2.0A, 2.5A to obtain a range of the magnetic controlling field

strength up to 400 Oe. The plating cell was carefully positioned such that it was at the centre of the solenoid.

The solenoid coil generates an external magnetic field when a DC current is passed through it and the magnetic flux is longitudinal at the centre of the plating cell and parallel to the wire under deposition. The maximum magnetic field strength H at any point along the centre of the solenoid in the field (Fig. 104) can be approximated by

$$H = \frac{n_t Ib}{2}\left(\cos\theta_2 - \cos\theta_1\right)a_z \tag{83}$$

where n_t is the turn density, i.e. $n_t = N / L$ (number of turns divided by the length of the solenoid), I is the magnitude of the current flowing through the solenoid and b is the number of layers and

$$\cos\theta_2 = \frac{l - z}{\sqrt{l^2 + r^2}}\ ,\ \cos\theta_1 = \frac{z}{\sqrt{z^2 + r^2}} \tag{84}$$

where l is the length of the solenoid and r is the radius of the solenoid.

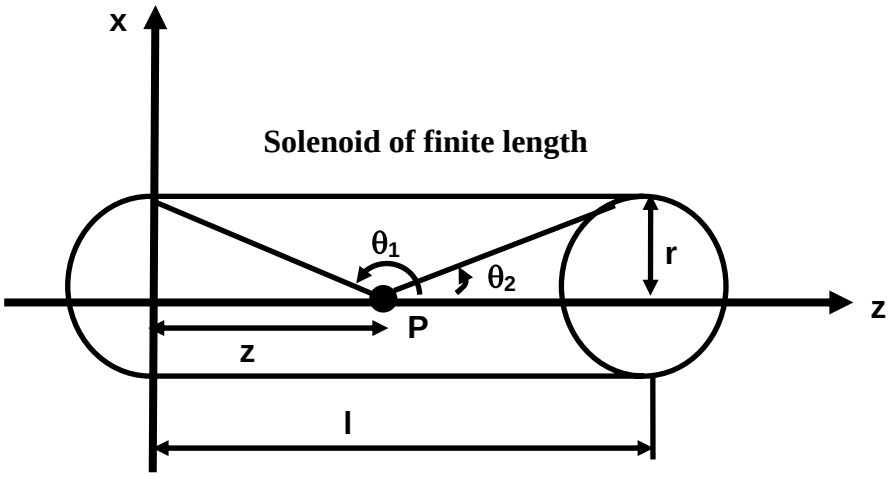

Fig. 105. Magnetic field strength calculation schematics.

7.1. Effect of longitudinal magnetic field on material properties

The compositions of the $Ni_{80}Fe_{20}$ layers plated under different controlling longitudinal magnetic fields and plating times were measured by EDX. It was found that the composition does not vary with the magnetic field. This can be seen from Fig. 106, in which at the same plating time of 3 minutes the variations of Fe percentage of the plated material against the magnetic controlling field remained almost constant as the magnetic controlling field was increased from 0 to 450 Oe. The slight fluctuations in the composition were most probably due to some other unknown factors that affected the electroplating process as well as measurement errors.

Fig. 106 also shows that the variation of the Fe percentage in the material deposited by magnetic controlled plating was much smaller compared to that from plating without magnetic controlling field.

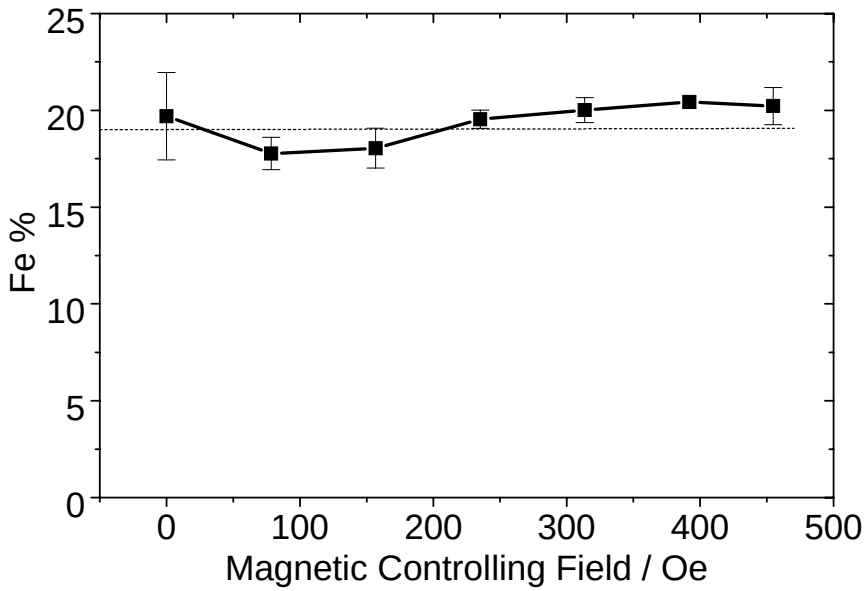

Fig. 106 Variation of Fe percentage against magnetic controlling field at the equal plating time of 3 minutes.

The results show that the controlling longitudinal magnetic field has no significant effect on the plated layer thickness. The slight fluctuation of plated layer thickness in Fig. 108a when the magnetic field was varied from 0 to 450 Oe should be due to

measurement errors or other unknown factors. The lack of correlation between thickness and the applied magnetic field can be explained by the analysis on the Lorentz forces acting on the Ni^{2+} and Fe^{2+} ions near the electrode surface under a combination of electrical and magnetic fields:

$$\vec{F} = q\vec{E} + q\vec{v} \times \vec{B}_l + q\vec{v} \times \vec{B}_c \tag{85}$$

where q is the electrical charge, $\vec{v}$ is its velocity, $\vec{E}$ is the electrical field, $\vec{B}_l$ and $\vec{B}_c$ are the imposed longitudinal field and the circumferential magnetic field induced by the plating current (Fig. 107). The vector directions of the two latter terms are perpendicular to the direction of motion of the ions; and will not change the magnitude of the velocity. Hence the plating rate is not affected by the longitudinal magnetic controlling field.

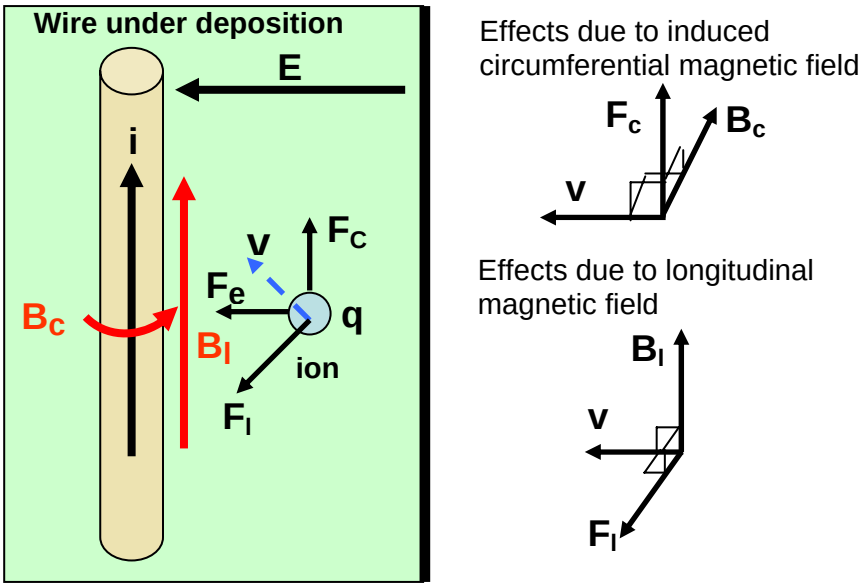

Fig. 107 Force diagram on an ion in magnetic controlled electrodeposition.

Under the influence of the controlling magnetic field in electroplating, the plated layers were more uniform and more regularly packed with smaller crystal sizes. The plated surface was found to be smoother, compared to plating without the controlling

magnetic field, as shown in Fig 109. These can be explained by mass transfer effects in the deposition of Ni^{2+} and Fe^{2+} ions where the imposed longitudinal magnetic field aligns the magnetic moment of the Ni^{2+} and Fe^{2+} ions, resulting in preferred NiFe growth orientation and microstructure uniformity.

(a)

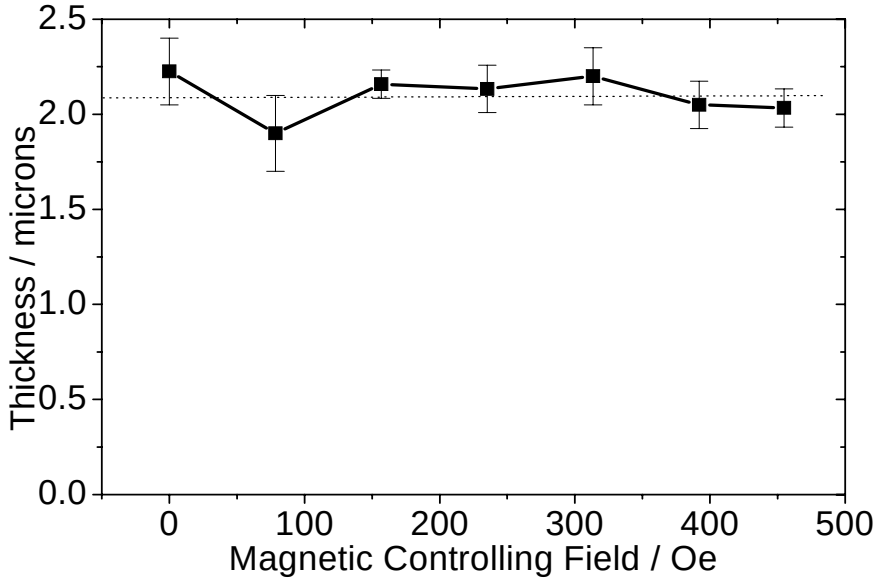

(b)

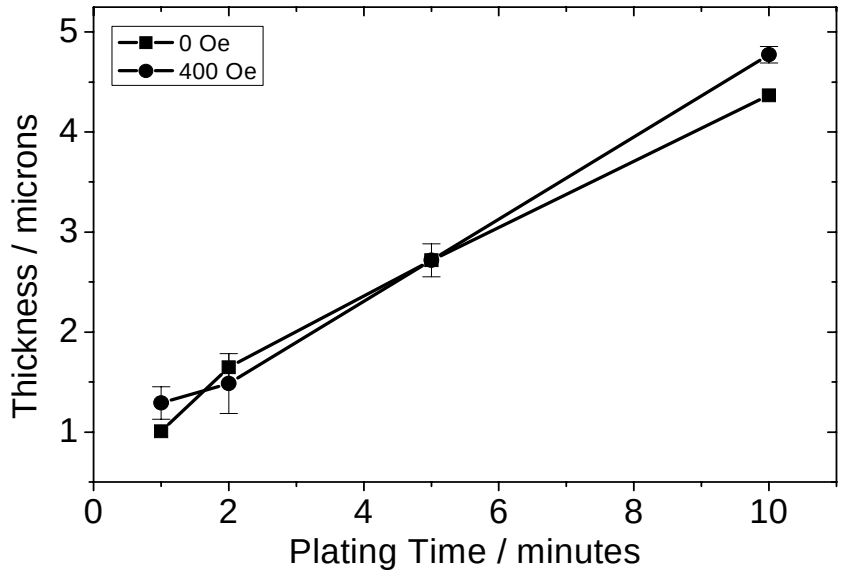

Fig. 108 (a) Plated layer thickness varying against the magnetic controlling field at plating time 3min.; (b) Plated layer thickness varying against the plating time at magnetic controlling field strength of 400Oe.

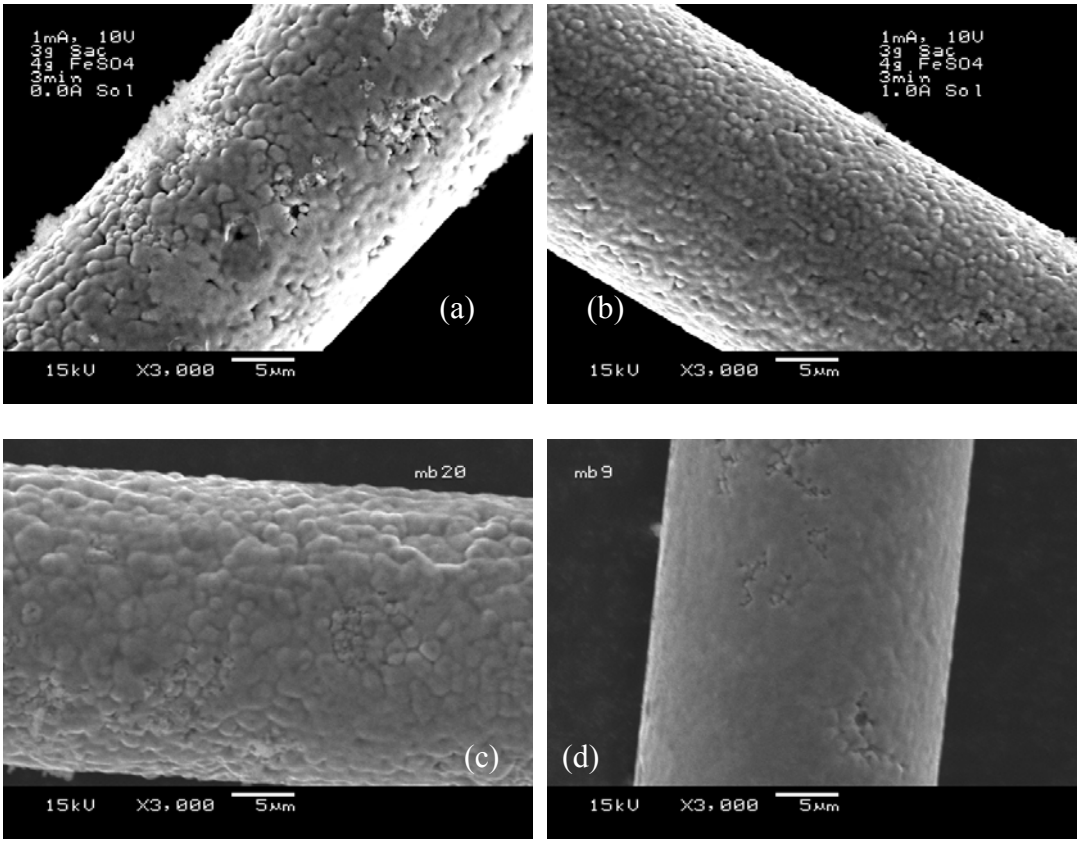

Fig. 109 SEM views for (a) the wire plated for 3 minutes without magnetic controlling field; (b) the wire plated for 3 minutes with a magnetic controlling field of 157Oe; (c) the wire plated for 5 minutes without magnetic controlling field; (d) the wire plated for 5 minutes with a magnetic controlling field of 400 Oe.

7.2. Effect of longitudinal magnetic field on magnetic properties

Fig. 110 and Fig. 111 show the MI ratio tested at 1MHz and 50 MHz, respectively, for the wires from electroplating under varying longitudinal magnetic field, ranging from 0 to 400 Oe. At low testing frequency, such as 1 MHz (see Fig. 110), single peak MI ratios in variation with the external magnetic field (the maximum MI ratio occurs at 0 external magnetic field) was observed for all the samples. The sample plated under the longitudinal magnetic field 235 Oe exhibited the highest MI ratio, about 380%. However, at high testing frequency, such as 50 MHz (see Fig. 111), most of the samples exhibit double-peak MI ratios in variation with the external magnetic field ($H_{ex} = \pm H_p$), the GMI ratio increases initially with H_{ex} to a peak and

then falls with further increase of the field. However, the samples plated under stronger longitudinal magnetic field still exhibit single-peak MI ratios in variation with the external field. According to the results from high frequency testing as shown in Fig. 111, for the samples plated under strong longitudinal magnetic field, the MI ratios monotonically decrease with increasing of the external field H_{ex}.

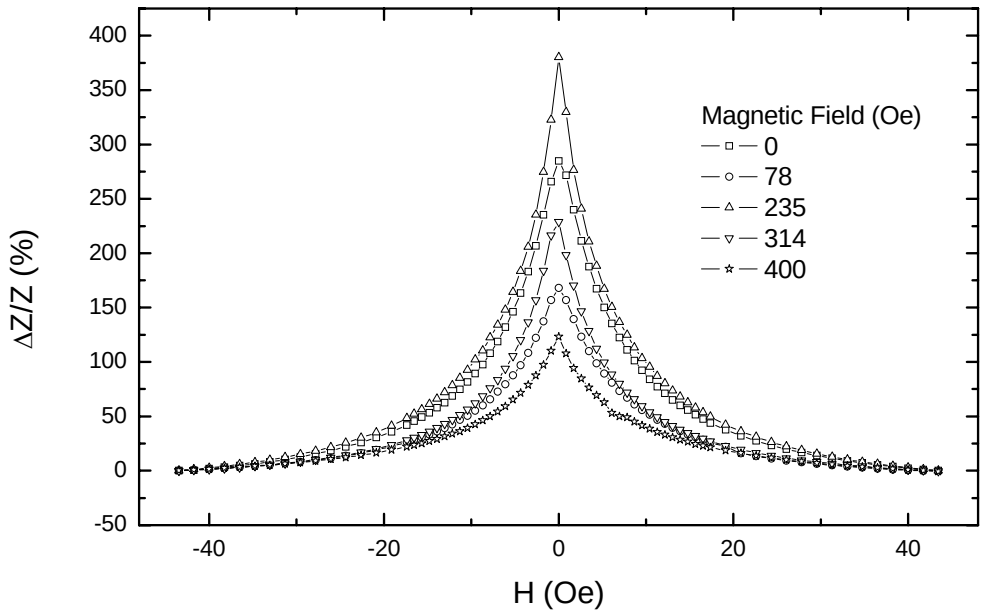

Fig. 110 GMI response of the composite wires plated under different intensities of longitudinal magnetic field, tested with 1MHz *ac* current.

The difference of the magnetic properties in terms of the MI curves can be explained by the magnetic anisotropy of the plated layer in variation with the magnetization process changes. First of all, at low testing frequency, such as at below the relaxation frequency of domain wall motion, domain displacement dominants the magnetization process, the total circumferential permeability monotonically decrease with respect to the external field. Therefore, the MI ratios of all samples decreased with the external magnetic field, H_{ex}, as shown in Fig. 110.

With the increase of MI testing frequency, in the plated layer the domain wall movements were nearly damped, the moment rotations thus dominated the

magnetization process. Therefore, the circumferential permeability increases with increasing external field until reaching the anisotropy field. After reaching the maximum value of the circumferential permeability, the dynamic circumferential permeability will decrease with increasing H_{ex}, till its saturation state.

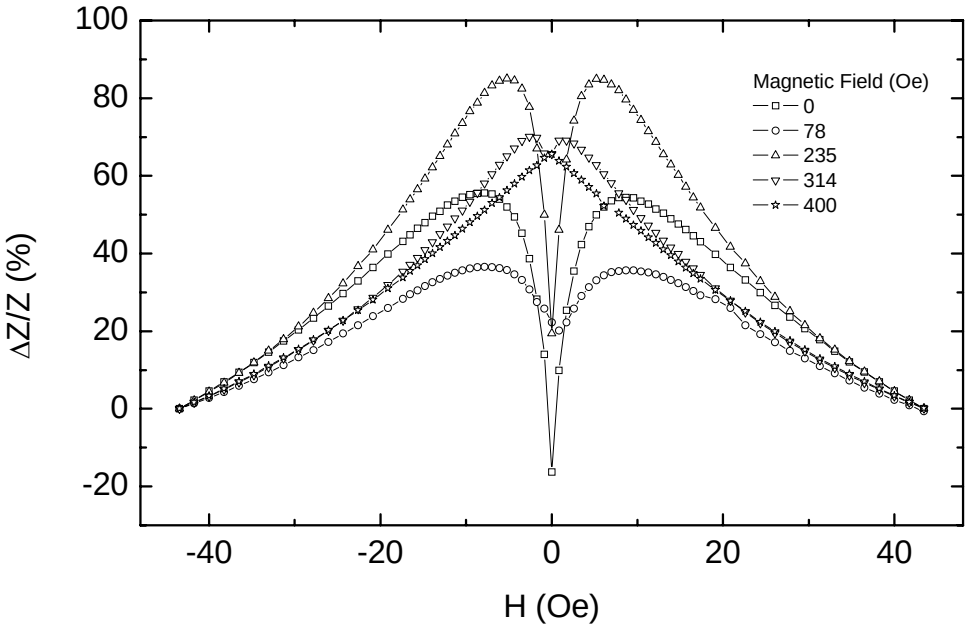

Fig. 111 GMI response of the composite wires plated under different intensities of longitudinal magnetic field, tested with 50MHz *ac* current.

According to the above described results on the MI curves tested at high frequency, the anisotropy variation of the plated layer can be predicted. Under conventional electroplating without a longitudinal magnetic controlling field, the anisotropy of the plated layer should generally be circumferential due to circumferential magnetization made by the electroplating current in the Cu core. The variation of the circumferential permeability μ_c with the external field strength H_{ex} can be calculated by considering the simplest model of an uniaxial single domain. Fig. 112 shows the schematic diagram for the rotational magnetization in the plated layer. The composite wire with an ac current i is under an external magnetic field H_{ex} along the wire axis direction, which magnetizes the plated layer. Supposing the easy axis

makes an angle θ_k with the circumferential direction and $\tilde{h}_c$ is the circumferential field produced by the current through the wire.

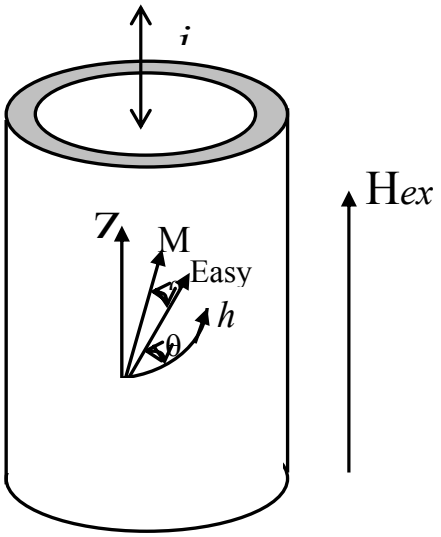

Fig. 112 Schematic diagram for the rotational magnetization of a composite wire in MI effect test.

The free energy of this system is

$$E = K\sin^2\theta - M_s H_{ex}\sin(\theta+\theta_k) - M_s\tilde{h}_c\cos(\theta+\theta_k) \tag{86}$$

where K and θ are the anisotropy constant and the angle between easy axis and magnetization M_s, respectively. The equilibrium angle is determined by minimizing the free energy,

$$\frac{\partial E}{\partial\theta} = K\sin(2\theta) - M_s H_{ex}\cos(\theta+\theta_k) + M_s\tilde{h}_c\sin(\theta+\theta_k) = 0 \tag{87}$$

Then, considering the moment rotation, the circumferential susceptibility can be obtained:

$$\chi_c = \frac{\partial M_c}{\partial\tilde{h}_c} = -\frac{\partial^2 E}{\partial\tilde{h}_c^2} \tag{88}$$

where M_c is the magnetization in circumferential direction. Taking small $\tilde{h}_c$ field approximation, the magnetic susceptibility in circumferential direction can be determined as:

$$\chi_c = \frac{M_s \sin^2(\theta + \theta_k)}{H_k \left\{ h \sin^2(\theta + \theta_k) + \cos(2\theta) \right\}} \tag{89}$$

where $H_k = 2K / M_s$ and $h = H_{ex} / H_k$, respectively. This analysis applies to ribbon or thin film structure composite wires [170].

Using Eqn. 87 and Eqn. 89, the field dependence of the circumferential permeability (μ_c=1+χ_c) for some given values of angle θ_k can be calculated, as shown Fig. 112. For small values of θ_k, the permeability exhibits double peak MI ratios when $H_{ex} = \pm H_k$. As θ_k increases, the value of h at the peak decreases and the peak eventually disappears with further increasing of θ_k over 60°, showing a monotonic decrease in circumferential permeability with h.

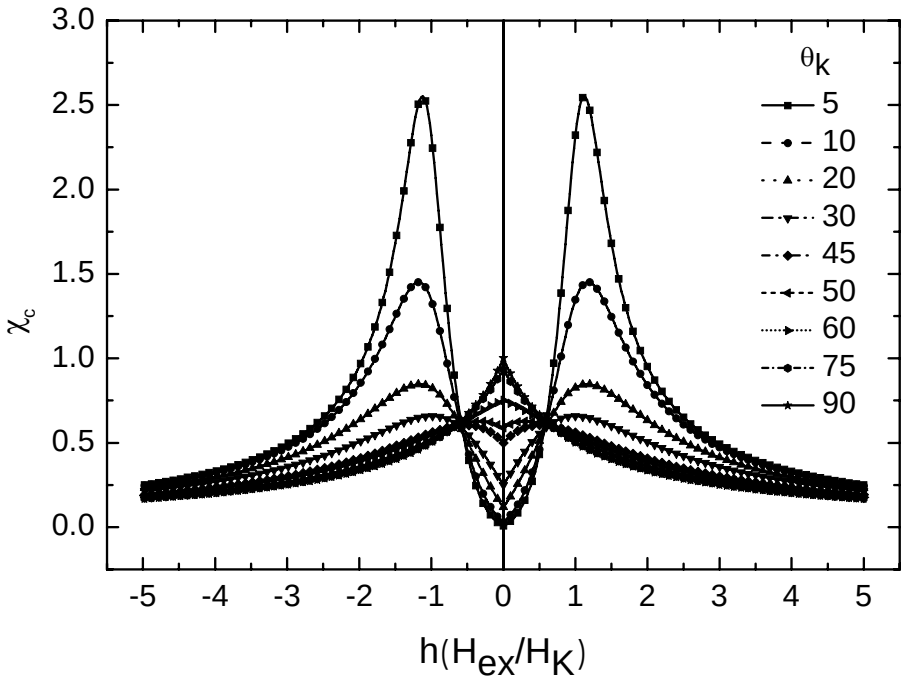

Fig. 113 Field dependence of the circumferential susceptibility at different anisotropy angles.

According to the simulation results as showing in Fig. 113, the MI ratio of the composite wire plated without longitudinal magnetic field should be the largest because of its circumferential anisotropy. However, in the results shown in Fig. 111, it

was not the case due to effect of the plated layer composition deviation and uniformity. It is important to note that not all the samples were having the NiFe composition ratio as 80:20. Those samples plated without a longitudinal magnetic controlling field were having the composition deviate slightly from 80:20. Also, as can be observed from Fig. 109, the plated layer of the sample from plating without longitudinal magnetic controlling field is less uniform compared to those plated under longitudinal magnetic field. These could result in less softness of the plated NiFe layer which made the MI ratios lower.

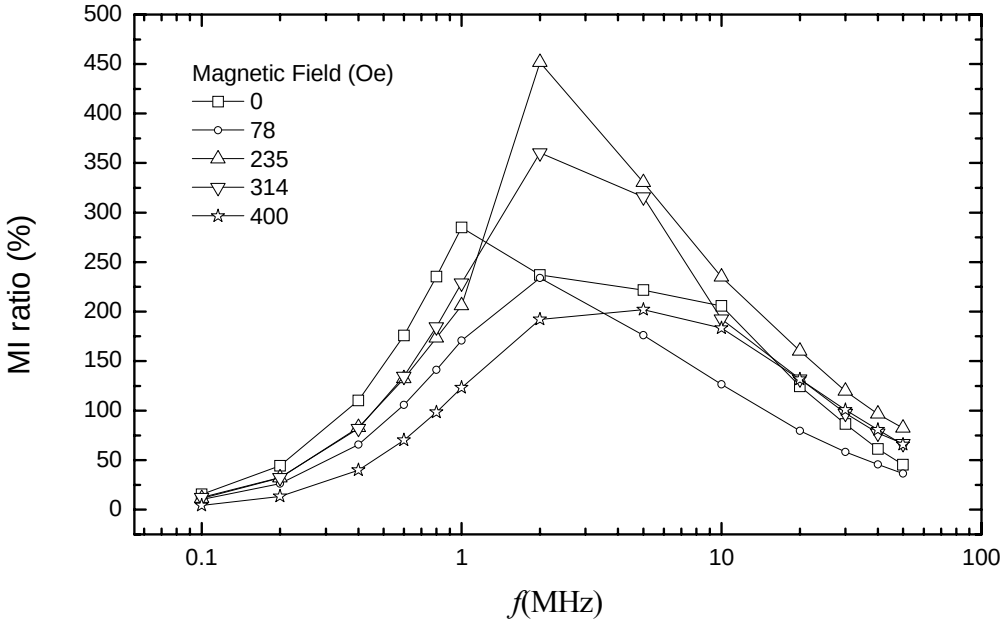

Fig. 114 Frequency dependence of the maximum of the GMI ratio of NiFe/Cu composite wires electroplated under different intensities of longitudinal magnetic field.

Fig. 114 shows the frequencies dependence of MI ratios of the samples plated under different intensity of the longitudinal magnetic controlling field. It can be seen that each sample had a maximum MI ratio at a critical testing frequency. Such a critical frequency varies with the wire samples plated under different level of the longitudinal magnetic field. The higher values of the critical frequency correspond to the higher intensities of the longitudinal field. This could be due to the longitudinal

anisotropy produced by plating under strong longitudinal controlling field. Theoretically [171], the largest MI ratio appears when the skin effect depth δ is equal to a certain value, *a*. If the current goes through only the Cu core, $a = r$, where *r* is the radius of the Cu core. For composite wire made by electroplating, the current goes through the Cu core as well as the plated NiFe layer, then $a = r'$, where $r' > r$, and the skin effect depth

$$\delta = \sqrt{\frac{2}{\omega\sigma\mu_\phi}} = r' \tag{90}$$

where ω is the circular frequency, σ is the conductivity, and μ_ϕ is the circumferential permeability of the composite wire. For the samples under testing, r' is a constant. Therefore, the increase of the critical testing frequency should be a result of decrease in the circumferential permeability, which was caused by the changing of anisotropy from circumferential to longitudinal in plating under the influence of the longitudinal field. This result is consistent with the simulation results as shown in Fig. 113.

7.3. Summary

The effects of an applied longitudinal magnetic field during the electroplating of NiFe/Cu composite wires on the composition, microstructure and magnetic properties of the plated layer have been investigated. The results showed that:

1. The imposed longitudinal magnetic field during electroplating makes the composition of the material more uniform, which has less variation compared to that in conventional plating without the controlling magnetic field.
2. The longitudinal controlling magnetic field has no obvious effect on the plating rate in terms of the thickness of plated layer.

3. The longitudinal magnetic field in composite wire plating makes the crystals in plated layer pack more orderly. This enhances the uniformity of plated material and therefore increases the magnetic softness of plated material.
4. The longitudinal magnetic field shifts the magnetic anisotropy of the plated composite wire from circumferential to longitudinal. The level of the anisotropy change is proportional to the intensity of the longitudinal magnetic field during the plating process. The variation of the anisotropy from circumferential to longitudinal, for composite wires plated under a range of longitudinal magnetic field, exhibit a variation from double peak MI ratio curve to single peak MI ratio curve in MI effect testing at high frequency of the testing current.
5. The critical MI effect frequency for a plated composite wire, at which the maximum MI ratio occurs, increase with increasing longitudinal magnetic field intensity, imposed during plating. This is due to the decrease of circumferential permeability of plated layer in response to the increase of intensity of the longitudinal magnetic field in the composite wire plating.

Chapter 8 Post Heat Treatment of Electroplated NiFe/Cu Composite Wires

Annealing is an essential post process that determines the quality of the composite wires. As such, it is important to investigate and optimize the annealing parameters in relation to the material and magnetic properties. In this chapter, furnace annealing and DC joule annealing was carried out on the composite wires and the influence of the various annealing parameters on the magnetic properties as well as sensing performance were investigated.

8.1. Furnace annealing of NiFe/Cu wires

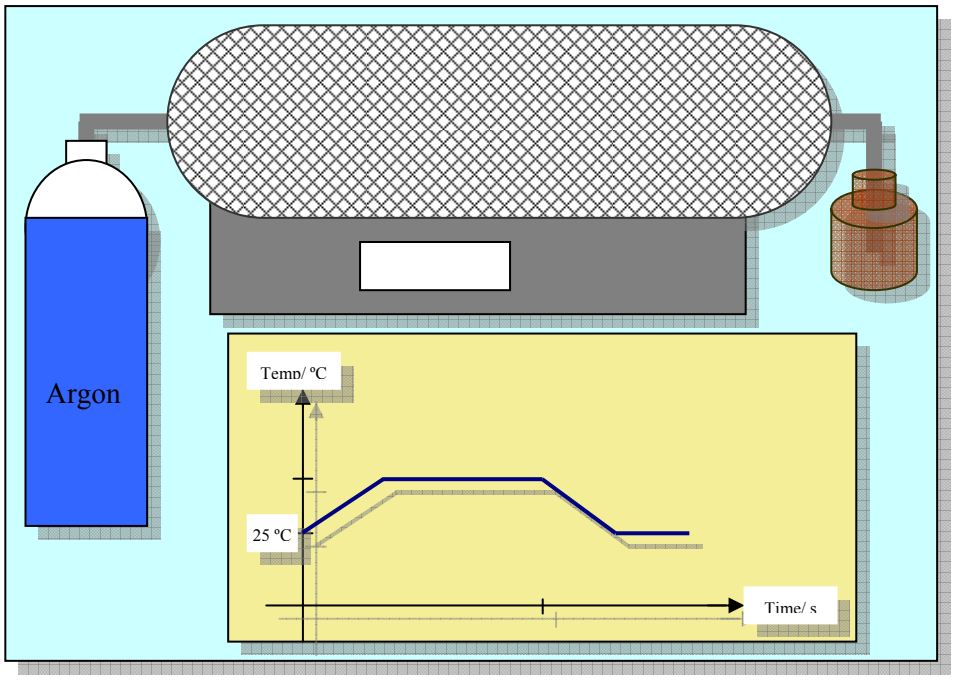

Fig. 115 Schematic Diagram of Furnace Setup

The setup for furnace annealing consists of a tube furnace, an argon tank and a bottle of water (Fig. 115). The furnace is capable of heating up to a temperature of

1200ºC and will be used in this study to vary the annealing temperature and duration. Unless otherwise stated, the annealing duration will be one hour, with heating and cooling rate at 10ºC/min. The argon gas will be turned on 1 hour prior to annealing to purge any impurities and ensure constant flow of noble gas during annealing. Specimens to be annealed will be placed on a ceramic tray and be positioned at the center of the tube furnace to ensure even heat distribution throughout the entire wire.

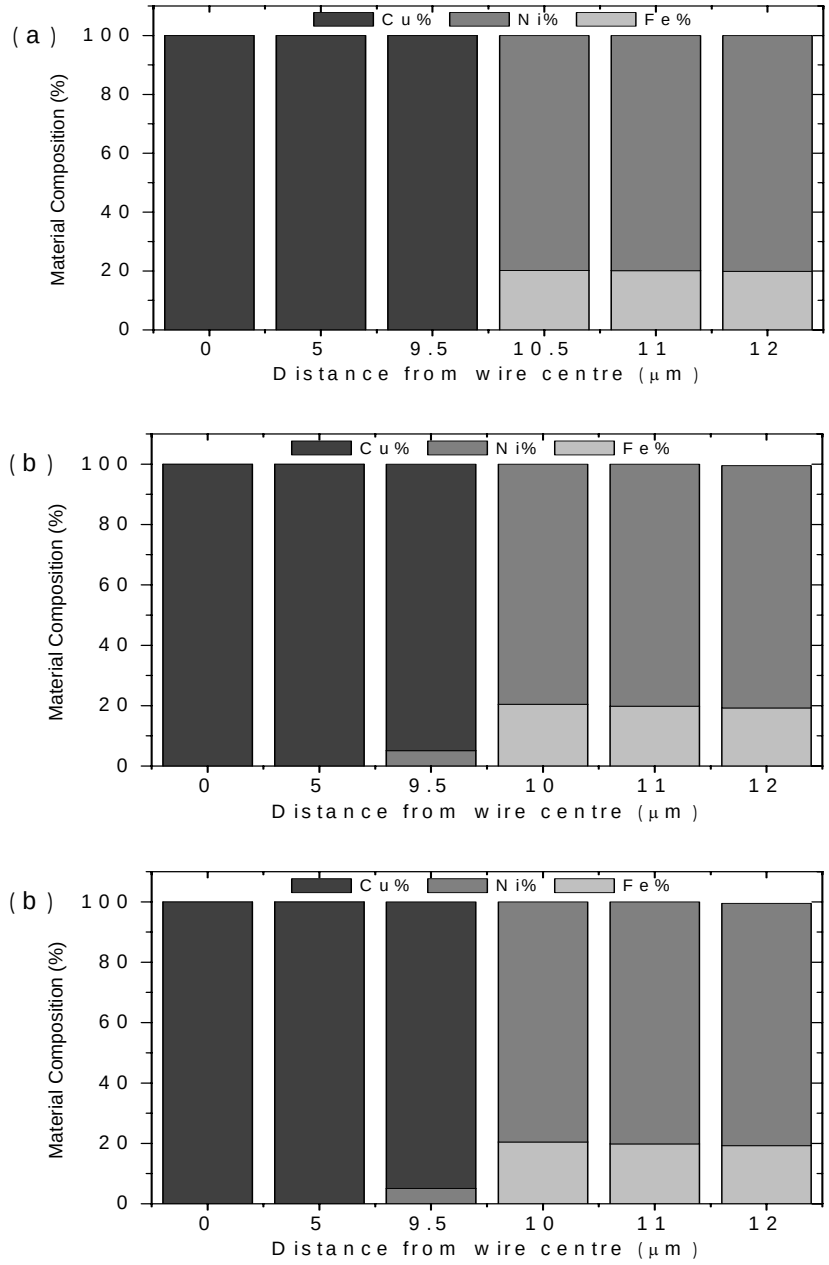

Fig. 116 Charts showing radial composition distribution of composite wires annealed at (a) 210 °C; (b) 350 °C; (c) 550 °C.

To investigate the radial composition distribution of the composite wires, the annealed composite wires were embedded in epoxy resin and the cross sections of the wires were mechanically and chemically polished to allow for EDX measurements to be conducted on the cross sections of the wires.

EDX measurements on the composite wire annealed at 210 °C displayed no inter-diffusion of Ni or Cu, as shown in Fig. 116a. However, when the composite wire was annealed at 350 °C, a small amount of Ni was observed within the outer boundary of Cu core, as presented in Fig. 116b. This amount of Ni was observed to increase, in Fig. 116c, when the annealing temperature was increased to 550 °C. Traces of Cu were also observed in the NiFe coating level.

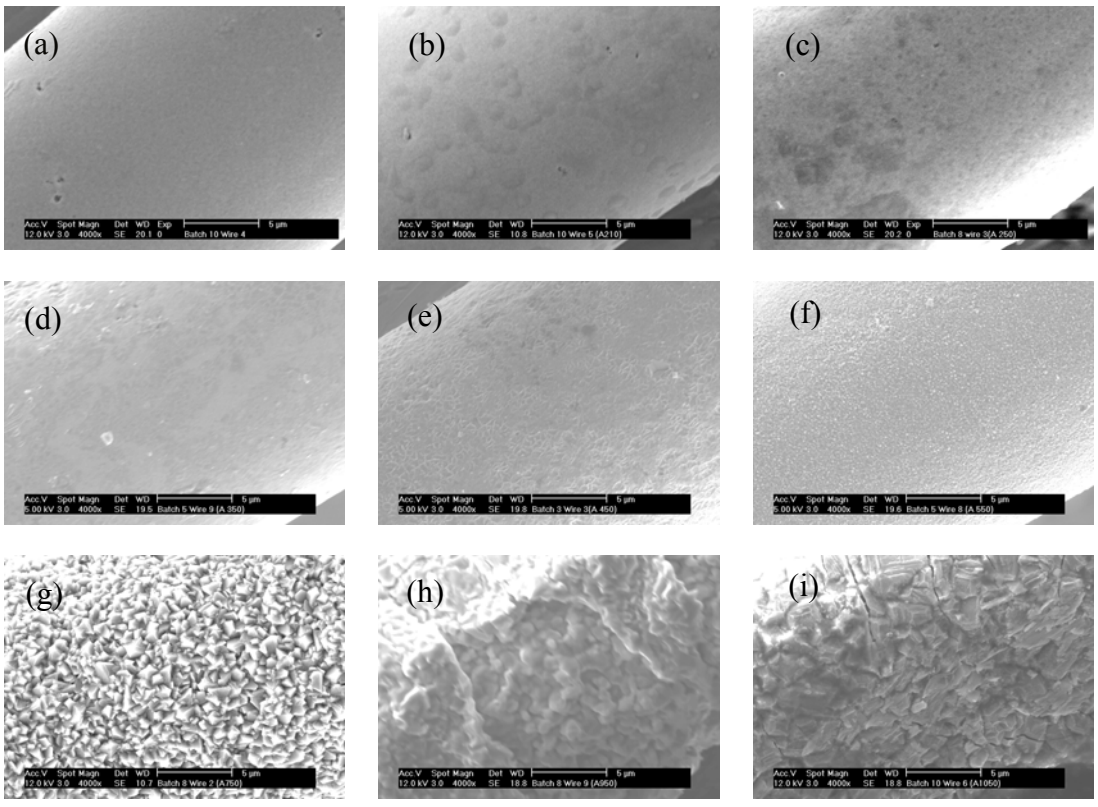

Fig. 117 SEM pictures showing surfaces of (a) as-plated NiFe/Cu composite wire and wires annealed at (b) 210 °C; (c) 250 °C; (d) 350 °C; (e) 450 °C; (f) 550 °C; (g) 750 °C; (h) 950 °C; (i) 1050 °C

In addition to the inter-diffusion effect, surface particle sizes were also observed to increase with increasing annealing temperatures, resulting in the increase in surface

roughness. The SEM photos showing the differences in surface morphology of the as-plated composite wires and also wires annealed at increasing temperature can be seen in Fig. 117. In particular, above recrystallization temperature of 550 °C, very rough surfaces of the composite wires can be observed (Fig. 117g, Fig. 117h, Fig. 117i), as compared to ultra-smooth surface of the as-plated wire (Fig. 117a).

Average grain sizes of thin films annealed at 210 °C, 350 °C, 550 °C and 750 °C were also measured using XRD. The values of the average grain sizes were calculated using Scherrer's formula (Eqn. 59). At 210 °C, no significant change in average grain size was observed. Fig. 118 shows the percentage increase in average grain sizes at different annealing temperatures. The increasing trend is similar to that obtained by F. Ebrahimi [172]. The mechanisms of grain growth are different at high and low temperatures. Grain growth at low temperature takes place via atomic movement within grain boundaries while lattice diffusion dominates grain growth at high temperatures.

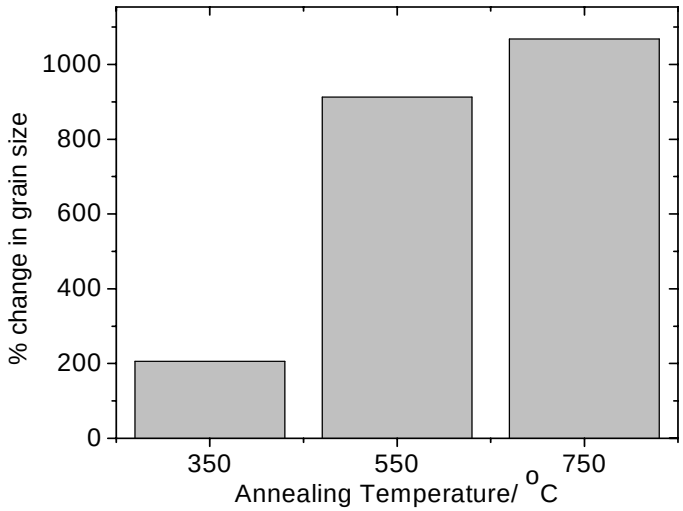

Fig. 118 Chart showing percentage changes in average grain size with annealing temperature.

Fig. 119 shows the percentage change in coercivity H_c with annealing temperatures. At values of annealing temperatures up to 550 ºC, there appear insignificant changes

to H_c. However, above that temperature, H_c was observed to drastically increase. Since high permeability materials have low H_c [101], therefore it can be inferred that as temperature increases, permeability decreases. This decrease in permeability, with increasing annealing temperature, can be attributed to the domination of inter-diffusion, surface roughening and grain growth effects, despite the obvious stress relief effects. According to the random anisotropy model (RAM), grain growth in the nano-size region, below the critical exchange length L_{ex} for the material, will result in an increase in coercivity which corresponds to a decrease in permeability [101]. For $Ni_{80}Fe_{20}$, L_{ex} was calculated to be at about 270 nm.

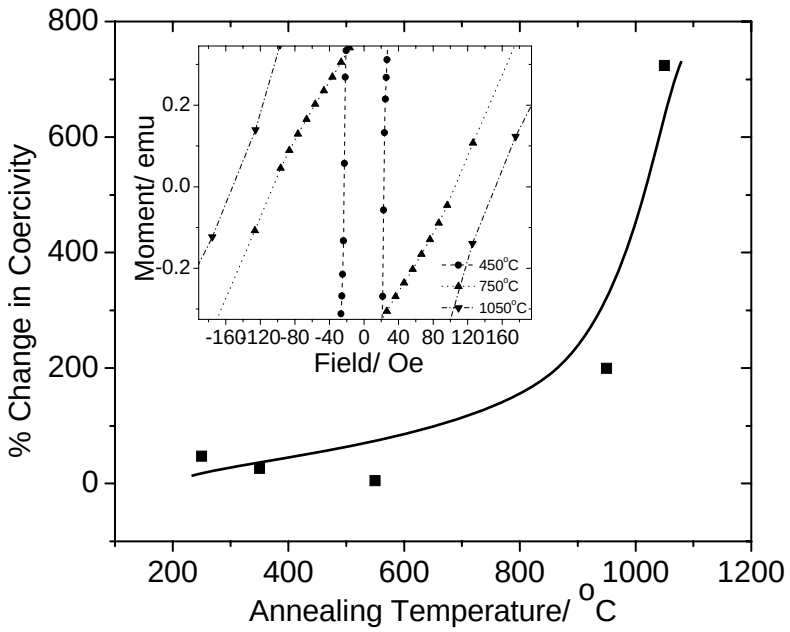

Fig. 119 Plot showing percentage increase in coercivity with annealing temperature. Inset graph displays the zoom-in of hysteresis loops at different annealing temperatures.

The effect of annealing temperature on the MI effect of composite wires was shown in Fig. 120. With increasing annealing temperature, reduction in MI ratio increased. Since MI effect is greatly affected by the geometrical factor as well as the transverse permeability, the reduction is, in this case, largely due to permeability effect as the

composite wires under study are similar in geometry. The reduction in permeability also resulted in the decrease in sensitivity, as observed in Fig. 124.

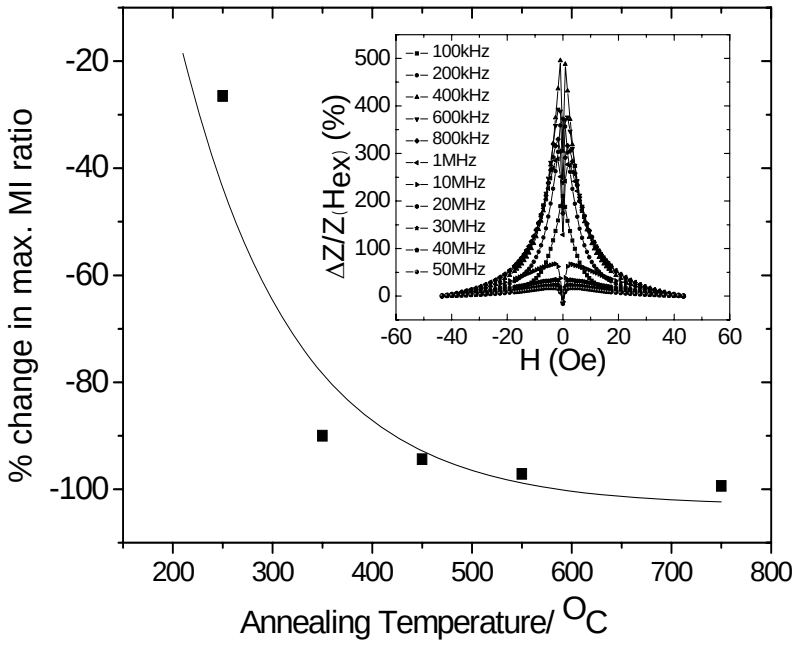

Fig. 120 Plot showing percentage reduction in MI ratio with annealing temperature. Inset graph displays the MI curve of as-plated composite wire.

The annealed specimens were then placed in the orthogonal fluxgate sensor circuit and their performance as sensing elements in the sensor was measured in terms of sensitivity. The values of sensitivity (mV/Oe) were obtained from the plot of voltage signal V versus applied field H.

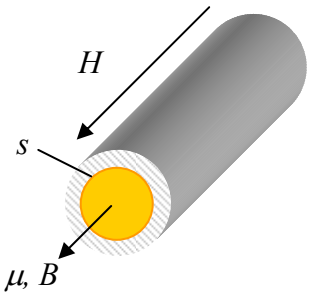

Fig. 121 Schematic diagram showing the directions of the various magnetic properties vector acting on the composite wire.

It is known that the voltage signal V arises from a change of flux ϕ over time t, i.e.

$$V = -\frac{d\phi}{dt} \tag{91}$$

Since $\phi = \vec{B}.s$ where s is the cross-sectional area of the wire (Fig. 121), the magnitude of V can then be expressed as function of flux density $\vec{B}$ and t:

$$|V| = \frac{d\phi}{dt} = \frac{d(\vec{B}.s)}{dt} = s.\frac{d\vec{B}}{dt} \tag{92}$$

Since $\vec{B} = \mu_0(\vec{M} + \vec{H})$ and $\vec{M} = \chi\vec{H}$ where μ_0 is the permeability of free space, $\vec{M}$ is the magnetization of the material (the magnetic dipole moment per unit volume, measured in A/m) and $\vec{H}$ is the applied field in the direction of the length of the wire, therefore

$$\vec{B} \approx \mu\vec{H} \tag{93}$$

where $\mu_0(1+\chi)$ is the relative permeability.

Simplifying Eqn. 91:

$$|V| = s(\mu\frac{d\vec{H}}{dt} + \vec{H}\frac{d\mu}{dt}) \tag{94}$$

Since the testing field is static, therefore $\frac{d\vec{H}}{dt} = 0$. It must be noted that the induced magnetic field by the alternating current through the wire is in the circumferential direction and thus not considered under this equation.

Thus, Eqn. 93 can be further simplified as:

$$|V| = s.\vec{H}.\frac{d\mu}{dt} \tag{95}$$

Using Eqn. 94, sensitivity S can be expressed as:

$$|S(\vec{H})| = \frac{d|V|}{d\vec{H}} \propto \frac{d\mu(\vec{H})}{dt} \tag{96}$$

Since μ is a function of both $\vec{H}$ and t, there must exist a certain relationship between the two parameters. Thus, it can be argued that the sensitivity trends will most likely follow those of μ with $\vec{H}$, although the magnitudes will be entirely different.

For wires with different anisotropies, the general hysteresis loops are entirely different as given Fig. 122.

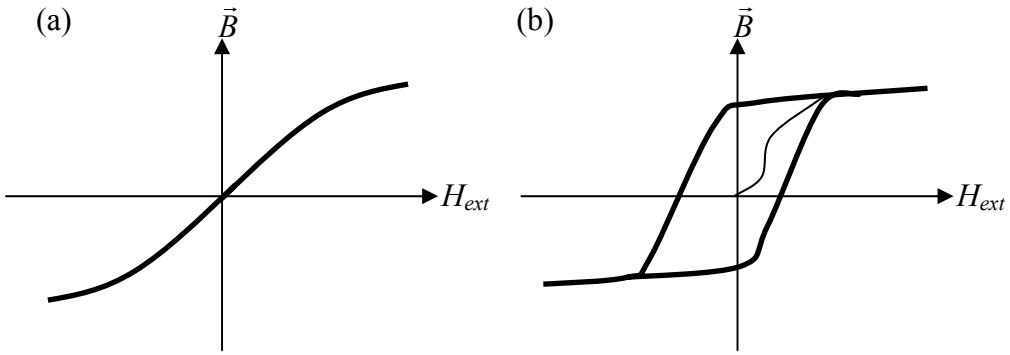

Fig. 122 Hysteresis loops of wires with (a) circumferential (out of plane) anisotropy; (b) longitudinal (in plane) anisotropy).

Therefore, since permeability is actually the gradient of the plot of $\vec{B}$ vs H_{ext} (hysteresis loops), the following relationship of μ and $\vec{H}$ can be inferred and shown in Fig. 123 below. Thus, sensitivity is believed to follow such trends.

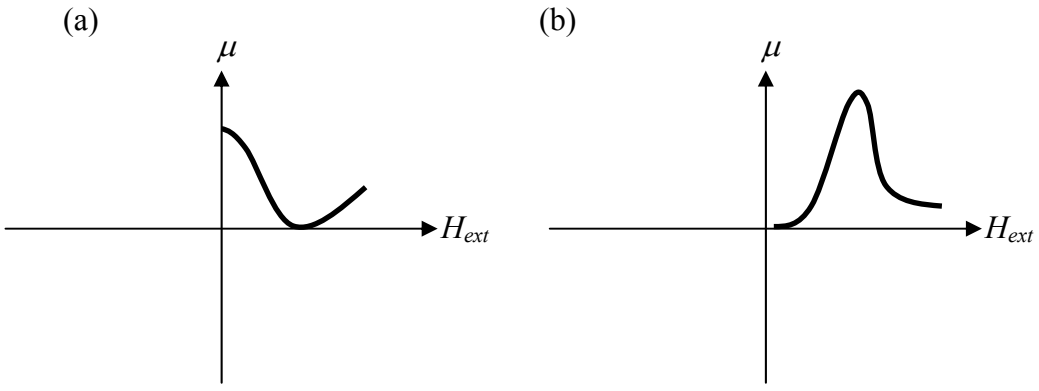

Fig. 123 Plot of permeability μ against H_{ext} for wires with (a) circumferential anisotropy; (b) longitudinal anisotropy.

As seen in Fig. 124, there is a negative percentage change in sensitivity with increasing T_A. This implied that sensitivity dropped upon annealing for duration of

one hour at increasing T_A, with the reduction rate reaching a maximum of over 99% at 750°C. During annealing, it can be observed that the resultant anisotropy direction of the wires was changed to a direction closer to the longitudinal direction and stress is relieved in the wire during the process. Although this may be advantageous to the sensitivity of the sensor [173], the permeability of the sensor was reduced in the process due to inter-diffusion and grain growth [101]. A change in composition at the surface was also noted after annealing, even at 210 °C. From Fig. 124, considering the decreasing trend in sensitivity with increasing T_A, it appears that the detrimental effect of inter-diffusion and grain growth, which leads to a reduction in magnetic properties, outweighs the benefits brought about by the longitudinal anisotropy and stress relief.

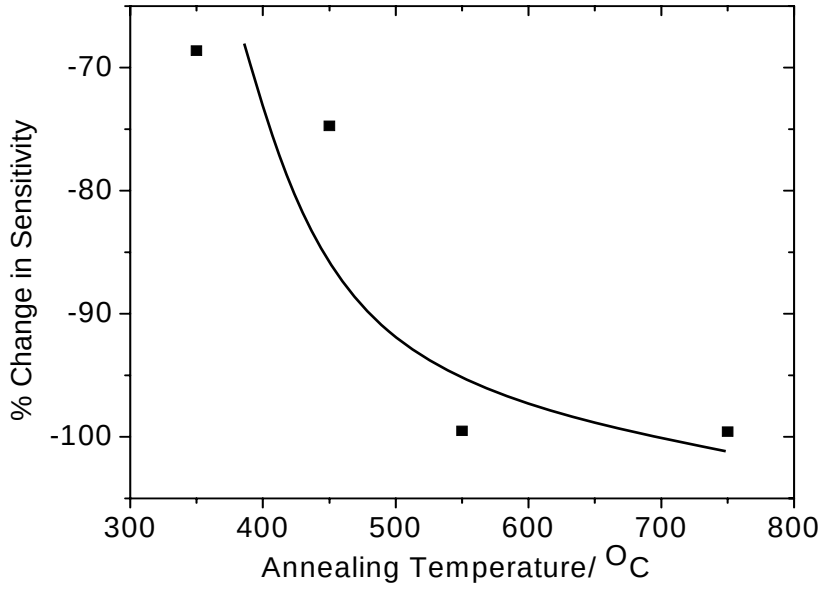

Fig. 124 Plot showing percentage reduction in sensitivity with annealing temperature.

8.2. DC joule annealing of NiFe/Cu wires

All the composite wire samples with 15 mm in length were annealed using a DC joule annealing technique, in which under the protection of argon gas the composite wire has a DC current passing through it for 1 minute and then cools down in air. The average annealing current densities used were varied from 2.4 to 9.6 $\times 10^8$ A/m^2.

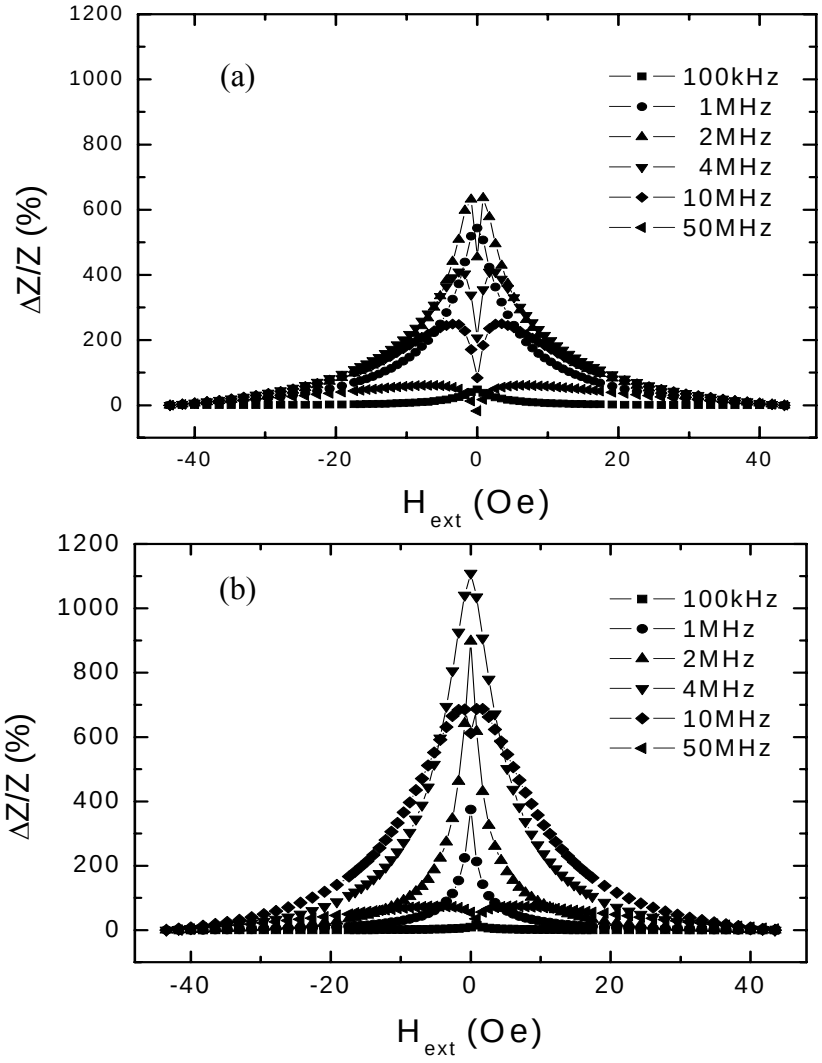

Fig. 125 MI ratio in variation with an external magnetic field for electroplated wire without and with the DC joule annealing: (a) without annealing; (b) with the DC joule annealing.

Significant differences between the GMI effects in electroplated composite NiFe/Cu wires without and with DC joule annealing can be seen from Fig. 125, where (a) and (b) show the MI effect curves tested under different AC driving frequencies for wires with 15 mm in length without and with DC Joule annealing, respectively. Fig. 125a shows that in the wire without DC Joule annealing, the MI ratio in variation with the external magnetic field depended on the driving frequency of the AC current in the GMI effect test. At the DC driving frequency of 2 MHz, the MI ratio reached the maximum of 637%. For the wire with DC joule annealing, Fig. 125b shows also

that the MI ratio in variation with the external magnetic field depended on the driving frequency of the AC in GMI effect test. At the AC driving frequency of 4MHz, the maximum MI ratio was 1110%, which was a 74% increase compared to the maximum MI ratio in the wire without annealing.

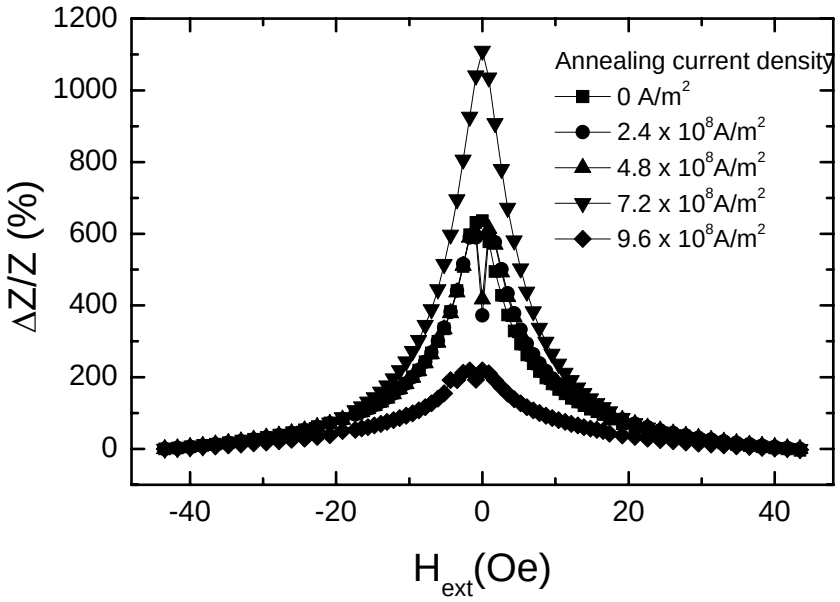

Fig. 126 The effect of annealing current density on the MI ratio of DC Joule annealed electroplated composite wire in variation with an external magnetic field.

The DC joule annealing on electroplated composite wires was further carried out to study the DC current density in relation to the GMI ratio of the wire in the DC joule annealing. Fig. 126 shows the MI effects relation to various annealing current densities. The MI ratios were measured at a testing frequency of 4 MHz. It was found that there was an optimum current density for the DC joule annealing, at which the annealed wire had the highest maximum MI ratio. The maximum MI ratios of the wires annealed in relation to the annealing current densities are shown in Fig. 127. It can be seen that the maximum MI ratio was in a slightly decreasing trend as the wires were annealed at lower current densities (below 4.8×10^8 A/m^2). When the annealing current density was increased beyond 4.8×10^8 A/m^2, the MI ratio started increasing. It reached the highest, 1110%, at the current density 7.2×10^8 A/m^2. Corresponding to

Fig. 127, Fig. 128 shows that the anisotropy field strength of the annealed magnetic coated layer reached the minimum under the annealing current density 7.2×10^8 A/m^2. As the annealing current density was further increased from 7.2×10^8 A/m^2, the MI ratio of the annealed wire dropped drastically (Fig. 127), and the anisotropy field strength increased (Fig. 128). A larger value of H_k deteriorated the soft magnetic properties, which leaded to the smaller MI ratio.

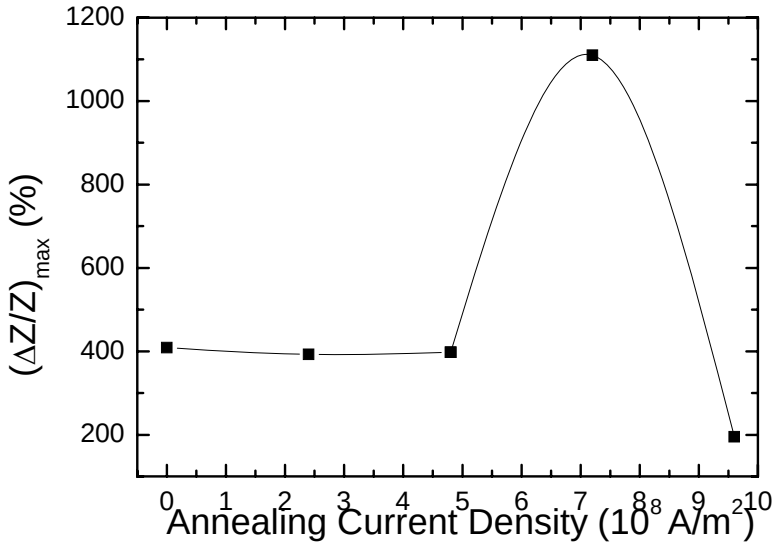

Fig. 127 The effect of the annealing current density on the maximum MI ratio in the DC Joule annealed electroplated composite wires.

It has been well documented that at low testing frequency, such as frequency below the relaxation frequency of domain wall motion, domain movement dominates the magnetization process and the total circumferential permeability monotonically decreases with respect to the external magnetic field. This explains why the MI ratio decreased with the external magnetic field H_{ext}, as shown in Fig. 126. With the increase in AC driving frequency, domain wall movements in the plated layer were nearly damped and thus the magnetization rotations dominated the magnetization process. Therefore, the circumferential permeability increased with the increase in the external field until the magnitude of the external field matched that of the anisotropy field, H_k. After the static circumferential permeability reached its peak, the dynamic

circumferential permeability decreased with the increase in H_{ext}, till its saturation state. This also agreed well with the results of the MI tested at high frequencies, as shown in Fig. 125.

Before undergoing the DC joule annealing, the plated layers of the composite wire samples contain residual stresses induced by the electrodepositing process. In annealing at the initial annealing current densities of 2.4×10^8 A/m^2 and 4.8×10^8 A/m^2, it was conjectured that there were tremendous inertia for the magnetic domains to rotate from their initial local anisotropy orientations to the circumferential anisotropy as induced by the annealing current. As a result of this magnetic hardening, a larger crystalline magnetic anisotropy k, was needed to rotate the domains, which were frozen in their initial directions, along the easy axis to the circumferential direction. This magnetic hardening also leaded to a slight drop in the MI ratio.

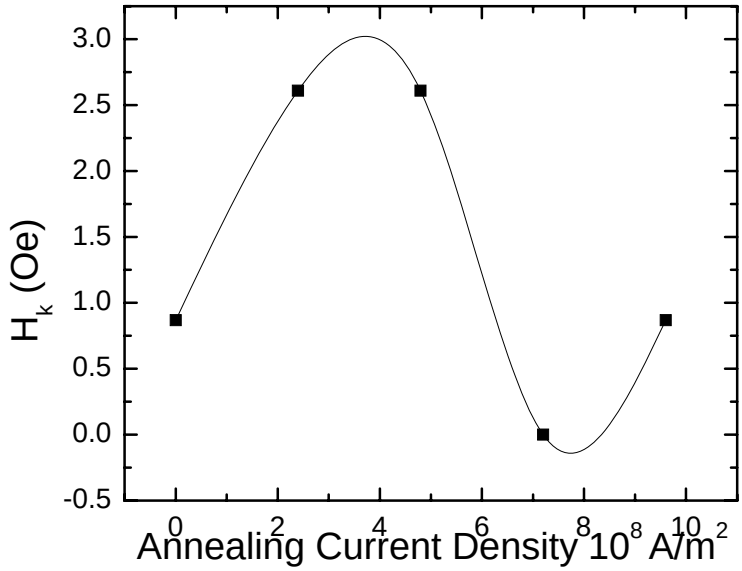

Fig. 128 The effect of the annealing current density on the anisotropy field strength, H_k, of the DC Joule annealed electroplated composite wires.

As the annealing current density was further increased, the maximum MI ratio increased steadily, till the annealing current density reached a peak, 7.2×10^8 A/m^2, at which the internal stresses was released by heating, which produced a lower constant

of magnetostriction as well as a lower constant of crystalline magnetic anisotropy for the ferromagnetic coating layer of the composite wire. The enhancement of the softer magnetic properties thus increased the MI ratio. Furthermore, the rotational factor of the magnetic susceptibility could be increased as the magnetocrystalline anisotropy constant k, magnetostriction constant λ_s and level of stresses in the material were decreased. This is precisely why heat treatment has long been recognized as an important tool for the improvement of magnetic properties of NiFe alloys [174].

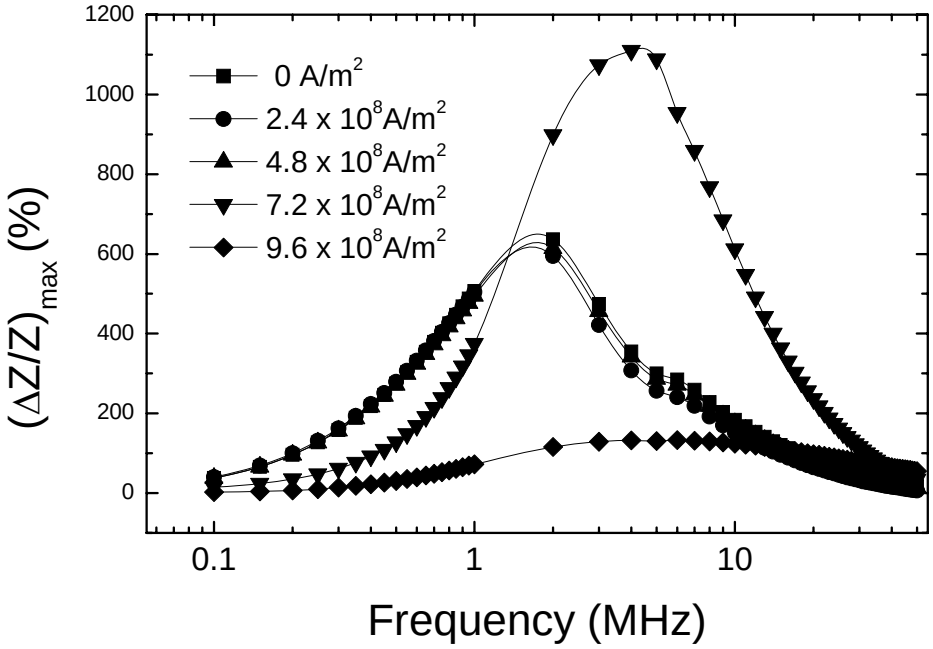

Fig. 129 The effect of the annealing current density on the frequency dependence of the MI ratio of the DC joule annealed electroplated composite wires.

Annealing at the current density beyond the optimal 7.2×10^8 A/m^2 resulted in a drastic decrease in MI ratio was due partially to the change in the phase composition of the solid solution and coarsening of the nanocrystalline grains, which caused a deterioration of the soft magnetic properties. This could be associated with the phase composition change or the ordering of NiFe alloy which increases the magnetic anisotropy constant [174]. Another possible reason for the decline in MI ratio is the inter-diffusion between Ni atoms and Cu atoms above 250^{o}C. This inter-diffusion

might have caused the decay of the MI ratio by altering the magnetic properties of magnetic coating layer. It was reported [114] that at 250^{o}C or above, Ni atoms preferentially diffuse into the Cu layer, thus increasing the resistivity of the material.

Fig. 129 displays the MI frequency spectrum of the composite wires before and after DC joule annealing at annealing current density ranging from 2.4 to 9.6×10^{8} A/m^{2}. For all the wires with length of 15 mm in the MI testing it was observed that the maximum MI ratio increased with the increase of the AC driving frequency up to the highest, and then decreased with further frequency increases. For the wires annealed with the current density 4.8×10^{8} A/m^{2} or lower, the maximum MI ratios peaked at 2 MHz. For the wire annealed was at the current density 7.2×10^{8} A/m^{2}, the maximum MI ratios peaked at 4 MHz. The maximum MI ratios of the wire annealed with current density 9.6×10^{8} A/m^{2} shows no obvious peak.

The respective upward and downward trends of the MI ratio in variation with the driving frequency can be explained by the circumferential permeability variation. At low frequency, the domain wall displacement dominated the magnetization. With the increase in the driving frequency, the dynamic permeability increased. At the frequency higher than the relaxation value, the magnetization processes was replaced by moment rotation, and the permeability dropped as a result of damping to the domain wall displacement.

The maximum MI ratio appears when the circumferential permeability has begun to decrease. It was normally believed [171] that the maximum MI ratio for such composite wires would appear at the condition when the skin penetration depth δ was of order of the dimensional size of the ferromagnetic materials. In this way if the conductivity of the NiFe layer was much larger than that of the copper core, the dimensional size was the radius of the copper core, and the same applied to the wires

with and without annealing. However, the present results show that the optimum frequency shifted with the annealing parameters, which indicates the variation of the skin depth δ with the annealing parameters, because

$$\delta = \sqrt{\frac{2}{\omega\sigma\mu_{\varphi}}}, \tag{90}$$

where ω is the angular frequency, σ is the conductivity, and μ_{φ} is the maximum differential circumferential permeability of the composite wire. The shifting of the optimum frequency could be due to variation of the magnetic permeability and conductivity of the ferromagnetic layer. Another possible effect might come from the domain structure change during the annealing process.

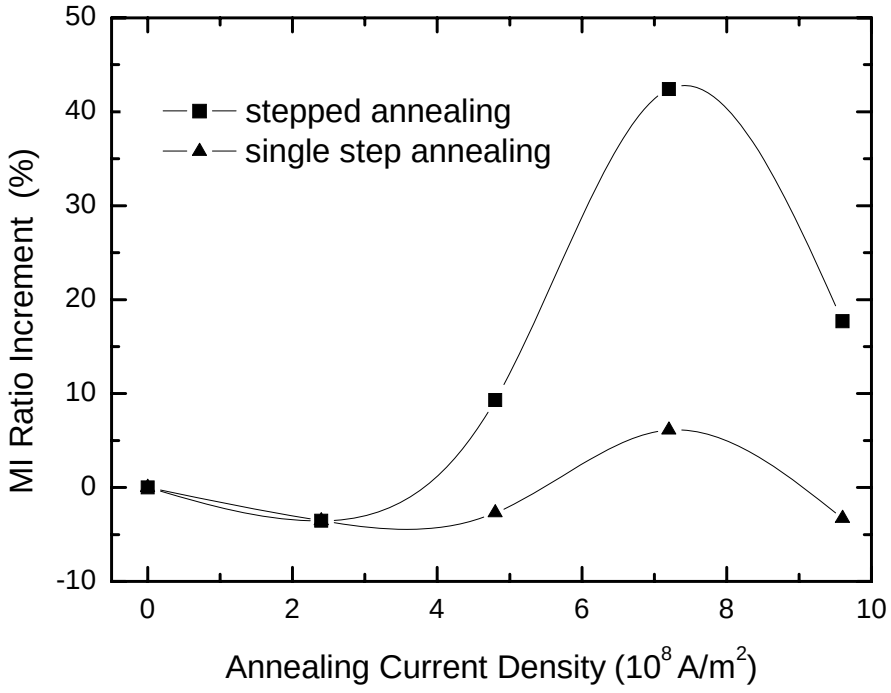

Fig. 130 The percentage increment in the MI ratios of single step annealed composite wire and stepped annealed wire.

Investigation was further carried out to study the differences between single step annealing and stepped annealing in DC joule annealing of the composite wires. The stepped annealing involved annealing of a composite wire using an increasing average

annealing current density from 2.4 to 9.6 $\times 10^8$ A/m^2 at the step of 2.4×10^8 A/m^2 and the subsequent measurement of the MI ratio of the wire. In the single step annealing, 5 composite wires of the same plated layer composition and thickness were used to test the effects of 4 levels of annealing current densities on the MI ratios of the wires. As shown in Fig. 130, in both the single step annealing and stepped annealing, the MI ratio of the annealed wire increased with increasing annealing current density, before it reached the maximum. However, stepped annealed wires had much higher MI ratio increments compared to the single step annealed wires. The MI ratio increments for wires annealed at the current density 7.2×10^8 A/m^2 was 42% for stepped current annealing and 6% for single step annealing. Hence, stepped current annealing can be concluded to be the better technique in achieving higher MI ratio. A possible reason could be that it was easier for the electroplated material to release its internal stresses after the smaller current density annealing.

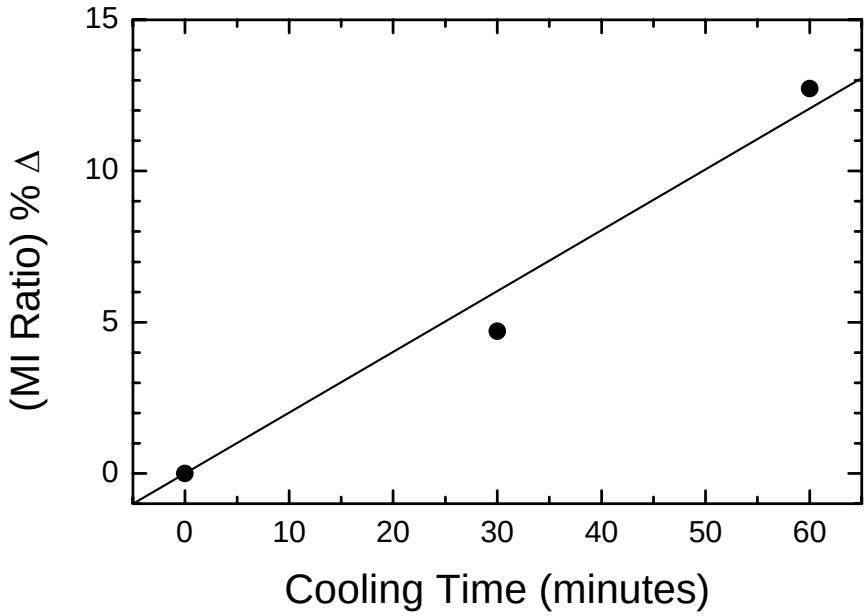

Fig. 131 Effect of the cooling time in the DC Joule annealing on the percentage increment in the MI ratio of the DC Joule annealed composite wires.

For the DC joule annealing method, the cooling rate in annealing was also investigated. Three composite wire samples of the same plated layers were annealed

at an annealing current density of 7.2×10^8 A/m^2 for 1 minute. Subsequently, for the first sample, the annealing current was stopped immediately, and for the second and third samples the current was reduced gradually to zero during 30 and 60 minutes, respectively. It was found that the MI ratio of the annealed wire increased almost linearly with the increase in the cooling time, as shown in Fig. 131. This can be explained by the better stress minimization of lower cooling rate in the annealing processes.

8.3. Summary

1. As the annealing temperature was increased from 210°C-1050°C, a general reduction in MI% ratio and sensitivity as well as an increase in coercivity was observed. This trend was due to a decrease in permeability that was attributed to grain growth and inter-diffusion between the two layers, despite the effects of stress relief. At high annealing temperatures, especially above the recrystallization temperature of 550°C, the degradation of the magnetic properties was more pronounced. Significant grain growth can also be observed with increasing annealing temperature. Inter-diffusion was observed. In particular, obvious diffusion of nickel into copper was observed at 350 °C and 550 °C, with traces of copper detected along the radial direction of the cross-section, right up to the surface.
2. A DC Joule annealing method has been developed and tested for the enhancement of the GMI effect of electroplated NiFe/Cu composite wires. The results showed that the annealing makes great improvement on the MI ratio of the composite wires. The highest MI ratio of 1110% has been obtained, which was a 74% increase compared to the maximum MI ratio in the wire without annealing. The

optimum conditions for the annealing method have also been studied. The results showed that for the tested wire samples there was an optimum annealing current density, at which the annealed wire has the highest MI ratio. The optimum AC driving frequency for the composite wire GMI sensor was found to be a function of the annealing current density which varies with the magnetic permeability and conductivity of the plated ferromagnetic layer. In terms of the increment in the MI ratio of the annealed wires, it has been found that stepped annealing is better than single step annealing and the MI ratio increment increases almost linearly with the cooling rate in the annealing.

Chapter 9 Development of NiFe/Cu Micro Composite Wires by Cold-drawing

Another approach taken by the author to develop NiFe/Cu composite wires was by the method of cold-drawing. The cold-drawing setup was developed and the details were given in Chapter 3. In cold-drawing, several issues need to be investigated. In particular, the effect of drawing on the NiFe:Cu ratio and the influence of the final annealing temperature have to be investigated. As such, the details of such studies were given in this chapter.

9.1. Effect of drawing on the NiFe:Cu ratio

Fig. 132 shows the value of the overall wire diameter and the inner copper core diameter at each draw from the 10^{th} to the 50^{th} draws. As can be observed in Fig. 133, the diameter of the copper core as well as the overall wire diameter decreases proportionally with respect to each other and the ratio of the diameter of copper core to that of the overall wire remains relatively unchanged at around 0.66 throughout the entire drawing process, which could be due to the extremely large frictional force at the permalloy layer/copper core interface. This observed phenomenon is of paramount importance as this means that the desired final diameter ratio of the composite wire can be easily predicted from the initial diameter ratio before drawing.

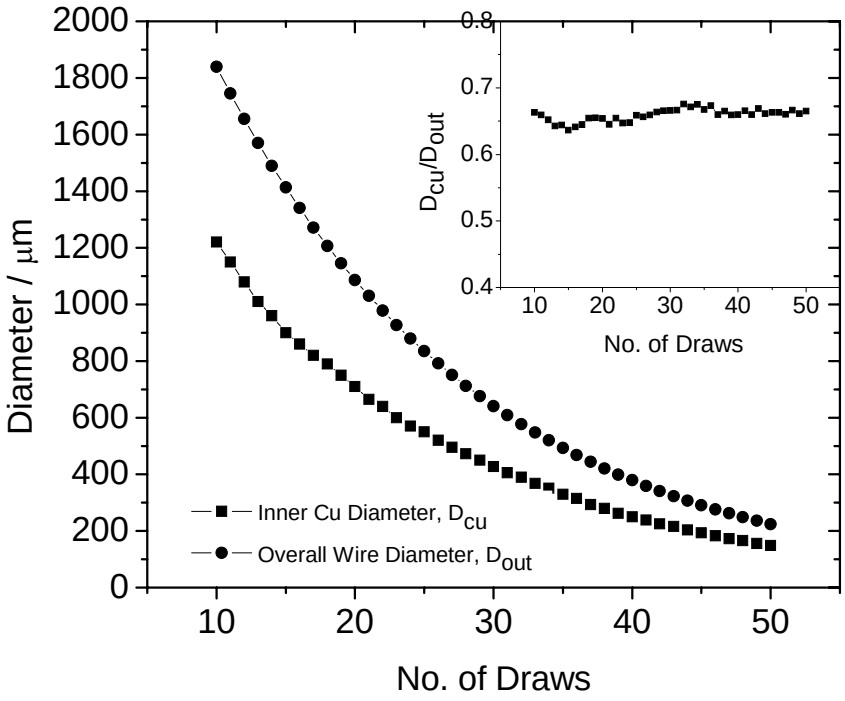

Fig. 132 Overall cold-drawn wire diameter and inner copper core diameter variations from 10th to 50th draws (the inset graph shows the ratio of diameter of copper core to that of overall wire).

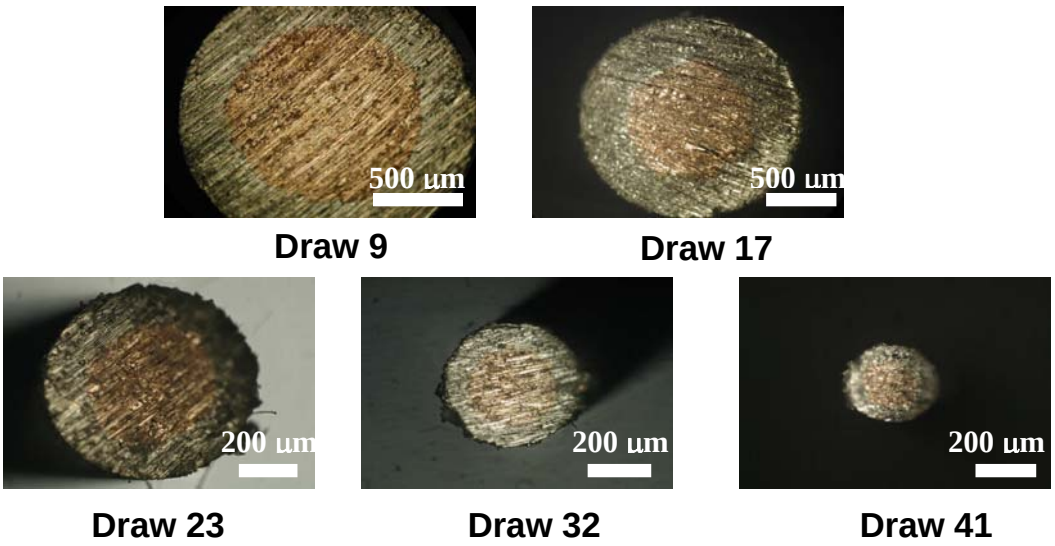

Fig. 133 Typical pictures of the cross-section of cold-drawn $Ni_{80}Fe_{20}$/Cu wire at different draws.

9.2. Phenomenon observed during drawing

9.2.1. Protrusion / Sinking-in effect at early draws

After the first draw, a substantial amount of Cu was observed to be protruding from $Ni_{80}Fe_{20}$ layer (Fig. 134). This protrusion effect was observed to be more

pronounced for the composite wires with the thickness ratio of 1:10:1 than those with the thickness ratio of 1:4:1. However, after the first draw, the amount of protrusion decreased, eventually leading to a slight sinking-in effect of the Cu. This phenomenon is mostly likely due to the initial slipping of the two layers as well as the initial manufacturing defects, leading the occurrence of voids in the composite wires. After 6 draws, this effect was observed to diminish and the changes became unobservable.

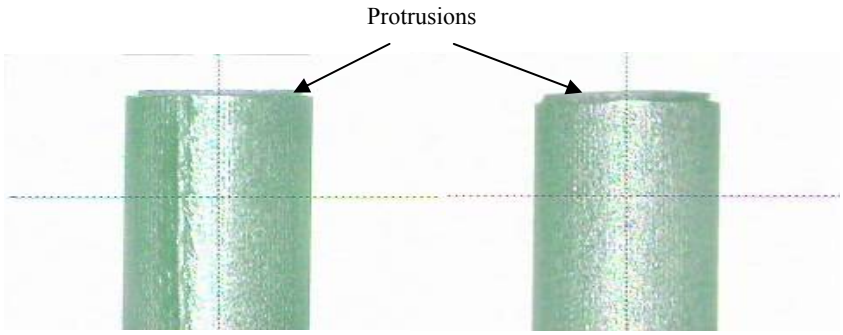

Fig. 134 Side view of two wires of thickness ratio of 1:10:1 after the first draw, showing protrusion.

9.2.2. Theoretical predictions of length

As mentioned previously, the ratio of $Ni_{80}Fe_{20}$ to Cu is observed to be constant after draws. This can be applied to the conservation of volume to predict the length of the microwires after draws. The lengths of the microwires were measured after each draw to verify this. As shown in Fig. 135, there is insignificant difference between the theoretical lengths of the wires (calculated using the rule of the conservation of volume as represented by (Eqn. 97)) and the experimental lengths measured after every draw.

$$\pi\left(\frac{d_o}{2}\right)^2 L_o = \pi\left(\frac{d_i}{2}\right)^2 L_i \tag{97}$$

The maximum deviation of the actual values from the theoretical values is 13% and 9% for wire (a) and (b) respectively, which may be due to dimensional inaccuracy

during the fabrication stage and also due to errors in the measurement technique. This trend for the first 27th draws reflects on the trends in the drawing process for subsequent draws. Hence, we can conclude that the conservation of volume is applicable for the prediction of the length of the microwires for all the draws.

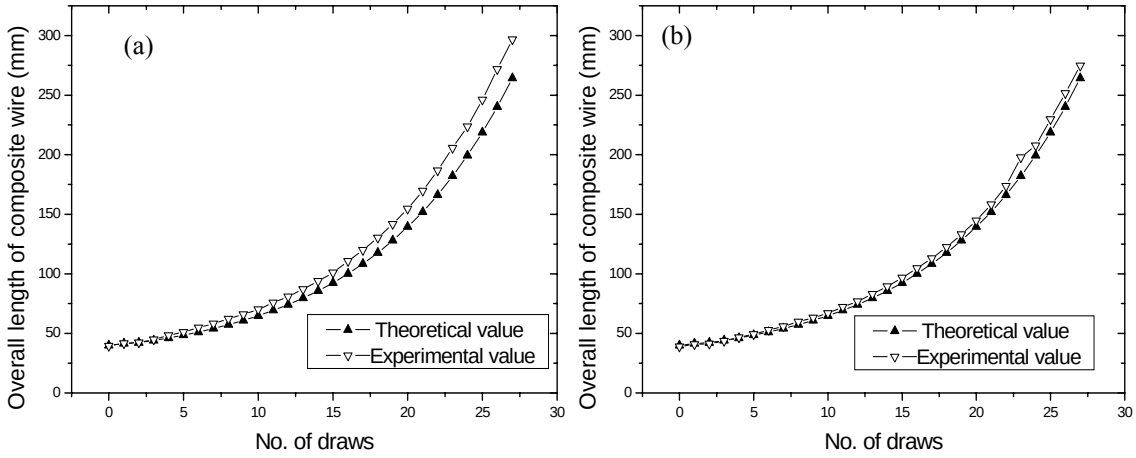

Fig. 135 Experimental and theoretical values of the length of two wire (a) and (b), each with thickness ratio 1:4:1.

9.3. Effect of final annealing on magnetic properties, MI effect & maximum sensitivity

Final annealing at different annealing temperatures: 550^{o}C, 650^{o}C, 750^{o}C, 850^{o}C, 950^{o}C was conducted on the composite wire samples of diameter 34 μm and thickness ratio 1:4:1. Fig. 136 shows the MI effect curves at different annealing temperatures. All the MI effect curves show single-peak curves, indicating dominantly longitudinal anisotropies of the composite wires.

The longitudinal anisotropies arise due to the nature of the cold-drawing process in which wires were drawn through the drawing dies, with the wires repeatedly drawn in the direction in line with the axis of the wire, causing the grains to become elongated. Annealing was essential in this process to release the residual stress induced during the cold-drawing process.

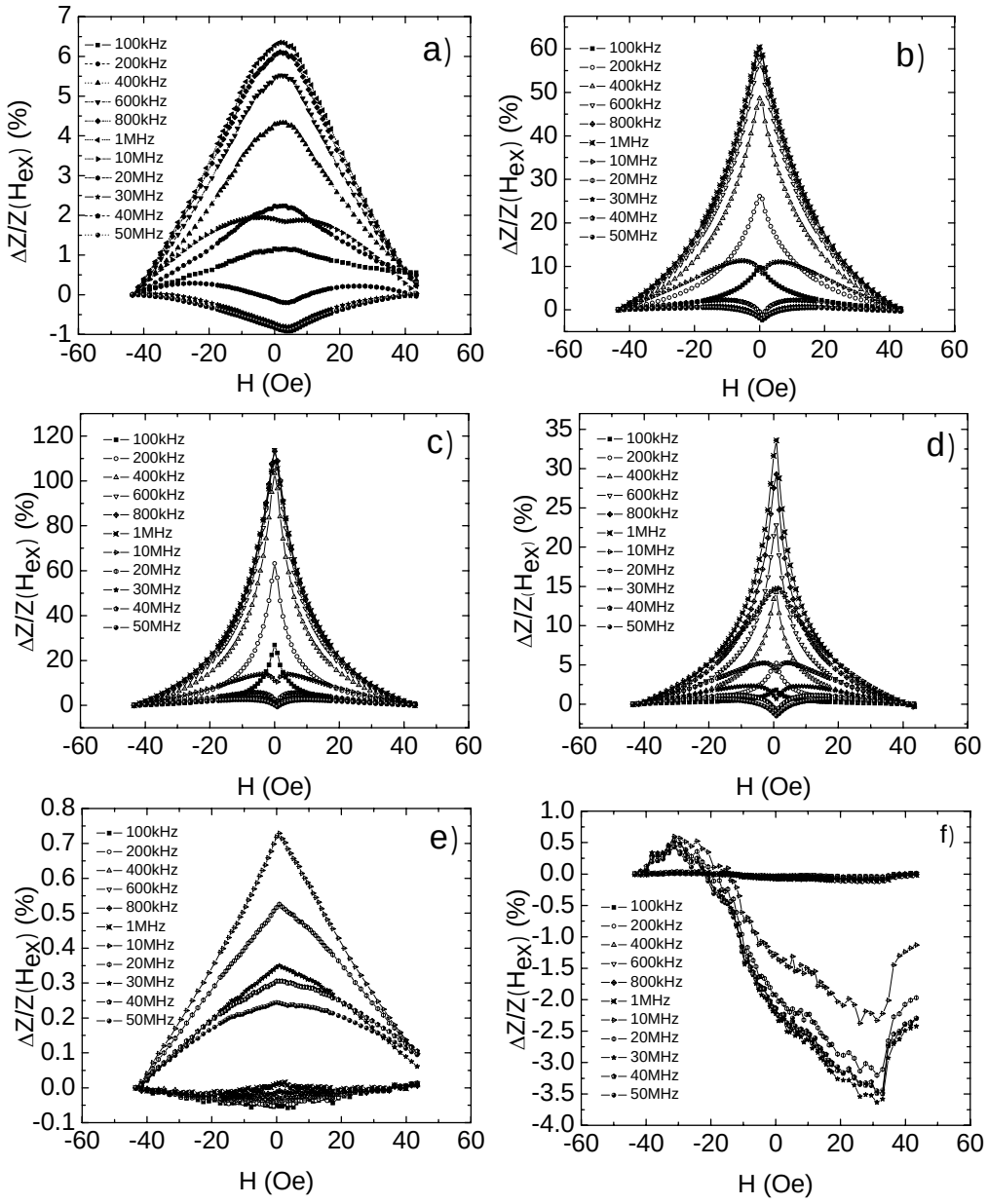

Fig. 136 MI effect curves of the 34 μm diameter composite wires at different annealing conditions: (a) without annealing, (b) annealed at 550°C, (c) annealed at 650°C, (d) annealed at 750°C, (e) annealed at 850°C, and (f) annealed at 950°C.

The release of residual stress is evident from the enhancement of MI effect, as shown in Fig. 136 (a) and (b). However, as annealing temperature was changed to 950^{o}C, MI ratio drops drastically to merely 0.6%. Typical features of the MI curve were also not observable at temperatures above 950^{o}C. This can be attributed to the fact that annealing temperature had risen to a point too close to the melting point of the metals.

This will inevitably lead to changes and degradation in the structure of the composite wires, leading to the loss of the MI effect.

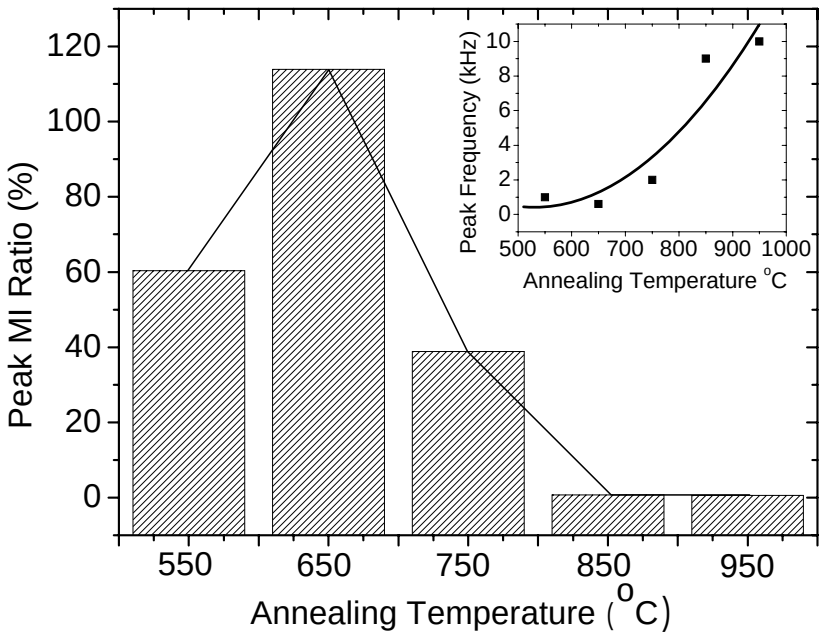

Fig. 137 Effect of annealing temperature on the peak MI% ratio (the inset graph displays the effect of annealing temperature on the peak frequency).

As shown in Fig. 137, as annealing temperature was increased, the magnitude of the MI effect initially increased from 60.4% at 550°C to 113.9% at 650°C and then decreased drastically to 0.60% at 950°C. There appears an optimum temperature range at around 650°C. At elevated annealing temperatures above 850°C, the magnitudes of the MI effect of the composite wires were observed to be extremely low. It must also be noted that peak frequency of the specimens annealing at different annealing temperature increases with increasing annealing temperature. This increase could be due to the occurrence of inter-diffusion between the two layers, causing a shift in the boundary of the magnetic and conductive layer and also a change in the value of skin depth. Correspondingly, as shown in Fig. 138, the coercivities of the magnetic layer were observed to increase with increasing annealing temperature,

strongly suggesting that the permeability of the magnetic layer was decreased with increasing annealing temperature.

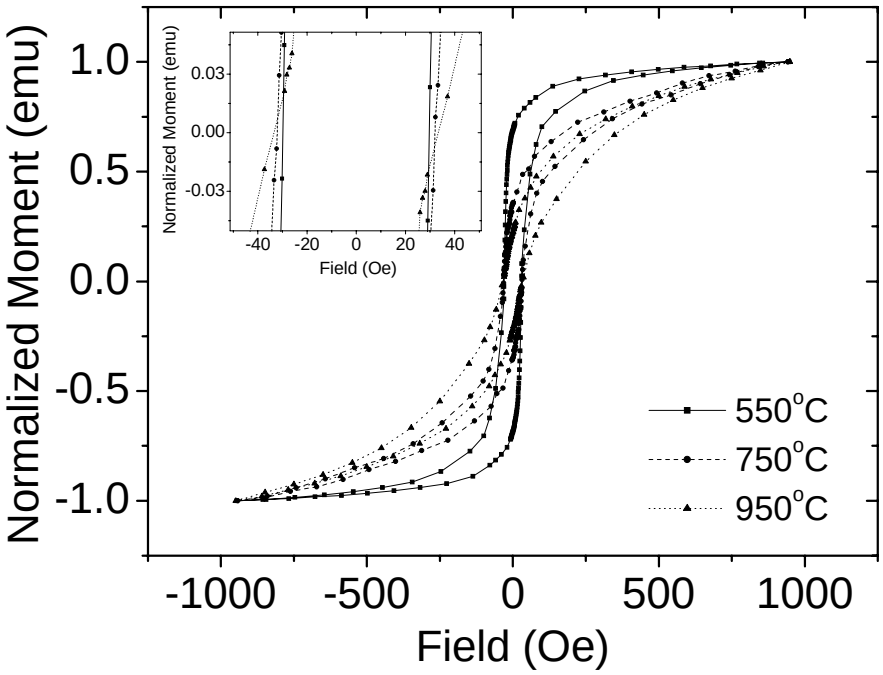

Fig. 138 Hysteresis loops for different annealing temperatures (the inset graph shows a zoom-in view of the hysteresis loops).

With increasing annealing temperature, from the shape of the hysteresis loops, the resultant anisotropy of the composite wires was also observed to be less longitudinal and more circumferential with increasing annealing temperature. This change in anisotropy may be caused by the recrystallization of the $Ni_{80}Fe_{20}$ grains and thus the magnetocrystalline anisotropy of the wires.

The results from surface morphology studies as well as compositional measurements pointed to several possible reasons for the decline in the permeability of the magnetic layer and the MI effect. As shown in Fig. 139, the average particle sizes of the magnetic layer were observed to increase gradually and then drastically at annealing temperatures above 750°C. Thus, the surface roughness of the wires increased. This strongly indicated a great increase in the average grain sizes of the magnetic layer. When the average grain size is below the exchange interaction length

L_{ex}, which was calculated to be 270nm for $Ni_{80}Fe_{20}$, coercivity increases as the average grain size increases [101]. Thus, it is postulated that the increasing average grain size of the magnetic layer is one of the contributions to the trends presented in Fig. 137 and Fig. 138. Furthermore, surface and cross-sectional compositional measurements have revealed an interesting phenomenon.

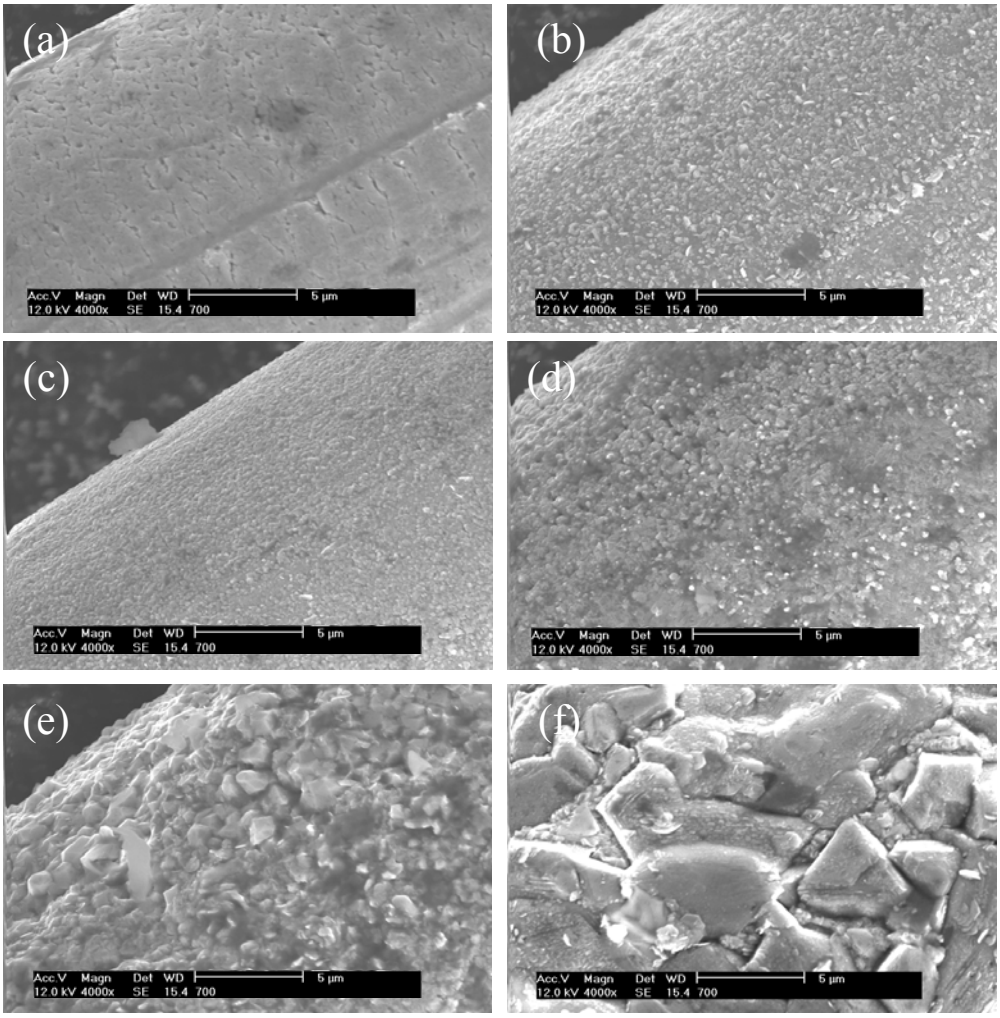

Fig. 139 SEM photos of the 34 µm diameter wire at different annealing conditions: (a) without annealing, (b) annealed at 550°C, (c) annealed at 650°C, (d) annealed at 750°C, (e) annealed at 850°C, and (f) annealed at 950°C.

Surface composition measurements revealed that the average Ni% decreased with increasing temperature (Fig. 140). It was reported [117] that above the annealing temperature of 250ºC, diffusion between the NiFe and Cu layers starts to occur. Cross sectional composition measurements displayed the occurrence of inter-diffusion of Ni

and Cu atoms between the magnetic and conductive layer, with the diffusion rate extremely high at the elevated high annealing temperatures. The cross-sectional distribution of the composition of the 34 μm in diameter composite wires before and after annealing (at 850°C) as well as the SEM photos of the cross-sections can be seen in Fig. 141. It should be noted that the diffusion rate was so high at 850°C that the boundary between $Ni_{80}Fe_{20}$ and Cu layer became unclear, as compared to that of the specimen before annealing.

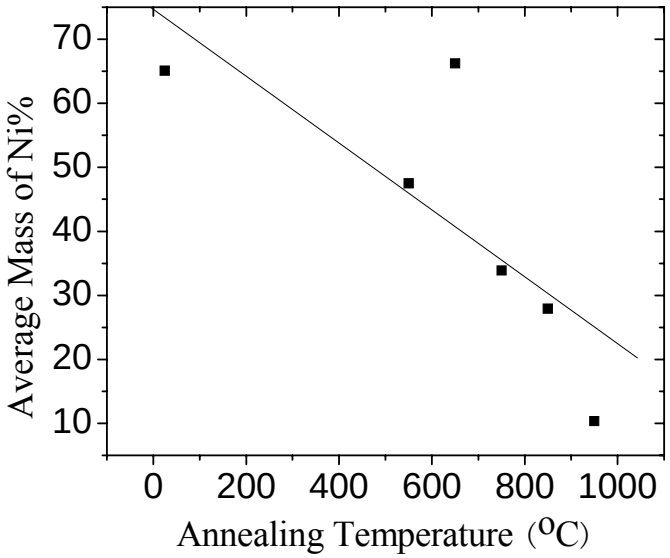

Fig. 140 Plot showing the (surface) variations of average Ni% with annealing temperature

Fig. 142 displays the effect of annealing temperature on the maximum sensitivity of the annealed composite wires as sensing elements in orthogonal fluxgate sensors. The maximum sensitivity was observed to initially increase, from 10 mV/Oe to 53.5 mV/Oe, till an annealing temperature of 750°C and then decreases drastically to 1 mV/Oe at 950°C. The initial increase in maximum sensitivity could be attributed to the increase in permeability due to stress release. However, at annealing temperatures were between 650°C and 750°C, the effect of the deviation of composition (from the ideal composition of permalloy), caused by the inter-diffusion of the magnetic and

conductive layer, as well as the effect of grain growth occurring during annealing overcome that of stress release, causing a decline in permeability. Thus, the maximum sensitivity of the composite wires annealed at temperatures of 750°C - 950°C decreased.

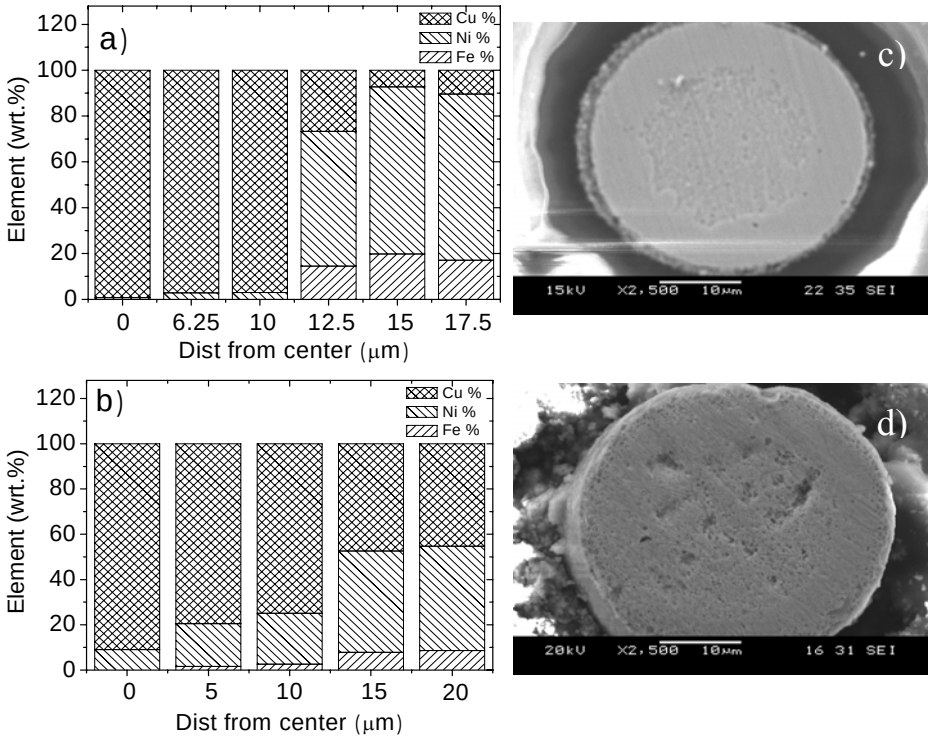

Fig. 141 Plot showing the composition distributions over the cross-sections of composite wires (from centre of wire) with and without annealing: a) without annealing, b) annealed at 850°C; SEM photos showing cross-section views of the wires with and without annealing: c) without annealing, d) annealed at 850°C.

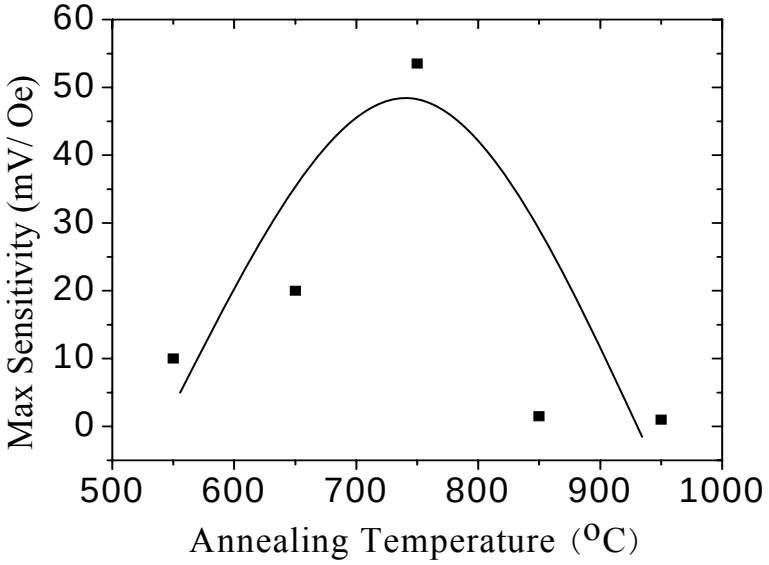

Fig. 142 Graph of maximum sensitivity of the wire in variation with the annealing temperature.

9.4. Summary

Cold-drawn NiFe wires of 34 μm in diameter have been successfully developed. The process consists of 82 draws, intermediate annealing after every nice draws and a final annealing at the end of the draws.

1. The ratio of NiFe:Cu has been found to remain relatively unchanged. This is of paramount importance as the thickness of the composite wire layers can be controlled.
2. During drawing, the following phenomenon has been observed: A) a considerable amount of Cu protruded from the $Ni_{80}Fe_{20}$ after the first draw. The protrusion later sunk back after subsequent draws at a reduced rate and then became unobservable after 6 draws; B) with the ratio of diameter of Cu core to the overall diameter remaining relatively unchanged, the prediction of the final length and diameter of the microwires can be facilitated by the theory of conservation of volume.
3. The effect of the annealing temperature, ranging from 550^{o}C to 950^{o}C, on the magnetic properties and sensing performance has been investigated. The results showed that the material permeability initially increased as the annealing temperature increased, till the temperature reached a critical value, and then decreased drastically with further increase in the annealing temperature. The initial increase in permeability could be attributed to the benefits of stress release, while the later decrease in permeability could be attributed to increasing inter-diffusion rate between the $Ni_{80}Fe_{20}$ and Cu layers with increasing annealing temperature.

Chapter 10 Deposition Methods on Magnetic Properties of NiFe/Cu Composite Wires

The $Ni_{80}Fe_{20}$/Cu composite wire specimens in this study were developed mainly by two deposition methods: 1) magnetron sputter deposition; and 2) electrodeposition. For magnetron sputtering, each sputtering process lasted for 100 s. The base pressure for the sputtering is approximately 2.5×10^{-6} torr. The deposition pressure is around 7 mTorr. The deposition power was set to be 200 W. The sputtered specimens were then annealed under various annealing temperature to obtain a range of nanocrystalline grain sizes. For electrodeposition, the process was carried out at the plating current density J of 2 A/dm^2 and at a deposition time of 3 minutes for direct current electrodeposition and 6 minutes for pulse and pulse reverse electrodeposition for 50% duty cycle. The plating time was manipulated in order to obtain deposited layers of similar thickness.

10.1. Nanocrystalline Permalloy by Sputter Deposition

Nanocrystalline $Ni_{80}Fe_{20}$/Cu specimens were made by magnetron sputter deposition and the specimens were then annealed at temperatures from 100°C to 500°C. The average grain sizes of the $Ni_{80}Fe_{20}$ layer increased from 7 nm to 25 nm as the annealing temperature was increased from 100°C to 500°C, as shown in Fig. 143. More energy is available at higher annealing temperature to overcome the threshold energy level for crystallite size growth. The XRD spectra of the specimens under different annealing temperatures, as shown in the inset graph in Fig. 143, displays the narrowing of the peaks with increasing annealing temperature.

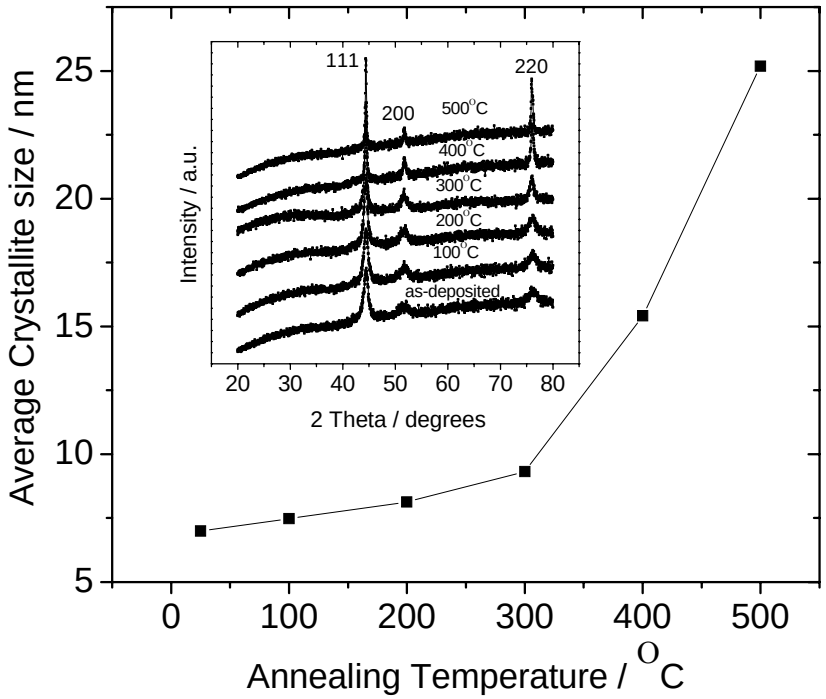

Fig. 143 Increase of average crystallite size with increasing annealing temperature. The inset graph gives the XRD spectra of specimens under different annealing temperature, showing texture orientation.

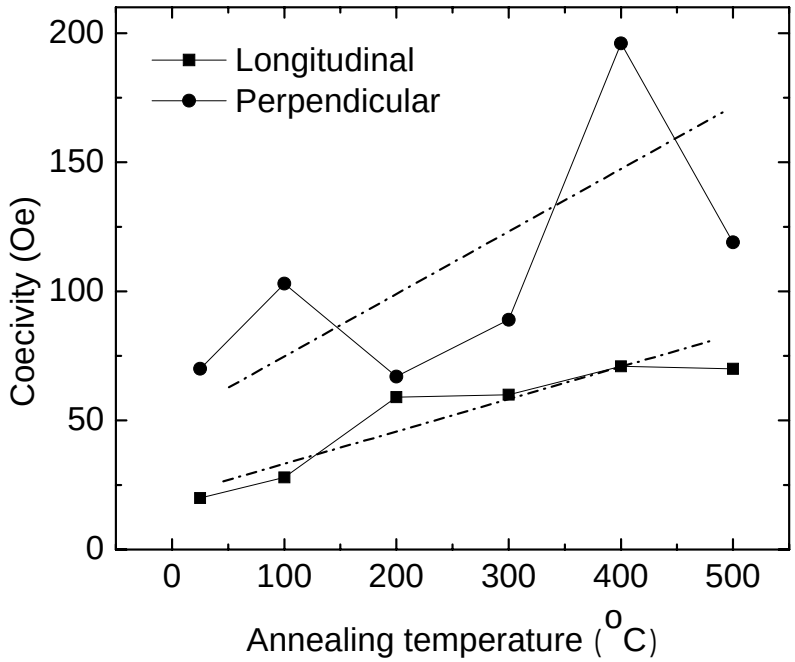

Fig. 144 Increase of longitudinal and perpendicular coercivity with increasing annealing temperature.

The coercivities of the specimens were then measured in the longitudinal and perpendicular directions. Apparently, the coercivity (longitudinal and perpendicular) increased as the annealing temperature increased, as shown in Fig. 144. The

experimental result is in good agreement with the random anisotropy model [101]. As the grain size was smaller than the ferromagnetic exchange interaction length, 270 nm in the case of permalloy, the coercivity decreased as the grain size decreased.

10.2. Nanocrystalline Permalloy by Electrodeposition

$Ni_{80}Fe_{20}$ specimens were developed by direct current electrodeposition, pulsed electrodeposition and pulsed reverse electrodeposition. Most of the electrodeposition processes were carried out with the addition of saccharin in the electrolyte solution as permalloy from such electroplating baths was found to possess much smaller grain sizes. Saccharin, being a well-known brightener, is used to refine the grains of the deposits by inhibiting surface diffusion of adatoms towards preferential growth centers and thus promoting nucleation. The electrodeposition current waveform of each method is shown in Fig. 145. Pulsed electrodeposition was carried at 50% duty cycle while pulsed reverse electrodeposition was also carried out at 50% duty cycle but with an anodic current I_N for improved smoothness.

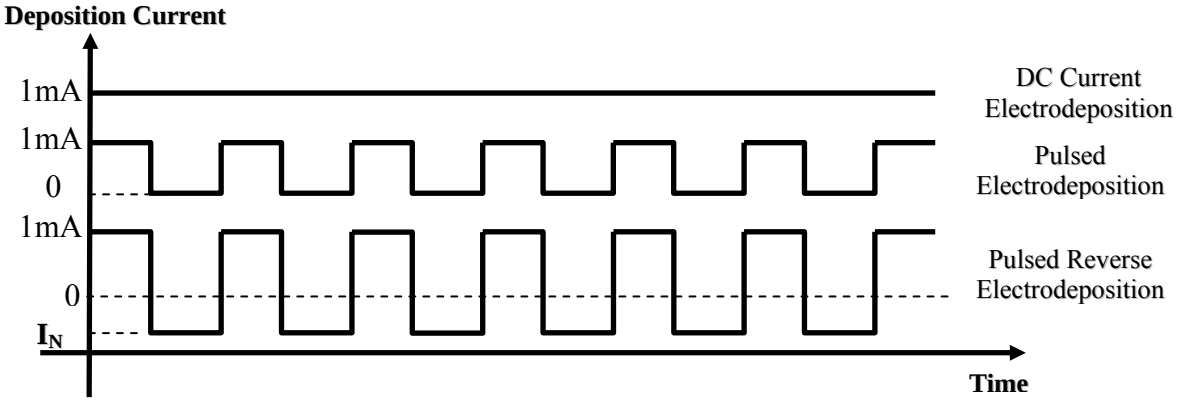

Fig. 145 Electrodeposition current waveform of various electrodeposition methods. I_A denotes anodic current (negative current).

The specimens from different electrodeposition methods were then measured under XRD and the average crystallite sizes were calculated. As shown in Fig. 146, the addition of saccharin into the electrolyte solution decreased the average grain size

of the permalloy layer from 51.7 nm to 14.8 nm. Saccharin exists as molecules in the electrolyte solution, inhibits surface diffusion of the adatoms at the surface and promotes nucleation. The pulse plated (or pulsed electrodeposition) specimens have been found to possess the smallest average grain size because of the presence of the off-time. Blocking of growth centers of the cathode occurs during the off-time as a result of absorption of inhibiting species [99]. This forces the system to create new nuclei at each new pulse. Fig. 146 also shows that introducing a seeded Cu layer below the $Ni_{80}Fe_{20}$ layer lowers the average grain size from 14.8 nm to 12.6 nm.

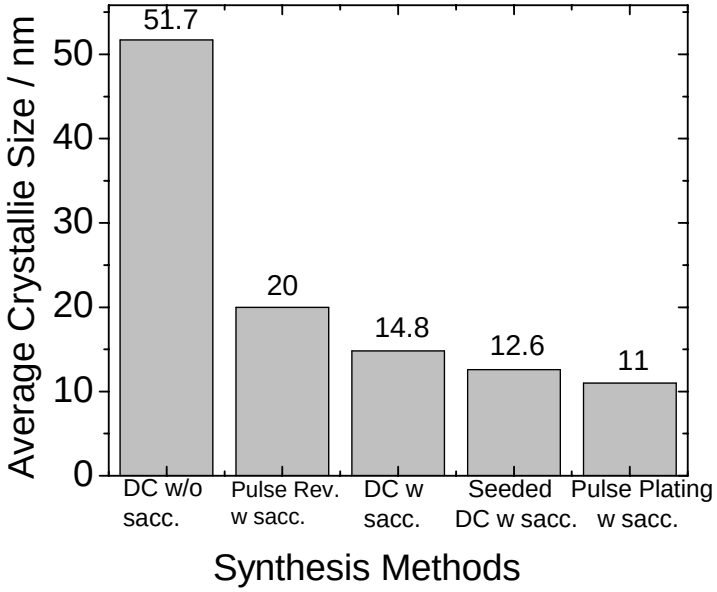

Fig. 146 Variation of crystallite sizes with different synthesis methods.

Pulsed reverse plated specimens possess $Ni_{80}Fe_{20}$ layers of average grain size of 20 nm, which was slightly larger than direct current electrodeposition with saccharin added. The reduction of the saccharin effect could be due to the changing polarity of the cathodic and anodic current. This reduces the possibility for the saccharin molecules to be at the surface of the deposited layer, limiting the surface diffusion of adatoms.

Fig. 147 shows the coercivity of the specimens developed by using different electrodeposition methods. Generally, the coercivity decreases with decreasing

nanocrystalline grain size below the ferromagnetic exchange length. The only exceptions are the direct current plated specimens with seeded Cu layer. The deposited layer could be slightly inhomogeneous because of the introduction of the seeded layer. In the overall trend, the coercivity results correspond well with the crystallite size results.

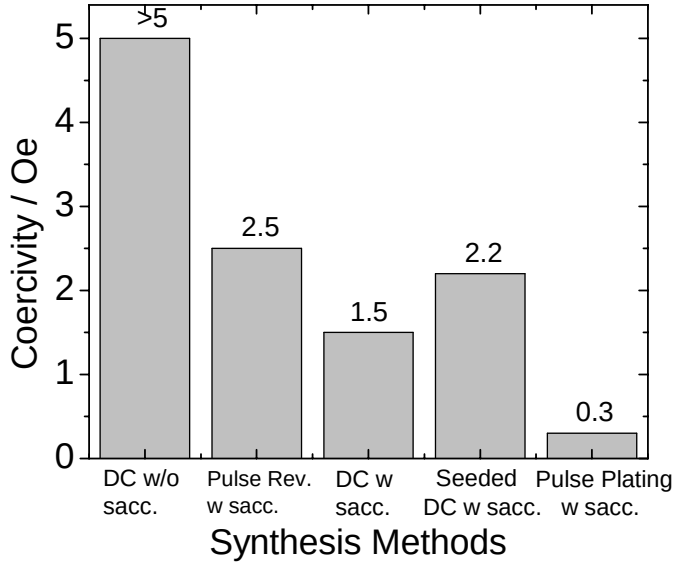

Fig. 147 Variation of coercivity of specimens from different electrodeposition methods.

10.3. Variation of Magnetic Properties with Crystallite Size

As shown in Fig. 148, coercivity of the specimens was found to generally decrease with decreasing crystallite sizes, regardless of the synthesis methods. The thickness of the deposited magnetic layer (as well as the copper core) had been controlled to be similar by the manipulation of the deposition time in order to study the effects of the crystallite size on coercivity, regardless of the thickness factor. However, Fig. 148 has shown that depending on the synthesis methods, the specimens produced from different synthesis methods tend to possess different material properties such as different levels of residual stress and uniformity. $Ni_{80}Fe_{20}$/Cu specimen, prepared in sputter deposition, were observed to possess coercivities in the range of 50-70 Oe, while in general, the specimens developed by electrodeposition

were observed to possess coercivity in the range less than 5 Oe. This may be largely due to the level of residual stress being higher in the sputtered specimens than that in the electrodeposited specimens.

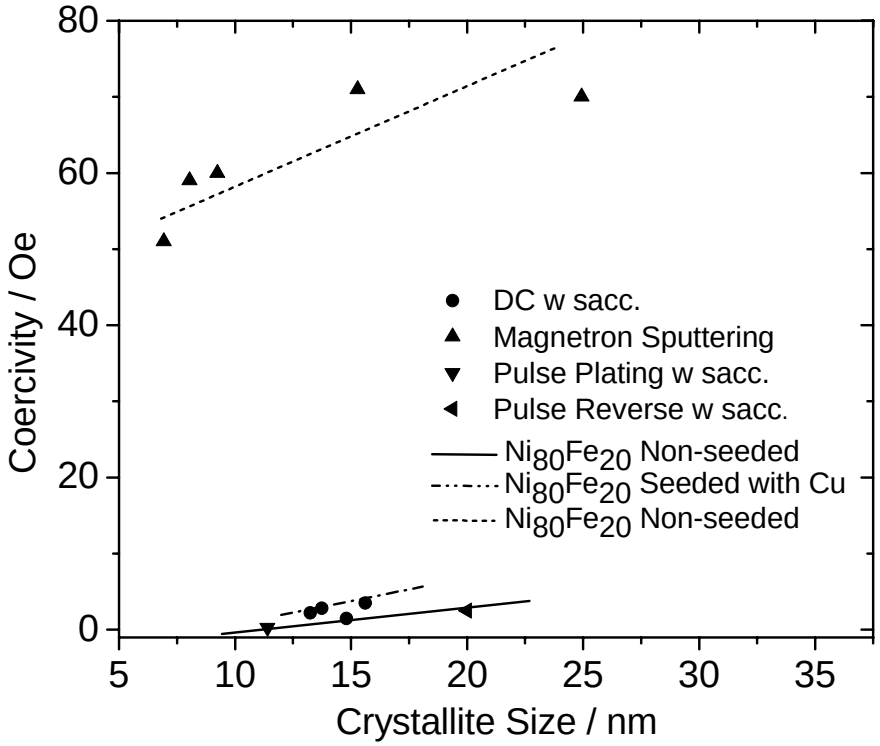

Fig. 148 Variation of coercivity with crystallite sizes for different synthesis methods.

10.4. Summary

Permalloy layer of $Ni_{80}Fe_{20}$/Cu with the nanocrystalline grain sizes ranging from 52 nm to 7 nm have been developed by using magnetron sputtering and different electrodeposition methods, including direct current electrodeposition with and without saccharin added, pulsed electrodeposition, pulsed reverse electrodeposition with saccharin added and the introduction of a Cu seeded layer. The results showed that apparently, the coercivity decreases as the grain size decreases. However, since different deposition methods produce specimens of varying level of residual stress and uniformity, the range of the coercivity trends is according to the deposition method used.

Chapter 11 Conclusions and Recommendations

11.1. Conclusions

In this study, research and development have been conducted on the fabrication technology for super permeability NiFe/Cu composite wires for micro magnetic sensor applications. The following conclusions can be drawn:

1. Magneto-optical micro-magnetometer studies revealed that in near-surface range of DC electrodeposited NiFe/Cu wires, there are circular domains with alternating left- and right-handled magnetization in adjacent domains, with the size of circular domains and the saturation field H_s found to be dependent on Fe% in the NiFe layers. This was attributed to variations of the effective constant of magnetic anisotropy K, caused by structural changes of the wires. The magnetic-field behaviour of the magnetization components, parallel and perpendicular to the magnetic field applied along the wire length, shows that there is the curling mode of the magnetization reversal in the examined wires.

2. The influence of the electroplating parameters was investigated in relation to the resulting magnetic properties of DC electrodeposited NiFe/Cu wires.
   a) The effect of plating current density J on the magnetic properties of the plated material in electroplating of NiFe/Cu composite wires has been studied and the results showed a critical value of plating current density J of 2A/dm^2 was found, below which soft magnetic properties decreased with increasing current density and above which soft magnetic properties increased with increasing current density. The results also showed that plating current density affects the magnetic anisotropy of plated wires.

b) Electrolyte pH value was found to affect the composition of plated layer in NiFe plating. The Fe% generally increases as pH value increases from 2.5 to 4.5. The magnetic property of plated layer, in terms of MI ratio, depends directly on the composition of plated layer rather than the electrolyte pH value.

c) The magnetic properties of deposited material in variation with thickness t_{FM} of deposited layer have been investigated. The results showed that thickness affects composition of deposited material, which makes coercivity increase with increasing thickness. It also affects average grain size of deposited material, which makes coercivity increase with increasing thickness. It further affects uniformity of the deposited material, which causes coercivity decrease with increasing thickness. As a combined effect of thickness on the magnetic properties of deposited material, the coercivity of the material can be in a dynamic constant state as the thickness varies. Under such circumstances, the thickness has mainly geometrical effect on the MI of the composite wire.

d) The alloying effect of molybdenum has been investigated. It has been found that at the composition of $Ni_{78}Fe_{18}Mo_{4,}$ the material alloy is magnetically softest, as indicated by the lowest longitudinal and circumferential coercivity of 0.88 Oe and 1.04 Oe, respectively, and also by the lowest peak field intensity of 0.80 Oe in the MI effect curve obtained. The magnetic properties of $Ni_{78}Fe_{18}Mo_4$ have been found to be better than $Ni_{79}Fe_{21}$.

3. A nannocrystalline electrodeposition technology has been developed, in which the grain size manipulation of the NiFe layer has been successfully carried out by two main approaches: 1) addition of additive saccharin; 2) altering the plating current

waveform, i.e. DC plating, pulse plating and pulse reverse plating, and also by varying the various process parameters.

a) The upper and lower limits of the nanocrystalline grain size have been theoretically estimated to be between 270 nm and 10 nm separately. Within this range, grain size reduction will benefit greatly magnetic properties.

b) The effect of the pulse plating parameter duty cycle on the composition, thickness and the grain size of the coating layer was investigated. At duty cycle 50%, average grain size has been found to be the smallest.

c) Nanocrystalline permalloy of grain sizes ranging from 52 nm to 11 nm has been developed, with the grain size controlled by using different electroplating methods—DC plating without saccharin added, DC plating with saccharin added, or pulse plating with saccharin added. The coercivity of nanocrystalline permalloy decreases rapidly and the MI effect ratio increases greatly as grain size decreases from 52 nm to 11 nm. This can be explained by the random anisotropy model.

d) Pulse-reverse electrodeposited $Ni_{80}Fe_{20}$/Cu composite wires have been developed. The theoretical calculations and experimental results showed that the working current efficiency of the pulse-reverse electrodeposition for permalloy is high, up to 87% in the present case studied. With the introduction of an anodic current, the deposited permalloy was found to be better in uniformity, which resulted in higher peak MI% ratio of $Ni_{80}Fe_{20}$/Cu wires, despite associated side effect of grain size enlargement. Within the tested range of the present study, smaller anodic current amplitudes resulted in lower coercivity of deposited material and higher MI effect of NiFe composite wires.

e) $Ni_{80}Fe_{20}$/Cu composite wires of a variety of nanocrystalline crystallite sizes have been developed using 4 different electrodeposition methods. The difference in electrodeposition methods lies in the current waveforms: DC electrodeposition, pulse electrodeposition, PR electrodeposition and PR electrodeposition with off-time. Introducing an off-time period was found to reduce average crystallite sizes of deposited material. The comparison of the resultant crystallite size was made and the order was observed to be (in descending crystallite size): PR electrodeposition with off-time, pulse electrodeposition, DC electrodeposition and PR electrodeposition. The magneto-impedance (MI) effect of the specimens produced by PR electrodeposition with off-time was higher than those produced by PR electrodeposition without off-time, due to grain size reduction caused by the off-time.

4. The effects of an applied longitudinal magnetic field in the electroplating of NiFe/Cu composite wires on composition, microstructure and magnetic properties of the plated layer have been investigated.
   a) The longitudinal magnetic field in electroplating makes the composition of plated material more uniform.
   b) The longitudinal controlling magnetic field was found to have no obvious effect on plating rate in terms of thickness of plated layer.
   c) The longitudinal magnetic field in the composite wire plating makes the crystals in the plated layer pack more orderly, which enhances uniformity of plated material and therefore increases magnetic softness of plated material.

d) The longitudinal magnetic field shifts the magnetic anisotropy of plated composite wire from circumferential to longitudinal, with the level of the anisotropy change proportional to the longitudinal magnetic field intensity. The variation of the anisotropy from circumferential to longitudinal for composite wires plated under a range of longitudinal magnetic field exhibit a variation from double peak MI ratio curve to single peak MI ratio curve in MI effect testing at high frequency of the testing current.

e) The critical MI effect frequency for a plated composite wire, at which the maximum MI ratio occurs, increase with increasing intensity of the longitudinal magnetic field.

5. The influence of annealing (furnace annealing and DC joule annealing) was investigated in relation to the magnetic properties of NiFe/Cu composite wires.

a) As the annealing temperature was increased from 210°C-1050°C, a general reduction in MI% ratio and sensitivity as well as an increase in coercivity was observed. This trend was due to a decrease in permeability that was attributed to grain growth and inter-diffusion between the two layers, despite stress relief effects. At high annealing temperatures, especially above the recrystallization temperature of 550°C, degradation of magnetic properties was more pronounced. Significant grain growth can also be observed with increasing annealing temperature. Inter-diffusion was observed and in particular, obvious diffusion of nickel into copper was observed at 350 °C and 550 °C, with traces of copper detected along the radial direction of the cross-section, right up to the surface.

b) A DC Joule annealing method has been developed and tested. The results showed that the annealing causes great improvement on MI ratio of composite wires. The highest MI ratio of 1110% has been obtained. The results showed that for the tested wire samples there was an optimum annealing current density, at which the annealed wire has the highest MI ratio. The optimum AC driving frequency for the composite wire GMI sensor was found to be a function of the annealing current density which varies with the magnetic permeability and conductivity of the plated ferromagnetic layer. In terms of the increment in MI ratio of the annealed wires, it has been found that stepped annealing is better than single step annealing and the MI ratio increment increases almost linearly with the cooling rate in the annealing.

6. Cold-drawn NiFe wires of 34 μm in diameter have been successfully developed. The process consists of 82 draws, intermediate annealing after every nice draws and a final annealing at the end of the draws.
   a) The ratio of NiFe:Cu has been found to remain relatively unchanged.
   b) During drawing, the following phenomenon has been observed: A) a considerable amount of Cu protruded from the $Ni_{80}Fe_{20}$ after the 1^{st} draw. The protrusion later sunk back after subsequent draws at a reduced rate and then became unobservable after 6 draws; B) with the ratio of diameter of Cu core to the overall diameter remaining relatively unchanged, the prediction of the final length and diameter of the microwires can be facilitated by the theory of conservation of volume.
   c) Investigations of the effects of the annealing temperature, ranging from 550^{o}C to 950^{o}C, on the magnetic properties and sensing performance revealed that

the material permeability initially increased as annealing temperature was increased, till the temperature reached a critical value, and then decreased drastically with further increases in the annealing temperature.

7. Permalloy layer of $Ni_{80}Fe_{20}$/Cu with the nanocrystalline grain sizes ranging from 52 nm to 7 nm have been developed by using magnetron sputtering and different electrodeposition methods, including direct current electrodeposition with and without saccharin added, pulsed electrodeposition, pulsed reverse electrodeposition with saccharin added and the introduction of a Cu seeded layer. The results showed that apparently, the coercivity decreases as the grain size decreases. However, since different deposition methods produce specimens of varying level of residual stress and uniformity, the range of the coercivity trends is according to the deposition method used.

11.2. Recommendations

1. Currently, the author does not have access to magnetostriction measurement equipments and as such, the magnetostriction of the developed magnetic materials cannot be characterized. This is a pity as magnetostriction measurement is the primary characterization of magnetic materials. As such, it is recommended that magnetostriction measurements be carried out on the composite wires.
2. In pulse plating, ultra-fast pulses (e.g. nano-second, pico-second) in the current waveform should be used to fabricate composite wires and studies should be conducted to investigate the effect of such ultra-fast pulses on the deposited structures.

Publication written from results described in thesis

1) H.L. Seet, S.H. See, X.P. Li, J.Y. Lee, K.Y.T. Lee, S.H. Teoh, C.T. Lim, "Study of the parameters of electroplating of ferromagnetic materials in relation to material permeability" *Materials Science Forum* **437-438** 475-478 (2003)

2) S.H. See, H.L. Seet, X.P. Li, J.Y. Lee, K.Y.T. Lee, S.H. Teoh, C.T. Lim, "Effect of nanocrystalline electroplating of NiFe on the material permeability", Materials Science Forum **437-438** 53-56 (2003)

3) X.P. Li, Z.J. Zhao, H.L. Seet, W.M. Heng, T.B. Oh, J.Y. Lee, "Effect of magnetic field on the magnetic properties of electroplated NiFe/Cu composite wires" *Journal of Applied Physics* **94(10)** 6655-6658 (2003)

4) X.P. Li, Z.J. Zhao, C. Chua, H.L. Seet, L. Lu, "Enhancement of giant magnetoimpedance effect of electroplated NiFe/Cu composite wires by DC joule annealing", *Journal of Applied Physics* **94(12)** 7626-7630 (2003)

5) X.P. Li, Z.J. Zhao, H.L. Seet, W.M. Heng T.B. Oh, J.Y. Lee, "Magnetically controlled electroplating of NiFe/Cu composite wires" *Electrochemical and Solid-State Letters* **7(1)** C1-C3 (2004)

6) X.P. Li, H.L. Seet, Z.J. Zhao, Y.K. Kong, H. Gong, "Nanocrystalline deposition for developing high permeability ferromagnetic materials", *Transactions of the Materials Research Society of Japan* **29(4)** 1695-1700 (2004) (Invited)

7) Z.J. Zhao, X.P. Li, C. Chua, H.L. Seet, L. Lu, "Effect of annealing on the GMI response of electroplated NiFe/Cu composite wires", *Transactions of the Materials Research Society of Japan* **29(4)** 1701-1704 (2004)

8) Z.J. Zhao, X.P. Li, C. Chua, H.L. Seet, L. Lu, "Effect of annealing on magnetic properties of NiFe/Cu composite wires", *Transactions of the Materials Research Society of Japan* **29(4)** 1705-1708 (2004)

9) X.P. Li, Z.J. Zhao, H.L. Seet, P.L. Lim, K.S. Lee, "Step current electrodeposition of nanocrystalline $Ni_{80}Fe_{20}$/Cu composite wires" *International Journal of Nanoscience* **4(2)** 179-186 (2005)

10) X.P. Li, H.L. Seet, Z.J. Zhao, Y.K. Kong, "Development of high permeability nanocrystalline ferromagnetic materials by pulse plating", *Journal of Metastable and Nanocrystalline Materials* **23** 163-166 (2005)

11) H.L. Seet, X.P. Li, Z.J. Zhao, Y.K. Kong, H.M. Zheng, W.C. Ng, "Development of high permeability nanocrystalline permalloy by electrodeposition", *Journal of Applied Physics* **97** 10N304-1-3 (2005)

12) H.L. Seet, X.P. Li, Z.J. Zhao, L.C. Wong, H.M. Zheng, K.S. Lee, "Current density effect on magnetic properties of nanocrystalline electroplated $Ni_{80}Fe_{20}$/Cu composite wires", *Journal of Magnetism and Magnetic Materials* **302** 113-117 (2006)

13) X.P. Li, H.L. Seet, J. Fan, J.B. Yi, "Electrodeposition and characteristics of $Ni_{80}Fe_{20}$/Cu composite wires", *Journal of Magnetism and Magnetic Material*s **304** 111-116 (2006) (invited)

14) H.L. Seet, X.P. Li, N. Ning, W.C. Ng, J.B. Yi, "Effect of magnetic coating layer thickness on the magnetic properties of electrodeposited NiFe/Cu composite wires", *IEEE Transactions on Magnetics* **42(10)** 2784-2686 (2006)

15) H.L. Seet, X.P. Li, K.S. lee, C.S. Yap, H.M. Zheng, "Development of micro $Ni_{80}Fe_{20}$/Cu composite wire by cold-drawing" *Thin Solid Films* **505** 148-151 (2006)

16) E.E. Shalyguina, X.P. Li, H.L. Seet, N.M. Abrosimova, A.N. Shalygin, "Magneto-optical investigation of local magnetic properties and micromagnetic structure of NiFe/Cu microwires", *Thin Solid Films* **505** 165-167 (2006)

17) H.L. Seet, X.P. Li, K.S. Lee, H.Y. Chia, "Nanocrystalline grain size control for $Ni_{80}Fe_{20}$/Cu micro-composite wires by different electrodeposition methods", *Journal of Materials Processing Technology* **192-193** 225-228 (2007)

18) H.L. Seet, X.P. Li, K.S. Lee, L.Q. Liu, "Cold-drawing of micro Ni80Fe20/Cu composite wires" *Journal of Materials Processing Technology* **192-193** 350-354 (2007)

19) H.L. Seet, X.P. Li, K.S. Lee, H.Y. Chia, H.M. Zheng. W.C. Ng, "The magnetic properties of pulse reverse electrodeposited nanocrystalline NiFe/Cu composite wires in relation to the anodic current" *Physica Scripta* **T129** 165-169 (2007)

20) H.L. Seet, X.P. Li, K.S. Lee, K.Y. Yee, L.Q. Liang, J.B. Yi, "Effect of annealing on the magnetic properties and performance of cold-drawn $Ni_{80}Fe_{20}$/Cu wires in magnetic sensors" *Physica Scripta* **T129** 160-164 (2007)

21) H.L. Seet, X.P. Li, H.J. Neo, K.S. Lee, "Magnetic properties of high permeability NiFeMo/Cu composite wires", *Journal of Alloys and Compounds* **449** 96-100 (2008)

22) H.L. Seet, X.P. Li, W.C. Ng, H.Y. Chia, H.M. Zheng, K.S. Lee, "Development of $Ni_{80}Fe_{20}$/Cu nanocrystalline composite wires by pulse-reverse electrodeposition" *Journal of Alloys and Compounds* **449** 279-283 (2008)

23) H.L. Seet, X.P. Li, J.B. Yi, W.Y. Ooi, K.S. Lee, “Effect of deposition methods on the magnetic properties of nanocrystalline permalloy” *Journal of Alloys and Compounds* **449** 284-287 (2008)

References

[1] D.K. Wood, K.K. Ni, D.R. Schmidt, A.N. Cleland, "Submicron giant magnetoresistive sensors for biological applications", *Sensors and Actuators A* **120** 1–6 (2005)

[2] Horia Chiriac_, Mihai Tibu, Anca-Eugenia Moga, Dumitru D. Herea, " Magnetic GMI sensor for detection of biomolecules", *Journal of Magnetism and Magnetic Materials* **293** 671–676 (2005)

[3] Per Dannemand Andersen, Birte Holst Jørgensen, Lars Lading, Birgitte Rasmussen, "Sensor foresight—technology and market", *Technovation* **24** 311–320 (2004)

[4] J.C. Rife, M.M. Miller, P.E. Sheehan, C.R. Tamanaha, M. Tondra, L.J. Whitmana "Design and performance of GMR sensors for the detection of magnetic microbeads in biosensors", *Sensors and Actuators A* **107** 209–218 (2003)

[5] Daniel L. Graham1, Hugo A. Ferreira1,2 and Paulo P. Freitas, "Magnetoresistive-based biosensors and biochips", *Trends in Biotechnology* **22 (9)** 455-462 (2004)

[6] Giselher Herzer, "Magnetic materials for electronic article surveillance", *Journal of Magnetism and Magnetic Materials* **254-255** 598-602 (2003)

[7] C. Bouligand, J. Dyment, Y. Gallet and G. Hulot, "Geomagnetic field variations between chrons 33r and 19r (83–41 Ma) from sea-surface magnetic anomaly profiles", *Earth and Planetary Science Letters* **250** 541–560 (2006)

[8] Gunther Kletetschk, Norman F. Ness, J.E.P. Connerney, M.H. Acuna, P.J. Wasilewski, "Grain size dependent potential for self generation of magnetic anomalies on Mars via thermoremanent magnetic acquisition and magnetic interaction of hematite and magnetite",*Physics of the Earth and Planetary Interiors* **148** 149–156 (2005)

[9] D.L. Grahama,, H.A. Ferreira, N. Feliciano, P.P. Freitas, L.A. Clarke, M.D. Amaral, "Magnetic field-assisted DNA hybridisation and simultaneous detection using micron-sized spin-valve sensors and magnetic nanoparticles", *Sensors and Actuators B* **107** 936–944 (2005)

[10] Judith D. Schaechter, Christopher Stokes, Brendan D. Connell, Katherine Perdue, and Giorgio Bonmassar, "Finger motion sensors for fMRI motor studies" , *NeuroImage* **31** 1549 – 1559 (2006)

[11] M. Pannetier, C. Fermona, G. Le Goff, E. Kerr, "Ultra-sensitive mixed sensors—Design and performance" , *Sensors and Actuators A* **129** 247–250 (2006)

[12] Yoshio Okada, Kevin Pratt, Christopher Atwood, Anthony Mascarenas, Richard Reineman, Jussi Nurminen, Douglas Paulson, "BabySQUID: A mobile, high-resolution multichannel magnetoencephalography system for neonatal brain assessment," *Review of Scientific Instruments* **77** 024301-1-024301-9 (2006)

[13] Florian Kaluza, Angelika Grüger, Heinrich Grüger, "New and future applications of fluxgate sensors", *Sensors and Actuators A* **106** 48–51 (2003)

[14] L. Perez, C. Aroca , P. Sánchez , E. López , M.C. Sánchez, "Planar fluxgate sensor with an electrodeposited amorphous core" *Sensors and Actuators A* **109** 208–211 (2004)

[15] K. Enpuku, T. Minotani, T. Gima, Y. Kuroki, Y. Itoh, M. Yamashita, Y. Katakura, S. Kuhara, "Detection of magnetic nanoparticles with superconducting quantum interference device (SQUID) magnetometer and application to immunoassays" *Japan Journal of Applied Physics 2* **38** L1102–L1105 (1999)

[16] P.A. Besse, G. Boero, M. Demierre, V. Pott, R. Popovic, "Detection of a single magnetic microbead using a miniaturized silicon Hall sensor", *Applied Physics Letter*s **80** 4199–4201 (2002)

[17] K.-M.H. Lenssen, D.J. Adelerhof, H.J. Gassen, A.E.T. Kuiper, G.H.J. Somers, J.B.A.D. van Zon, "Robust giant magnetoresistance sensors", *Sensors and Actuators* **85** 1–8 (2000)

[18] D.L. Graham, H. Ferreira, J. Bernardo, P.P. Freitas, J.M.S. Cabral, "Single magnetic microsphere placement and detection on-chip using current line designs with integrated spin valve sensors: biotechnological applications", *Journal of Applied Physics* **91** 7786–7788 (2002).

[19] Y.S. Kim, L.A. Tuanb, S.C. Yu, J.R. Rhee, C.O. Kim, Heebok Lee," Super-giant magneto-resonance effect in glass coated Co83.2B3.3Si5.9Mn7.6 microwires", *Journal of Magnetism and Magnetic Materials* **304** e365–e367 (2006)

[20] Y. Nishibe, H. Yamadera, N. Ohta, K. Tsukada, Y. Nonomura, "Thin film magnetic field sensor utilizing Magneto Impedance effect", *Sensors and Actuators* **82** 155–160 (2000)

[21] K. Postava, J. Pištora, T. Yamaguchi, "Magneto-optic vector magnetometry for sensor applications", *Sensors and Actuators A* **110** 242–246 (2004)

[22] M. Vazquez, "Soft magnetic wires", *Physica B* **299** 302-313 (2001)

[23] Ryusuke Hasegawa, "Magnetic wire fabrication and applications", *Journal of Magnetism and Magnetic Materials* **249** 346-350 (2002)

[24] Ryusuke Hasegawa, "Design and fabrication of new soft magnetic materials", *Journal of Non-Crystalline Solids* **329** 1-7 (2003)

[25] Hans Warlimont, "Amorphous metals driving materials and process innovations", *Materials Science and Engineering A* **304-306** 61-67 (2001)

[26] A. Fert, L. Piraux, "Magnetic nanowires", *Journal of Magnetism and Magnetic Materials* **200** 338-358 (1999)

[27] F. Borza, T.A. Ovari, T. Meydan, "Mechanical torque in the ac field induced rotation of amorphous wires", *Sensors and Actuators A* **129** 224-226 (2006)

[28] H. Chiriac, A.M. Fecioru, T.-A. Ovari, "FMR investigation of surface anisotropy in twisted amorphous wires", *Sensors and Actuators A* **106** 251-254 (2003)

[29] N.A. Buznikov, A.S. Antonov, CheolGi Kim, Chong-Oh Kim, A.A. Rakhmanov, Seok-Soo Yoon, "The effect of domain-walls motion on second harmonic amplitude of magnetoinductive response in Co-based amorphous wires", *Journal of Magnetism and Magnetic Materials* **285** 101-111 (2005)

[30] L.V. Panina, H. Katoh, K. Mohri, "Magnetization processes in amorphous wires in orthogonal fields", *IEEE Transactions on Magnetics* **29(6)** 2524-2526 (1993)

[31] L.V. Panina, K. Mohri, D.P. Makhnovskiy, "Mechanism of asymmetrical magnetoimpedance in amorphous wires", *Journal of Applied Physics* **85(8)** 5444-5446 (1999)

[32] D. Garcia, V. Raposo, O. Montero, J.I. Iniguez, "Theoretical estimation of magnetoimpedance frequency dependence in amorphous wires", *Journal of Magnetism and Magnetic Materials* **316** e846-e849 (2007)

[33] R. Malmhall, K. Mohri, F.B. Humphry, T. Manabe, H. Kawamura, J. Yamasaki, I. Ogasawara, "Bistable magnetization reversal in 50μm diameter annealed cold-drawn amorphous wires", *IEEE Transactions on Magnetics* **23(5)** 3242-3244 (1987)

[34] A. Chizhik, C. Garcia, J. Gonzalez, J.M. Blanco, "Investigation of magnetic structure in cold-drawn Fe-rich amorphous wire", *Journal of Magnetism and Magnetic Materials* **279** 359-362 (2004)

[35] H. Chiriac, E. Hristoforou, Maria Neagu, Firuta Barariu, I. Darie, "Inverse wiedemann effect in glass-covered amorphous wires", *Sensors and Actuator*s **81** 147-149 (2000)

[36] H. Chiriac, T.A. Ovari, Gh. Pop, Firuta Barariu, "Amorphous glass-covered magnetic wires for sensing applications", *Sensors and Actuators A* **59** 243-252 (1997)

[37] H. Chiriac, M. Tibu, V. Dobrea, "Magnetic properties of amorphous wires with different diameters", *Journal of Magnetism and Magnetic Materials* **290-291** 1142-1145 (2005)

[38] T. Meydan, "Influence of stress on Matteucci and search coil voltages in amorphous wires", *Journal of Magnetism and Magnetic Materials* **249** 382-386 (2002)

[39] V. Raposo, D. Garcia, M. Zazo, A.G. Flores, J.I. Iniguez, "Frequency dependence of the giant magnetoimpedance in current annealed amorphous wires", *Journal of Magnetism and Magnetic Materials* **272-276** 1463-1465 (2004)

[40] T. Sanchez, P. Alvarez, J. Olivera, M.J. Perez, F.J. Belzunce, J.D. Santos, J.L. Sanchez LI., M.L. Sanchez, P. Gorria, B. Hernando, "Torsion annealing influence on the impedance behaviour in amorphous FeSiB and CoSiB wires", *Journal of Non-Crystalline Solids* **353** 914-918 (2007)

[41] T. Meydan, F. Borza, N. Derebasi, "Large gyromagnetic effect in as-cast and post-poduction treated amorphous wires", *Sensors and Actuators A* **106** 278-281 (2003)

[42] N. Bayri, S. Atalay, "Giant stress-impedance effect in Fe71Cr7Si9B13 amorphous wires", *Journal of Alloys and Compounds* **381** 245-249 (2004)

[43] G. Bordin, G. Buttino, A. Cecchetti, M. Poppi, "Magnetoresistance and magnetic properties in amorphous Fe-based wires" *Journal of Magnetism and Magnetic Materials* **231** 179-184 (2001)

[44] K. Mohri, T. Kohzawa, K. Kawashima, H. Yoshida, L.V. Panina, "Magneto-inductive effect (MI effect) in amorphous wires", *IEEE Transactions on Magnetics* **28(5)** 3150-3152 (1992)

[45] L.V. Panina, K. Mohri, "Magneto-impedance effect in amorphous wires", *Applied Physics Letters* **65(9)** 1189-1191 (1994).

[46] S.K. Pal, A.K. Panda, M. Vazquez, A. Mitra, "The effect of magnetoelastic interaction on the GMI behaviour of Fe-, Co-, Co-Fe-based amorphous wires", *Journal of Materials Processing Technology* **172** 182-187 (2006)

[47] M.L. Sanchez, B. Hernando, J. Olivera, V.M. Prida, J.D. Santos, M.J. Perez, P. Gorria, "Torsion and magnetic field effect in the impedance of FeSiBNbCu soft magnetic amorphous wires", *Journal of Magnetism and Magnetic Materials* **304** e865-e867 (2006)

[48] A.A. Rakhmanov, N. Perov, P. Sheverdyaeva, A. Granovsky, A.S. Antonov, "The temperature dependence of the magneto-impedance effect in the Co-based amorphous wires", *Sensors and Actuators A* **106** 240-242 (2003)

[49] C. Moron, M.T. Carracedo, J.G. Zato, A. Garcia, "Stress and field dependence of the giant magnetoimpedance effect in Co-rich amorphous wires", *Sensors and Actuators A* **106** 217-220 (2003)

[50] J.G.S. Duque, A.E.P. De Araujo, M. Knobel, "Asymmetric impedance in field-annealed Co-based amorphous wires and its bias field dependence", *Journal of Magnetism and Magnetic Material*s **299** 419-424 (2006)

[51] R.S. Beach, N. Smith, C.L. Platt, F. Jeffers, A.E. Berkowitz, "Magneto-impedance effect in NiFe plated wire", *Applied Physics Letters* **68(19)** 2753-2755 (1996)

[52] Anatoly S. Antonov, Alexander L. Rakhmanov, Nikita A. Buznikov, Anatoly F. Prokoshin, Alexander B. Granovsky, Nicolai S. Perov, Nicolai A. Usov, "Magnetic properties and magneto-impedance of cold-draw permalloy-copper composite wires", *IEEE Transactions on Magnetics* **35(5)** 3640-3642 (1999)

[53] A.S. Antonov, N.A. Buznikov, A.B. Granovsky, I.T. Iakubov, A.F. Prokoshin, A.L. Rakhmanov, A.M. Yakunin, "Magnetization reversal process and nonlinear magneto-impedance in Cu/NiFe and Nb/NiFe composite wires", *Journal of Magnetism and Magnetic Materials* **249** 315-318 (2002)

[54] Tetsuya Osaka, Madoka Takai, Katsuyoshi Hayashi, Keishi Ohashi, Mikiko Saito, Kazuhiko Yamada, "A soft magnetic CoNiFe film with high saturation magnetic flux density and low coercivity", *Nature* **392** 796-798 (1998)

[55] F.E. Atalay, H. Kaya, S. Atalay, "Giant magnetoimpedance effect in electroplated CoNiFe/Cu wires with varying Ni, Fe and Co content", *Journal of Alloys and Compounds* **420** 9-14 (2006)

[56] L.P. Liu, Z.J. Zhao, J.C. Zhang, Z.M. Wu, J.Z. Ruan, Q.J. Wang, X.L. Yang, "Giant magneto-impedance and skin effect in CuBe/CoNiP composite wires", *Journal of Magnetism and Magnetic Materials* **305** 212-215 (2006)

[57] G.V. Kurlyandskaya, A. Garcia-Arribas, J.M. Barandiaran, "Advantages of nonlinear giant magnetoimpedance for sensor applications", *Sensors and Actuators A* **106** 234-239 (2003)

[58] J. Velleuer, A.G. Munoz, H. Yakabchuk, C. Schiefer, A. Hackl, E. Kisker, "Giant magneto impedance in electroplated NiFeMo/Cu microwires", *Journal of Magnetism and Magnetic Materials* **311** 651-657 (2007)

[59] N.A. Buznikov, A.S. Antonov, A.B. Granovsky, C.G. Kim, C.O. Kim, X.P. Li, S.S. Yoon, "Current distribution and giant magnetoimpedance in composite wires with helical magnetic anisotropy", *Journal of Magnetism and Magnetic Materials* **296** 77-88 (2006)

[60] N.A. Buznikov, A.S. Antonov, A.B. Granovsky, C.G. Kim, C.O. Kim, X.P. Li, S.S. Yoon, "Giant magnetoimpedance in composite wires with insulator layer between non-magnetic core and soft magnetic shell", *Journal of Magnetism and Magnetic Materials* **300** e63-e66 (2006)

[61] Richard M. Bozorth, "Ferromagnetism", D. Van Nostrand Company, Inc, 1st Edition (1951)

[62] W. Pepperhoff, M. Acet, "Constitution and Magnetism of Iron and its Alloy", Springer-Verlag Berlin Heidelberg (2001)

[63] Haiwen Xi, Bo Bian, Zailong Zhuang, David E. Laughlin and Robert M. White, "Annealing Effect on Exchange Bias in Ni81Fe19/Cr50Mn50 Bilayers", *IEEE Transactions on Magnetics* **36 (5)** 2644-2646 (2000)

[64] Taylor, W. P., Schneider, M., Baltes, H., & Allen, M. G., "Electroplated Soft Magnetic Materials for Microsensors and Microactuators" *1997 International Conference on Solid-state Sensors and Actuators, Chicago*, 1445-1448 (1997).

[65] Bai, A. & Hu, C. C. "Iron–cobalt and iron–cobalt–nickel nanowires deposited by means of cyclic voltammetry and pulse-reverse electroplating" *Electrochemistry Communications* ***5*** 78–82 (2003)

[66] Jerzy Bielinski and Jan Przyluski, "Selected Problems in the Continuous Electrodeposition of Ni-Fe Alloys," *Surface Technology* **9** 53-64 (1979)

[67] Wikipedia The Free Encyclopedia. *Supermalloy.* Retrieved March 21, 2007, from http://en.wikipedia.org/wiki/Supermalloy.

[68] Nie, H. B., Pakhomov, A. B., Yan, X., Zhang, X. X., & Knobel, M., "Giant magnetoimpedance in crystalline Mumetal", *Solid State Communications* ***112*** 285-289 (1999)

[69] Magnet Sales & Service Limited. *Cast Alcomax Magnets.* Retrieved March 20, 2007, from http://www.magnetsales.co.uk/magnets/castalcomax.html.

[70] Magnet Sales & Manufacturing Company, Inc. (2000). *Alnico Magnets.* Retrieved on March 21st 2007 from http://www.magnetsales.com/Alnico/Al1.htm.

[71] Abner Brenner, "Electrodeposition of Alloys – Principles and Practice – Volume 1", Academic Press, New York and London (1963)

[72] Abner Brenner, "Electrodeposition of Alloys – Principles and Practice – Volume 2", Academic Press, New York and London (1963)

[73] Mordechay Schlesinger, Milan Paunovic, "Modern Electroplating", John Wiley & Sons, Inc., New York (2000)

[74] N.V. Parthasaradhy, "Practical Electroplating Handbook", Prentice Hall, New Jersy (1989)

[75] Penny Tsay, Chi-Chang Hu and Chun-Kuo Wang, "Compositional effects on the physical properties of iron-nickel deposits prepared by means of pulse-reverse electroplating," *Materials Chemistry and Physics* **89** 275 – 282 (2005)

[76] Allen Bai and Chi-Chang Hu, "Compositional controlling of Co-Ni and Fe-Co alloys using pulse-reverse electroplating through means of experimental strategies," *Electrochimica Acta* **50** 1335-1345 (2005)

[77] K.-M. Yin, S.-L. Jan, C.-C. Lee, "Current Pulse with Reverse Plating of Nickel-Iron Alloys in a Sulphate Bath," *Surface and Coatings Technology* **88** 219-225 (1996)

[78] E. Beltowska-Lehman and A. Riesenkampf, "An Investigation of the Electrodeposition Kinetics of Permalloys Thin Films Using a Rotating Disc Electrode," *Surface Technology* **11** 349-355 (1980)

[79] K.-M. Yin and B.-T. Lin, "Effects of boric acid on the electrodeposition of iron, nickel and iron-nickel", *Surface and Coatings Technology* **78** 205-210 (1996)

[80] N. Feninche, A.M.Chaze, C.Coddet, "Effect of pH and current density on the magnetic properties of electrodeposited Co-Ni-P alloys", *Surface and Coatings Technology* **88** 264-268 (1996)

[81] Virginia Costa Kieling, "Parameters influencing the electrodeposition of Ni-Fe alloys," *Surface and Coatings Technology* **96** 135-139 (1997)

[82] D. Zhu, W.N. Lei, N.S. Qu, H.Y. Xu, "Nanocrystalline electroforming process", *CIRP Annals – Manufacturing Technology*, **51** 173-176 (2002)

[83] F.E. Atalay, S. Atalay, "Giant magnetoimpedance effect in NiFe/Cu plated wire with various plating thickness", *Journal of Alloys and Compound* **392** 322-328 (2005)

[84] R.A. McCurrie, "Ferromagnetic Materials: Structure and Propertie*s*", Academic Press Limited, New York, 40-43 (1994)

[85] William P. Taylor, Michael Schneider, Henry Baltes and Mark G. Allen, "A NiFeMo Electroplating Bath for Micromachined Structures", *Electrochemical and Solid-state Letters* **2(12)** 624-626 (1999)

[86] J Y Park and M G Allen, "Development of magnetic materials and processing techniques applicable to integrated micromagnetic devices", *Journal of Micromechanics and Microengineering* **8(4)** 307-316 (1998)

[87] K. Hoshino, M. Sano, S. Narumi and M. Fuyama, **"**Magnetic properties and thermal stability of electroplated NiFeCr and NiFeMo films with high resistivity**"** *IEEE Transactions on Magnetics* **35(5)** 3433-3435 (1999)

[88] J.M.D Coey, G.Hinds, M.E.G. Lyons, "Magnetic-field effects on fractal electrodeposits", *Europhysics Letters* **47(2)** 267-272 (1999)

[89] J.M.D Coey, G. Hinds, M.E.G. Lyons, "Magnetoelectrolysis of copper", *Journal of Applied Physics* **83(11)** 6447-6449 (1998)

[90] I. Mogi, M. Kamiko, "Striking effects of magnetic field on the growth morphology of electrochemical deposits", *Journal of Crystal Growth* **166** 276-280 (1996)

[91] C. O'Reilly, G. Hinds, J.M.D. Coey, "Effect of a Magnetic Field on Electrodeposition: Chronoamperometry of Ag, Cu, Zn, and Bi" *Journal of the Electrochemical Society* **148(10)** 674-678 (2001)

[92] O. Devos, O. Aaboubi, J.P. Chopart, E. Merienne, A. Olivier, and J. Amblard *"*Magnetic field effects on nickel electrodeposition*"*, *Journal of the Electrochemical Society*, **145(12)** 4135-4139 (1998)

[93] K. Msellak, J.-P. Chopart, O. Jbara, O. Aaboubi, J. Amblard, "Magnetic field effects on Ni-Fe alloys codeposition", *Journal of Magnetism and Magnetic Materials* **281** 295-304 (2004)

[94] T.Z. Fahidy, "Characteristics of surfaces produced via magnetoelectrolytic deposition", *Progress in Surface Science* **68** 155-188 (2001)

[95] J.M.D Coey, G. Hinds, "Magnetic electrodeposition", *Journal of Alloys and Compounds* **326** 238-245 (2001)

[96] Ibro Tabakovic, Steve Riemer, Ming Sun, Vladyslav A. Vas'ko, and Mark T. Kief, "Effect of Magnetic Field on NiCu Electrodeposition from Citrate Plating Solution and Characterization of Deposit", *Journal of The Electrochemical Society,* **152(12)** C851-C860 (2005)

[97] Ibro Tabakovic, Steve Riemer, Vladyslav Vas'ko, Victor Sapozhnikov,and Mark Kief, "Effect of Magnetic Field on Electrode Reactions and Properties of Electrodeposited NiFe Films", *Journal of The Electrochemical Society*, **150(9)** C635-C640 (2003)

[98] J.-Cl. Puippe, F. Leaman: "Theory and Practice of Pulse Plating", American Electroplaters and Surface Finishers Society, Orlando, Florida (1987)

[99] Hongqi Li, Fereshteh Ebrahimi, "Synthesis and characterization of electrodeposited nanocrystalline nickel–iron alloys", *Materials Science and Engineering: A* **347** 93-101 (2003)

[100] C. Cheung, F. Djuanda, U. Erb, G. Palumbo, "Electrodeposition of nanocrystalline Ni-Fe alloys", *Nanostructured Materials* **5(5)** 513-523 (1995)

[101] G. Herzer, "Grain size dependence of coercivity and permeability in nanocrystalline ferromagnets" *IEEE Transactions on Magnetics* **26(5)** 1397-1402 (1990)

[102] Beddoes J., Bibby M. J., "Principles of Metal Manufacturing Processes*",* London: Arnold (1999)

[103] Song, J. S., Ahn, J. H., Kim, H. S., & Hong, S. I., "Comparison of microstructure and strength in wire-drawn and rolled Cu-9 Fe-1.2 Ag filamentary microcomposite", *Journal of Materials Science* **36** 5881-5884 (2001)

[104] Överstam H., "The influence of bearing geometry on the residual stress state in cold-drawn wire, analysed by the FEM" *Journal of Materials Processing Technology* **171** 446-450 (2006)

[105] Sawamiphakdi, K., Lahoti, G. D., Gunasekera, J. S., Kartik, R., "Development of utility programs for a cold-drawing process", *Journal of Materials Processing Technology* **80–81** 392–397 (1998)

[106] Vazquez, M., Garcia-Benetez, J. M., Sinnecker, J. P., & Li, L, "Magneto-impedance effect in high permeability NiFeMo permalloy wires", *Journal of Applied Physics* **83** 6578-6580 (1998)

[107] Schaffer, J. E., Gordon, R.,"Engineering characteristics of drawn filled nitinol tube", *Proceedings of the International Conference on Shape Memory and Superelastic Technology, California, USA* (2003)

[108] Elgun, S. Z. (1999). *Annealing*. Retrieved March 28th, 2007, from http://info.lu.farmingdale.edu/depts/met/met205/annealingstages.html.

[109] Callister W. D., "Materials Science and Engineering: An Introduction" (6th ed.). New York: John Wiley (1985)

[110] M. Knobel, K.R. Pirota, "Giant magnetoimpedance: concepts and recent progress" *Journal of Magnetism and Magnetic Materials* **242** 33-40 (2002)

[111] B. Hernando, V. M. Prida, M. L. Sanchez, P. Gorria, G. V. Kurlyandskaya, M. Tejedor and M. Vazquez, "Magnetoimpedance effect in Co-rich metallic glasses", *Journal of Magnetism and Magnetic Materials* **258-259**183-188 (2003)

[112] D.Garcia, G.V.Kurlyandskaya, M.Vázquez, F.I.Toth, L.K.Varga. "Influence of filed annealing on the hysteretic behaviour of the giant magneto-impedance effect of Cu wires covered with $Ni_{80}Fe_{20}$ outer shells". *Journal of Magnetism and Magnetic Materials* **203** 208-210(1999)

[113] W. Bruckner, S. Baunack, M. Hecker, J.-I. Monch, L. van Loyen and C.M.Schneider, "Interdiffusion in NiFe/Cu/NiFe trilayers: Possible failure mechanism for magnetoelectronic devices", *Applied Physics Letters* **77(3)** 358-360(2000)

[114] M. Hecker, D. Tietjen, H. Wendrock, C. M. Schneider, N.Cramer, L.Malkinski, R.E.Cramley, Z.Celinski., "Annealing effects and degradation mechanism of NiFe/Cu GMR multilayers", *Journal of Magnetism and Magnetic Materials* **247** 62-69 (2002)

[115] John E. Mahan, "Physical vapor deposition of thin films", John Wiley & Sons, Inc., New York (2000)

[116] P.J. Kelly, R.D. Arnell, "Magnetron sputtering: a review of recent development and applications", *Vacuum* **56** 159-172 (2000)

[117] B. Window, N. Savvides, “Unbalanced DC magnetrons as sources of high ion fluxes”, *Journal of Vacuum Science Technology A* **4(3)** 453-456 (1986)

[118] N. Savvides, B. Windows, “Unbalanced magnetron ion-assisted deposition and property modification of thin films”, *Journal of Vacuum Science Technology A* **4(3)** 504-508 (1986)

[119] P.J. Kelly, R.D. Arnell, “Characterization studies of the structure of Al, Zr, and W coatings deposited by closed-field unbalanced magnetron sputtering”, *Surface and Coating Technology* **97** 595-602 (1997)

[120] M.W. Ormston, A.K. Petford-Long, D.G. Teer, “Study of magnetic thin films deposited by closed-field unbalanced magnetron sputtering”, *Journal of Applied Physics* **85(8)** 5747-5749 (1999)

[121] John A. Thornton, “Influence of apparatus geometry and deposition conditions on the structure and topography of thick sputtered coatings”, *Journal of Vacuum Science Technology A* **11(4)** 666-670 (1986)

[122] John A. Thornton, “The microstructure of sputter-deposited coatings”, *Journal of Vacuum Science Technology A* **4(6)** 3059-3065 (1986)

[123] A. Zendehnam, M. Ghanati, M. Mirzaei, “ Study and comparison of deposition rates, grain size of Ag and Cu thin films with respect to sputtering parameters, and annealing temperature.”, *Journal of Physics: Conference Series* **61** 1322-1325 (2007)

[124] Z.S. Zhang, L. Yang, C.C. Yang, B.C. Cai, “Effect of sputtering parameters on the magnetic properties of Mo-Permalloy”, *Journal of Applied Physics* **64(10)** 5670-5672 (1988)

[125] Prasanna Shah, A. Gavin, “Effect of varying sputtering parameters on the observation of magnetic domains using high-resolution Bitter microscopy technique” *Journal of Applied Physics* **99** 08H305-1-3 (2006)

[126] Robert G. Johanson, William G. Carruthers, “In-line sputtering parameters for magnetic recording films”, *Journal of Vacuum Science Technology A* **4(3)** 550-552 (1986)

[127] Masayuki Sagoi, Reiji Nishikawa, Toshiyuki Suzuki, “Film structure and magnetic properties for Co-Cr sputtered films”, *IEEE Transactions on Magnetics* **20(5)** 2019-2024 (1984)

[128] Z.S. Zhang, L. Yang, C.C. Yang, B.C. Cai, “Effect of sputtering parameters on the magnetic properties of Mo-Permalloy”, *Journal of Applied Physics* **64(10)** 5670-5672 (1988)

[129] B. Warot, J. Imrie, A.K. Petford-Long, J.H. Nickel, T.C. Anthony, “Influence of seed layers on the microstructure of NiFe layers”, *Journal of Magnetism and Magnetic Materials* **272-276** e1498-e1496 (2004)

[130] R.S. Tebble, “Magnetic Domains”, Bulter and Tanner Ltd, Frome and London (1969)

[131] J.P. Jakubovics, “Magnetism and magnetic materials”, The Institute of Metals, Brookfield, USA (1987)

[132] E.C. Stoner, F.R.S., E.P. Wohlfarth, “A mechanism of magnetic hysteresis in heterogeneous alloys”, *IEEE Transactions on Magnetics* **27(4)** 3475-3518 (1991)

[133] R.A. McCurrie, “Ferromagnetic materials: structure and properties”, Academic Press Limited, San Diego, USA (1994)

[134] F. Pfeiffer, C. Radeloff, “Soft magnetic Ni-Fe and Co-Fe alloys - some physical and metallurgical aspects”, *Journal of Magnetism and Magnetic Materials* **19(1-3)** 190-207 (1980)

[135] G. Herzer, “Grain structure and magnetism of nanocrystalline ferromagnets” *IEEE Transactions on Magnetics* **25(5)** 3327-3329 (1989)

[136] R. Alben, J.J. Becker, M.C. Chi, “Random anisotropy in amorphous ferromagnets” *Journal of Applied Physics* **49** 1653-1658 (1978)

[137] Giselher Herzer, “Nanocrsyalline Soft Magnetic Alloys” *Handbook of Magnetic Materials* **10** 418-462 (1997)

[138] O. Kazakova, M. Hanson, P. Blomquist, R. Wappling, “Arrays of epitaxial Co submicron particles: Critical size for single-domain formation and multidomain structures”, *Journal of Applied Physics* **90(5)** 2440-2446 (2001)

[139] C.N. Chinnasamy, B. Jeyadevan, K. Shinoda, K. Tohki, D.J. Djayaprawira, M. Takahashi, R. Justin Joseyphus, A. Narayanasamy, “Unusually high coercivity and critical single-domain size monodispersed CoFe2O4 nanoparticles”, *Applied Physics Letters* **83(14)** 2862-2864 (2003)

[140] Carlo Luna, M del Puerti Morales, Carlos J Serna, Manuel Vazquez, “Multidomain to single-domain transition for uniform Co80Ni20 nanoparticles” *Nanotechnology* **14** 268-272 (2003)

[141] M. Knobel, M. Vazquez, L. Kraus, “Giant magnetoimpedance” *Handbook of Magnetic Materials* **15** 497-563 (2003)

[142] K.R. Pirota, L. Kraus, H. Chiriac, M. Knobel, “Magnetostriction and GMI in Joule-heated CoFeSiB glass-covered microwires” *Journal of Magnetism and Magnetic Materials* **226-230** 730-732 (2001)

[143] A.S. Antonov, N.A. Buznikov, I.T. Iakubov, A.N. Lagarkov, A.L. Rakhmanov, “Nonlinear magnetization reversal of Co-based amorphous microwires induced by an ac current” *Journal of Physics D: Applied Physics* **34** 752-757 (2001)

[144] G.V. Kurlyandskaya, E.Krisker, H. Yakabchuk, N.G. Bebenin, "Non-linear giant magnetoimpedance" *Journal of Magnetism and Magnetic Material* **240** 206-208 (2002)

[145] J. Hernando, J.M. Barandiaran, "Circular magnetization measurement in ferromagnetic wires", *Journal of Physics D: Applied Physics* **11** 1535-1538 (1978)

[146] R.S. Beach, A.E. Berkowitz, "Sensitive field- and frequency-dependent impedance spectra of amorphous FeCoSiB wire and ribbon", *Journal of Applied Physics* **76(10)** 6209-6213 (1994)

[147] L. Landau, E.M. Lifshitz, "Electrodynamics of continuous media", Pergamon Press, London (1975)

[148] L.V. Panina, K. Mohri, T. Uchiyama, M. Noda, "Giant magneto-impedance in Co-riched amorphous wires and films", *IEEE Transactions on Magnetics* **31(2)** 1249-1260 (1995)

[149] Raul Valenzuela, Israel Betancourt, "Giant magnetoimpedance, skin depth and domain wall dynamics" IEEE Transactions on Magnetics **38(5)** 3081-3083 (2002)

[150] R. Valenzuela, "The analysis of magnetoimpedance by equivalent circuits", *Journal of Magnetism and Magnetic Materials* **249** 300-304 (2002)

[151] R. Valenzuela, "Low-frequency magnetoimpedance: domain wall magnetization processes" *Physica B* **299** 280-285 (2001)

[152] L. Kraus, "Theory of giant-impedance in the planar conductor with uniaxial magnetic anisotropy", *Journal of Magnetism and Magnetic Materials* **195** 764-778 (1999)

[153] K.R. Pirota, L. Kraus, M.Knobel, P.G. Pagliuso, C. Rettori, "Angular dependence of giant magnetoimpedance in an amorphous Co-Fe-Si-B ribbon", *Physical Review B* **60(9)** 6685-6691 (1999)

[154] A. Yelon, D. Menard, M. Britel, P. Ciureanu, "Calculations of giant magnetoimpedance and of ferromagnetic resonance response are rigorously equivalent", *Applied Phyiscs Letters* **69(20)** 3084-3085 (1996)

[155] P. Ciureanu, C. Akyel, M. Britel, J. Gauthier, A. Yelon, "Rf and uhf giant magnetoimpedance effects in soft magnetic fibers and wires", *IEEE Transactions on Magnetics* **32(5)** 4678-4680 (1996)

[156] D. Menard, M. Britel, P. Ciureanu, A. Yelon, V.P. Paramonov, A.S. Antonov, P. Rudkowski, J.O. Strom-Olsen, "High frequency impedance spectra of soft amorphous fibers" *Journal of Applied Physics* **81(8)** 4032-4034 (1997)

[157] O. Acher, J.L. Vermeulen, P.M. Jacquart, J.M. Fontaine, P. Baclet, "Permeability measurement on ferromagnetic thin films from 50MHz up to 17 GHz" *Journal of Magnetism and Magnetic Materials* **136** 269-278 (1994)

[158] A.D.C. Viegas, A.M.H. de Andrade, R.L. Sommer, J.S. Jiang, C.L. Chien, "Magneto-impedance in Fe73.5Cu1Nb3Si13.5B9 amorphous films at microwave frequencies", *Journal of Magnetism and Magnetic Materials* **226-230** 707-708 (2001)

[159] B.D. Cullity, S.R. Stock, "Elements of x-ray diffraction, Prentice Hall", Inc. (3rd Ed.) New Jersy, US (2001)

[160] S.E. Hadian, D.R. Gabe, "Residual stresses in electrodeposits of nickel and nickel–iron alloys" *Surface and Coatings Technology* **122** 118-135 (1999)

[161] David Jiles, *Introduction to magnetism and magnetic materials*, Bury St Edmunds, Sufflok, GB, St Edmundsbury Press Ltd, 1991.

[162] N. Usov, A. Antonov, A. Granovsky, "Theory of giant magneto-impedance effect in composite amorphous wire," *Journal of Magnetism and Magnetic Materials* **171** 64-68 (1997)

[163] L. Ricq_, F. Lallemand, M. P. Gigandet, J. Pagetti, "Influence of sodium saccharin on the electrodeposition and characterization of CoFe magnetic film", *Surface and Coatings Technology* **138** 278-283 (2001)

[164] D. Mockute, G. Bernotiene, "The interaction of additives with the cathode in a mixture of saccharin, 2-butyne-1, 4-diol and phthalimide during nickel electrodeposition in a Watts-type electrolyte", *Surface and Coatings Technology* **135** 42-47 (2000)

[165] T. C. Franklin, "Some mechanisms of action of additives in electrodeposition processes", *Surface and Coatings Technology*, **30** 415-428 (1987)

[166] L. Oniciu, L. Muresan, "Some fundamental aspects of leveling and brightening in metal electrodeposition", *Journal of Applied Electrochemistry* **21** 565-574 (1991)

[167] Tetsuya Osaka, Takahiro Sawaguchi, Fumio Mizutani, Tokihiko Yokoshima, Madoka Takai, Yutaka Okinaka, "Effects of Saccharin and Thiourea on Sulfur Inclusion and Coercivity of Electroplated Soft Magnetic CoNiFe Film", *Journal of the Electrochemical Society* **146 (9)** 3295-3299 (1999)

[168] Y.-F. Li, M. Vazquez, et al, **"**Giant magnetoimpedance effect and magnetoelastic properties in stress-annealed FeCuNbSiB nanocrystalline wire**",** *IEEE Transactions on Magnetics* **38** 3096-3098 (2002)

[169] M. Knobel, M. L. Sanchez, J. Velazquez, and M. Vazquez, "Stress dependence of the giant magneto-impedance effect in amorphous wires", *Journal of Physics: Condense Matter* **7** L115-L120 (1995)

[170] S.S. Yoon, S. C. Yu, G. H. Ryu, C.G. Kim, "Effect of annealing on anisotropy field in Fe84Zr7B8Cu1 amorphous ribbons evaluated by giant magnetoimpedance", *Journal of Applied Physics* **85** 5432-5434 (1999)

[171] J M Barandiarán, A García-Arribas, J L Muñoz, and G V Kurlyandskaya, "Influence of magnetization processes and device geometry on the GMI effect**",** *IEEE Transactions on Magnetics* **38(5)** 3051-3056 (2002)

[172] F. Ebrahimi, Hongqi Li, "Grain growth in electrodeposited nanocrystalline fcc Ni-Fe alloys", *Scripta Materialia* **55(3)** 263-266 (2006)

[173] X.P. Li, Z.J.Zhao, T.B.Oh, H.L.Seet, "Effect of Magnetic Field on the Magnetic Structure of Nanocrystalline Electroplated NiFe Layers", *Journal of Metastable and Nanocrystalline Materials* **23** 167-170 (2005)

[174] H.B. Nie, A.B. Pakhomov, X. Yan, X.X. Zhang, M. Knobel, "Giant magnetoimpedance in crystalline Mumetal", *Solid State Communications* **112** 285-289 (1999)